КОНДЕНСИРОВАННЫЕ СРЕДЫ И МЕЖФАЗНЫЕ ГРАНИЦЫ

CONDENSED MATTER AND INTERPHASES

Sc 21 44.956 Scandium
Ti 22 47.867 Titanium
V 23 50.942 Vanadium
Cr 24 51.996 Chromium
Y 39 88.906 Yttrium
Zr 40 91.224 Zirconium
Nb 41 92.906 Niobium
Mo 42 95.94 Molybdenum

Научный журнал по проблемам конденсированного состояния
и физико-химическим процессам
на границах раздела фаз и в их объеме

The scientific journal "Kondensirovannye sredy i mezhfaznye granitsy"
(CONDENSED MATTER AND INTERPHASES)
is the leading scientific publication in Russia on key problems
of condensed matter and physico–chemical processes
at the interfaces and in the volume.

Co 27 58.933 Cobalt
Ni 28 58.693 Nickel
Cu 29 63.546 Copper
Rh 45 102.91 Rhodium
Pd 46 106.42 Palladium
Ag 47 107.87 Silver
Ir 77 192.22 Iridium
Pt 78 195.08 Platinum
Au 79 196.97 Gold

Condensed Matter and Interphases
(Kondensirovannye sredy i mezhfaznye granitsy)

Peer-reviewed scientific journal
Issued 4 times a year

Volume 22, No. 3 (2020)

Full-text version is available in the Russian language
on the website: https://journals.vsu.ru/kcmf/about

CONTENTS

Condensed Matter and Interphases
(Kondensirovannye sredy i mezhfaznye granitsy)

Random First Order Transition from a Supercooled Liquid to an Ideal Glass (Review)

© 2020 Yu. V. Agrafonov✉, I. S. Petrushin

Irkutsk State University,
1 ul. Karla Marksa, Irkutsk 664003, Russian Federation

Abstract

The random first order transition theory (RFOT) describing the transition from a supercooled liquid to an ideal glass has been actively developed over the last twenty years. This theory is formulated in a way that allows a description of the transition from the initial equilibrium state to the final metastable state without considering any kinetic processes. The RFOT and its applications for real molecular systems (multicomponent liquids with various intermolecular potentials, gel systems, etc.) are widely represented in English-language sources. However, these studies are practically not described in any Russian sources. This paper presents an overview of the studies carried out in this field.

Keywords: supercooled liquid, ideal glass, distribution functions, replicas, random first order transition.

Introduction

Equilibrium statistical physics views a macroscopic body as a system consisting of an infinite number of identical subsystems (replicas). Intermolecular interactions within each replica are identical, which ensures the microscopic homogeneity of the body. The probability distribution of each subsystem over various phases is described by means of the Gibbs measure. This is based on the ergodic hypothesis which states that macroscopic averages are equal to the averages of the Gibbs ensemble. Using the Gibbs distribution we can calculate the average of any observable either directly, employing the statistical integral, or using the particle size distribution functions of the positions of several particles in set points at the same time.

The ergodic hypothesis, however, is not applicable to metastable states. The random distribution of particles between fixed points results in local microscopic inhomogeneity. At the moment, there are two approaches used to describe the structure of the amorphous state: phenomenological approach and the method of particle size distribution functions employed in equilibrium statistical physics. The phenomenological approach [1] is based on intuitive ideas regarding the local structure of glass and its connection with the glass transition and melting temperatures. However, it does not describe the physics of the glass transition of melts [2]. [3] attempts to provide a microscopic explanation of the particle confinement time in melts.

According to the method of particle size distribution functions [4], the glass transition is performed following a specific increase in the density or a decrease in the temperature of the metastable system. Glass transition is determined

✉ Yuri V. Agrafonov, e-mail: agrafonov@physdep.isu.ru

substantially by the kinetic phenomena depending on the heat removal rate and the duration of the structural transformation. Therefore, there is still no single opinion regarding the way we can use the notions of thermodynamic equilibrium to describe metastable states.

[5, 6, 7] present heuristic considerations pertaining to the transition from a supercooled liquid to an ideal glass. A breakthrough was made by Mezard and Parisi [8] followed by further studies [3, 9–27] that formulated the replica theory of the "Random First Order Transition" (RFOT) based on the modernised method of particle size distribution functions. Replicas are identical copies of subsystems. Analogous to the systems in the state of thermodynamic equilibrium, the molecular interaction within the replicas is identical. It was determined, however, that the replicas themselves interact with each other. The parameters of the interaction are set so that the mean distance between the particles is smaller than that in a liquid. Basically, this is how we can differentiate between a supercooled liquid and an ideal glass. We can thus describe the transition from the initial equilibrium state to the final metastable state without considering any kinetics processes. The RFOT and its applications for real molecular systems (multicomponent liquids with various intermolecular potentials [28–31], viscous fluids and gel-like liquids [32–39], colloids [40–41], medicinal solutions [42–43], amorphous polymers [44], polydisperse crystals [45–48], etc.) are widely represented in English-language scientific literature. However, these studies are practically not mentioned in any Russian sources. The significance of the replica theory is similar to that of the Gibbs canonical distribution and the integral equations method used in the statistical theory of liquids in the state of thermodynamic equilibrium. It should be noted, however, that the RFOT does not in any way describe relaxation processes. The integral equations for particle size distribution functions only describe the structural characteristics of thermodynamic equilibrium and metastable states reached through infinitely large time intervals. Microscopic description of the kinetic processes occurring in dense gases and liquids is based on the Bogoliubov–Born–Green–Kirkwood–Yvon hierarchy [49] for nonequlibrium

particle size distribution functions. This field of study is now actively being developed, but it is out of the scope of this paper. Listed below are just a few studies focusing on the issues closely related to the problem discussed in this paper. [50–51] focus on various implementations of the Bogoliubov and Boltzmann equations, particularly for granular media [52]. [53] develops a model for discrete velocity-jumps in a molecular system. [54] describes the asymptotic behaviour of the observables of a low-density fluid. [55] analyses the transport processes within a system of hard spheres.

There are also studies focusing on the thermodynamic [56–61], statistical [62-66], and kinetic [67–68] aspects when describing the transition of hard spheres and multidimensional hyperspheres from liquid to solid states [69–71].

2. Theoretical part

2.1. The method of distribution functions in the study of fluids

The statistical physics of fluids is based on the BBGKY (Bogoliubov–Born–Green–Kirkwood–Yvon) hierarchy for l-particle distribution functions $G_{l,...,i} = (\mathbf{r}_l,...,\mathbf{r}_i)$, equivalent to the Gibbs canonical distribution. The particles interact through the pair potential $\Phi_{ij}(r_{ij})$, where $r_{ij} = |\mathbf{r_i} - \mathbf{r_j}|$ is the distance between the centres of the particles i, j. By subsequently removing higher-order distribution functions from the equation chain, we can transform the BBGKY hierarchy into the Ornstein–Zernike (OZ) equation [72–73] describing single- and two-particle distribution functions

$$\omega_1 = n \int G_2 C_{12}^{(1)} d(2) + \mu,$$
$$h_{12} = C_{12}^{(2)} + n \int G_3 C_{13}^{(2)} h_{23} d(3), \tag{1}$$

The integration is performed over the coordinates of the ith particle, $d(i) = d\mathbf{r}_i$, n is the density. A single-particle distribution function can always be represented as $G_i = \exp(-\Phi_i / kT + \omega_i)$, where the first summand in the exponent describes the direct interaction of the particle with the external field Φ_i, while the second summand describes the indirect interaction via the environment. The chemical potential μ is determined using the conditions of the transition to a spatially homogeneous

system in the absence of external fields. The pair correlation function $h_{ij} = \exp(-\Phi_{ij}/kT + \omega_{ij}) - 1$ is presented as a direct interaction of two particles Φ_{ij} and their indirect interaction with the environment ω_{ij}. Direct correlation functions $C_{ij}^{(k)}$

$$C_{ij}^{(1)} = h_{ij} - \omega_{ij} - 1/2 h_{ij}\left(\omega_{ij} + M_{ij}^{(1)}\right);$$
$$C_{ij}^{(2)} = h_{ij} - \omega_{ij} + M_{ij}^{(2)} \tag{2}$$

are represented as infinite functional series $M_{ij}^{(1)}$, $M_{ij}^{(2)}$ of the required distribution functions. When using these series to solve particular problems, we use only those summands that can be summed, while leaving out the others. As a result, we obtain a connection (closure) between the direct and pair correlation function, which makes the OZ equation approximate to nonlinear integral equations that have numerical solutions. The most common are the hypernetted chain, Percus–Yevick, Rogers–Young, and Martynov–Sarkisov closures [72–75].

Of great importance are also spatially homogeneous isotropic media (isotropic fluids without external fields and far from boundary surfaces), where $G_1(\mathbf{r}) \equiv 1$, $\omega_1(\mathbf{r}) \equiv 0$, $C_{12}^{(1)}(\mathbf{r}_1, \mathbf{r}_2) = C_{12}^{(1)}(r_{12})$. As a result, the first equation in the system (1–2) is reduced to the definition of the excess chemical potential $\mu = \ln a = \mathrm{const}$. The second equation in the system determines the direct correlation function $C_{12}^{(2)}(\mathbf{r}_1, \mathbf{r}_2) = C_{12}^{(2)}(r_{12})$, which can be calculated using a number of well-established methods. We should note that the Percus–Yevick equation includes the direct correlation function $C_{12}^{(2)}(r_{12}) = h_{12} - \left(\exp(\omega_{12}) - 1\right)$. Consequently, the exponential nonlinearity for a hard sphere system is replaced by the quadratic nonlinearity, i.e. decreases significantly. Therefore, we can obtain an analytical solution for the function $C_{12}^{(2)}(r_{12})$ [74, 76].

For spatially inhomogeneous systems (a molecular system near hard surface), functions $G_1(\mathbf{r}_1)$, $G_{12}(\mathbf{r}_1, \mathbf{r}_2)$ help to determine the microstructure of the substance and calculate all thermodynamic parameters. We should note that for the multivariable functions, a substantial numerical calculations are required to solve the equations (1–2). To simplify the calculation process, we can replace the direct correlation function $C_{12}^{(1)}(\mathbf{r}_1, \mathbf{r}_2)$ (the so-called singlet approximation) with its boundary value $C_{12}^{(1)}(r_{12})$. Then, depending on the closure used in the calculation, $M_{ij}^{(1)}$, we obtain a certain nonlinear integral equation for a single-particle distribution function depending on a single variable, namely the distance between the particle and the surface. This equation is also solved numerically, but is much less resource intensive. The existing approaches are described in [77–79].

The analytical solution for a single-particle distribution function is only possible in individual cases, for instance, for one-dimensional and two-dimensional liquids [80]. An analytical solution of the singlet Percus–Yevick equation for a three-dimensional hard sphere system on the boundary with a hard surface was suggested in our earlier study [81]. The key idea is that all the summands left out in (2) are taken into account so that they could compensate for all the nonlinearities. Due to its axial symmetry, a single-particle distribution function depends only upon the coordinate z which denotes the distance between the particle and the hard surface. As a result, we obtain the following linear integral equation

$$e^{\omega_1(z_1)} - 1 = 2\pi n \int_0^\infty dz_2 (e^{\omega_1(z_2)} - 1) \int_{|z_{12}|}^\infty r_{12} dr_{12} C_{12}^{(1)}(r_{12}) -$$
$$-2\pi n \int_{z_1}^\infty dz_{12} \int_{|z_{12}|}^\infty r_{12} dr_{12} C_{12}^{(1)}(r_{12}), \tag{3}$$

which takes into account the fact that the liquid particles interact with the surface through the hard sphere potential $G_i = \exp(\omega_i)$. This equation is a linear Fredholm integral equation of second kind. It can be solved analytically, if the kernel and the right-hand side of the equation are solved analytically. Other closures first require a numerical solution of the corresponding integral equations. Then, standard application software packages can be used to solve the Fredholm integral equation numerically. This framework is significantly easier as compared to the solution of the equation system (1)–(2) for multivariable functions.

2.2. The main approaches to the description of the liquid–glass transition

When a liquid temperature falls rapidly below the crystallisation temperature T_f the liquid goes through a number of metastable

states before forming a stable amorphous phase. This phenomenon was well investigated by means of numerous calorimetric measurements, dielectric and spin relaxation, nuclear magnetic-resonance, and neutron scattering on various materials. However, despite the obvious progress reached in [12–15], the theory behind this phenomenon is still incomplete. Presented below is the commonly acknowledged approach to the description of the amorphisation of a supercooled liquid. At the temperature $T_c < T_f$ the kinetic transition to the equilibrium state is predicted by the phase connectivity theory. The chaos (ergodicity), however, is distorted by dynamic processes. Calorimetric measurements of supercooled liquids indicate rapid alterations in the molar volume or the enthalpy as the function of temperature. When the calorimetric glass transition temperature is $T_g < T_c$, the specific heat capacity C_p reaches its maximum. However, since T_g depends on the cooling rate, it is not a characteristic parameter of the material; T_g decreases at a lower cooling rate. Therefore, the "calorimetric glass transition" is not a true phase transition. In fact, the temperature T_g fixes the temperature at which the duration of structural relaxation becomes compatible with the experimental value (usually in minutes or hours). The temperature T_g is determined by comparing the Maxwell relaxation time $\tau_M = \eta / G_\infty$ (where τ is the shear viscosity and G_∞ is the instantaneous shear modulus) to the experimental value $\tau_{\text{exp}} = 10^3$ s. When the shear modulus is $G_\infty = 10^9 Nm^{-2}$, which is common for most materials, T_g is defined as the temperature at which the shear viscosity reaches $\tau = 10^{12} N \cdot m^{-2} \cdot s$ (or 10^{13} poise).

At a temperature of $T < T_g$ a supercooled liquid is always in a metastable state. At the same time, the calorimetric measurements predict the entropy crisis (Kauzmann temperature) at the temperature of $T = T_K$, when the configurational entropy S_{conf} of the supercooled liquid disappears (equals zero or becomes insignificant). The possible connection between the disappearance of S_{conf} and the change in the time of structural relaxation of an extremely supercooled liquid is determined by the phenomenological Vogel–Fulcher–Tamman equation for highly viscous liquids $\eta = \eta_0 \exp(-A/(T - T_0))$. It was then assumed that $T_0 = T_K$. A detailed analysis of the structural relaxation time for glasses is performed in [82]. The hierarchy of the characteristic length scales in liquid-glass transitions is considered in [83–85].

The key concept is that the Kauzmann temperature precedes the transition of a supercooled liquid into glass. The transition corresponds to a lower non-crystalline minimum of the dependence of the free energy on the temperature. An ideal glass is characterised by chaotic equilibrium position of the particles in the space $\{X_i\}$ $(1 \le i \le N)$. This kind of random first order transition is a formal analogue of the mean field theory of spin glasses [10–11, 86–88]. This concept was effectively employed by the replica model (random first order transition). The replicas, or copies (clones), of a multiparticle system are used to define the parameter (configurational overlap) that helps to differentiate between supercooled liquids and glasses. The two states have identical spatial symmetry and similar unordered microscopic structure, as opposed to the translational symmetry of the crystals. Various modifications of the RFOT theory are considered in [9, 22–25].

Generally, the studies using the RFOT theory consider m replicas. Every atom of each replica interacts with all the atoms of the other $m-1$ replicas. The most basic option [89] is to consider ($m = 2$) two weakly coupled replicas and calculate the statistical correlations between them based on the numerical solution of the hypernetted-chain and Rogers–Young (RY) integral equations in a wide range of thermodynamic states. The study demonstrated that in the limit of vanishing inter-replica coupling, there are three branches of solutions for the pair distribution function. The main drawback of this study is the fact that the hypernetted-chain integral equation is thermodynamically inconsistent and too rough for high densities [74]. The equilibrium thermodynamics of glass is determined using the free-energy functional of Morita and Hiroike, which allows analytical calculation for any number of replicas m, followed by the limit transition $m \to 1$ [12–15]. This elegant approach was first applied to "soft spheres" and their mixtures and then extended to hard sphere models.

The calculations of the free energy and configurational overlap predict a random first order transition from a supercooled liquid to glass. The present-day situation in this field of study is described in [90].

3. The replica method as applied to the description of the liquid-glass transition

3.1 A two-replica model

Let us consider N particles of each replica (marked as a and b) interacting through the repulsive potential of "soft spheres"

$$v(r) = \varepsilon(\sigma / r)^n, \qquad (4)$$

where ε and σ are the characteristic energy and the size of the particle, $\rho^* = N\sigma^3 / V$ is the dimensionless density (σ is the characteristic size of the particle, V is the volume), and $T^* = k_B T / \varepsilon$. Therefore, the distance can be measured in dimensionless units $x = r / \sigma$. The applicability of the potential (4) to real systems is supported by two assumptions. The first is that the dependence of thermodynamic properties on the temperature and density is determined by a single parameter $\Gamma = \rho^* / T^{*3/n}$, rather than by ρ^* and T^* separately. Therefore, the excess Helmholtz free energy for one particle is

$$\frac{F^{ex}(\rho,T)}{Nk_B T} = f_{ex}(\Gamma). \qquad (5)$$

At the same time, the pair distribution function is invariant to the arbitrary scale parameter λ

$$g(x,\rho^*,T^*) = g(\lambda x, \rho^* / \lambda^3, T^* / \lambda^{12}). \qquad (6)$$

The second assumption is proved by the results of the numerical experiment [91], which demonstrated that $n = 12$ is crystallised to a face-centred cubic lattice, if $\Gamma = \rho^* / T^{*1/4} = \Gamma_f = 1.15$ [7, 88–89].

We should take into account that the atoms of identical replicas interact through the pair potential $v_{aa}(r) \equiv v_{bb}(r) = v(r)$, while the pair potential $v_{ab}(r)$ of the atoms of different replicas is of attractive type

$$v_{\alpha\beta}(x) = -\varepsilon_{\alpha\beta} w(x) = -\varepsilon_{\alpha\beta} \left[\frac{c^2}{x^2 + c^2} \right]^6. \qquad (7)$$

The constant C was chosen so that the size of the interaction area was smaller than the mean distance between the neighbouring atoms $d^* = d / \sigma \simeq \rho^{*-1/3}$, i.e. $A/d^* \ll 1$. Thus, due to strong repulsion between the atoms within one replica they interact with a larger number of atoms of the other replica. For the non-zero $\varepsilon_{\alpha\beta}$ the interaction (2) reduces the mean distance between the atoms of the other replica at lower temperatures. The exact value of the function $w(r)$ is irrelevant, since we focus on the limit $\varepsilon_{\alpha\beta} \to 0$. Full potential energy of the two replicas equals

$$V_{N,N}(\{x_i^1\},\{x_j^2\}) = \sum_i \sum_{j>i} v(|x_i^1 - x_j^1|) + \\ + \sum_i \sum_{j>i} v(|x_i^2 - x_j^2|) + \sum_i \sum_{j>i} v(|x_i^1 - x_j^2|), \qquad (8)$$

where $\{x_i^1\},\{x_j^2\}$ is a set of coordinates of the particles of each replica. The equilibrium structure of the two replicas is determined by two pair distribution functions, $g_{11}(x) \equiv g_{22}(x)$ and $g_{12}(x) \equiv g_{21}(x)$ respectively. The summands corresponding to the cross coupling in the equation (8) disturb the scaling invariance characteristic of the interaction between soft spheres (4). This means that the equilibrium properties of the two-replica system depend on two thermodynamic values as the function of the parameter Γ. The scaling invariance is restored for completely uncorrelated replicas ($\varepsilon_{12} = 0$) when the cross-correlation disappears, so $g_{12}(x) = 1$ for all the values of x. The spatial correlation between two replicas is

$$q_{1,2} = \frac{1}{N} \sum_{i=1}^{N} w(|x_i^1 - x_i^2|) \qquad (9)$$

$g_{12}(x)$ allows us to calculate the order parameter Q for configurations $\{x_i^1\},\{x_j^2\}$ of the two replicas using the following formula

$$Q = \langle q_{1,2} \rangle = 4\pi\rho^* \int_0^\infty g_{12}(x) w(x) x^2 dx \qquad (10)$$

If there is no correlation between two replicas ($g_{12}(x) = 1$), the direct calculation of the "random spatial correlation" performed using the formula (10) results in $Q_r = (7\pi^2 / 128)(c / d^*)^3 \ll 1$. In a supercooled liquid, Q tends to Q_r. However, we can expect it to be higher than in an ideal glass, since the coordinates $\{\vec{x}_i^1\},\{\vec{x}_j^2\}$ of the

atoms of the two replicas are fixed in random equilibrium points $\{X_i\}$. We assume that in the thermodynamic limit, the random first order transition is accompanied by a discrete change in the parameter Q.

3.2. Integral equations

$g_{11}(x)$ and $g_{12}(x)$ pair distribution functions of a symmetric two-replica system can be calculated using the Ornstein–Zernike (OZ) equation which connects the pair correlation function $h_{ij}(x) = g_{ij}(x) - 1$ and the direct correlation function $c_{ij}(x)$ $(1 \le i, j \le 2)$:

$$h_{11}(x) = c_{11}(x) + \rho^*[c_{11} \otimes h_{11}(x) + c_{12} \otimes h_{12}(x), \quad (11)$$

$$h_{12}(x) = c_{12}(x) + \rho^*[c_{11} \otimes h_{12}(x) + c_{12} \otimes h_{11}(x), \quad (12)$$

where $\otimes$ denotes the convolution, ρ^* is the density of each of the equivalent replicas. The OZ equation should be supplemented with the equation of closure between $h_{12}(x)$ and $c_{12}(x)$. A positive definite pair distribution function can always be represented as $g_{ij}(x) = \exp[-\beta v_{ij}(x) + \omega_{ij}(x)]$. We differentiate between a direct (vacuum) interaction $v_{ij}(x)$ an indirect (collective) interaction via environment $\omega_{ij}(x)$. The most common closures used in the study of fluids are the Percus–Yevick (PY), hypernetted chain (HPC), Martynov–Sarkisov (MS), and Rogers–Young (RY) closures. The latter can be used for the function $\gamma_{ij}(x) = h_{ij}(x) - c_{ij}(x)$, which for the first three looks like

$$\gamma_{ij}(x) = \exp(\omega_{ij}(x)) - 1, \; \gamma_{ij}(x) = \omega_{ij}(x),$$
$$\gamma_{ij}(x) = \omega_{ij}(x) + \omega_{ij}^2 / 2. \quad (13)$$

PY is more applicable for repulsive potentials and especially for the hard sphere potential than the HPC closure. However, at lower temperatures and with a moderate density, HPC produces better results than PY for more realistic pair potentials with attractive regions. At the same time, both closures are thermodynamically inconsistent: the characteristics calculated using the equation of state and compressibility result in an error margin of over 10 % [74]. The most thermodynamically consistent closure is the Martynov–Sarkisov closure: the error margin is below 2 % [72–73].

The ROFT theory most commonly employs either the HPC closure or the RY closure

$$g_{ij}(x) = \exp(-\beta v_{ij}(x) \times [1 + \frac{\exp(f_{ij}(x)\omega_{ij}(x)) - 1}{f_{ij}(x)}], (14)$$

where the function $f_{ij}(x) = 1 - \exp(-\alpha_{ij}x)$, depending on the adjusting parameters $\alpha_{11} = \alpha_{22}$ and α_{12}, makes the RY closure thermodynamically consistent. Within the limit $\alpha_{ij} \to \infty$ $(f_{ij}(x) = 1)$ we obtain the previous function definition g_{ij}.

The solutions of the two integral equations (11)–(12) were first obtained in [89] for $\varepsilon_{12} = 0$ by gradually increasing Γ form the stable liquid state ($\Gamma < \Gamma_f$) to $\Gamma \approx 2$, corresponding to a supercooled liquid. The comparison of the values for $g(x)$, obtained via the HNC and RY closures demonstrates that the solution of RY is more structured than that of the HNC. A two-replica system ($\varepsilon_{12} > 0$) is used as an attempt to find a branch corresponding to an ideal glass in the state equation. For each $\Gamma > \Gamma_f$ the solutions of two integral equations are sought for the finite values ε_{12}. The accuracy of the obtained values $h_{12}(x)$ and Q is controlled by the correct limit transition ε_{12} which tends towards zero. It was determined [89] that there are two glass branches: glass G_1 and glass G_2. The first branch corresponds to the equilibrium transition from glass to a crystalline state. The second corresponds to the nonequilbrium transition to the metastable state of a supercooled liquid. Described below are the main assumptions that led to such results [89]. If the correlation of a two-replica system in the limit transition is $h_{12}(x) = 0$ and $Q = Q_r$, the supercooled state of the liquid is restored. Conversely, if the correlation between the configuration is too strong (i.e. if $h_{12}(x) \gg 0$ and $Q \gg Q_r$), the system remains in the state of an ideal glass. [89] describes three algorithms (a, b, c) used to reveal the expected random transition (RFOT) from a supercooled liquid to an ideal glass. In the algorithm a) the initial value ε_{12}^0 is preset and Γ is gradually increased. The central peak appears in $h_{12}(x)$ near $x = 0$, whose amplitude gradually increases with the growth of Γ, since the coupling between the atoms of the opposite replicas becomes stronger. Algorithms b) and c) are based on the gradual transition of a liquid from the "molecular" state to an ideal glass by gradually decreasing ε_{12}^0 from its initially high values corresponding to the strong coupling of the atoms of the opposite replicas. The difference

in the pair distribution function of a supercooled liquid and an ideal glass is demonstrated in Fig. 1.

We should note that the ROFT theory has been so far used to describe spatially homogeneous systems without external fields and far from the boundary surfaces. We suggest using the ROFT theory to describe the structure of a liquid on the boundary with the solid surface by means of equation (3). We first calculate the kernel and the right-hand side of the equation (3) using the RFOT, and then solve the integral equation using common approaches. As a result, we can describe the surface amorphisation of supercooled liquids using the methods of statistical physics.

3.3. Pair structure and thermodynamics

The thermodynamic properties of a supercooled liquid based on the HNC and RY closures for hard sphere liquids without replicas ($\varepsilon_{12} = 0$) for the parameter $\Gamma > \Gamma_f$: excess inner energy per one particle $u_{ex} = U_{ex} / N k_B T$; the equation of state $\Pi_{ex}(\Gamma) = P / \rho k_B T - 1 = 4 u_{ex}(\Gamma)$; and the compressibility $\chi(\Gamma) = \chi_T / \chi_T^{id} = (\partial \beta P / \partial \rho)_T^{-1}$ can be calculated from the pair distribution function $g(x)$ using standard methods [49].

For the HNC approximation, the excess chemical potential $\beta \mu_{ex}$ is also calculated from the function $h(x)$ and $c(x)$ according to (11–12).

The excess free energy per one particle is then calculated from the standard thermodynamic correlation $f_{ex}(\Gamma) = \beta \mu_{ex} - \Pi_{ex}$, while the excess entropy per one particle is described by the formula

$$s_{ex}(\Gamma) = S_{ex} / N k_B = u_{ex}(\Gamma) - f_{ex}(\Gamma) =$$
$$= \frac{\Gamma}{4} f_{ex}'(\Gamma) - f_{ex}(\Gamma).$$

The RY approximation does not describe μ_{ex} (and therefore f_{ex}) through $h(x)$ and $c(x)$. f_{ex} It is, however, calculated by integrating the inner energy along Γ.

$$f_{ex}(\Gamma) = f_{ex}(\Gamma_0) + 4 \int_{\Gamma_0}^{\Gamma} u_{ex}(\Gamma') \frac{d\Gamma'}{\Gamma'}.$$

The initial point Γ_0 can be quite small ($\Gamma_0 \simeq 0.5$), which allows accurate calculation of $\mu_{ex}(\Gamma_0)$ based on the HNC closure, and therefore, integration.

For the supercooled region ($\Gamma > \Gamma_f$) the atomic configurations $\{x_i\}$ remain at the local minimum of the free energy for a long time oscillating near the equilibrium positions $\{X_i\}$. This enables us to differentiate between the "configurational" and entropy contributions to the free energy and entropy
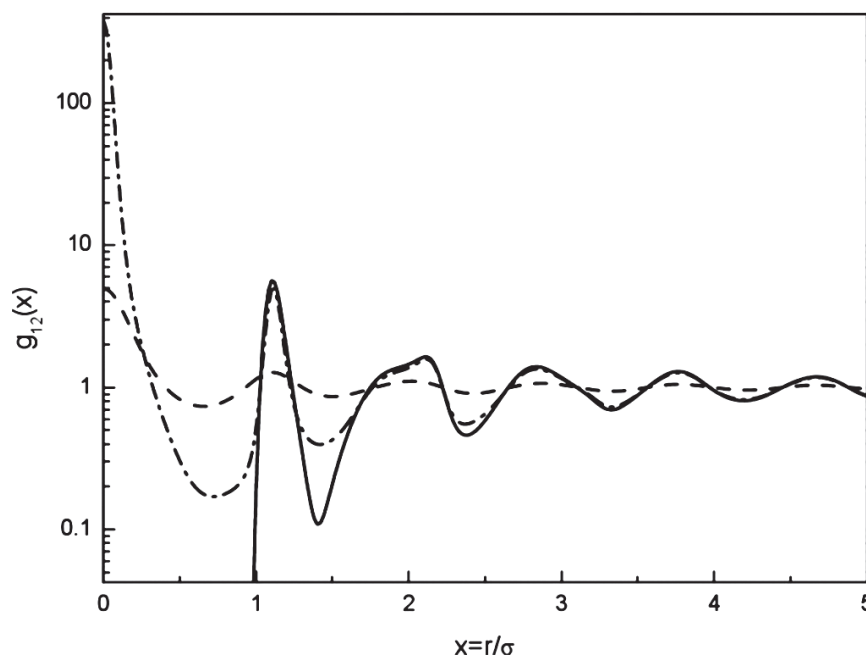

Fig. 1. RY results for the pair distribution function $g_{12}(x)$. Γ = 1.8. Dotted line denotes branch G_1; dash-and-dot line denotes branch G_2; the solid curve $g(x)$ is given for comparison and denotes the pair distribution function of the supercooled liquid. All pair distribution functions are plotted on a logarithmic scale

$$f = f_{id} + f_{ex} = f_c + f_v,$$

$$s = s_{id} + s_{ex} = s_c + s_v,$$

where s_c determines the exponentially large number of metastable states in the supercooled liquid $N_m \approx \exp(N s_c)$.

A detailed analysis of the calculation methods of statistical and thermodynamic values by means of numerical modelling is performed in [92–98].

4. Discussion

Let us name the development stages of the theory of classical molecular media.

The statistical theory of thermodynamically equilibrium classical molecular systems is based on the canonical Gibbs distribution. For imperfect gases of low density the statistical integral is calculated as an expansion in powers of density. This expansion is practically inapplicable to dense liquids when calculating the terms with higher exponents.

The problem is somewhat eliminated by the method of integral equations for the particle size distribution functions. There are integral equations describing the structural and thermodynamic properties of liquids with high accuracy (for real molecular systems). However, some basic problems remain unsolved. In particular, we still cannot describe the transitions from a thermodynamic equilibrium state to a metastable state.

A new stage of the statistical theory of classical molecular media is connected with the development of the random first order transition theory, based largely on the extension of the Gibbs distribution to metastable states. However, the random first order transition theory only describes the connection between the structure of a supercooled liquid and an ideal glass, while it does not consider the kinetic process. Nevertheless, a large number of English-language sources focus on the calculation of the structural and thermodynamic properties of real molecular systems. We hope that this overview will compensate for the lack of such studies published in Russian.

Conflict of interests

The authors declare that they have no known competing financial interests or personal relationships that could have influenced the work reported in this paper.

References

1. Sanditov D. S., Ojovan M. I. Relaxation aspects of the liquid—glass transition. *Uspekhi Fizicheskih Nauk*. 2019;189(2): 113–133. DOI: https://doi.org/10.3367/ufnr.2018.04.038319

2. Tsydypov Sh. B., Parfenov A. N., Sanditov D. S., Agrafonov Yu. V., Nesterov A. S. Application of the molecular dynamics method and the excited state model to the investigation of the glass transition in argon. Available at: http://www.isc.nw.ru/Rus/GPCJ/Content/2006/tsydypov_32_1.pdf (In Russ.). *Glass Physics and Chemistry*. 2006;32(1): 83–88. DOI: https://doi.org/10.1134/S1087659606010111

3. Berthier L., Witten T. A. Glass transition of dense fluids of hard and compressible spheres. *Physical Review E*. 2009;80(2): 021502. DOI: https://doi.org/10.1103/PhysRevE.80.021502

4. Sarkisov G. N. Molecular distribution functions of stable, metastable and amorphous classical models. *Uspekhi Fizicheskih Nauk*. 2002;172(6): 647–669. DOI: https://doi.org/10.3367/ufnr.0172.200206b.0647

5. Hoover W. G., Ross M., Johnson K. W., Henderson D., Barker J. A., Brown, B. C. Soft-sphere equation of state. *The Journal of Chemical Physics*, 1970;52(10): 4931–4941. DOI: https://doi.org/10.1063/1.1672728

6. Cape J. N., Woodcock L. V. Glass transition in a soft-sphere model. *The Journal of Chemical Physics*, 1980;72(2): 976–985. DOI: https://doi.org/10.1063/1.439217

7. Franz S., Mezard M., Parisi G., Peliti L. The response of glassy systems to random perturbations: A bridge between equilibrium and off-equilibrium. *Journal of Statistical Physics*. 1999;97(3–4): 459–488. DOI: https://doi.org/10.1023/A:1004602906332

8. Marc Mezard and Giorgio Parisi. Thermodynamics of glasses: a first principles computation. *J. of Phys.: Condens. Matter*. 1999;11: A157–A165.

9. Berthier L., Jacquin H., Zamponi F. Microscopic theory of the jamming transition of harmonic spheres. *Physical Review E*, 2011;84(5): 051103. DOI: https://doi.org/10.1103/PhysRevE.84.051103

10. Berthier L., Biroli, G., Charbonneau P., Corwin E. I., Franz S., Zamponi F. Gardner physics in amorphous solids and beyond. *The Journal of Chemical Physics*. 2019;151(1): 010901. DOI: https://doi.org/10.1063/1.5097175

11. Berthier L., Ozawa M., Scalliet C. Configurational entropy of glass-forming liquids. *The Journal of Chemical Physics.* 2019;150(16): 160902. DOI: https://doi.org/10.1063/1.5091961

12. Bomont J. M., Pastore G. An alternative scheme to find glass state solutions using integral equation theory for the pair structure. *Molecular Physics.* 2015;113(17–18): 2770–2775. DOI: https://doi.org/10.1080/00268976.2015.1038325

13. Bomont J. M., Hansen J. P., Pastore G. Hypernetted-chain investigation of the random first-order transition of a Lennard-Jones liquid to an ideal glass. *Physical Review E.* 2015;92(4): 042316. DOI: https://doi.org/10.1103/PhysRevE.92.042316

14. Bomont J. M., Pastore G., Hansen J. P. Coexistence of low and high overlap phases in a supercooled liquid: An integral equation investigation. *The Journal of Chemical Physics.* 2017;146(11): 114504. DOI: https://doi.org/10.1063/1.4978499

15. Bomont J. M., Hansen J. P., Pastore G. Revisiting the replica theory of the liquid to ideal glass transition. *The Journal of Chemical Physics.* 2019;150(15): 154504. DOI: https://doi.org/10.1063/1.5088811

16. Cammarota C., Seoane B. First-principles computation of random-pinning glass transition, glass cooperative length scales, and numerical comparisons. *Physical Review B.* 2016;94(18): 180201. DOI: https://doi.org/10.1103/PhysRevB.94.180201

17. Charbonneau P., Ikeda A., Parisi G., Zamponi F. Glass transition and random close packing above three dimensions. *Physical Review Letters.* 2011;107(18): 185702. DOI: https://doi.org/10.1103/PhysRevLett.107.185702

18. Ikeda A., Miyazaki K. Mode-coupling theory as a mean-field description of the glass transition. *Physical Review Letters.* 2010;104(25): 255704. DOI: https://doi.org/10.1103/PhysRevLett.104.255704

19. McCowan D. Numerical study of long-time dynamics and ergodic-nonergodic transitions in dense simple fluids. *Physical Review E.* 2015;92(2): 022107. DOI: https://doi.org/10.1103/PhysRevE.92.022107

20. Ohtsu H., Bennett T. D., Kojima T., Keen D. A., Niwa Y., Kawano M. Amorphous–amorphous transition in a porous coordination polymer. *Chemical Communications.* 2017;53(52): 7060–7063. DOI: https://doi.org/10.1039/C7CC03333H

21. Schmid B., Schilling R. Glass transition of hard spheres in high dimensions. *Physical Review E.* 2010;81(4): 041502. DOI: https://doi.org/10.1103/PhysRevE.81.041502

22. Parisi G., Slanina, F. Toy model for the mean-field theory of hard-sphere liquids. *Physical Review E.* 2000;62(5): 6554. DOI: https://doi.org/10.1103/PhysRevE.62.6554

23. Parisi G., Zamponi F. The ideal glass transition of hard spheres. *The Journal of Chemical Physics.* 2005;123(14): 144501. DOI: https://doi.org/10.1063/1.2041507

24. Parisi G., Zamponi F. Amorphous packings of hard spheres for large space dimension. *Journal of Statistical Mechanics: Theory and Experiment.* 2006;03: P03017. DOI: https://doi.org/10.1088/1742-5468/2006/03/P03017

25. Parisi G., Procaccia I., Shor C., Zylberg J. Effective forces in thermal amorphous solids with generic interactions. *Physical Review E.* 2019;99(1): 011001. DOI: https://doi.org/10.1103/PhysRevE.99.011001

26. Stevenson J. D., Wolynes P. G. Thermodynamic–kinetic correlations in supercooled liquids: a critical survey of experimental data and predictions of the random first-order transition theory of glasses. *The Journal of Physical Chemistry B.* 2005;109(31): 15093–15097. DOI: https://doi.org/10.1021/jp052279h

27. Xia X., Wolynes P. G. Fragilities of liquids predicted from the random first order transition theory of glasses. *Proceedings of the National Academy of Sciences.* 2000;97(7): 2990–2994. DOI: https://doi.org/10.1073/pnas.97.7.2990

28. Kobryn A. E., Gusarov S., Kovalenko A. A closure relation to molecular theory of solvation for macromolecules. *Journal of Physics: Condensed Matter.* 2016;28(40): 404003. DOI: https://doi.org/10.1088/0953-8984/28/40/404003

29. Coluzzi B., Parisi G., Verrocchio P. Thermodynamical liquid-glass transition in a Lennard-Jones binary mixture. *Physical Review Letters.* 2000;84(2): 306. DOI: https://doi.org/10.1103/PhysRevLett.84.306

30. Sciortino F., Tartaglia P. Extension of the fluctuation-dissipation theorem to the physical aging of a model glass-forming liquid. *Physical Review Letters.* 2001;86(1): 107. DOI: https://doi.org/10.1103/PhysRevLett.86.107

31. Sciortino, F. One liquid, two glasses. *Nature Materials.* 2002;1(3): 145–146. DOI: https://doi.org/10.1038/nmat752

32. Farr R. S., Groot R. D. Close packing density of polydisperse hard spheres. *The Journal of Chemical Physics.* 2009;131(24): 244104. DOI: https://doi.org/10.1063/1.3276799

33. Barrat J. L., Biben T., Bocquet, L. From Paris to Lyon, and from simple to complex liquids: a view on Jean-Pierre Hansen's contribution. *Molecular Physics.* 2015;113(17-18): 2378–2382. DOI: https://doi.org/10.1080/00268976.2015.1031843

34. Gaspard J. P. *Structure of Melt and Liquid Alloys. In Handbook of Crystal Growth.* Elsevier; 2015. 580 p. DOI: https://doi.org/10.1016/B978-0-444-56369-9.00009-5

35. Heyes D. M., Sigurgeirsson H. The Newtonian viscosity of concentrated stabilized dispersions: comparisons with the hard sphere fluid. *Journal of Rheology.* 2004;48(1): 223–248. DOI: https://doi.org/10.1122/1.1634986

36. Ninarello A., Berthier L., Coslovich D. Structure and dynamics of coupled viscous liquids. *Molecular*

Physics. 2015;113(17-18): 2707–2715. DOI: https://doi.org/10.1080/00268976.2015.1039089

37. Russel W. B., Wagner N. J., Mewis J. Divergence in the low shear viscosity for Brownian hard-sphere dispersions: at random close packing or the glass transition? *Journal of Rheology.* 2013;57(6): 1555–1567. DOI: https://doi.org/10.1122/1.4820515

38. Schaefer T. Fluid dynamics and viscosity in strongly correlated fluids. *Annual Review of Nuclear and Particle Science.* 2014;64: 125–148. DOI: https://doi.org/10.1146/annurev-nucl-102313-025439

39. Matsuoka H. A macroscopic model that connects the molar excess entropy of a supercooled liquid near its glass transition temperature to its viscosity. *The Journal of Chemical Physics.* 2012;137(20): 204506. DOI: https://doi.org/10.1063/1.4767348

40. de Melo Marques F. A., Angelini R., Zaccarelli E., Farago B., Ruta B., Ruocco, G., Ruzicka B. Structural and microscopic relaxations in a colloidal glass. *Soft Matter.* 2015;11(3): 466–471. DOI: https://doi.org/10.1039/C4SM02010C

41. Deutschländer S., Dillmann P., Maret G., Keim P. Kibble–Zurek mechanism in colloidal monolayers. *Proceedings of the National Academy of Sciences.* 2015;112(22): 6925–6930. DOI: https://doi.org/10.1073/pnas.1500763112

42. Chang J., Lenhoff A. M., Sandler S. I. Determination of fluid–solid transitions in model protein solutions using the histogram reweighting method and expanded ensemble simulations. *The Journal of Chemical Physics.* 2004;120(6): 3003–3014. DOI: https://doi.org/10.1063/1.1638377

43. Gurikov P., Smirnova I. Amorphization of drugs by adsorptive precipitation from supercritical solutions: a review. *The Journal of Supercritical Fluids.* 2018;132: 105–125. DOI: https://doi.org/10.1016/j.supflu.2017.03.005

44. Baghel S., Cathcart H., O'Reilly N. J. Polymeric amorphous solid dispersions: a review of amorphization, crystallization, stabilization, solid-state characterization, and aqueous solubilization of biopharmaceutical classification system class II drugs. *Journal of Pharmaceutical Sciences.* 2016;105(9): 2527–2544. DOI: https://doi.org/10.1016/j.xphs.2015.10.008

45. Kalyuzhnyi Y. V., Hlushak S. P. Phase coexistence in polydisperse multi-Yukawa hard-sphere fluid: high temperature approximation. *The Journal of Chemical Physics.* 2006;125(3): 034501. DOI: https://doi.org/10.1063/1.2212419

46. Mondal C., Sengupta S. Polymorphism, thermodynamic anomalies, and network formation in an atomistic model with two internal states. *Physical Review E.* 2011;84(5): 051503. DOI: https://doi.org/10.1103/PhysRevE.84.051503

47. Bonn D., Denn M. M., Berthier L., Divoux T., Manneville S. Yield stress materials in soft condensed matter. *Reviews of Modern Physics.* 2017;89(3): 035005. DOI: https://doi.org/10.1103/RevModPhys.89.035005

48. Tanaka H. Two-order-parameter model of the liquid–glass transition. I. Relation between glass transition and crystallization. *Journal of Non-Crystalline Solids.* 2005;351(43-45): 3371–3384. DOI: https://doi.org/10.1016/j.jnoncrysol.2005.09.008

49. Balesku R. *Ravnovesnaya i neravnovesnaya statisticheskaya mekhanika* [Equilibrium and non-equilibrium statistical mechanics]. Moscow: Mir Publ.; 1978. vol. 1. 404 c. (In Russ.)

50. Chari S., Inguva R., Murthy K. P. N. A new truncation scheme for BBGKY hierarchy: conservation of energy and time reversibility. *arXiv preprint* arXiv:1608.02338. DOI: https://arxiv.org/abs/1608.02338

51. Gallagher I., Saint-Raymond L., Texier B. From Newton to Boltzmann: hard spheres and short-range potentials. *European Mathematical Society.* arXiv:1208.5753. DOI: https://arxiv.org/abs/1208.5753

52. Rudzinski J. F., Noid W. G. A generalized-Yvon-Born-Green method for coarse-grained modeling. *The European Physical Journal Special Topics.* 224(12), 2193–2216. DOI: https://doi.org/10.1140/epjst/e2015-02408-9

53. Franz B., Taylor-King J. P., Yates C., Erban R. Hard-sphere interactions in velocity-jump models. *Physical Review E.* 2016;94(1): 012129. DOI: https://doi.org/10.1103/PhysRevE.94.012129

54. Gerasimenko V., Gapyak I. Low-Density asymptotic behavior of observables of hard sphere fluids. *Advances in Mathematical Physics.* 2018: 6252919. DOI: https://doi.org/10.1155/2018/6252919

55. Lue L. Collision statistics, thermodynamics, and transport coefficients of hard hyperspheres in three, four, and five dimensions. *The Journal of Chemical Physics.* 2005;122(4): 044513. DOI: https://doi.org/10.1063/1.1834498

56. Cigala G., Costa D., Bomont J. M., Caccamo C. Aggregate formation in a model fluid with microscopic piecewise-continuous competing interactions. *Molecular Physics.* 2015;113(17–18): 2583–2592. DOI: https://doi.org/10.1080/00268976.2015.1078006

57. Jadrich R., Schweizer K. S. Equilibrium theory of the hard sphere fluid and glasses in the metastable regime up to jamming. I. Thermodynamics. *The Journal of Chemical Physics.* 2013;139(5): 054501. DOI: https://doi.org/10.1063/1.4816275

58. Mondal A., Premkumar L., Das S. P. Dependence of the configurational entropy on amorphous structures of a hard-sphere fluid. *Physical Review E.* 2017;96(1): 012124. DOI: https://doi.org/10.1103/PhysRevE.96.012124

59. Sasai M. Energy landscape picture of supercooled liquids: application of a generalized random energy model. *The Journal of Chemical Physics.*

2003;118(23): 10651–10662. DOI: https://doi.org/10.1063/1.1574781

60. Sastry S. Liquid limits: Glass transition and liquid-gas spinodal boundaries of metastable liquids. *Physical Review Letters.* 2000;85(3): 590. DOI: https://doi.org/10.1103/PhysRevLett.85.590

61. Uche O. U., Stillinger F. H., Torquato S. On the realizability of pair correlation functions. *Physica A: Statistical Mechanics and its Applications.* 2006;360(1): 21–36. DOI: https://doi.org/10.1016/j.physa.2005.03.058

62. Bi D., Henkes S., Daniels K. E., Chakraborty B. The statistical physics of athermal materials. *Annu. Rev. Condens. Matter Phys.* 2015;6(1): 63–83. DOI: https://doi.org/10.1146/annurev-conmatphys-031214-014336

63. Bishop M., Masters A., Vlasov A. Y. Higher virial coefficients of four and five dimensional hard hyperspheres. *The Journal of Chemical Physics.* 2004;121(14): 6884–6886. DOI: https://doi.org/10.1063/1.1777574

64. Sliusarenko O. Y., Chechkin A. V., Slyusarenko Y. V. The Bogolyubov-Born-Green-Kirkwood-Yvon hierarchy and Fokker-Planck equation for many-body dissipative randomly driven systems. *Journal of Mathematical Physics.* 2015;56(4): 043302. DOI: https://doi.org/10.1063/1.4918612

65. Tang Y. A new grand canonical ensemble method to calculate first-order phase transitions. *The Journal of chemical physics.* 2011;134(22): 224508. DOI: https://doi.org/10.1063/1.3599048

66. Tsednee T., Luchko T. Closure for the Ornstein-Zernike equation with pressure and free energy consistency. *Physical Review E.* 2019;99(3): 032130. DOI: https://doi.org/10.1103/PhysRevE.99.032130

67. Maimbourg T., Kurchan J., Zamponi, F. Solution of the dynamics of liquids in the large-dimensional limit. *Physical review letters.* 2016;116(1): 015902. DOI: https://doi.org/10.1103/PhysRevLett.116.015902

68. Mari, R., & Kurchan, J. Dynamical transition of glasses: from exact to approximate. *The Journal of Chemical Physics.* 2011;135(12): 124504. DOI: https://doi.org/10.1063/1.3626802

69. Frisch H. L., Percus J. K. High dimensionality as an organizing device for classical fluids. *Physical Review E.* 1999;60(3): 2942. DOI: https://doi.org/10.1103/PhysRevE.60.2942

70. Finken R., Schmidt M., Löwen H. Freezing transition of hard hyperspheres. *Physical Review E.* 2001;65(1): 016108. DOI: https://doi.org/10.1103/PhysRevE.65.016108

71. Torquato S., Uche O. U., Stillinger F. H. Random sequential addition of hard spheres in high Euclidean dimensions. *Physical Review E.* 2006;74(6): 061308. DOI: https://doi.org/10.1103/PhysRevE.74.061308

72. Martynov G. A. *Fundamental theory of liquids; method of distribution functions.* Bristol: Adam Hilger; 1992, 470 p.

73. Vompe A. G., Martynov G. A. The self-consistent statistical theory of condensation. *The Journal of Chemical Physics.* 1997;106(14): 6095–6101. DOI: https://doi.org/10.1063/1.473272

74. Krokston K. *Fizika zhidkogo sostoyaniya. Statisticheskoe vvedenie* [Physics of the liquid state. Statistical introduction]. Moscow: Mir Publ.; 1978. 400 p. (In Russ.)

75. Rogers F. J., Young D. A. New, thermodynamically consistent, integral equation for simple fluids. *Physical Review A.* 1984;30(2): 999. DOI: https://doi.org/10.1103/PhysRevA.30.999

76. Wertheim M. S. Exact solution of the Percus–Yevick integral equation for hard spheres *Phys. Rev. Letters.* 1963;10(8): 321–323. DOI: https://doi.org/10.1103/PhysRevLett.10.321

77. Tikhonov D. A., Kiselyov O. E., Martynov G. A., Sarkisov G. N. Singlet integral equation in the statistical theory of surface phenomena in liquids. *J. of Mol. Liquids.* 1999;82(1–2): 3– 17. DOI: https://doi.org/10.1016/S0167-7322(99)00037-9

78. Agrafonov Yu., Petrushin I. Two-particle distribution function of a non-ideal molecular system near a hard surface. *Physics Procedia.* 2015;71. 364–368. DOI: https://doi.org/10.1016/j.phpro.2015.08.353

79. Agrafonov Yu., Petrushin I. Close order in the molecular system near hard surface. *Journal of Physics: Conference Series.* 2016;747: 012024. DOI: https://doi.org/10.1088/1742-6596/747/1/012024

80. He Y., Rice S. A., Xu X. Analytic solution of the Ornstein-Zernike relation for inhomogeneous liquids. *The Journal of Chemical Physics.* 2016;145(23): 234508. DOI: https://doi.org/10.1063/1.4972020

81. Agrafonov Y. V., Petrushin I. S. Using molecular distribution functions to calculate the structural properties of amorphous solids. *Bulletin of the Russian Academy of Sciences: Physics.* 2020;84: 783–787. DOI: https://doi.org/10.3103/S1062873820070035

82. Bertheir L., Ediger M. D. How to "measure" a structural relaxation time that is too long to be measured? *arXiv*:2005.06520v1. DOI: https://arxiv.org/abs/2005.06520

83. Karmakar S., Dasgupta C., Sastry S. Length scales in glass-forming liquids and related systems: a review. *Reports on Progress in Physics.* 2015;79(1): 016601. DOI: https://doi.org/10.1088/0034-4885/79/1/016601

84. De Michele C., Sciortino F., Coniglio A. Scaling in soft spheres: fragility invariance on the repulsive potential softness. *Journal of Physics: Condensed Matter.* 2004;16(45): L489. DOI: https://doi.org/10.1088/0953-8984/16/45/L01

85. Niblett S. P., de Souza V. K., Jack R. L., Wales D. J. Effects of random pinning on the potential energy landscape of a supercooled liquid. *The Journal of Chemical Physics.* 2018;149(11): 114503. DOI: https://doi.org/10.1063/1.5042140

86. Wolynes P. G., Lubchenko V. *Structural glasses and supercooled liquids: Theory, experiment, and applications*. New York: John Wiley & Sons; 2012. 404 p. DOI: https://doi.org/10.1002/9781118202470

87. Jack R. L., Garrahan J. P. Phase transition for quenched coupled replicas in a plaquette spin model of glasses. *Physical Review Letters*. 2016;116(5): 055702. DOI: https://doi.org/10.1103/PhysRevLett.116.055702

88. Habasaki J., Ueda A. Molecular dynamics study of one-component soft-core system: thermodynamic properties in the supercooled liquid and glassy states. *The Journal of Chemical Physics*. 2013;138(14): 144503. DOI: https://doi.org/10.1063/1.4799880

89. Bomont J. M., Hansen J. P., Pastore G. An investigation of the liquid to glass transition using integral equations for the pair structure of coupled replicae. *J. Chem. Phys*. 2014;141(17): 174505. DOI: https://doi.org/10.1063/1.4900774

90. Parisi G., Urbani P., Zamponi F. *Theory of Simple Glasses: Exact Solutions in Infinite Dimensions*. Cambridge: Cambridge University Press; 2020. 324 p. DOI: https://doi.org/10.1017/9781108120494

91. Robles M., López de Haro M., Santos A., Bravo Yuste S. Is there a glass transition for dense hard-sphere systems? *The Journal of Chemical Physics*. 1998;108(3): 1290–1291. DOI: https://doi.org/10.1063/1.475499

92. Grigera T. S., Martín-Mayor V., Parisi G., Verrocchio P. Asymptotic aging in structural glasses. *Physical Review B*, 2004;70(1): 014202. DOI: https://doi.org/10.1103/PhysRevB.70.014202

93. Vega C., Abascal J. L., McBride C., Bresme F. The fluid–solid equilibrium for a charged hard sphere model revisited. *The Journal of Chemical Physics*. 2003;119(2): 964–971. DOI: https://doi.org/10.1063/1.1576374

94. Kaneyoshi T. Surface amorphization in a transverse Ising nanowire; effects of a transverse field. *Physica B: Condensed Matter*. 2017;513: 87–94. DOI: https://doi.org/10.1016/j.physb.2017.03.015

95. Paganini I. E., Davidchack R. L., Laird B. B., Urrutia I. Properties of the hard-sphere fluid at a planar wall using virial series and molecular-dynamics simulation. *The Journal of Chemical Physics*. 2018;149(1): 014704. DOI: https://doi.org/10.1063/1.5025332

96. Properzi L., Santoro M., Minicucci M., Iesari F., Ciambezi M., Nataf L., Di Cicco A. Structural evolution mechanisms of amorphous and liquid $As_2 Se_3$ at high pressures. *Physical Review B*. 2016;93(21): 214205. DOI: https://doi.org/10.1103/PhysRevB.93.214205

97. Sesé L. M. Computational study of the melting-freezing transition in the quantum hard-sphere system for intermediate densities. I. Thermodynamic results. *The Journal of Chemical Physics*. 2007;126(16): 164508. DOI: https://doi.org/10.1063/1.2718523

98. Shetty R., Escobedo F. A. On the application of virtual Gibbs ensembles to the direct simulation of fluid–fluid and solid–fluid phase coexistence. *The Journal of Chemical Physics*. 2002;116(18): 7957–7966. DOI: https://doi.org/10.1063/1.1467899

Information about the authors

Yury V. Agrafonov, Dsc in Physics and Mathematics, Professor, Department of Radiophysics and Radioelectronics, Faculty of Physics, Irkutsk State University, Irkutsk, Russian Federation; e-mail: agrafonov@physdep.isu.ru. ORCID iD: https://orcid.org/0000-0002-9023-1739.

Ivan S. Petrushin, PhD in Technical Sciences, Associate Professor, Department of Radiophysics and Radioelectronics, Faculty of Physics, Irkutsk State University, Irkutsk, Russian Federation; e-mail: ivan.kiel@gmail.com. ORCID iD: https://orcid.org/0000-0002-8788-5352

All authors have read and approved the final manuscript.

Computer Simulation of Sorption Interactions of L-Arginine and L-Lysine with Carbon Nanotubes

© 2020 E. V. Butyrskaya✉[a], S. A. Zapryagaev[a], E. A. Izmailova[b], S. V. Artyshchenko[c]

[a]Voronezh State University
1 Universitetskaya pl., Voronezh 394018, Russian Federation

[b]Joint Stock Company "Concern "Sozvezdie"
14 Plekhanovskaya str., Voronezh 394018, Russian Federation

[c]Voronezh State Technical University
84 ul. 20-Letiya Oktyabrya, Voronezh 394006, Russian Federation

Abstract

Carbon nanotubes (CNTs) are a new class of nanomaterials with a high potential for different technological applications. The prospects of using them in biomedicine is associated with the ability of CNTs to cross the cell's membrane without being impaired, which determines the significance of the study of the interactions of CNTs with biologically active substances, especially amino acids. This work presents a computer simulation of the structure and characteristics of arginine (lysine) – single-wall carbon nanotube (CNT) systems using the B3LYP/6-31G(d,p) density functional theory with GD3 dispersion correction. We calculated the energies of adsorption, dipole moments, total charge on the amino acid and nanotube atoms, and the smallest distances from the amino acid atoms to the CNT. Taking into account the dispersion correction, which is almost absent in scientific literature, allows more accurate calculations of the energies of adsorption of amino acids on CNT to be obtained as compared to the existing calculations due to the high polarizability of CNTs. We considered scenarios with the amino acid position on the open end and on the external and internal lateral surfaces of the CNT. The calculated series of adsorption energies satisfies the conditions $E_{end} > E_{inside} > E_{lateral}$. This is due to the fact that when the amino acid is placed on the external lateral surface of a CNT the sorbate interacts with a part of the lateral surface of the tube. When it is placed inside the CNT the sorbate interacts with the whole surface through van der Waals forces and when the sorbate is placed on the end of the sorbent a covalent bond is formed between them. The formation of the covalent bond on the open end of the CNT is due to the higher electron density near the ends of the nanotube as compared to the external and internal lateral surfaces of the tube. An explanation is given of the mechanisms of adsorption and enhancement of the antibacterial action of the CNT functionalised by arginine and lysine, as compared to nonfunctionalised CNTs.

Keywords: carbon nanotubes, amino acids, computer simulation, adsorption.

✉ Elena V. Butyrskaya, e-mail: bev5105@yandex.ru

1. Introduction

Carbon nanotubes (CNTs) are one of the most widely studied nanomaterials due to their unique physicochemical properties and wide range of possible technological applications in biomedicine, nanoelectronics, and material science [1–7]. The unique sorption, electronic, and optic properties of CNTs as well as their size and mechanical strength make nanotubes a critical material for biotechnologies such as the development of targeted drug delivery platforms, tissue engineering, and next-generation biosensors [8–11]. To take advantage of the unique properties of CNTs in biotechnologies it is necessary to understand the nature of the immobilisation of biomolecules on CNTs [12–18]. One of the methods for the immobilisation of biological molecules on CNTs is adsorption, and amino acids (AA) are an elementary unit of many biomolecules. Thus, the interaction between CNTs and AAs is important for understanding the mechanism of the interaction of nanotubes with biomolecules. The goal of this work was to identify the features of sorption interactions of L-Arginine and L-Lysine with single-wall carbon nanotubes in aqueous solutions.

2. Experimental

2.1 Computer-aided experiments

A chiral nanotube (6,6) with open ends and a length 13.53 Å was used as the model of a carbon nanotube in a computer simulation of amino acid adsorption on CNTs. Using these nanotubes we studied the adsorption of the main amino acids of L-Lysine [HOOCCH(NH$_2$)(CH$_2$)$_4$NH$_2$] and L-Arginine [NH-C(NH$_2$)NH(CH$_2$)$_3$CH(NH$_2$)-COOH] from an aqueous solution with pH ~ 7. With this pH value, both acids are mainly in the form of cation (Fig.1), which was taken into account while constructing an initial structural model of the sorbate.

The cations of amino acid were positioned in the initial structures in three different ways: on the open end of the CNT, on the lateral surface of the CNT, and inside the CNT.

The aqueous environment was taken into account using the method of solvation of polarisation continuum (PCM) [19].

The structures were optimised using the Gaussian 09 program [20, 21] and the B3LYP/6-31G(d,p) method with GD3 dispersion correction [22]. As CNTs have high polarisation, taking into account the dispersion correction allows obtaining more accurate energies of amino acids sorption on CNTs. The adsorption energies were calculated using the following formula:

$$E^{\text{ads}} = E^{\text{sorbate}} + E^{\text{CNT}} - E^{\text{sorbate + CNT}}, \qquad (1)$$

E^{ads} is the adsorption energy, E^{sorbate} is the energy of the particle whose sorption is being studied, E^{CNT} is the energy of the carbon nanotube.

The consideration of dispersion corrections means adding an additive term into the expression of energy of the atomic-molecular system
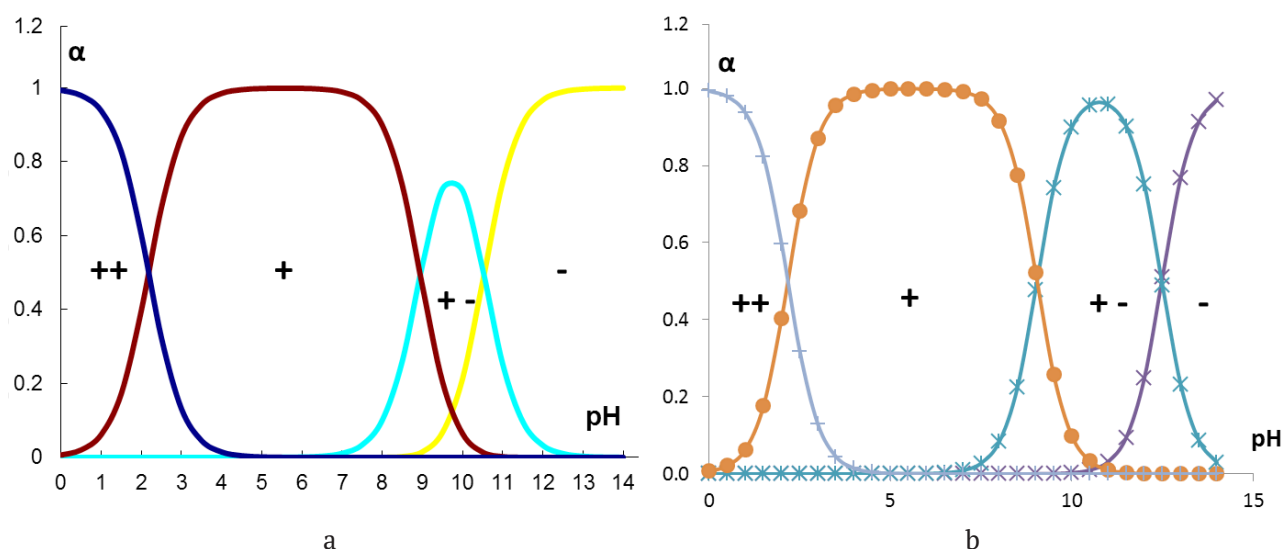
Fig. 1. Change in the content of ionic forms of lysine (a) and arginine (b) depending on the pH of the solution at a temperature of 293 K

$$E_{\text{DFT-D}} = E_{\text{DFT}} + E_{\text{disp}}, \tag{2}$$

where E_{DFT} is the energy of the system calculated using the calculation model of the density functional theory (DFT) B3LYP/ 6-31G(d,p), E_{disp} is the empirical dispersion correction. As for the quantum-chemical calculation, the GD3 method [22] takes into account the scaling and damping fitting the values of the specified series of dispersion energy

$$E_{\text{disp}} = -\frac{C_6}{R^6} - \frac{C_8}{R^8} - \frac{C_{10}}{R^{10}} - \cdots, \tag{3}$$

in the form of

$$E_{\text{disp}} = -\sum_{n=6,8} s_n \sum_{i,j>i}^{N_{\text{at}}} \frac{C_n^{ij}}{\left(R_{ij}\right)^n} f_{\text{damp}}, \tag{4}$$

$$f_{\text{damp}}\left(R_{ij}\right) = \frac{1}{1 + 6(R_{ij} / (s_{r,n} R_0^{ij})^{-\alpha_n}}. \tag{5}$$

Here the dispersion coefficients C_n^{ij} for each pair of atoms i and j were obtained as the geometric average of the elementary table values summarised by all the intercore distances. These coefficients are modulated using the damping function f_{damp}. The fitting parameters for the B3LYP functional are $s_6 = 1.0000$, $s_8 = 1.7030$, $s_{r,6} = 1.2610$.

3. Results and discussion

Several optimised structures were obtained for each of the CNT+AA systems when placing the amino acid on the open end of the CNT, on the lateral surface of the CNT, and inside the CNT. The structures of the optimised systems with the greatest energy of adsorption, their dipole moments (d, Debye), total charges on the atoms of the amino acid and CNTs, adsorption energies (E_{ads}, kcal/mol), and the smallest distances from the oxygen and nitrogen atoms of the amino acid cation to the carbon atom of the nanotube (R_{CO1}, R_{CO2}, R_{CN1}, R_{CN2}, Å) are presented in Tables 1 (lysine) and 2 (arginine).
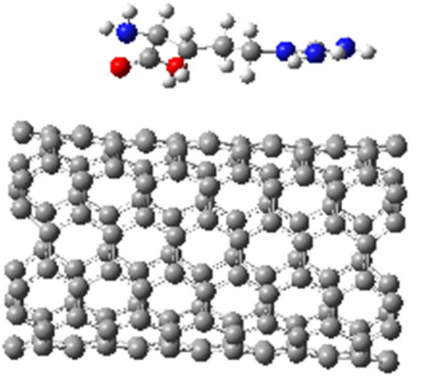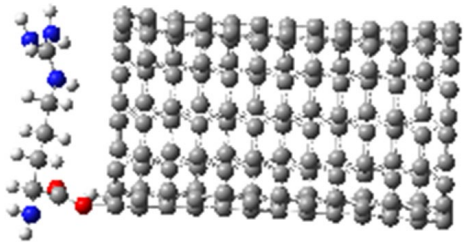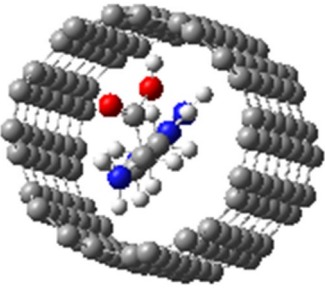
The series of adsorption energies on the CNT for both amino acids satisfies the condition $E_{\text{end}} > E_{\text{inside}} > E_{\text{lateral}}$. The value of the dipole moment of the amino acid – CNT system is within the range from 13.38 to 42.74 D (arginine) and within the range from 9.01 to 13.83 D (lysine). The values of the charges on the atoms of amino acid and CNT (q_{AA} and q_{CNT}) (Tables 1, 2) indicate

an insignificant transfer of the charge from the amino acid to the nanotube. Thus, a complex with the transfer of the charge over the course of adsorption is not formed, and there is no donor-acceptor sorbent-sorbate interaction.

The values of the distances from the atom O (N) of the amino acid to the atom C of the nanotube allow drawing a conclusion about the method of fixing the amino acid on the CNT. Their values $R_{\text{CO2}} = 1.38$ Å (arginine on the end of the CNT, Table 1) and $R_{\text{CN1}} = 1.50$ Å (lysine on the end of the CNT) show that there is covalent bond between the atoms of oxygen (nitrogen) of the amino acid and the carbon atom of the nanotube as the sum of the covalent radii approximates the length of the covalent bond between the corresponding atoms. The highest adsorption energy of the amino acid is conditional on the end of the CNT (E_{end}). The formation of the covalent bond on the open end of the CNT is due to the higher electron density near the ends of the nanotube as compared to the external and internal lateral surfaces of the tube. It is associated with the fact that on the end of the open CNT each carbon atom has two neighbouring atoms and forms triple and single bonds $-C\equiv C-$ [23, 24], while the inside carbon atoms form one and a half bonds with three neighbouring atoms C. The triple bond on the end of the nanotube breaks when a cation of amino acid is attached, which ensures the formation of the sorbent-sorbate covalent bond in this case.

The lowest values of the distances from the atoms of oxygen (nitrogen) of the amino acid to the carbon atom when attaching the sorbate on the external and internal lateral surfaces of the sorbent are within the range of 3.2–3.4 Å. This value is significantly greater than the sum of the corresponding covalent radii, which is indicative of the absence of the sorbent-sorbate covalent bond in case of the amino acid sorption by the lateral surface of the CNT. The absence of the covalent bond and donor-acceptor interaction in this case shows that the adsorption is conditioned by the van der Waals forces. The $E_{\text{inside}} > E_{\text{lateral}}$ ratio is determined by the fact that when placing the amino acid on the external lateral surface the sorbate is connected to the half of the lateral surface of the tube, and when placing it inside the CNT it is connected to the whole surface

Table 1. Structure, dipole moment (*d*, Debye), Mulliken charges on AA and CNTs, adsorption energy (E_{ads}, kcal/mol), the smallest distances from the oxygen and nitrogen atoms of the arginine cation to the carbon atom of the nanotube (R_{CO1}, R_{CO2}, R_{CN1}, R_{CN2})

No	Visualisation of the optimised structure	*d,* D	q_{AA} q_{CNT}	E_{ads}, kcal/mol	R_{CO1}, R_{CO2}, Å	R_{CN1} R_{CN2} R_{CN3} R_{CN4}, Å
	Arginine cation on the lateral surface of a CNT					
1		36.25	0.97 0.03	19.02	3.24 3.25	4.17 3.38 3.46 3.41
	Arginine cation on the open end of a CNT					
2		42.74	0.99 0.01	91.15	1.38 2.83	4.33 4.56 3.20 3.24
	Arginine cation inside a CNT					
3		13.38	0.93 0.07	35.21	3.03 2.72	3.19 4.15 3.47 3.47

of the tube, which results in a greater value of adsorption energy.
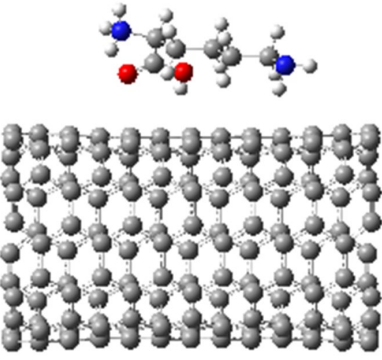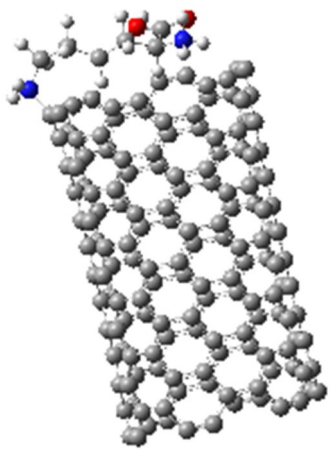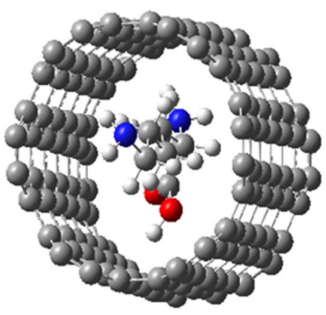
According to the reported data, multilayer CNTs functionalised by arginine and lysine have greater antibacterial activity against various bacteria [25]. In accordance with the calculated total charges on the atoms of amino acids and CNTs obtained in this work (column 4 of the Tables 1, 2), the enhancement of antibacterial activity of the CNTs functionalised by arginine and lysine (in the form of a cation in solution), as compared to nonfunctionalised CNTs, is due to the presence of a positive charge on the amino acid and the nanotube. This positive charge makes the adsorption of bacteria with the negative charge of the surface more effective.

4. Conclusions

1. The quantum-chemical calculation of structural and electrical properties of the

Table 2. Structure, dipole moment (*d*, Debye), Mulliken charges on AA and CNTs, adsorption energy (E_{ads}, kcal/mol), the smallest distances from the oxygen and nitrogen atoms of the lysine cation to the carbon atom of the nanotube (R_{CO1}, R_{CO2}, R_{CN1}, R_{CN2}

No	Visualisation of the optimised structure	*d*, D	q_{AA} q_{CNT}	E_{ads}, kcal/mol	R_{CO1}, R_{CO2}, Å	R_{CN1} R_{CN2}, Å
	Lysine cation on the lateral surface of a CNT					
4.		34.93	0.95 0.05	15.71	4.35 4.03	3.61 3.33
	Lysine cation on the end of a CNT					
5.		48.70	0.97 0.03	49.89	3.19 3.21	1.50 3.20
	Lysine cation inside a CNT					
6.		12.51	0.92 0.08	32.31	3.31 3.27	3.39 3.35

L-Lysine (L-Arginine) – chiral single-wall carbon nanotube (6,6) systems was conducted with the open ends in the aqueous solution with pH = 7 for three positions of sorbate: on the external lateral surface, on the end, and inside the CNT.

2. The row of adsorption energies of amino acids on the CNT satisfies the condition $E_{end} > E_{inside} > E_{lateral}$. A covalent bond is formed between the sorbent and the sorbate on the open end of the tube, and the amino acid is attached to the lateral surface through the van der Waals interactions.

4. The value of the dipole moment of the amino acid – CNT system is within the range

from 13.38 to 42.74 D (arginine) and within the range from 9.01 to 13.83 D (lysine). The charge transfer from the amino acid to the nanotube in the course of adsorption is insignificant (0.01 - 0.08e), which indicates the absence of the donor-acceptor interaction between the sorbent and the sorbate.

3. The enhancement of antibacterial activity of the CNTs functionalised by arginine and lysine, as compared to nonfunctionalised CNTs, found in the reported data, is due to the presence of a positive charge on the amino acid and the nanotube. As a result, the value of adsorption is higher on the functionalised CNTs for bacteria with a negative charge.

Acknowledgements

Conflict of interests

The authors declare that they have no known competing financial interests or personal relationships that could have influenced the work reported in this paper.

References

1. Rakov E. G. Carbon nanotubes in new materials. *Russian Chemical Reviews*. 2013;82(1): 27–47. DOI: https://doi.org/10.1070/rc2013v082n01abeh004227

2. Rakov E. G. Materials made of carbon nanotubes. The carbon nanotube forest. *Russian Chemical Reviews*. 2013;82(6): 538–566. DOI: https://doi.org/10.1070/rc2013v082n06abeh004340

3. Dai H., Hafner J., Rinzler A., Colbert D., Smalley R. Nanotubes as nanoprobes in scanning probe microscopy. *Nature.* 1996;384(6605): 147–150. DOI: https://doi.org/10.1038/384147a0

4. Zhai P., Isaacs J., Eckelman M. Net energy benefits of carbon nanotube applications. *Appl. Energy.* 2016;173: 624–634. DOI: https://doi.org/10.1016/j.apenergy.2016.04.001

5. Tuchin A. V., Tyapkina V. A., Bityutskaya L. A., Bormontov E. N. Functionalization of capped ultra-short single-walled carbon nanotube (5,5). *Kondensirovannye sredy i mezhfaznye granitsy = Condensed Matter and Interphases.* 2016;18(4): 568–577. Available at: Https://journals.vsu.ru/kcmf/article/view/167 (In Russ., abstract in Eng.)

6. Atlukhanova L. B., Dolbin I. V., Kozlov G. V. The physical characteristics of nanofiller and interfacial regions in nanocomposites with polymer/carbon nanotubes and elastomeric vitreous matrix. *Kondensirovannye sredy i mezhfaznye granitsy = Condensed Matter and Interphases.* 2019;21(4): 471–477, DOI: https://doi.org/10.17308/kcmf.2019.21/2358 (In Russ., abstract in Eng.)

7. Atlukhanova L. B., Dolbin I. V., Kozlov G. V. The Physics of Interfacial Adhesion between a Polymer Matrix and Carbon Nanotubes (Nanofi bers) in Nanocomposites. *Kondensirovannye sredy i mezhfaznye granitsy = Condensed Matter and Interphases.* 2020;22(2):190–196 DOI: https://doi.org/10.17308/kcmf.2020.22/2822

8. Nowack B., David R., Fissan H., Morris H., Shatkin J., Stintz M., Zepp R., Brouwer D. Potential release scenarios for carbon nanotubes used in composites. *Environ. Int.* 2013;59: 1–11. DOI: https://doi.org/10.1016/j.envint.2013.04.003

9. Kumar S., Rani R., Dilbaghi N., Tankeshwarab K. Carbon nanotubes: a novel material for multifaceted applications in human healthcare. *The Royal Society of Chemistry.* 2017;46(1): 158–196. DOI: https://doi.org/10.1039/c6cs00517a

10. Liu Z., Chen K., Davis C., Sherlock S., Cao Q., Chen X., Dai H. Drug Delivery with Carbon Nanotubes for *In vivo* Cancer Treatment. *Drug delivery Cancer Treatment Cancer Res.* 2008;68: 6652–6660. DOI: https://doi.org/10.1158/0008-5472.can-08-1468

11. Postnov V. N., Rodinkov O. V., Moskvin L. N., Novikov A. G., Bugaichenko A. S., Krokhina O. A. From carbon nanostructures to high-performance sorbents for chromatographic separation and preconcentration. *Russian Chemical Reviews* 2016;85(2): 115–138. DOI: https://doi.org/10.1070/rcr4551

12. Vardanega D., Picaud F. Detection of amino acids encapsulation and adsorption with dielectric carbon nanotube. *Journal of Biotechnology.* 2009;144(2): 96–101. DOI: https://doi.org/10.1016/j.jbiotec.2009.08.016

13. Ganji M. Density functional theory based treatment of amino acids adsorption on single-walled carbon nanotubes. *Diamond & Related Materials* 2009;18(4): 662–668. DOI: https://doi.org/10.1016/j.diamond.2008.11.021

14. Roman T., Dino W., Nakanishi H., Kasai H. Amino acid adsorption on single-walled carbon nanotubes. *Eur. Phys. Journal D.* 2006;38(1): 117–120. DOI: https://doi.org/10.1140/epjd/e2006-00043-1

15. He Z., Zhou J. Probing carbon nanotube–amino acid interactions in aqueous solution with molecular

dynamics simulations. *Carbon*. 2014;78: pp. 500–509. DOI: https://doi.org/10.1016/j.carbon.2014.07.031

16. Garalleh H. A., Thamwattan, N., Cox B. J., Hill J. M. Encapsulation of L-histidine amino acid inside single-walled carbon nanotubes. *J. of Biomaterials and Tissue Engineering*. 2016;6(5): 362–369. DOI: https://doi.org/10.1166/jbt.2016.1459

17. Tu Y., Lv M., Xiu P., Huynh T., Zhang M., Castelli M., ... Zhou R. Destructive extraction of phospholipids from Escherichia coli membranes by graphene nanosheets. *Physical and Chemical Properties of Carbon Nanotubes*. 2013;8(8): 594–601. DOI: https://doi.org/10.1038/nnano.2013.125

18. Piao L., Liu Q., Li Y. Interaction of amino acids and single-wall Carbon nanotubes. *J. Phys. Chem. C*. 2012;116 (2): 1724–1731. DOI: https://doi.org/10.1021/jp2085318

19. Foresman J., Keith T., Wiberg K., Snoonian J., Frisch M. Influence of cavity shape, truncation of electrostatics, and electron correlation on ab initio reaction field calculations. *J. Phys Chem*. 1996;100(40): 16098–16104. DOI: https://doi.org/10.1021/jp960488j

20. Frisch. M. J., Trucks G. W., Schlegel H. B. *Gaussian 09. Gaussian*. Wallingford CT Inc; 2009.

21. Butyrskaya E. V. *Komp'yuternaya khimiya: osnovy teorii i rabota s programmami Gaussian i GaussView* [Computer chemistry: basic theory and work with Gaussian and GaussView programs]. Moscow: Solon-press; 2011. 224 p. (in Russ.)

22. Grimme S., Antony J., Ehrlich S. A consistent and accurate ab initio parameterization of density functional dispersion correction (DFT-D) for the 94 elements H-Pu. *J. Chem. Phys*, 2010, vol. 132, p. 154104. DOI: https://doi.org/10.1063/1.3382344

23. Butyrskaya E. V., Zapryagaev S. A., Nechaeva L. S., Karpushin A. A., Izmailova E. A. Effect of the calculation method and the basis set on the structure and electric properties of (4,4) carbon nanotubes with different lengths and open ends. . *Journal of Structural Chemistry*. 2016;57(4): 688–694. DOI: https://doi.org/10.15372/JSC20160403

24. Nechaeva L. S., Butyrskaya E. V., Zapryagaev S. A. Computer simulation of size effects and adcorption properties of one-wall carbon nanotubes (6,6). *Russian Journal of General Chemistry*. 2016;86(7): 1208–1215. DOI: https://doi.org/1010.1134/S1070363216070252

25. Zardini H. Enhanced antibacterial activity of amino acids-functionalized multi walled carbon nanotubes by a simple method. *Biointerfaces*. 2012;92: 196–202. DOI: https://doi.org/10.1016/j.colsurfb.2011.11.045

Information about the authors

Elena V. Butyrskaya, DSc in Chemistry, Full Professor, Department of Analytical Chemistry,Voronezh State University, Voronezh, Russian Federation; e-mail: bev5105@yandex.ru. ORCID iD: https://orcid.org/0000-0003-4096-6224.

Sergey A. Zapryagaev, DSc in Physics and Mathematics, Full Professor, Voronezh State University, Voronezh, Russian Federation; e-mail: zsa@cs.vsu.ru. ORCID iD: https://orcid.org/0000-0001-8695-5382.

Ekaterina A. Izmailova, technologist, Joint Stock Company "Concern "Sozvezdie", Voronezh, Russian Federation; e-mail: ekaterina.izmajlova@mail.ru. ORCID iD: https://orcid.org/0000-0002-8163-3111.

Stepan V. Artyshchenko, PhD in Physics and Mathematics, Associate Professor, Voronezh State Technical University, Voronezh, Russian Federation; e-mail: art.stepan@mail.ru. ORCID iD: https://orcid.org/0000-0002-8567-9192.

All authors have read and approved the final manuscript.

Translated by Marina Strepetova
Edited and proofread by Simon Cox

Condensed Matter and Interphases
(Kondensirovannye sredy i mezhfaznye granitsy)

Thermodynamic investigation of the Bi₂Se₃–Bi₂Te₃ system by the EMF method

© 2020 G. S. Hasanovaᵃ, A. I. Aghazadeᵇ, Yu. A. Yusibovᵃ, M. B. Babanlyᵇ✉

ᵃGanja State University
425, H. Aliyev, Ganja AZ-2001, Azerbaijan

ᵇInstitute of Catalysis and Inorganic Chemistry, Azerbaijan National Academy of Sciences
113, H. Javid ave., Baku AZ-1143, Azerbaijan

Abstract

Binary and complex chalcogenides with a tetradimite-like layered structure are of great practical interest as topological insulators, thermoelectric, and optoelectronic materials. Their fundamental thermodynamic functions in combination with phase diagrams are important for the development and optimization of methods for the synthesis and growth of crystals.

The work presents the results of a thermodynamic study of the starting compounds and solid solutions of the Bi_2Se_3-Bi_2Te_3 system using the method of electromotive forces (EMF). Various modifications of this method are widely used to study binary and complex metal chalcogenides. Studies were carried out by EMF measurements of the concentration chains of the following type:

(−) Bi (solid) | ionic liquid + Bi³⁺ | Bi in the alloy (solid) (+)

in the temperature range 300–450 K.

The pre-synthesized equilibrium $Bi_2Se_{3-x}Te_x$ alloys (*x* = 0; 0.6; 1.2; 1.8; 2.0; 2.4; 3.0) with a 0.5 at% excess tellurium were used as right electrodes. Ionic liquid (morpholine formate) with the addition of $BiCl_3$ was used as the electrolyte.

The acquired experimental data were processed by the Microsoft Office Excel 2003 computer program using the least-squares method and linear equations of the type $E = a + bT$ were obtained. The obtained equations of the EMF temperature dependences were used to calculate the relative partial molar functions of bismuth in the alloys. The diagram of solid-phase equilibria of the Bi–Se–Te system was used to determine the equations of potential-forming reactions and the latter were used to calculate the standard thermodynamic functions of the formation and standard entropies of Bi_2Se_3, Bi_2Te_3 compounds and $Bi_2Se_{3-x}Te_x$ solid solutions of the above compositions. The thermodynamic functions of the formation of $Bi_2Se_{3-x}Te_x$ solid solutions from the initial binary compounds were also calculated. The results correlate well with the structural data that suggests some ordering in the arrangement of selenium and tellurium atoms in the b-phase crystal lattice of the Bi_2SeTe_2 composition: selenium atoms predominantly occupy the central layer of the five-layer, and tellurium atoms are located in the two outer layers.

Keywords: bismuth selenides, bismuth telluride, solid solutions, EMF method, thermodynamic properties.

✉ Mahammad B. Babanly, e-mail: babanlymb@gmail.com

1. Introduction

The Bi_2Se_3, Bi_2Te_3 compounds, as well as solid solutions and composites based on them are of great interest as thermoelectric and optoelectronic materials [1–6]. Recent studies have shown that they are also topological insulators and are extremely promising for use in spintronics, quantum computers, and other high technology areas [7–12]. The introduction of magnetic elements into the crystal structure of these compounds led to the creation of a new class of innovative functional materials, i.e. magnetic topological insulators [13–16].

The thermodynamic functions of compounds and variable phases are their fundamental characteristics and, in combination with phase diagrams, form the basis for the synthesis and growth of crystals [17, 18]. Analysis of the reported data has shown that the thermodynamic properties of Bi_2Se_3 and Bi_2Te_3 have been studied in many works by various methods [19–23]. Experimental studies of the thermodynamic properties of the Bi_2Se_3–Bi_2Te_3 solid solutions were carried out by the electromotive force (EMF) method in the temperature range of 670–840 K [23]. An analysis showed that Bi_2Te_3+Te and $Bi_2Se_xTe_{3-x}$+Te alloys used as electrodes in the concentration cell contain a Te-based liquid solution in the indicated temperature range. According to the phase diagrams of the Bi-Te and Bi–Se–Te systems, the composition of this liquid phase varies with temperature, which should lead to a distortion of the EMF values, especially their temperature coefficient [24].

The aim of this work is the thermodynamic study of the initial compounds and solid solutions of the Bi_2Se_3–Bi_2Te_3 system by the EMF method.

Various modifications of the EMF method are widely used to study binary and complex metal chalcogenides [25–33]. In high-temperature studies, as a rule, eutectic melts of alkali metal salts are used as an electrolyte. In the study of solid metal chalcogenides, it is advisable to make measurements at temperatures below solidus. For this purpose, the most suitable electrolytes were glycerol solutions of alkali metal salts, first used in [34] in the study of amalgam systems. In our recent studies [35, 36], an ionic liquid was successfully tested as a liquid electrolyte.

2. Experimental

To study the thermodynamic properties of the Bi_2Se_3-Bi_2Te_3 system by the EMF method, the concentration cells of the following type

$$(-) \text{ Bi (solid)} \mid \text{ionic liquid} + Bi^{3+} \mid$$
$$\mid \text{Bi in the alloy (solid) (+)} \qquad (1)$$
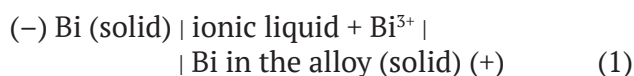
were assembled and their EMF in the temperature range 300–450 K were measured.

Elemental bismuth was used as the left electrode, and $Bi_2Se_{3-x}Te_x$ equilibrium alloys (x = 0; 0.6; 1.2; 1.8; 2.0; 2.4; 3.0) with a 0.5 at% excess tellurium were used as the right electrodes.

The alloys of the right electrodes were synthesized by the melting of the previously synthesized and identified Bi_2Se_3, Bi_2Te_3 compounds, and excess tellurium in evacuated (~ 10^{-2} Pa) quartz ampoules at 1000 K, followed by annealing at 750 K (500 h) and 400 K (20 h). The phase composition of the obtained alloys was confirmed by XRD.

Ionic liquid (morpholine formate) with the addition of $BiCl_3$ was used as the electrolyte. Morpholine, formic acid, and anhydrous $BiCl_3$ purchased from Alfa Aesar were used to produce the ionic liquid. The ionic liquid was obtained using the procedure described in [37]. The assembly of electrochemical cells of type (1) and the method for measuring EMF are described in detail in [27, 36].

The first equilibrium EMF values were obtained after maintaining the electrochemical cell at ~350 K for 40–60 hours; the subsequent values were obtained every 3–4 hours after a specific temperature was established. The EMF values were considered equilibrium if they did not differ from each other by more than 0.2 mV when measured repeatedly at a given temperature, regardless of the direction of the temperature change.

3. Results and discussion

The measurements showed that for each studied sample, the EMF value varied linearly with temperature (Fig. 1), and the EMF concentration dependence was a monotonic function. This confirms the phase diagram of the Bi_2Se_3–Bi_2Te_3 system, according to which, it is characterized by the formation of a continuous series of solid solutions [38].
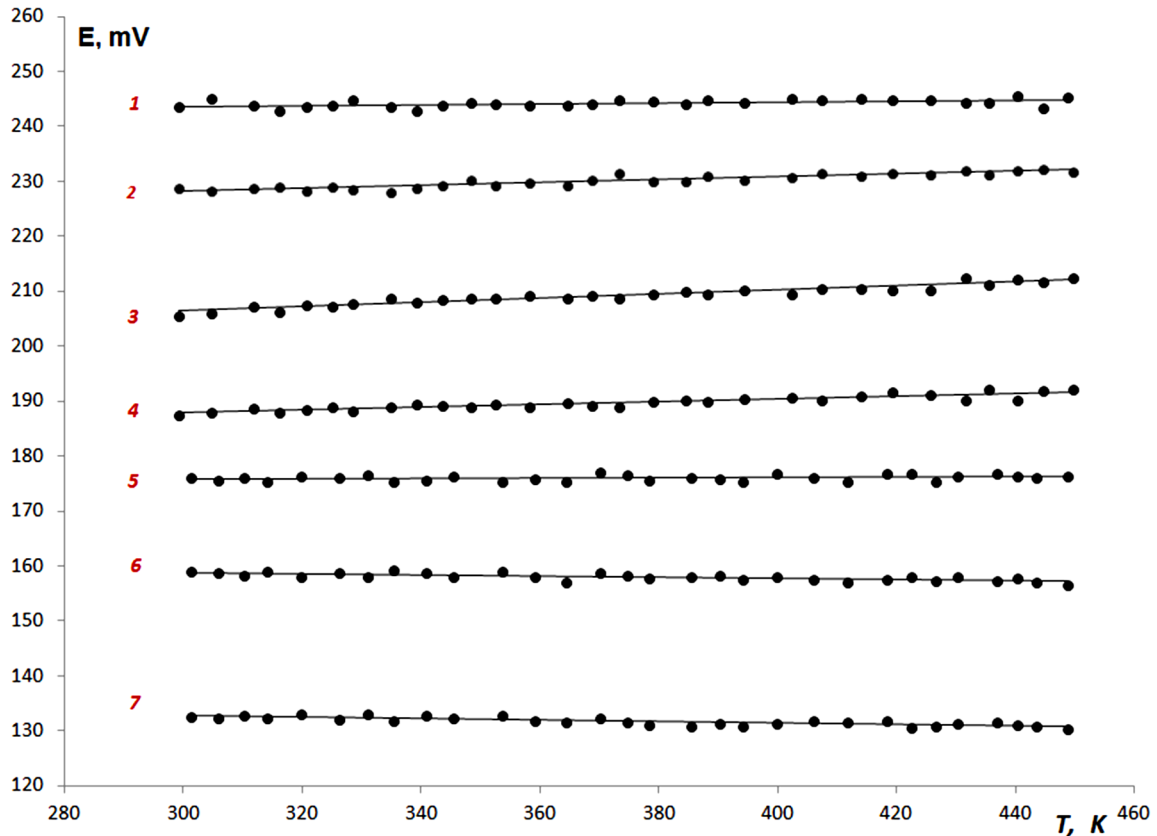
Fig. 1. Temperature dependencies of EMF for the alloys of the Bi$_2$Se$_3$–Bi$_2$Te$_3$ system. *1* – Bi$_2$Se$_3$; *2* – Bi$_2$Se$_{2.4}$Te$_{0.6}$; *3* – Bi$_2$Se$_{1.8}$Te$_{1.2}$; *4* – Bi$_2$Se$_{1.2}$Te$_{1.8}$; *5* – Bi$_2$SeTe$_2$; *6* – Bi$_2$Se$_{0.6}$Te$_{2.4}$; *7* – Bi$_2$Te$_3$

The acquired experimental data were processed by the Microsoft Office Excel 2003 computer program using the least-squares method and linear equations of the type $E = a + bT$ were obtained. The calculation steps for the Bi$_2$Se$_{2.4}$Te$_{0.6}$ sample are given in Table 1. The linear equations obtained during the calculations are shown in Table 2 in accordance with modern recommendations [26,27]:

$$E = a + bT \pm t \left[\frac{\delta_E^2}{n} + \delta_b^2 (T - \overline{T})^2 \right]^{1/2} \quad (2)$$

In equation (2), a and b are coefficients, n is the number of pairs of values of E and T; $\overline{T}$ is the average temperature, K; t is Student's t-test, δ_E^2 and δ_b^2 are dispersions of individual values of EMF and constant b. Given that the number of experimental points is $n = 30$, at a confidence level of 95 %, the Student test is $t \leqslant 2$ [26].

The obtained equations (Table 2) and known expressions [26]:

$$\overline{\Delta G}_{Bi} = -zFE \quad (3)$$

$$\overline{\Delta S}_{Bi} = zF \left(\frac{\partial E}{\partial T} \right)_P = zFb \quad (4)$$

$$\overline{\Delta H}_{Bi} = -zF \left[E - T \left(\frac{\partial E}{\partial T} \right)_P \right] = -zFa \quad (5)$$

were used to calculate the partial molar Gibbs free energy, enthalpy, and entropy of bismuth in the alloys (Table 3).

As can be seen from Fig. 2, these partial molar functions continuously change with composition, which reflects the formation of a continuous series of solid solutions in the system.

To calculate the integral thermodynamic functions of Bi$_2$Se$_x$Te$_{3-x}$ solid solutions, we constructed a diagram of the solid-phase equilibria of the Bi–Se–Te system in the Bi$_2$Se$_3$–Bi$_2$Te$_3$–Te–Se composition range (Fig. 3) using the data from [38, 39]. According to [38], alloys of the Bi–Se and Bi–Te boundary systems in the composition range < 40 at% Bi consist of the two-phase mixtures Bi$_2$Se$_3$+Se and Bi$_2$Te$_3$+Te accordingly. Another boundary Se–Te system

Table 1. Experimentally obtained data for temperature (T_i) and EMF (E_i) and data associated with the calculation steps for the $Bi_2Se_{2.4}Te_{0.6}$ sample

T_i, K	E_i, мВ	$T_i - \bar{T}$	$E_i(T_i - \bar{T})$	$(T_i - \bar{T})^2$	$\tilde{E}$	$E_i - \tilde{E}$	$(E_i - \tilde{E})^2$
299.3	228.63	−74.26	−16978.83	5515.04	228.13	0.50	0.25
304.8	228.12	−68.76	−15686.29	4728.40	228.27	−0.15	0.02
311.7	228.71	−61.86	−14148.76	3827.07	228.45	0.26	0.07
316.2	228.95	−57.36	−13133.34	3290.55	228.57	0.38	0.14
320.6	228.23	−52.96	−12087.82	2805.11	228.69	−0.46	0.21
325.1	229.02	−48.46	−11099.07	2348.69	228.81	0.21	0.05
328.6	228.56	−44.96	−10276.82	2021.70	228.90	−0.34	0.11
334.8	228.11	−38.76	−8842.30	1502.60	229.06	−0.95	0.90
339.2	228.86	−34.36	−7864.39	1180.84	229.18	−0.32	0.10
343.5	229.17	−30.06	−6889.61	903.80	229.29	−0.12	0.01
348.4	230.13	−25.16	−5790.84	633.19	229.42	0.71	0.51
352.5	229.14	−21.06	−4826.45	443.66	229.53	−0.39	0.15
358.2	229.78	−15.36	−3530.19	236.03	229.68	0.10	0.01
364.7	229.22	−8.86	−2031.65	78.56	229.85	−0.63	0.39
368.8	230.23	−4.76	−1096.66	22.69	229.96	0.27	0.07
373.4	231.42	−0.16	−37.80	0.03	230.08	1.34	1.80
379.1	230.08	5.54	1273.88	30.65	230.23	−0.15	0.02
384.6	229.86	11.04	2536.89	121.81	230.37	−0.51	0.26
388.2	230.98	14.64	3380.78	214.23	230.47	0.51	0.26
394.3	230.13	20.74	4772.13	430.01	230.63	−0.50	0.25
402.4	230.82	28.84	6656.08	831.55	230.84	−0.02	0.00
407.5	231.47	33.94	7855.32	1151.70	230.98	0.49	0.24
414.1	230.86	40.54	9358.29	1643.22	231.15	−0.29	0.08
419.2	231.58	45.64	10568.54	2082.71	231.28	0.30	0.09
425.8	231.12	52.24	12072.94	2728.67	231.46	−0.34	0.11
431.6	232.07	58.04	13468.57	3368.25	231.61	0.46	0.21
435.5	231.32	61.94	14327.19	3836.15	231.71	−0.39	0.15
440.3	231.83	66.74	15471.56	4453.78	231.84	−0.01	0.00
444.7	232.27	71.14	16522.91	5060.43	231.96	0.31	0.10
449.8	231.78	76.24	17670.13	5812.03	232.09	−0.31	0.10
$\bar{T} = 373.56$	$\bar{E} = 230.08$						

[39], as well as the Bi_2Se_3–Bi_2Te_3 [38] system, is characterized by the formation of a continuous series of solid solutions. Therefore, in the diagram of solid-phase equilibria in the Bi_2Se_3–Bi_2Te_3–Te–Se composition range, the α- and β-solid solutions are in the conode connection. Moreover, in the two-phase region α+β, the directions of the conodes will coincide with the ray lines from the bismuth angle of the concentration triangle.

On the other hand, according to the available data [40], the mixing heat of α-solid solutions of the Se–Te system with an accuracy of ±1 kJ is zero, i.e. these solid solutions are close to ideal. Therefore, the entropy and Gibbs free energy of mixing the α-phase can be calculated by the following relations:

$$\Delta S_{mix} = -RT[\ln x + (1-x)\ln(1-x)] \qquad (6)$$

$$\Delta G_{mix} = RT[\ln x + (1-x)\ln(1-x)] \qquad (7)$$

Taking into account the ray nature of the conode in the two-phase region α+β (Fig. 3),
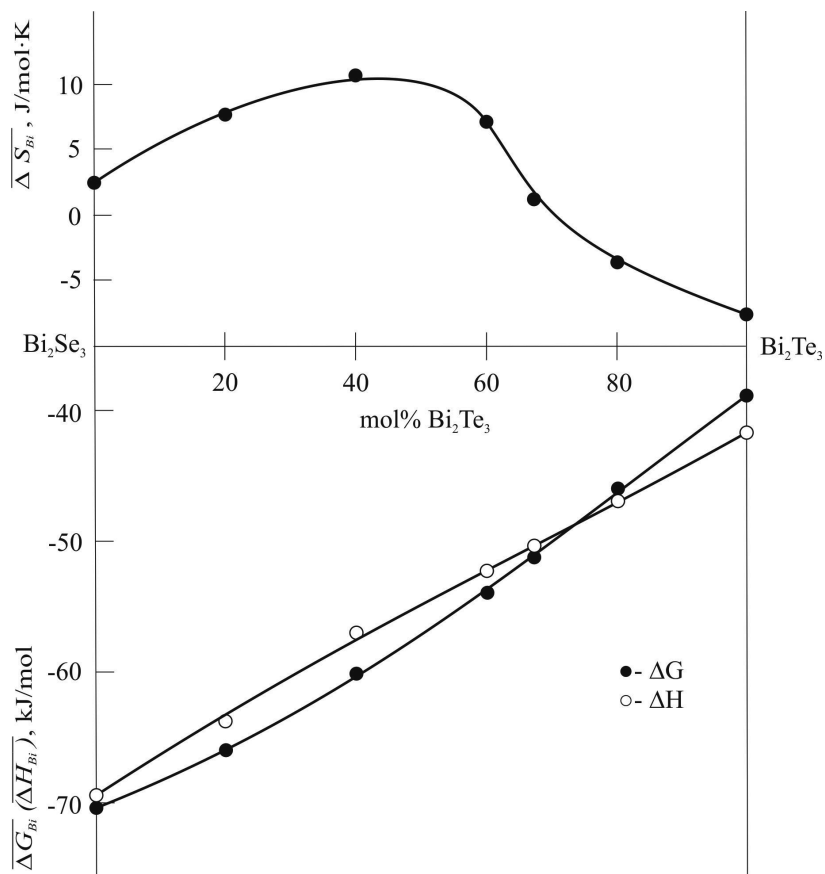
Fig. 2. Composition dependences of the partial molar functions of bismuth in the Bi_2Se_3–Bi_2Te_3 system at 298 K
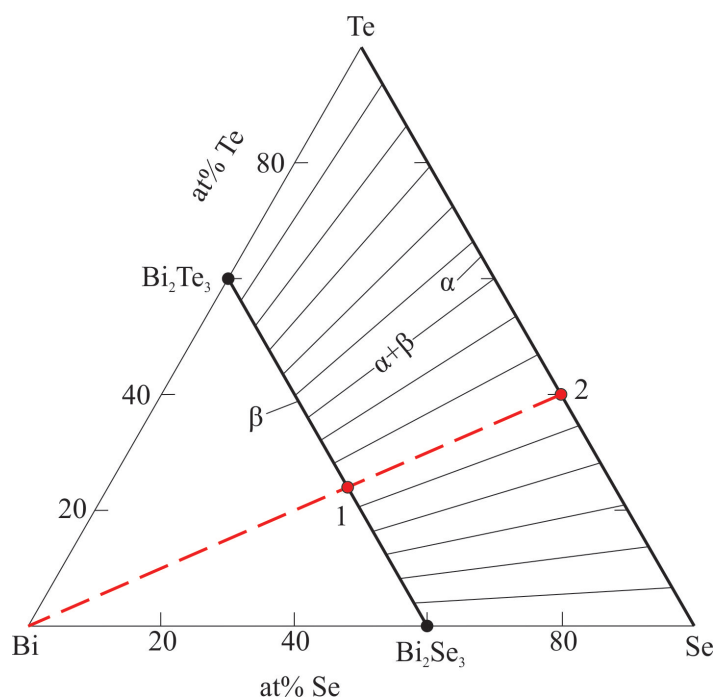
Fig. 3. Diagram of solid-phase equilibria of the Bi–Se–Te system in the Bi_2Se_3–Bi_2Te_3–Te-Se composition range

Table 2. Relations between the EMF and the temperature for type (1) cells for some samples of the Bi_2Se_3- Bi_2Te_3 system in the 300–450 K temperature interval

Phase	E, mV $= a + bT \pm t \cdot d_E(T)$
Bi_2Se_3	$241.08 + 0.0082T \pm 2\left[\dfrac{0.33}{30} + 5.4 \cdot 10^{-6}(T - 373.53)^2\right]^{1/2}$
$Bi_2Se_{2.4}Te_{0.6}$	$220.24 + 0.0263T \pm 2\left[\dfrac{0.22}{30} + 3.6 \cdot 10^{-6}(T - 373.56)^2\right]^{1/2}$
$Bi_2Se_{1.8}Te_{1.2}$	$195.02 + 0.0379T \pm 2\left[\dfrac{0.27}{30} + 4.4 \cdot 10^{-6}(T - 373.56)^2\right]^{1/2}$
$Bi_2Se_{1.2}Te_{1.8}$	$180.17 + 0.0256T \pm 2\left[\dfrac{0.22}{30} + 3.7 \cdot 10^{-6}(T - 373.56)^2\right]^{1/2}$
Bi_2SeTe_2	$175.56 + 0.0018T \pm 2\left[\dfrac{0.2}{30} + 3.2 \cdot 10^{-6}(T - 376.17)^2\right]^{1/2}$
$Bi_2Se_{0.6}Te_{2.4}$	$162.40 - 0,0117T \pm 2\left[\dfrac{0.21}{30} + 3.3 \cdot 10^{-6}(T - 376.17)^2\right]^{1/2}$
Bi_2Te_3	$136.73 - 0.0133T \pm 2\left[\dfrac{0.21}{30} + 3.4 \cdot 10^{-6}(T - 376.17)^2\right]^{1/2}$

Table 3. Partial molar functions of bismuth in the alloys of the $Bi_2Se_3-Bi_2Te_3$ system at $T = 298$ K

Phase	$-\Delta \overline{G}_{Bi}$, kJ/mol	$-\Delta \overline{H}_{Bi}$, kJ/mol	$\Delta \overline{S}_{Bi}$, J/(mol·K)
Bi_2Se_3	70.50 ± 0.08	69.78 ± 0.33	2.41 ± 0.87
$Bi_2Se_{2.4}Te_{0.6}$	66.03 ± 0.07	63.75 ± 0.28	7.62 ± 0.74
$Bi_2Se_{1.8}Te_{1.2}$	59.73 ± 0.07	56.45 ± 0.30	10.98 ± 0.81
$Bi_2Se_{1.2}Te_{1.8}$	54.36 ± 0.07	52.15 ± 0.28	7.40 ± 0.74
Bi_2SeTe_2	50.97 ± 0.06	50.82 ± 0.26	0.52 ± 0.69
$Bi_2Se_{0.6}Te_{2.4}$	46.00 ± 0.06	47.01 ± 0.27	-3.38 ± 0.69
Bi_2Te_3	38.86 ± 0.06	41.50 ± 0.26	-7.71 ± 0.70

the potential-forming reaction for any given composition of the β-phase should have the following form:

$$Bi + 1.5Se_{1-y}Te_y = 0.5Bi_2Se_{3-x}Te_x. \qquad (8)$$
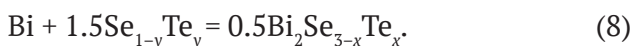
In our case y = 0.2, 0.4, 0.6, 0.67, 0.8. For specific compositions, for example, $x = 0.6$, $y = 0.2$, this reaction has the following form:

$$Bi + 1.5Se_{0.8}Te_{0.2} = 0.5Bi_2Se_{2.4}Te_{0.6}. \qquad (9)$$

According to reaction (9), for the β-phase of the $Bi_2Se_{2.4}Te_{0.6}$ composition, the standard thermodynamic functions of formation and the standard entropy can be calculated by the following relations:

$$\Delta_f G^0(Bi_2 Se_{2.4} Te_{0.6}) = 2\Delta \overline{G}_{Bi} + 3\Delta G_{mix}(Se_{0.8} Te_{0.2}), \quad (10)$$

$$\Delta_f H^0(Bi_2 Se_{2.4} Te_{0.6}) = 2\Delta \overline{H}_{Bi}, \qquad (11)$$

$$\Delta_f S^0(Bi_2 Se_{2.4} Te_{0.6}) = \qquad (12)$$
$$= 2\Delta \overline{S}_{Bi} + 2S_{Bi}^0 + 3\Delta S_{mix}(Se_{0.8} Te_{0.2}),$$

$$S^0(Bi_2Se_{2.4} Te_{0.6}) = 2\Delta \overline{S}_{Bi} + 2S_{Bi}^0 + \qquad (13)$$
$$+3\Delta S_{mix}(Se_{0.8} Te_{0.2}) + 2.4S^0(Se) + 0.6S^0(Te).$$

The calculation results for the starting compounds and $Bi_2Se_{3-x}Te_x$ solid solutions are presented in Table 4.

As can be seen from Table 4, for the initial compounds, our data are coherent with the

Table 4. Standard integral thermodynamic functions of alloys of the $Bi_2Se_3-Bi_2Te_3$ system

Phase	$-\Delta G^o$ (298 K), kJ/mol	$-\Delta H^o$ (298K), kJ/mol	S^o (298K), J/(mol·K)	Ref.
	141.0 ± 0.2	139.6 ± 0.7	245.1 ± 4.3	This work
Bi_2Se_3	141.1±1.1	142.5±2.0		[41]
	143.6±0.4	145.0±4.0		[23]
	151.6±2.0	153.5±6.5		[42]
		140.2±3.0	240±8	[19–22]
$Bi_2Se_{2.4}Te_{0.6}$	135.8±0.2	127.5±0.6	272.0±3.0	This work
$Bi_2Se_{1.8}Te_{1.2}$	124.5±0.2	112.9±0.6	287.6±3.3	This work
$Bi_2Se_{1.2}Te_{1.8}$	113.7±0.2	104.3±0.6	284.6±3.2	This work
Bi_2SeTe_2	106.0±0.2	101.6±0.6	269.0±3.0	This work
$Bi_2Se_{0.6}Te_{2.4}$	95.7±0.2	94.0±0.6	263.2±3.1	This work
	76.9±0.2	79.2±0.6	254.2±3.0	This work
	77.9±0.6	80.0±4.4		[43]
	82.8	87.0		[42]
Bi_2Te_3	89.5±0.9	99.5±9.5		[23]
	77.3±1.7	78.4±2.1	261.0±8.4	[20. 22]
	75.3±1.7	78.6±0.2	251.0±8.4	[21]

results of [41, 43] acquired by the EMF method and recommended in modern handbooks [19–22]. Results [42] for both compounds are somewhat overestimated. It should also be noted that the data of [23] for Bi_2Se_3 are in agreement with our data, while for Bi_2Te_3, they are somewhat overestimated.

By combining the standard thermodynamic functions of the formation of the β-phase of various compositions with the corresponding data for the initial binary compounds, we calculated the Gibbs free energy of the formation and the heat of the formation of β-solid solutions from binary compounds, i.e. thermodynamic mixing functions of $Bi_2Se_3-Bi_2Te_3$ (Table 5).

Table 5. Thermodynamic functions of mixing of $(Bi_2Se_3)_{1-y}(Bi_2Te_3)_y$ solid solutions (T = 298 K)

y	$-\Delta G^{\circ}_{mix}$, kC/mol	$-\Delta H^{\circ}_{mix}$, kC/mol
0.2	7.6±0.4	−3.1±1.2
0.4	9.1±0.4	−2.6±1.2
0.6	11.2±0.4	0.9±1.2
0.667	8.8±0.4	2.3±1.2
0.8	6.3±0.4	1.7±1.2

It is obvious that the data given in Table 5, characterize the substitution of selenium atoms by tellurium atoms in the $Bi_2Se_{3-x}Te_x$ crystal lattice

per 3 mole chalcogen. Therefore, for 1 mole of the solution, these values should be divided by 3. Fig. 4 shows the dependences of the heat and Gibbs free energy of mixing on the composition obtained in this way. As can be seen, the enthalpy of mixing in absolute value does not exceed 1 kJ/mol. In this case, the sign of this function changes from positive to negative in the composition range > 0.6. A similar change in a sign is also observed for the partial entropy of bismuth (Fig. 2). This, as well as the fact that the deepest negative ΔG_{mix} values are observed for the β-phase with compositions x = 0.6–0.7, indicates the structural ordering in solid solutions of these compositions. This correlates well with structural data [38] suggesting some ordering in the arrangement of selenium and tellurium atoms composition in the crystal lattice of the β- phase of the Bi_2SeTe_2: selenium atoms predominantly occupy the central layer of the five-layer and tellurium atoms are located in the two outer layers.

A comparison of the data in Tables 4 and 5 with the results of [23] shows their general agreement. A more detailed analysis of data [23] is difficult since, in the temperature range of EMF measurements (670–840 K), a change in the liquid composition of the electrode of Bi_2Te_3+Te (L) and $Bi_2Se_xTe_{3-x}$+Te (L)
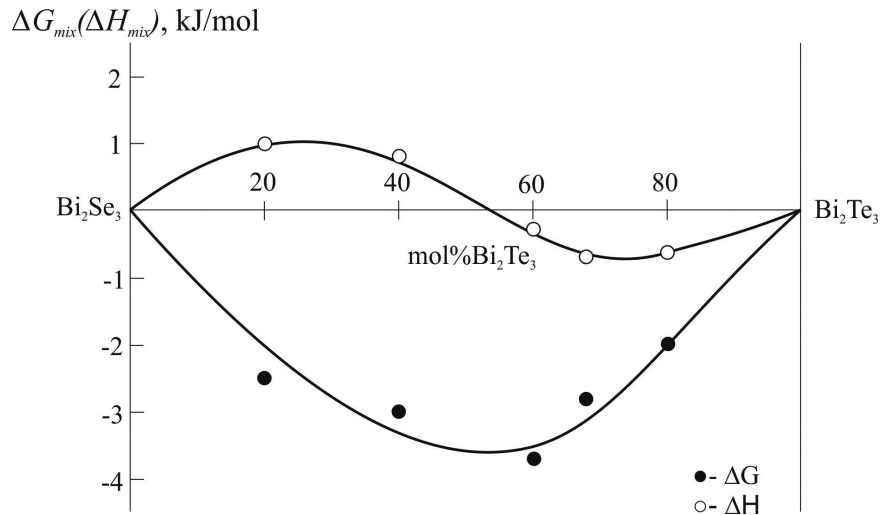
Fig. 4. Concentration dependences of the thermodynamic mixing functions of Bi_2Se_3 and Bi_2Te_3 during the formation of $Bi_2Se_{3-x}Te_x$ solid solutions per 1 mol of chalcogen

alloys along the liquidus is inevitable. It means that the EMF temperature coefficient reflects not only the partial entropy of bismuth but also the change in the melt composition [24].

4. Conclusions

The Bi_2Se_3–Bi_2Te_3 system was studied by analysing the EMF measurements of the concentration cells relative to the bismuth electrode in the temperature range 300–450 K. The obtained experimental data was used to calculate the partial thermodynamic functions of bismuth in the alloys. The diagram of solid-phase equilibria of the Bi–Se–Te system in the Bi_2Se_3–Bi_2Te_3–Te–Se composition range was used to determine the potential-forming reactions and the latter were used to calculate the standard thermodynamic functions of the formation and standard entropies of the Bi_2Se_3, Bi_2Te_3, and $Bi_2Se_xTe_{3-x}$ solid solutions. The thermodynamic functions of mixing binary compounds during the formation of these solid solutions were calculated by combining these data. The analysis of these functions allowed us to make the conclusion about the ordered arrangement of selenium and tellurium atoms in the crystal lattice of solid solutions with Bi_2Te_2Se composition.

Acknowledgements

Conflict of interests

The authors declare that they have no known competing financial interests or personal relationships that could have influenced the work reported in this paper.

References

1. Rowe D. M. *Thermoelectrics Handbook: Macro to Nano*. Boca Raton, FL, USA: CRC Press, Taylor & Francis Group; 2006. 1008 p.

2. Shevelkov A. V. Chemical aspects of the design of thermoelectric materials. *Russ. Chem. Rev.* 2008;77(1): 1–19. DOI: https://doi.org/10.1070/RC2008v077n01ABEH003746

3. Adam A. M., Lilov E., Ibrahim E. M. M., Petkov P., Panina L. V., Darwish M. A. Correlation of structural and optical properties in as-prepared and annealed Bi_2Se_3 thin films. *Journal of Materials Processing Technology*. 2019;264: 76–83. DOI: https://doi.org/10.1016/j.jmatprotec.2018.09.005

4. Wang Q., Wu X., Wu L., Xiang Y. Broadband nonlinear optical response in Bi_2Se_3–Bi_2Te_3 heterostructure and its application in all-optical switching. *AIP Advances 9*. 2019; 025022. DOI: https://doi.org/10.1063/1.5082725

5. Hosokawa Y., Wada K., Tanaka M., Tomita K., Takashiri M. Thermal annealing effect on structural and thermoelectric properties of hexagonal Bi_2Te_3 nanoplate thin films by drop-casting technique.

Japanese Journal of Applied Physics. 2017;57(2S2): 02CC02. DOI: https://doi.org/10.7567/jjap.57.02cc02

6. Adam A. M., Elshafaie A., Abd El-Moez A. M., Petkov P., Ibrahim E. M. M. Thermoelectric properties of Te doped bulk Bi$_2$Se$_3$ system. *Materials Research Express*. 2018;5(3): 035514. DOI: https://doi.org/10.1088/2053-1591/aab5e8

7. Flammini R., Colonna S., Hogan C., Mahatha S., Papagno M., Barla A., Sheverdyaeva P., Moras P., Aliev Z., Babanly M. B, Chulkov E. V., Carbone C., Ronci F. Evidence of β-antimonene at the Sb/Bi$_2$Se$_3$ interface. *Nanotechnology.* 2018;29(6): 065704. DOI: https://doi.org/10.1088/1361-6528/aaa2c4

8. Hogan C., Holtgrewe K., Ronci F., Colonna S., Sanna S., Moras P., Sheverdyaeva P. M., Mahatha S., Papagno M., Aliev Z. S., Babanly M. B., Chulkov E. V., Carbone C., Flammini R. Temperature driven phase transition at the antimonene/Bi$_2$Se$_3$ van der Waals heterostructure. *ACS Nano*. 2019;13(9): 10481–10489. DOI: https://doi.org/10.1021/acsnano.9b04377

9. Otrokov M. M., Ernst A., Mohseni K., Fulara H., Roy S., Castro G. R., Rubio-Zuazo J., Ryabishchenkova A. G., Kokh K. A., Tereshchenko O. E., Aliev Z. S., Babanly M. B., Chulkov E. V., Meyerheim H. L., Parkin S. S. P. Geometric and electronic structure of the Cs-doped Bi$_2$Se$_3$(0001) surface. *Phys. Rev. B*. 2017;95(20): 205429. DOI: https://doi.org/10.1103/physrevb.95.205429

10. Lamuta C., Cupolillo A., Politano A., Aliev Z. S., Babanly M. B., Chulkov E. V., Pagnotta L. Indentation fracture toughness of a single-crystal Bi$_2$Te$_3$ topological insulator. *Nano Research*. 2016;9(4): 1032–1042. DOI: https://doi.org/10.1007/s12274-016-0995-z

11. Viti L., Coquillat D., Politano A., Kokh K. A., Aliev Z. S., Babanly M. B., Tereshchenko O. E., Knap W., Chulkov E. V., Vitiello M. S. Plasma-wave terahertz detection mediated by topological insulators surface states. *Nano Letters*. 2016;16(1): 80–87. DOI: https://doi.org/10.1021/acs.nanolett.5b02901

12. Babanly M. B., Chulkov E. V., Aliev Z. S., Shevel'kov A. V., Amiraslanov I. R. Phase diagrams in materials science of topological insulators based on metal chalcogenides. *Russ. J. Inorg. Chem.* 2017;62(13): 1703–1729. DOI: https://doi.org/10.1134/S0036023617130034

13. Otrokov M. M., Klimovskikh I. I., Bentmann H., et al. Prediction and observation of the antiferromagnetic topological insulator. *Nature*. 2019;576(7787): 416–422. DOI: https://doi.org/10.1038/s41586-019-1840-9

14. Shanna Z., Gang S., Peng Z., Dechao M., Genhao L., Xiaofang Z., Yalin L., Yongqing L., Lan C., Kehui W. Growth and transport properties of topological insulator Bi$_2$Se$_3$ thin film on a ferromagnetic insulating substrate. *Chinese Physics B*. 2017;27(7). DOI: https://doi.org/10.1088/1674-1056/27/7/076801

15. Walsh L. A., Smyth C. M., Barton A. T., Qingxiao W., Zifan C., Ruoyu Y., Jiyoung K., Moon J. K.,

Wallace R.M., Hinkle C. L. Interface chemistry of contact metals and ferromagnets on the topological insulator Bi$_2$Se$_3$. *J. Phys. Chem. C*. 2017;121(42): 23551–23563. DOI: https://doi.org/10.1021/acs.jpcc.7b08480

16. Liguo Z., Dapeng Z., Yunyi Z., Yonghao Y., Gaoyuan J., Menghan L., Ding Z., Ke H., Xucun M., Qikun X. Ferromagnetism in vanadium-doped Bi$_2$Se$_3$ topological insulator films. *APL Materials*. 2017;5(7): 076106. DOI: https://doi.org/10.1063/1.4990548

17. Voronin G. F., Gerasimov Ya. I. The role of chemical thermodynamics in the development of semiconductor materials science In: *Thermodynamics and Semiconductor Materials*. Moscow: MIET Publ., 1980. p. 3–10. Available at: https://search.rsl.ru/ru/record/01001069961 (In Russ.)

18. Babanly M. B., Mashadiyeva L. F., Babanly D. M., Imamaliyeva S. Z., Taghiyev D. B., Yusibov Y. A. Some issues of complex investigation of the phase equilibria and thermodynamic properties of the ternary chalcogenid systems by the EMF method. *Russian J. Iniorg.Chem*. 2019;64(13): 1649–1671. DOI: https://doi.org/10.1134/S0036023619130035

19. Barin I. *Thermochemical data of pure substances*. Third Edition. Weinheim: Wiley-VCH; 1995. DOI: https://doi.org/10.1002/9783527619825

20. Kubaschewski O., Alcock C. B., Spenser P. J. *Materials Thermochemistry*. New York: Pergamon Press; 1993. 350 p.

21. Baza dannykh termicheskikh konstant veshchestv. Elektronnaya versiya pod. red. V. S. Yungmana. 2006 [Database of thermal constants of substances. Electronic version under. ed. V. S. Yungman. 2006]. Available at: http://www.chem.msu.su/cgi-bin/tkv.pl?show=welcom.html

22. Gerasimov Ya. I., Krestovnikov A. N, Gorbov S. I. *Khimicheskaya termodinamika v tsvetnoi metallurgii. Spravochnik. t. 6* [Chemical thermodynamics in nonferrous metallurgy. Directory. vol. 6] Moscow: Metallurgiya Publ.; 1974. 312 p. (In Russ.)

23. Sidorko V. R., Goncharuk L. V., Antonenko R. V. Thermodynamic properties of bismuth sesquiselenide and sesquitelluride and their solid solutions. *Powder Metallurgy and Metal Ceramics*. 2008;47: 234–241. DOI: https://doi.org/10.1007/s11106-008-9009-3

24. Voronin G. F. *Partsial'nye termodinamicheskie funktsii geterogennykh smesei i ikh primenenie v termodinamike splavov* [Partial thermodynamic functions of heterogeneous mixtures and their application in the thermodynamics of alloys]. In: Modern problems of physical chemistry, vol. 9. Moscow: MSU Publ., 1976. pp. 29–48. (In Russ.)

25. Wagner K. *Termodinamika splavov* [Thermodynamics of alloys]. Moscow: Metallurgizdat Publ.; 1957. 179 p. (In Russ.)

26. Morachevsky A. G., Voronin G. F., Geyderich V. A., Kutsenok I. B. *Elektrokhimicheskie metody issledovaniya v termodinamike metallicheskikh sistem ITsK* [Electrochemical methods of investigation in

thermodynamics of metal systems]. Moscow: Akademkniga Publ.; 2003. 334 p. (In Russ.)

27. Babanly M. B., Yusibov Y. A. *Elektrokhimicheskie metody v termodinamike neorganicheskikh sistem* [Electrochemical methods in thermodynamics of inorganic systems]. Baku: BSU Publ.; 2011. 306 p.

28. Vassiliev V., Gong W. Electrochemical cells with the liquid electrolyte in the study of semiconductor, metallic and oxide systems. In: *Electrochemical cells – new advances in fundamental researches and applications*. Shao Y. Rijeka (ed.) IntechOpen; 2012. pp. 71–102. DOI: https://doi.org/10.5772/39007

29. Babanly D. M., Veliyeva G. M., Imamaliyeva S. Z., Babanly M. B. Thermodynamic functions of arsenic selenides. *Russ. J. Phys. Chem. A.* 2017;91(7): 170–1173. DOI: https://doi.org/10.1134/s0036024417070044

30. Aliev Z. S., Musayeva S. S., Jafarli F. Y., Amiraslanov I. R., Shevelkov A. V., Babanly M. B. The phase equilibria in the Bi–S–I ternary system and thermodynamic properties of the BiSI and Bi1_9S$_{27}$I$_3$ ternary compounds. *Journal of Alloys and Compounds.* 2014;610: 522–528. DOI: https://doi.org/10.1016/j.jallcom.2014.05.015

31. Jafarov Y. I., Ismaylova S. A., Aliev Z. S., Imamaliyeva S. Z., Yusibov Y. A., Babanly M. B. Experimental study of the phase diagram and thermodynamic properties of the Tl–Sb–S system. *Calphad.* 2016;55: 231–237. DOI: https://doi.org/10.1016/j.calphad.2016.09.007

32. Imamaliyeva S. Z., Babanly D. M., Gasanly T. M., Tagiev D. B., Babanly M. B. Thermodynamic properties of Tl$_9$GdTe$_6$ and TlGdTe$_2$. *Russian Journal of Physical Chemistry A.* 2018;92(11): 2111–2117. DOI: https://doi.org/10.1134/s0036024418110158

33. Moroz M. V., Prokhorenko M. V., Prokhorenko S. V., Yatskov M. V., Reshetnyak O. V. Thermodynamic properties of AgIn$_2$Te$_3$I and AgIn$_2$Te$_3$Br, determined by the EMF method. *Russian Journal of Physical Chemistry A.* 2018;92(1): 19–23. DOI: https://doi.org/10.1134/s0036024418010168

34. Kozin L. F., Nigmetova R. Sh. *Termodinamicheskie svoistva zhidkikh splavov olovo-rtut'* [Thermodynamic properties of liquid tin-mercury alloys]. *Russian J. Inorgan.Chem.* 1963;8(11): 2556–2562. (In Russ.)

35. Aliev Z. S., Musayeva S. S. Imamaliyeva S. Z., Babanlə M. B. Thermodynamic study of antimony chalcoiodides by EMF method with an ionic liquid. *J. Therm. Anal. Calorim.* 2018;133(2): 1115–1120. DOI: https://doi.org/10.1007/s10973-017-6812-4

36. Imamaliyeva S. Z., Musayeva S. S., Babanly D. M., Jafarov Y. I., Tagiyev D. B., Babanly M. B. Determination of the thermodynamic functions of bismuth chalcoiodides by EMF method with morpholinium formate as electrolyte. *Thermochimica Acta.* 2019;679: 178319.DOI: https://doi.org/10.1016/j.tca.2019.178319

37. Brigouleix C., Anouti M., Jacquemin J., Caillon-Caravanier M., Galiano H., Lemordant D. Physico-chemical characterization of morpholinium cation based protic ionic liquids used as electrolytes. *J. Phys. Chem. B.* 2010;114(5): 1757–1766. DOI: https://doi.org/10.1021/jp906917v

38. Abrikosov N. Kh., Bankina V. F., Poretskaya L. V., et al. *Poluprovodnikovye khal'kogenidy i splavy na ikh osnove* [Semiconductor chalcogenides and alloys based on them]. Moscow: Nauka Publ.; 1975. 220 p. (In Russ.)

39. Chizhevskaya S. N. Shelimova L. E. Se–Te phase diagram and structures of amorphous and crystalline Se$_{1-x}$Te$_x$ alloys: critical review. *Russ. J. Inorg. Chem.* 1997;42(5): 827-837.

40. Ghosh G., Lukas H. L., Delaey L. A thermodynamic assessment of the Se-Te system. *Calphad.* 1988;12(3): 295–299. DOI: https://doi.org/10.1016/0364-5916(88)90010-7

41. Vasilev V. P., Somov A. P., Nikol'skaya A. V., Gerasimov Ya. I. *Issledovanie termodinamicheskikh svoistv selenida vismuta metodom EDS* [Investigation of the thermodynamic properties of bismuth selenide by the EMF method]. *Zh. Fiz. khimii.*, 1968;42(3): 675–677. (In Russ.)

42. Melekh B. T. and Semenkovich S. A. *Termodinamicheskie svoistva tellurida i selenida trekhvalentnogo vismuta* [Thermodynamic properties of telluride and selenide of trivalent bismuth]. *Izv. AN SSSR. Neorgan. Mater.* 1968;4(8): 1346–1348. (In Russ.)

43. Gerasimov Ya. I. and Nikol'skaya A. V. *Termodinamicheskie svoistva tellurida vismuta (Bi$_2$Te$_3$) i tellurida sur'my (Sb$_2$Te$_3$)* [Thermodynamic properties of bismuth telluride (Bi$_2$Te$_3$) and stibium telluride (Sb$_2$Te$_3$). In: Metallurgy and Physics of Semiconductors. Moscow: 1961. p. 30–33. (In Russ.)

Information about the authors

Gunel S. Hasanova, Researcher, Ganja State University, Ganja, Azerbaijan; e-mail: gzeynalova1989@gmail.com. ORCID iD: https://orcid.org/0000-0002-5610-7363.

Ayten I. Aghazade, Research Assistant, Institute of Catalysis and Inorganic Chemistry, Azerbaijan National Academy of Sciences; e-mail: aytenagazade94@gmail.com. ORCID iD: https://orcid.org/0000-0002-6072-1075.

Yusif A. Yusibov, DSc in Chemistry, Rector of Ganja State University, Ganja, Azerbaijan; e-mail: yusifyusibov1951@gmail.com. ORCID iD: https://orcid.org/0000-0002-9172-3508.

Mahammad B. Babanly, DSc in Chemistry, Deputy-Director of the Institute of Catalysis and Inorganic Chemistry, Azerbaijan National Academy of Sciences; e-mail: babanlymb@gmail.com. ORCID iD: https://orcid.org/0000-0001-5962-3710.

All authors have read and approved the final manuscript.

Translated by Irina Charychanskaya
Edited and proofread by Simon Cox

Condensed Matter and Interphases
(Kondensirovannye sredy i mezhfaznye granitsy)

Original articles

Cathodic Deposition of Zinc-Nickel Coatings from a Dilute Ammonium Chloride Electrolyte with a High Glycine Concentration

© 2020 O. A. Kozaderov✉, K. E. Tinaeva, A. E. Tinaeva, D. V. Burliaev

Voronezh State University,
1 Universitetskaya pl., Voronezh 394018, Russian Federation

Abstract

This study determined the kinetics of the synthesis, the chemical composition, and morphology of zinc-nickel coatings electrolytically obtained from low-concentration (0.04 M $ZnCl_2$, 0.08 M $NiCl_2$) ammiacate and ammonia-glycinate chloride solutions. Transient electrochemical methods (cyclic voltammetry and linear sweep voltammetry) allowed us to determine that the cathodic deposition of Zn–Ni alloy costings, regardless of the presence of glycine in the ammonium chloride electrolyte, is limited by the stage of diffusion mass-transfer of ions, whose electrochemical reduction (the charge transfer stage) is irreversible. The introduction of relatively high concentrations of glycine (0.3 M) in the electrolyte allows obtaining smoother coatings, which is demonstrated by the results of scanning electron microscopy. At the same time, energy dispersive X-ray spectroscopy demonstrated that the atomic fraction of nickel in the potentiostatically deposited coating increases on average by 9.7%. It is possible that the alteration of the chemical composition results in a significant decrease (on average by ~15 %) in the current efficiency in electrolytes with glycine, since it catalyses the side reaction of hydrogen evolution.

Keywords: electrodeposition, zinc-nickel coatings, ammine electrolyte, glycine, current efficiency, voltammetry.

1. Introduction

Zinc coatings acting as anodes in a "zinc-iron" pair ensure the effective protection of steel from corrosion [1]. The protective effect remains even when the galvanized surface has scratches or even exposed areas. When exposed to a moist atmosphere, carbon dioxide, and chlorides, the protective effect is enhanced by the formation of a dense layer on the metal surface. This layer consists of ZnO, basic salts of complex composition (including simonkolleite, $Zn_5(OH)_8Cl_2 \cdot H_2O$, and hydrozincite, $2ZnCO_3 \cdot 3Zn(OH)_2$), and other products of atmospheric corrosion of zinc [2]. Electrolytic zinc-containing alloys have a certain advantage over monometallic coatings: they combine the properties of two and more metals, obtained by cathodic deposition from the electrolyte solution. Consequently, such coatings are often characterized by higher corrosion resistance in aggressive environments. Of particular interest are zinc-nickel coatings, as they form a smaller number of corrosion products and comply with the high standards of anticorrosion protection of steel [3, 4]. Zinc-nickel coatings with the concentrations of nickel of 8–17 % demonstrate 3–10 times better corrosion resistance than zinc coatings. Furthermore, the degree of steel hydrogenation is lower [4]. The protective properties of Zn–Ni coatings do not deteriorate at higher temperatures or after interaction with aluminium alloys.

Electrolytic formation of Zn–Ni alloys is performed by means of anomalous codeposition

✉ Oleg A. Kozaderov, e-mail: ok@chem.vsu.ru

[6], when the deposition rate of nickel, which is more electropositive, is lower, than the deposition rate of zinc. Therefore, the coatings obtained from an electrolyte solution with equimolar concentrations of nickel and zinc ions, are characterised by relatively smaller concentrations of nickel [7]. By further adjusting the concentrations of nickel and zinc salts in the electrolyte solution, it is possible to obtain an optimal concentration of metals in the alloy coating required for the effective protection of a steel substrate from corrosion.

Zn and Ni yield high current efficiency when deposited from sulphate, chloride, and sulphate-chloride electrolytes. The concentrations of the doping element, i.e. nickel, in such zinc-nickel coatings may vary greatly. Coatings with nickel concentrations of 10–15 %, which is optimal regarding both the anticorrosive properties and resistance to hydrogen embrittlement, are obtained from industrial ammiacate electrolytes. These electrolytes have high scattering ability [8], but are characterised by the high concentrations of their components.

If we change the concentration of ions of the deposited metals and introduce organic additives to the electrolyte solution, we can optimise the codeposition of metals, by altering the conditions of the complexation process, and obtain coatings with better functional properties, such as increased corrosion resistance, low porosity, and luster. This paper considers the codeposition of zinc and nickel from an electrolyte with comparatively low concentrations of metal chlorides (0.04 M $ZnCl_2$, 0.08 M $NiCl_2$). Besides ammonia, we also used a considerably large concentration (0.3 M) of aminoacetic acid (glycine) as an additional complexation additive. An advantage of glycine is the buffer effect occurring due to its protonation/deprotonation ability. Another advantage of glycine is that it can be adsorbed on both positively and negatively charged electrode surfaces, which happens because glycine ions are bipolar in aqueous solutions [9].

The aim of our study was to determine the kinetics of cathodic deposition, the chemical composition and morphology of zinc-nickel coatings, electrolytically deposited from low-concentration ammiacate and ammonia-glycinate chloride solutions.

2. Experimental

The zinc-nickel alloy was cathodically deposited on an Au or Cu substrate at room temperature from a slightly acidic ammonium chloride solution prepared on double distilled water. The solution had the following composition: zinc chloride – 0.04; nickel chloride – 0.08; ammonium chloride – 2, either without glycine (ammiacate deposition electrolyte, pH = 3.4), or with the concentration of glycine of 0.3 mol/l (ammonia-glycinate deposition electrolyte, pH = 4.1).

The potential region of the cathodic deposition of the metals and their anodic dissolution in the deposition electrolytes was determined using cyclic voltammetry. Polarization curves were obtained in potentiodynamic mode at a potential scan rate $V = dE/dt = 10$ mV/s starting at the open-circuit potential $E(0) \approx 400$ mV and sweeping to the cathode region up to $E_c = -1200$ mV. It was then swept back to $E_a = 200$ mV according to the standard hydrogen electrode (SHE) scale. The kinetics of the electrodeposition was determined using linear sweep voltammetry. The cathodic polarization curves were registered at various scan rates V within the potential range from $E(0)$ to E_c. For the potentiodynamic measurements the working electrode was a golden electrode, which was preliminary washed with double distilled water, polished using suede leather and an MgO aqueous suspension, degreased in ethanol, and dried in a flow of argon.

Zinc-nickel coatings of 4,5 μm thickness were obtained using potentiostatic cathodic polarization of a copper electrode at the deposition potential $E_{dep} = -1000, -900, -880, -860$ mV (according to the SHE scale). The working electrode, a copper plate with the geometric area of 1 cm^2, was preliminary washed with double distilled water, degreased in ethanol, and dried in a flow of argon. The current efficiency was measured gravimetrically based on the difference between the mass of the copper plate before and after the electrodeposition and the corresponding transferred electric charge.

Potentiodynamic and potentiostatic measurements were performed using an IPC-PRO L computer-aided potentiostat. The reference electrode was a saturated silver chloride electrode, the auxiliary electrode was a platinum plate.

The measurements were performed at room temperature with natural aeration. The solution was not stirred.

The morphology of the surface of the obtained coatings was assessed and characterised using scanning electron microscopy (SEM) (JSM-6380LV microscope). The chemical composition of the coatings was determined by means of energy dispersive X-ray spectroscopy (EDX) (INCA 250 system). The results of the SEM and EDX studies were obtained using the equipment of the Centre for Collective Use of Scientific Equipment of Voronezh State University (http://ckp.vsu.ru).

3. Results and discussion

Fig.1 shows cyclic voltammograms obtained on the golden electrode in the ammiacate and ammonia-glycinate solutions. We can see that when glycine is added, the cathodic peak potential (K) shifts in the positive direction by about 30–40 mV. The position of the peaks on the anodic branch of the cyclic voltammogram (A_1, A_2, A_3) is hardly influenced by the presence of glycine. According to [10], anodic peaks correspond to the dissolution of phases of various chemical composition. We can thus assume, that the presence of glycine in the electrolyte solution has practically no effect on the phase composition of the coating. According to [10], peak A_1 may

correspond to the oxidation of metallic Zn, peak A_2 to its dissolution from the zinc-nickel phase, and peak A_3 to the anodic oxidation of the nickel phase formed as a result of the selective dissolution of zinc at more negative potentials. It should be noted that the peaks registered for the solution with glycine are much lower than those registered for the solution without glycine. Taking into account the fact that the surface area below the anodic peaks is proportional to the number of the deposited metals, we can assume that the observed effect is caused by a decrease in the rate of electrodeposition. This may happen because the discharge from the metal glycinate complexes at the cathode is hindered, for instance, by electrostatic repulsion from the negatively charged surface [6].

At higher scan rates the peak current of the cathodic deposition (i_{max}) increases, and the peak potential (E_{max}) shifts towards the negative region regardless of the presence of glycine in the electrolyte (Fig. 2). The currents of the side cathodic process, hydrogen evolution reaction, also increase.

The dependency of i_{max} on the potential scan rate is presented as a linear plot of i_{max} vs. $V^{1/2}$, according to the Randles-Sevcik equation (Fig. 3). According to the theory of voltammetry of electrochemical processes [11], this indicates that the process of non-stationary diffusion
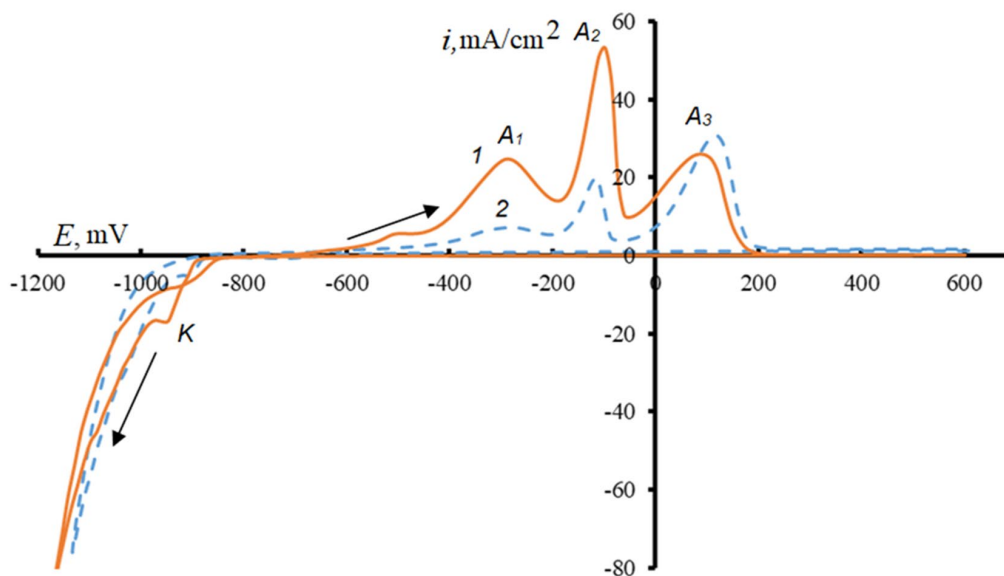
Fig. 1. Cyclic voltammograms, obtained on gold in a 0.04 M $ZnCl_2$ + 0.08 M $NiCl_2$ + 2 M NH_4Cl + x M NH_2CH_2COOH solution with $x = 0$ (1) and 0.3 (2)
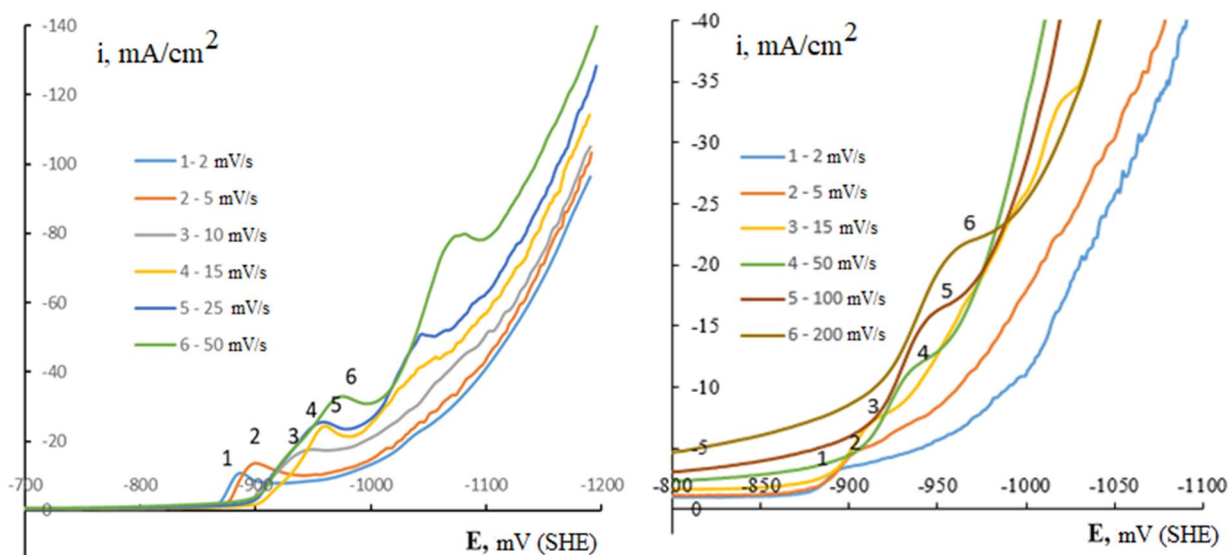
Fig. 2. Cathodic polarization curves of the Zn-Ni alloy deposition from a 0.04 M $ZnCl_2$ + 0.08 M $NiCl_2$ + 2 M NH_4Cl + x M NH_2CH_2COOH solution with $x = 0$ (a) and 0.3 (b), obtained at different potential scan rates
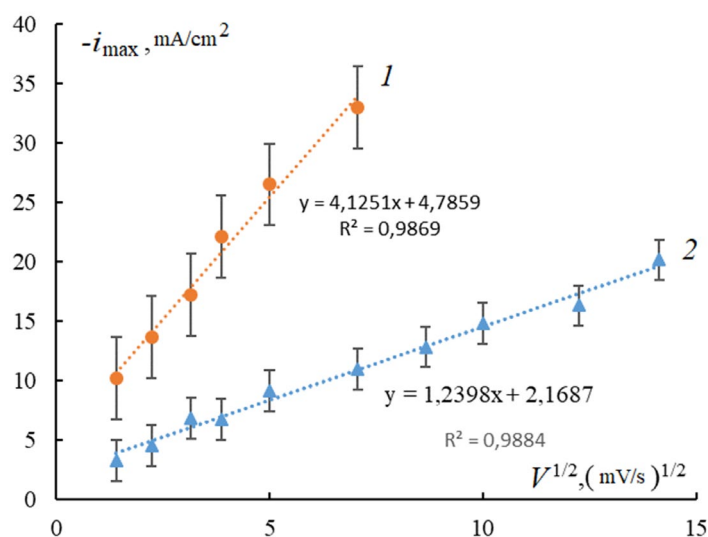
Fig. 3. The dependency of the density of the peak current of the Zn-Ni alloy cathodic deposition from a 0.04 M $ZnCl_2$ + 0.08 M $NiCl_2$ + 2 M NH_4Cl + x M NH_2CH_2COOH solution with $x = 0$ (1) and 0.3 (2) on the potential scan rate, according to Randles–Sevcik equation

mass-transfer is inhibited. It should be noted that the curves are not extrapolated to the origin of the coordinates, which indicates the presence of side processes (namely, hydrogen evolution). The Y-interception corresponding to the rate of such processes is much lower, when glycine is added to the electrolyte solution.

In turn, the dependency of the peak potential on the cathodic voltammogram on the potential scan rate is linearized in the logarithmic coordinates

(Fig. 4). According to [11], this indicates that the charge transfer stage is irreversible.

The analysis of the morphology of the coatings deposited at a constant cathodic potential (Fig. 5) demonstrated that the zinc-nickel coatings deposited from the ammonium chloride solution without glycine are fine-grained. The size of the grains increases when the cathodic potential shifts towards the negative region. At the same time, adding aminoacetic acid to the electrolyte
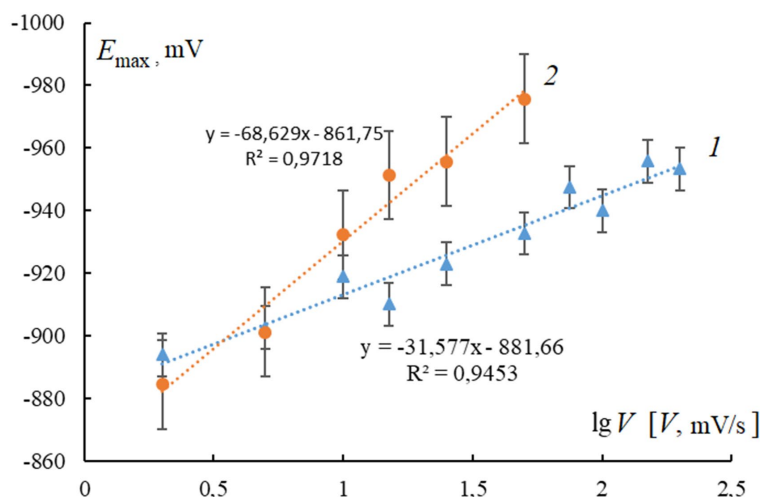
Fig. 4. The dependency of the peak potential of the Zn–Ni alloy cathodic deposition from a 0.04 M $ZnCl_2$ + 0.08 M $NiCl_2$ + 2 M NH_4Cl + x M NH_2CH_2COOH solution with $x = 0$ (1) and 0.3 (2) on the potential scan rate
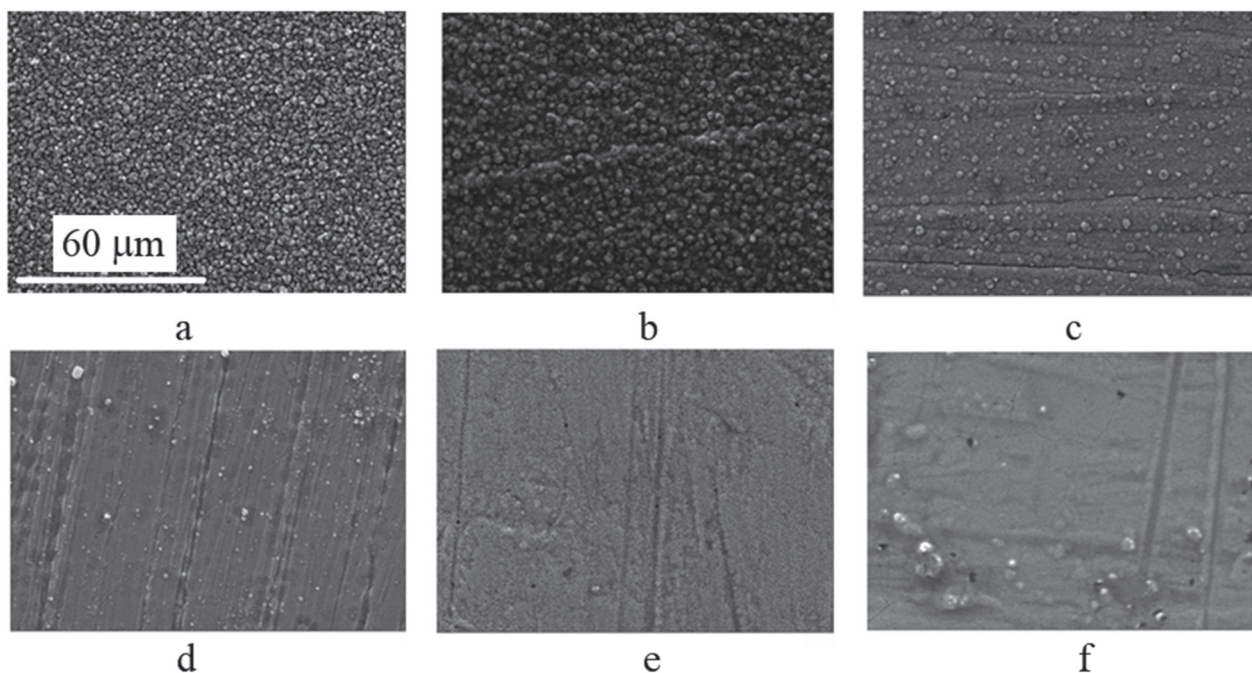
Fig. 5. SEM photographs of the surface of the zinc-nickel coatings deposited from the ammine (a, b, c) and ammonia-glycinate (d, e, f) electrolytes at different potentials: $E_{dep} = -860$ mV (a, d); -880 mV (b, e); -900 mV (c, f)

allowed us to obtain much smoother coatings regardless of the value of E_{dep}.

Is is important to note that, according to the results of energy dispersive X-ray spectroscopy, the presence of glycine leads to the increase in the concentration of nickel in the coating on average by 9.7 at% (Table 1). At the same time, the coatings obtained from the ammiacate electrolyte consist primarily of zinc, although its concentration in the electrolyte is low (0.04 M $ZnCl_2$).

The maximum current efficiency was obtained at the same electrode potential ($E_{dep} = -880$ mV) in ammonium chloride electrolytes both with and without glycine. The current efficiency of the zinc-nickel coatings deposited from the ammonia-glycinate deposition electrolyte is much lower (on average by ~15 %), than that of the coatings deposited from the ammonium chloride electrolyte without glycine. It is possible that the increase in the atomic fraction of nickel in the coating catalyses the side cathodic process,

Table 1. The current efficiency of the zinc-nickel coatings deposited from the ammiacate (numerator) and ammonia-glycinate (denominator) electrolytes

E_{dep}, mV	Atomic fraction of Ni, %	Current efficiency, %
–1000	35.2 / –	57.4 / –
–900	10.1 / 17.3	73.3 / 70.9
–880	10.1 / 17.0	94.2 / 74.6
–860	6.3 / 21.3	88.6 / 66.0

hydrogen evolution, which results in a decrease in the current efficiency.

4. Conclusions

The kinetics of the electrodeposition of zinc-nickel coatings from dilute aqueous (0.04 M $ZnCl_2$, 0.08 M $NiCl_2$) slightly acidic (pH 3–4) ammonium chloride solutions is not influenced by the presence of glycine: the limiting stage is the diffusion mass-transfer, and the charge transfer stage is irreversible. The addition of a relatively high amount of glycine (0.3 M) to the electrolyte resulted in a significant decrease in the rate of electrodeposition of the zinc-nickel alloy, an increase in the concentration of nickel in the coating on average by 9.7 at%, and better visual characteristics. The current efficiency in the solution with glycine is much lower. Presumably, this is the result of an increase in the rate of side processes, such as hydrogen evolution reaction, caused by a comparatively larger concentration of nickel as compared to zinc-nickel coatings deposited from the ammonium chloride electrolyte without glycine.

Conflict of interests

The authors declare that they have no known competing financial interests or personal relationships that could have influenced the work reported in this paper.

References

1. Shekhanov R. F., Gridchin S. N., Balmasov A. V. Elektroosazhdenie tsink-nikelevykh pokrytii iz shchelochnykh kompleksnykh elektrolitov [Electrodeposition of zinc-nickel coatings from alkaline complex electrolytes]. *Izvestiya VUZOV. Ser. khimiya i khim. Tekhnologiya = Russian Journal of Chemistry and Chemical Technology.* 2016;59(1): 51–53. DOI:https://doi.org/10.6060/tcct.20165901.5296 (In Russ.)

2. Mamaev V. I. *Funktsional'naya gal'vanotekhnika* [Functional Electroplating]. Kirov: VyatGU Publ.; 2013. 208 p. (In Russ.)

3. Gaevskaya T. V., Tsybulskaya L. S., Byk T. V. Formirovanie, struktura i svoistva elektrokhimicheski osazhdaemykh tsink-nikelevykh splavov [The formation, structure, and properties of electro-chemically deposited zinc-nickel alloys]. *Khimicheskie problemy sozdaniya novykh materialov i tekhnologii* [Chemical problems of creating new materials and technologies]. 2003;(2): 100–110. Available at: http://elib.bsu.by/handle/123456789/31638 (In Russ.)

4. Baptista E., Preikschat P., Roesch M., Serov A. N. Corrosion Protection with Zinc-Nickel Alloy Coatings. *Electroplating and surface treatment.* 2012;(1): 29–31. Available at: https://www.elibrary.ru/item.asp?id=17588284 (In Russ., abstract in Eng.)

5. Maizelis A. A., Artemenko V. M., Bairachnyi B. I, Lyubimov, A. I., Proglyada S. A., Kaplun A. V. Elektroosazhdenie funktsional'nykh tsink-nikelevykh plenok [Electrodeposition of functional zinc-nickel films]. *In: Sovremennye elektrokhimicheskie tekhnologii i oborudovanie [Modern Electrochemical Technologies and Equipment]: Proc. Int. Conf., 28–30 November 2017.* Minsk: BSTU Publ.; 2017. p. 190–193. Available at: https://elib.belstu.by/handle/123456789/23837 (In Russ.)

6. Gamburg Yu. D., Zangari J. *Teoriya i praktika elektroosazhdeniya metallov* [Theory and practice of metal electrodeposition]. Moscow: BINOM. Laboratoriya znanii Publ.; 2015. 438 p. (In Russ.)

7. Shtin S. V., Gabidulin V. V., Yusupova L. I. *Issledovanie sostava i struktury tsink-nikelevykh pokrytii, osazhdennykh iz slabokislogo elektrolita na zheleznyi podsloi* [A study of the composition and structure of zinc-nickel coatings deposited from slightly acidic electrolytes on an iron sublayer]. *Bulletin of the South Ural State University. Ser. Metallurgy.* 2016;(4): 147–153. DOI: https://doi.org/10.14529/met160417 (In Russ.)

8. Bobrikova I. G., Chernaya E. V. Regularities of electrodeposition of zinc-nickel alloy in ammonia complex electrolytes. *University News. North-Caucasian Region. Technical Sciences Series.* 2011;(5): 112–115. Available at: https://www.elibrary.ru/item.asp?id=17027116 (In Russ., abstract in Eng.)

9. Berezin N. B., Gudin N. V., Filippova A. G., Chevela V. V., Mezhevich Zh. V., Yakhyaev E. D., Sagdeev K. A. *Elektroosazhdenie metallov i splavov iz vodnykh rastvorov kompleksnykh soedinenii* [Electrodeposition of metals and alloys from aqueous solutions of complex compounds]. Kazan: Kazan. gos. tekhnol. un-ta Publ.; 2006. 276 p. (In Russ.)

10. Elkhatab F., Sarret M., Miiller C. Chemical and phase compositions of zinc + nickel alloys determined by stripping techniques. *J. Electroanal. Chem.*

1996;404(1): 45–53. DOI: https://doi.org/10.1016/0022-0728(95)04359-4

11. Damaskin B. B., Petrii O. A., Tsirlina G. A. *Elektrokhimiya* [Electrochemistry]. Moscow: Khimiya Publ.; 2001. 624 p. (In Russ.)

Information about the authors

Oleg A. Kozaderov, DSc in Chemistry, Associate professor, Head of the Department of Physical Chemistry, Faculty of Chemistry, Voronezh State University, Voronezh, Russian Federation; e-mail: ok@chem.vsu.ru. ORCID iD: https://orcid.org/0000-0002-0249-9517.

Ksenia E. Tinaeva, student, Department of Physical Chemistry, Faculty of Chemistry, Voronezh State University, Voronezh, Russian Federation; e-mail: tinaeva.98@mail.ru. ORCID iD: https://orcid.org/0000-0002-4244-3657.

Alina E. Tinaeva, student, Department of Physical Chemistry, Faculty of Chemistry, Voronezh State University, Voronezh, Russian Federation; e-mail: lina.tinaeva.98@mail.ru. ORCID iD: https://orcid.org/0000-0003-1382-6728.

Dmitrii V. Burliaev, postgraduate student, Department of Physical Chemistry, Faculty of Chemistry, Voronezh State University, Voronezh, Russian Federation; e-mail: dimn0@yandex.ru. ORCID iD: https://orcid.org/ 0000-0003-3826-686X.

All authors have read and approved the final manuscript.

Usage of the Kolmogorov–Johnson–Mehl–Avrami Model for the Study of the Kinetics of the Formation of Natural Gas Hydrate in Inverse Oil Emulsions.

© 2020 V. V. Koryakina✉, E. Yu. Shitz

Federal Research Centre "The Yakut Scientific Centre",
Institute of Oil and Gas Problems of the Siberian Branch of the RAS
20, Avtodorozhnaya ul., Yakutsk 677007, Russian Federation

Abstract

The article presents the results of a study of the hydration of the aqueous phase in inverse oil emulsions with natural gas rich in methane (more than 90 vol.%). The aim of the work was to study the kinetics of the crystallisation of oil emulsions during the formation of natural gas hydrates in them using the method of differential scanning calorimetry (DSC).

The objects of the study were inverse oil emulsions containing 20, 40, 60, and 80 wt% of water. DSC is used under quasi-equilibrium experiment conditions to study the kinetics of hydration of oil emulsions with gas.

The study showed the applicability of the Kolmogorov–Johnson–Mehl–Avrami model (KJMA) in order to describe the crystallisation process of inverse oil emulsions in a quasi-equilibrium DSC experiment. The kinetic parameters of the KJMA model in emulsions were determined for the processes of water drops conversion into ice, as well as their hydration with natural gas. It was shown that within the system "natural gas-oil-water" the process of ice formation is characterised by high values of the Avrami exponent ($n > 3$) and the degree of freedom ($\lambda = 3$), and the process of natural gas hydrate formation is characterised by low values of the Avrami exponent ($n < 3$) and medium degree of freedom ($\lambda = 1$-3). It was shown that in a continuous aqueous phase, natural gas hydrates are formed by instantaneous nucleation in the form of separate one-dimensional crystals; while in oil, hydrates are nucleated at a constant rate and, depending on the water content, grow in the form of disparate crystallites, shell, or spherulites. The obtained research results make it possible to deepen our knowledge of the kinetics and hydration mechanisms in oil emulsions, they can be used to complement the scientific basis for creating new technologies for the joint transportation of oil and hydrated natural gas in it.

Keywords: crystallisation, kinetics, Kolmogorov–Johnson–Mehl–Avrami model, differential scanning calorimetry, oil emulsion, natural gas hydrate, hydrate formation.

✉ Vladilina K. Koryakina, e-mail: koryakinavv@ipng.ysn.ru

1. Introduction

Gas hydrates are non-stoichiometric clathrate compounds of water and non-polar gases that are formed at low temperatures and high gas pressure by introducing "guest" molecules of the hydrate-forming gas (G) into the water cavities of the "host" lattice according to the scheme [1]:

$$G(g)+nH_2O(liquid) \leftrightarrow G \cdot nH_2O(solid) \qquad (1)$$

At the same time, water hydration, its binding by hydrate-forming gas molecules, occurs without violating the integrity of the clathrate frame consisting of water molecules linked together by hydrogen bonds [2].

In addition to bulk aqueous solutions, water-in-oil emulsions are one of the media for the potential formation of gas hydrates. The practical application of this phenomenon in inverse oil emulsions can be demonstrated using the currently known technologies of joint multi-phase transportation of oil and gas, whose core principle is hydration of the aqueous component of the emulsion with associated gas, turning the emulsion into a suspension of hydrated particles in oil [3].

Almost all kinetic models for the process of hydrate formation in continuous aqueous solutions are improved types of the Englezos-Bishnoi model [4, 5], which is based on the crystallisation theory and two-film interphase mass transfer. In this model, the diffusion factor can be omitted by the forced mixing of the "hydrate-forming gas – continuous liquid" system, and the reaction rate (1) between the process participants is considered proportional to the specific area of the interphase boundary.

The kinetic and thermodynamic parameters of nucleation, growth, and dissociation of gas hydrate particles in the emulsion media have their own differences and peculiarities because of the presence of an oil matrix. Moreover, the mechanisms and kinetics of the formation of gas hydrates are fundamentally different in different types of emulsions. For example, in direct emulsions, hydrate formation usually occurs directly at the "gas-liquid (aqueous phase)" interphase boundary at a higher rate than in inverse emulsions, where hydrate formation occurs at the "liquid (oil)-liquid (water)" interphase, with the necessary stage of diffusion of the hydrate-forming gas to the hydrate growth sites on the surface of the droplets of the aqueous phase of the emulsion [6, 7].

When describing the process for the formation of gas hydrates in the aqueous medium of inverse emulsion systems, gas diffusion cannot always be omitted, even with forced mixing of the reacting phases. Therefore, the most famous kinetic model describing hydrate formation in inverse emulsions is the Talatori formal model [8], based on the Kolmogorov-Johnson-Mehl-Avrami equation (KJMA) and originally used for topochemical reactions [9]:

$$\alpha(t) = 1 - \exp\left[-(kt)^n\right], \qquad (2)$$

where $\alpha(t)$ is the conversion degree, t is time, k is the rate constant, n is the Avrami kinetic exponent, containing information regarding the geometry of the growing formations and the degree of freedom of the crystallisation process.

In modern studies, the KJMA equation is widely used to describe the crystallisation and decomposition of solid substances, including the kinetics of hydrate formation under pressure in various water-containing systems [8, 10–12]. In a study [10], it was shown that the KJMA model satisfactorily describes the initial stage of crystallisation of gas hydrates until the degree of conversion of water to hydrate is no more than 40–50 %. In [8], it was found that in an oil emulsion with 80 % water content, the formation of methane hydrates has two stages. The first is characterised by a slow crystallisation rate $K_c = (2–5) \cdot 10^{-4}$ s^{-1}, and Avrami exponent $n_1 = 0.9–1.0$. The second stage, compared to the first, is relatively fast, $K_c = (3.5–11)\ 10^{-4}$ s^{-1} at $n_2 = 1.6–2.9$. It was shown in [11, 12] that the Avrami exponent of the process of methane hydrate formation in distilled water is $n = 0.5–2.5$, depending on the presence of surfactants in the system and forced mixing.

It is known that the KJMA equation is successfully used to describe phase conversions and reactions in various substances, particularly in polymer composites and metal alloys, studied using the method of differential scanning calorimetry (DSC) [13, 14]. The method makes it possible to obtain statistically average values of kinetic parameters of the processes without a range of experiments, including those in emulsions [15–18].

Purpose: To determine the kinetic parameters of the Kolmogorov–Johnson–Mehl–Avrami model during the crystallisation of the aqueous phase of

oil emulsions during the formation of natural gas hydrates in their medium using the DSC method.

2. Experimental

The object of research was water-in-oil emulsions with the oil (o) and water (w) mass ratio of 20o : 80w, 40o : 60w, 60o : 40w, and 80o : 20w, obtained by mechanical mixing of distilled water and oil from the Irelyakh GOF (Yakutia, Russia), with a density of 0.869 g/cm³, containing 1.47 wt% paraffin hydrocarbons, 0.3 wt% asphaltenes, and 10.4 wt% resins. More details about obtaining oil emulsions can be found in [19].

As an atmosphere for the DSC experiment, a naturally-occurring gas was used, with the following composition, vol.%: CH_4 – 92.87, C_2H_6 – 5.25, C_3H_8 – 1.21, i-C_4H_{10} – 0.12, n-C_4H_{10} – 0.12, N_2 – 0.38, CO_2 – 0.05 (Sredneviluyskoe gas-condensate field (Yakutia, Russia)).

The kinetic parameters of the crystallisation processes of water-in-oil systems with the formation of natural gas hydrates in their medium were determined using a high-pressure differential scanning calorimeter DSC 204 HP Phoenix by Netzsch (Germany). The DSC thermograms showed successive cooling and heating segments, which were obtained in the temperature range from +25 to –10 °C, with a cooling rate of 0.1 °/min and a heating rate of 0.2 °/min. The temperature measurement accuracy was ± 0.1 °C, the gas pressure throughout the experiment was 5.0 MPa, and the sample weight was ~30 mg. The relative enthalpy measurement error was ± 3 %.

The DSC thermograms of water-in-oil systems in the presence of natural gas were obtained (Fig. 1).

It can be seen that in the cooling segment of the emulsion there is one crystallisation peak in the temperature range of –8 ÷ –12 °C, which breaks up into peaks of melting ice and natural gas hydrate in the heating segment at temperature values of –1.2° and +11.3° C, respectively. Thus, it was found that when the emulsion is cooled in the presence of natural gas, water droplets, when frozen, partially hydrate.
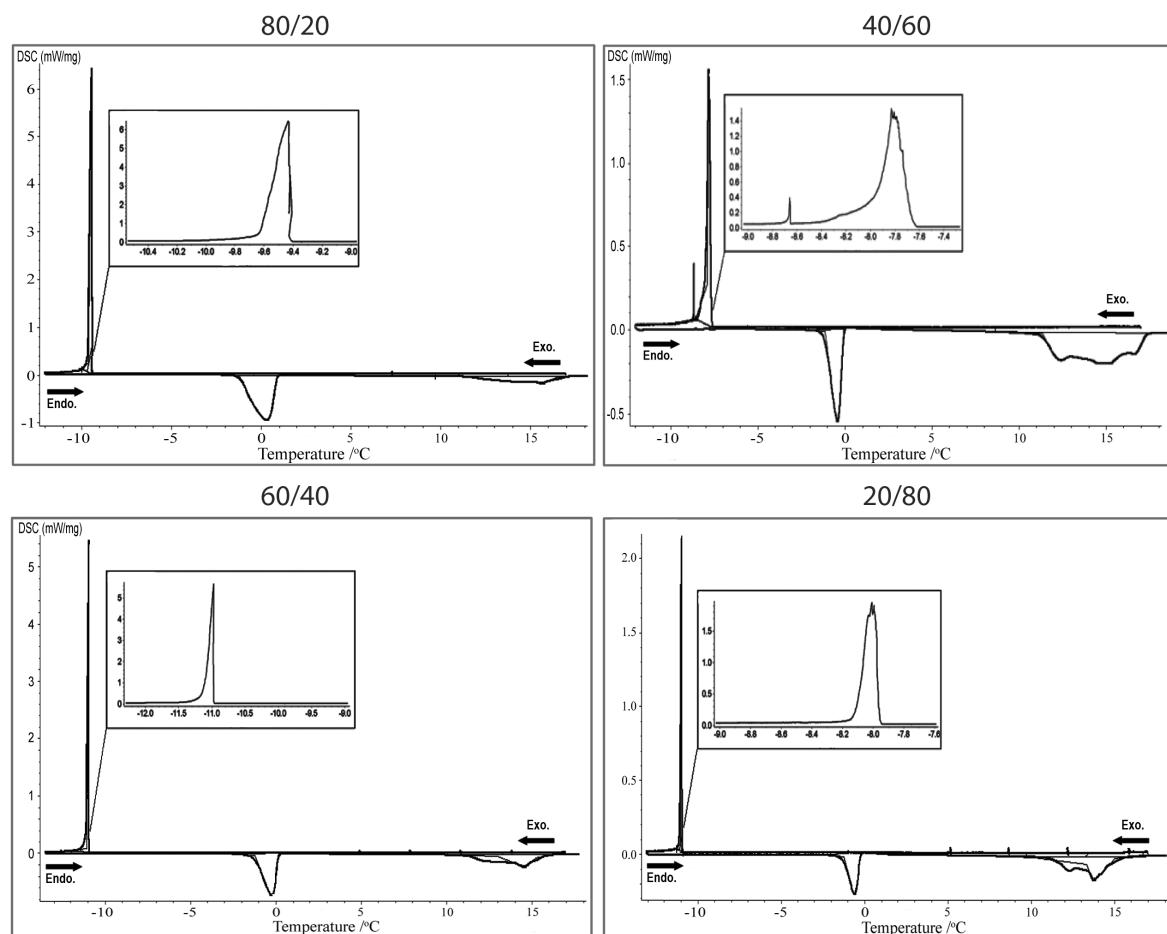
Fig. 1. The DSC thermograms of water-in-oil systems cooling in the presence of natural gas

The curves of the degree of water conversion during crystallisation were obtained according to the ratio:

$$\alpha(t) = \frac{\int_{t_0}^{t}\left(\frac{dH_c}{dt}\right)dt}{\int_{t_0}^{t_\infty}\left(\frac{dH_c}{dt}\right)dt} = \frac{S_t}{S_\infty},$$ (3)

where α is the degree of conversion of the liquid phase of emulsion to the solid hydrate-containing phase; index 0 is the initial time of crystallisation; ∞ is the total time of crystallisation; H_c is the heat of crystallisation, S is the peak area. On the obtained kinetic curves, we graphically determined the reaction half-life $t_{1/2}$.

The obtained curves of the degree of water conversion to the hydrate-containing phase were analysed according to the KJMA equation (2). The Avrami exponent n was found by double logarithmic transformation of equation (2):

$$\ln\left[-\ln(1-\alpha)\right] = n\ln(t) + \ln(k),$$ (4)

and construction for the process a kinetic anamorphosis of the second order in the coordinates $\ln[-\ln(1-\alpha)] - \ln(t)$. In this case, the slope angle of the kinetic anamorphosis, which has the form of a straight line, equals to the constant n. The Avrami exponent is $n = \varphi + \lambda$, where φ is the number of stages of a nucleus formation, usually it is 1 or 0 for nucleation at continuous rate or instantaneous nucleation, respectively; and λ is the number of degrees of freedom, or the nuclei effective growth directions, it is 3 when spheres are formed; 2 when two-dimensional surfaces are formed; and 1 for rod-like structures and unidirectional one-dimensional growth processes [20].

By constructing an anamorphosis of the first order in the coordinates $\ln(1-\alpha) - t^n$ we defined the k^n value by the slope angle of the line. The crystallisation rate constants (K_c) were determined using the Sakovich ratio in accordance with [21]:

$$K_c = nk^{1/n}.$$ (5)

The water conversion degree of the water-in-oil system to the natural gas hydrate (γ) was calculated using the ratio:

$$\gamma = \frac{\Delta H_m}{500} \times 100\,\%,$$ (6)

where ΔH_m is the heat of fusion of the natural gas hydrate released during the heating segment, 500 kJ/kg is the theoretical amount of heat released during the fusion of the natural gas hydrate at a 100% degree of conversion [22].

3. Results and discussion

During the initial stage of using the Kolmogorov–Johnson–Mehl–Avrami model to analyse the crystallisation process of any system, it is necessary to verify its applicability under the specific conditions of the experiment.

3.1 Applicability of the KJMA model for the interpretation of the DSC data from the process of crystallisation of water-in-oil emulsions in the presence of natural gas

It is known that the shape of the DSC signal is significantly affected by the cooling rate of the system and its effect becomes noticeable in the experiments involving high cooling rates $\beta > 1-5\,°/$ min [23]. It is difficult to apply the KJMA equation in such cases, since processing the conversion curves leads to significant deviations and errors. Therefore, with high cooling rates ($\beta > 1$) of the experiment, the non-isothermal model of KJMA is used to process the DSC signal [24].

With lower cooling rates $\beta \ll 1\,°/\text{min}$, quasi-isothermal crystallisation conditions are implemented. Under them the application of the isothermal KJMA equation provides satisfactory results, and the applicability of the KJMA model for interpreting the kinetics of the process is estimated by the form of anamorphosis curves. Such an approximation is known as a quasi-isothermal condition for the realisation of a DSC experiment [23]. The curves of the degree of conversion of water to the hydrate-containing phase obtained under such conditions are provided in Fig. 2.

It can be seen (Fig. 2) that all curves of the degree of conversion of water to the crystalline phase are S-shaped.

It was found that, at $\alpha < 0.05$ (or 5%), the crystallisation curves of the water phase in water-in-oil systems have a small acceleration period. It is an induction period, which, as can be seen from Fig. 2, is absent on the crystallisation curve of distilled water. It is apparently due to the instantaneous nucleation of many crystallisation centres ($\varphi = 0$), while the presence of an induction period in emulsions can be associated with the fact that only part of the hydrate nuclei survive
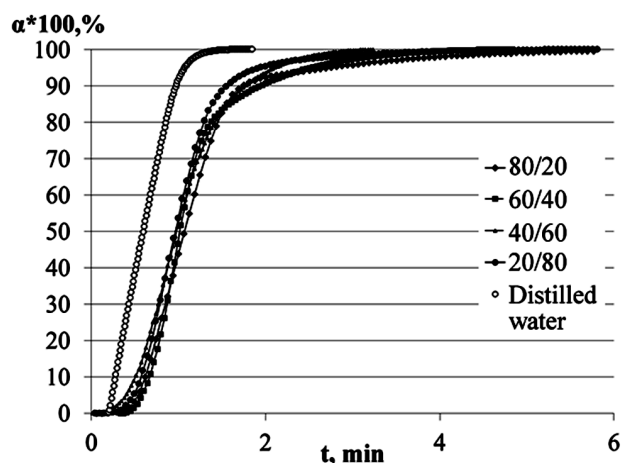
Fig. 2. The curves of the degrees of conversion α to the hydrate-containing phase, when cooling distilled water and water-in-oil emulsions in the presence of natural gas

and keep growing [25], that is nucleation at a constant rate (φ = 1). Thus, it was shown that the mechanisms of hydrated nucleation in the continuous water phase and in the dispersed water-in-oil medium are different.

With α > 0.80 (or 80 %), the crystallisation process in water-in-oil systems slows down and is associated with a change in the crystallisation mode from kinetic to diffusion-controlled. The duration of this period is more than half of the total crystallisation time of the system. The formation of natural gas hydrate in this section of the crystallisation curve is explained by the slow advance of the hydrate formation front deeper into the reaction zone (water droplets). It can be described by the model that is described in detail in [26].

Thus, in the range of degrees of conversion of water into a hydrate-containing phase $0.05 < α < 0.80$, there is a zone of active nucleation and crystal growth, whose formation can be described without taking into account the diffusion of natural gas across the water-oil boundary.

Secondary anamorphoses of the curves of the degrees of conversion of water from water-in-oil systems into a hydrate-containing phase are shown in Fig. 3. It was determined that all obtained secondary anamorphoses are straight-lined ($R^2 > 0.98$) in the range of the function $f = \ln[-\ln(1 - α)] \in [-0.09; -2.97]$, which corresponds with the range of conversion degrees $α \in [0.05; 0.60]$.

Therefore, in the range of conversion degrees α from 0.05 to 0.60, the kinetic DSC curves of the process of quasi-isothermal crystallisation in water-in-oil systems with the formation of natural gas hydrate can be analysed using the KJMA equation.

3.2. Kinetic parameters of crystallisation of the water phase of water-in-oil systems during the formation of natural gas hydrates in them

The kinetics of hydrate formation in oil emulsions, as a crystallisation process, can be characterised by the Avrami exponent, the number of nucleation stages, the degree of freedom, and the direction of the process of crystallisation of water droplets.

It was determined (Table 1) that during the crystallisation of the continuous phase of distilled water, only a small part of it (not more than 5%)
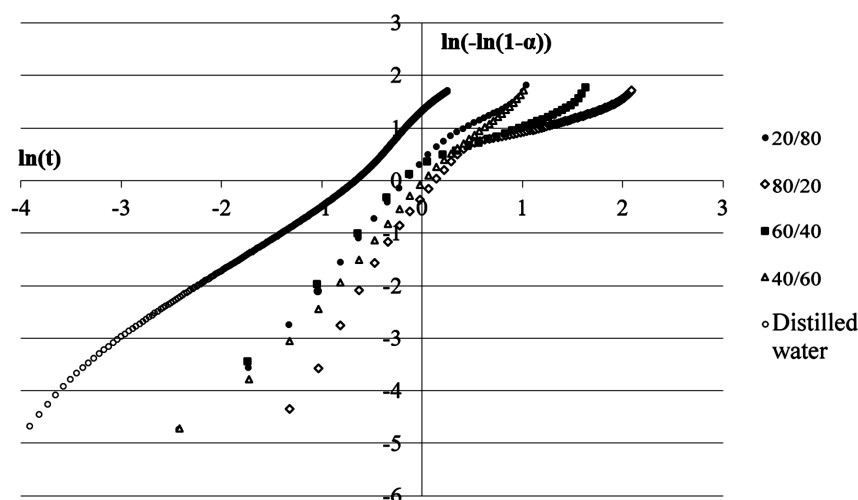
Fig. 3. The second-order anamorphoses of the curves of the degrees of conversion to the crystal phase, when cooling distilled water and water phase within water-in-oil emulsions

Table 1. The values of the fraction of hydrated water (γ), the Avrami parameter (n), the degree of freedom (λ), the number of nucleation stages (φ), and the crystal geometry upon crystallisation of water-in-oil emulsions and continuous water phase in the presence of natural gas and in its absence (*) (R^2 is the regression coefficient)

Object, %	γ, %	n	φ	λ	Object, %	R^2
Distilled water	5	1.5	0	1	Filaments, single crystallites	0.991
80o:20w	60	2.5	1	1	Single crystallites	0.998
60o:40w	60	2.5	1	1	Single crystallites	0.999
40o:60w	44	2.7	1	2	Shell	0.997
20o:80w	26	3.9	1	3	Spherulite	0.984
80o:20w*	0	4.2	1	3	Spherulite	0.999

undergoes hydration, while the crystals of natural gas hydrate are formed by instant nucleation of the nuclei ($\varphi = 0$) with subsequent unidirectional growth ($\lambda = 1$) in the form of filaments or separate formations (Fig. 4, I). It is consistent with the morphology of natural gas hydrates growing from the surface of distilled water deep into the continuous phase in the form of single crystallites and dendritic formations [27].

In water-in-oil systems, an increase in the Avrami exponent of the crystallisation process is observed, both due to the number of stages of the nucleation process φ, and due to the degree of freedom λ, which determines the shape of the growing crystals of natural gas hydrate (Table 1).

It was determined that in water-in-oil systems, the hydration crystals nucleate continuously, with their subsequent growth throughout the entire crystallisation process ($\varphi = 1$). In this case, the remaining part of the water phase, which are drops, turns into ice.

It was found that the crystallisation degree of freedom increases with the increase in water content in a water-in-oil system, which entails

changes in the geometry of growing crystals. So, with a water content of up to 40 wt%, single hydrate crystallites are formed in oil (Fig. 4, II). In these emulsions with a low water content, the formation of "serpentine" hydrates can probably occur that are growing from the surface of a water droplet [28] up to the formation of "wool balls". It can be explained by the presence of a high surfactant content in oil: both synthetic and natural. [29]. It is possible that oil surfactants concentrated on the surface of water droplets interfere with the free growth of hydrate crystals, forcing it to "cling" between the surfactant macromolecules.

When the water content in the emulsion is 60 wt%, the hydrate is formed in the form of a shell on the droplet surface (Fig. 4, III), and at 80 wt% of water in the oil, spherulitic formations grow (Fig. 4, IV), which is confirmed by generally accepted models of hydrate formation in emulsions on the surface of water droplets [30]. It was found that the formation of the ice phase in the water-in-oil system (80o:20w*) is characterised by a high degree of freedom ($\lambda = 3$),
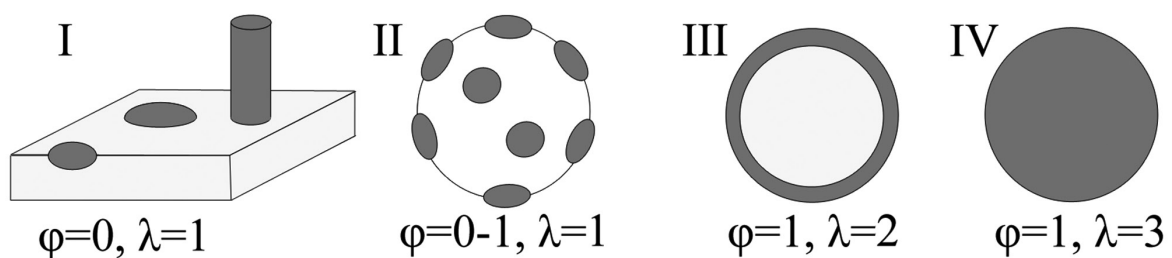
Fig. 4. Crystal growth patterns of natural gas hydrate on: I) the surface of distilled water; and on the drops of water-in-oil emulsion with a water content of: II) no more than 40 wt%; III) 60 wt% (sectional view); IV) 80 wt% (sectional view). The hydrate phase is marked in grey, and the ice phase is white

it goes in all directions and leads to the formation of a spherulite.

It should be noted that the growth patterns of natural gas hydrate crystals shown in Fig. 4, are theoretically-calculated, model schemes that need further confirmation and more detailed study using direct methods of studying the supramolecular structure (TEM, AFM, etc.).

It was determined that with an increase in the water content in oil, the fraction of hydrated water (γ) decreases and, consequently, the proportion of ice in the system increases, which leads to an increase in the Avrami exponent and the degree of freedom of crystallisation. When the Avrami exponent $n < 3$, water in the emulsion predominantly crystallises into natural gas hydrate, and when $n \geqslant 3$ the formation of ice prevails in the system. Thus, it is shown that the Avrami exponent is inversely related to the amount of natural gas hydrate formed in the water-in-oil system.

Differences in the nature of the processes of natural gas hydrate and ice formation in oil emulsions also affect their kinetic characteristics (Table 2).

It was found that the crystallisation rate constants of oil emulsions of all compositions in the presence of natural gas are 38.3–56.7 s^{-1}, which is 13–20 times higher than that for an 80o:20w* emulsion containing no natural gas (Table 2) and 7–11 times higher than the rate of emulsion hydration with methane [8].

Thus, the formation of natural gas hydrate in the water-in-oil system occurs faster than ice formation.

It was found that the reaction half-life of the aqueous phase conversion into a crystalline hydrate-containing phase is almost the same for all compositions of water-in-oil emulsions and is ~60 s, which is 3 times less than the ice formation process (Table 2).

The process of ice formation in the absence of natural gas in water-in-oil systems proceeds at a lower speed at a temperature of 255 K, that is, under conditions of deeper supercooling of the system, and it is longer than hydrate formation, which is characteristic of the process of homogeneous crystallisation.

Moreover, it was found that a decrease in the temperature of the water-in-oil system

Table 2. The values of kinetic exponents and temperature of the process of crystallisation of water in water-in-oil systems in the presence/absence (*) of natural gas in the system

Object	T_c, K	K_c, 10^{-3} s^{-1}	$t_{1/2}$, s
80o:20w	265	48.3	58
60o:40w	266	38.3	59
40o:60w	262	56.7	61
20o:80w	264	53.3	64
80o:20w*	255	2.8	181

from 266 to 262 K results in an increase in the crystallisation rate constant of the aqueous phase by 1.5 times. Thus, the overcooling of the system is the driving force of the crystallisation of water-in-oil emulsions, leading to the formation of natural gas hydrate in them.

4. Conclusions

Therefore, it was shown that the Kolmogorov-Johnson-Mehl-Avrami model is suitable for describing the experimental data of the DS calorimetry of the process of nucleation of natural gas hydrate in water-in-oil systems. The use of the KJMA model in studying the crystallisation of the aqueous phase of oil emulsions in the presence of natural gas allowed us to draw the following main conclusions:

1. The growth of hydrate crystals on the surface of water droplets in oil depends on the water content in the oil and proceeds in the form of a rod-like unidirectional growth: in oil with low water content (< 40 wt%), or completely taking the surface of a water droplet (> 60 wt%);

2. The Avrami exponent indirectly characterises the prevailing process during crystallisation of the "water-oil-natural gas" system: when $n < 3$, natural gas hydrate predominantly forms in the emulsion, and when $n \geqslant 3$ the formation of ice prevails in the system;

3. The crystallisation rate of oil emulsions with the formation of natural gas hydrate is 13-20 times higher than the rate of ice formation in the emulsion.

The obtained experimental data allow us to deepen our knowledge of the kinetics and mechanisms of nucleation of natural gas hydrates in water-in-oil systems, and can be used to model the process of hydrate formation in a water-oil emulsion medium.

Knowledge of the fundamental physical and chemical parameters of the process of formation of natural gas hydrates in inverse oil emulsions is one of the key factors for the successful and effective development of oil and gas fields with high water content that are located in the regions of the Far North, Eastern Siberia, and the Arctic.

In practical terms, the results of the study of the features and differences of the formation of natural gas hydrates in oil emulsions can be helpful in creating the scientific foundations of new technologies for the joint transportation of oil and hydrated natural gas in it.

Acknowledgements

Conflict of interests

The authors declare that they have no known competing financial interests or personal relationships that could have influenced the work reported in this paper.

References

1. Carroll J. *Natural Gas Hydrates: A Guide for Engineers*. Oxford, UK: Gulf Professional Publishing; 2020. 392 p.

2. Maninder K., Zhenyuan Y., Praveen L. A Review of clathrate hydrate nucleation. *Sustainable Chemistry & Engineering*. 2017;5(12): 11176–11203. DOI: https://doi.org/10.1021/acssuschemeng.7b03238

3. Straume E. O., Morales R., Sum A. K. Perspectives on gas hydrates cold flow technology. *Energy & Fuels*. 2019;33(1): 1–15. DOI: https://doi.org/10.1021/acs.energyfuels.8b02816

4. Ribeiro C. P., Lage P. L. C. Modelling of hydrate formation kinetics: State-of-the-art and future directions. *Chemical Engineering Science*. 2008;63(8): 2007–2034. DOI: https://doi.org/10.1016/j.ces.2008.01.014

5. Englezos P., Kalogerakis N. E., Dholabhai P. D., Bishnoi P. R. Kinetics of gas hydrate formation from mixtures of methane and ethane. *Chemical Engineering Science*. 1987;42(11): 2659–2666. DOI: https://doi.org/10.1016/0009-2509(87)87016-1

6. Song G., Li Y., Wang W., Zhao P., Jiang K., Ye X. Experimental study of hydrate formation in oil-water systems using a high-pressure visual autoclave. *AIChE Journal*. 2019;65(9): e16667. DOI: https://doi.org/10.1002/aic.16667

7. Liu Z., Song Y., Liu W., Lang C., Zhao J., Li Y. Formation of methane hydrate in oil–water emulsion governed by the hydrophilic and hydrophobic properties of non-ionic surfactants. *Energy & Fuels*. 2019;33(6): 5777–5784. DOI: https://doi.org/10.1021/acs.energyfuels.9b01046

8. Talatori S., Barth T. Rate of hydrate formation in crude oil/gas/water emulsions with different water cuts. *Journal of Petroleum Science and Engineering*. 2012;80(1): 32–40. DOI: https://doi.org/10.1016/j.petrol.2011.10.010

9. Avrami M. Kinetics of phase change. II Transformation-time relations for random distribution of nuclei. *Journal of Chemical Physics*. 1940;8(2): 212–224. DOI: https://doi.org/10.1063/1.1750631

10. Palodkar A. V., Mandal S., Jana A. K. Modeling growth kinetics of gas hydrate in porous media: Experimental validation. *Energy & Fuels*. 2016;30(9): 7656–7665. DOI: https://doi.org/10.1021/acs.energyfuels.6b01397

11. Susilo R., Ripmeester J. A., Englezos P. Methane conversion rate into structure H hydrate crystals from ice. *AIChE Journal*. 2007;53(9): 2451–2460. DOI: https://doi.org/10.1002/aic.11268

12. Naeiji P., Varaminian F. Differential scanning calorimetry measurements and modeling of methane + THF hydrate growth kinetics based on non-equilibrium thermodynamics. *Journal of Molecular Liquids*. 2018; 263: 22–30. DOI: https://doi.org/10.1016/j.molliq.2018.04.107

13. Choupin T., Fayolle B., Régnier G., Paris C., Cinquin J., Brule B. A more reliable DSC-based methodology to study crystallization kinetics: Application to poly(ether-ketone-ketone) (PEKK) copolymers. *Polymer*. 2018; 155: 109–115. DOI: https://doi.org/10.1016/j.polymer.2018.08.060

14. Tan C., Zhu J., Wang Z., Zhang K., Tian X., Cai W. The crystallization kinetics of Co doping on Ni–Mn–Sn magnetic shape memory alloy thin films. *RSC Advances*. 2018;8(45): 25819–25828. DOI: https://doi.org/10.1039/c8ra04618b

15. Derkach S. R., Kolotova D. S., Simonsen G., Simon S. C., Sjöblom J., Andrianov A. V., Malkin A. Y. Kinetics of crystallization of aqueous droplets in water-in-crude oil emulsions at low temperatures. *Energy & Fuels*. 2018;32(2): 2197–2202. DOI: https://doi.org/10.1021/acs.energyfuels.7b03457

16. Liu Z., Liu W., Lang C., Li Y., Yang M., Zhao J., Song Y. DSC studies of methane hydrate formation and dissociation in water-in-mineral oil emulsions. In: *Proc. 16th International Heat Transfer Conference (IHTC-16)*. 2018, 10-15 August, Beijing, China: 2018. p. 1607–1613. DOI: https://doi.org/10.1615/ihtc16.cat.023453

17. Drelich A., Dalmazzone C., Pezron I., Liggieri L., Clausse D. DSC (Differential Scanning Calorimetry) used to follow the evolution of W/O emulsions versus time on ground and in space in the ISS. *Oil & Gas Sciences and Technology – Revue d'IFP Energies Nouvelles*. 2018;73(16): 1–9. DOI: https://doi.org/10.2516/ogst/2018003

18. Leister N., Karbstein H. Evaluating the stability of double emulsions — A review of the masurement techniques for the systematic investigation of instability mechanisms. *Colloids and Interfaces*. 2020;4(8): 1–18. DOI: https://doi.org/10.3390/colloids4010008

19. Koryakina V.V., Ivanova I.K., Semenov M.E., Rozhin I.I., Fedorova A.F., Shits E.Y. Specific features of the growth, composition, and content of natural gas hydrates synthesized in inverted oil emulsions. *Russian Journal of Applied Chemistry*. 2017;90(8): 1258–1265. DOI: https://doi.org/10.1134/s1070427217080110

20. Dill E. D., Folmer J. C. W., Martin J. D. Crystal growth simulations to establish physically relevant kinetic parameters from the empirical Kolmogorov–Johnson–Mehl–Avrami Model. *Chemistry of Materials*. 2013;25(20): 3941–3951. DOI: https://doi.org/10.1021/cm402751x

21. 2. Sakovich G.V. Zamechaniya o nekotorykh uravneniyakh kinetiki reaktsii s uchastiem tverdykh veshchestv, primenyaemykh v nastoyashchee vremya [Remarks on some equations of the kinetics of reactions involving solids currently used]. *Uchenye zapiski Tomskogo universiteta*. 1955; 26: 103–110. (In Russ.)

22. 3. Groysman A. G. *Teplofizicheskie svoistva gazovykh gidratov* [Thermophysical properties of gas hydrates]. Novosibirsk: Nauka Publ.; 1985. 95 p. (In Russ.)

23. 4. *Principles and Applications of Thermal Analysis*. Ed. P. Gabbott. Oxford, UK: Blackwell Publishing Ltd.; 2008. 464 p.

24. Ruitenberg G., Woldt E., Petford-Long A. K. Comparing the Johnson–Mehl–Avrami–Kolmogorov equations for isothermal and linear heating conditions. *Thermochimica Acta*. 2001;378(1–2): 97–105. DOI: https://doi.org/10.1016/s0040-6031(01)00584-6

25. Stoporev A. S., Manakov A. Yu., Kosyakov V. I., Shestakov V. A., Altunina K. A., Strelets L. A. Nucleation of methane hydrate in water-in-oil emulsions: role of the phase boundary. *Energy & Fuels*. 2016;30(5): 3735–3741. DOI: https://doi.org/10.1021/acs.energyfuels.5b02279

26. Kislitsin A. A., Drachuk A. O., Molokitina N. S., Podenko L. S. Diffusion model of methane hydrate formation in "Dry Water". *Russian Journal of Physical Chemistry A*. 2020;94(2): 405–411. DOI: https://doi.org/10.1134/s003602442002017x

27. Kodama T., Ohmura R. Crystal growth of clathrate hydrate in liquid water in contact with methane + ethane + propane gas mixture. *Journal of Chemical Technology & Biotechnology*. 2014; 89(12): 1982–1986. DOI: https://doi.org/10.1002/jctb.4292

28. Adamova T. P., Stoporev A. S., Manakov A. Y. Visual studies of methane hydrate formation on the water – oil boundaries. *Crystal Growth & Design*. 2018;18(11): 6713–6722. DOI: https://doi.org/10.1021/acs.cgd.8b00986

29. Dong S., Liu C., Han W., Li M., Zhang J., Chen G. The effect of the hydrate antiagglomerant on hydrate crystallization at the oil–water interface. *ACS Omega*. 2020;5(7): 3315–3321. DOI: https://doi.org/10.1021/acsomega.9b03395

30. Guo D., Ou W., Ning F., Fang B., Liu Z., Fang X., He Z. The effects of hydrate formation and dissociation on the water-oil interface: Insight into the stability of an emulsion. *Fuel*. 2020; 266: 116980. DOI: https://doi.org/10.1016/j.fuel.2019.116980

Information about the authors

Vladilina V. Koryakina, research fellow, Federal Research Centre "The Yakut Scientific Centre of the Siberian Branch of the RAS", autonomous division of the Institute of Oil and Gas Problems of the Siberian Branch of the RAS, Technogenic Gas Hydrate Laboratory No. 3, Yakutsk, Russian Federation; e-mail: koryakinavv@ipng.ysn.ru. ORCID ID: https://orcid.org/0000-0002-6650-0038.

Elena Yu. Shits, DSc in Engineering, Associate Professor, retired; e-mail: l.u.shitz@mail.ru.

All authors have read and approved the final manuscript.

Condensed Matter and Interphases
(Kondensirovannye sredy i mezhfaznye granitsy)

Original articles

Synthesis and characterisation of ternary molybdates $AgZn_3R(MoO_4)_5$ (R = In, Fe)

© 2020 I. Yu. Kotova✉ᵃ, T. S. Spiridonovaᵃ, Yu. M. Kadyrovaᵃ, A. A. Savinaᵇ

ᵃBaikal Institute of Nature Management, Siberian Branch of the Russian Academy of Sciences,
6, Sakhyanova str., 670047 Ulan-Ude, Republic of Buryatia, Russian Federation

ᵇSkolkovo Institute of Science and Technology,
30, Bolshoy Boulevard, bld. 1, 121205 Moscow, Russian Federation

Abstract

An important role in the study and the obtaining of new phases with valuable physical and chemical properties is taken by ternary compounds with a tetrahedral anion containing various combinations of mono- and multivalent cations, including ternary molybdates and tungstates. Silver ternary molybdates $AgA_3R(MoO_4)_5$ with the $NaMg_3In(MoO_4)_5$ structural type (triclinic crystal system, space group P$\bar{1}$, Z = 2) are of particular interest and have a high ion conductivity (10^{-3}–10^{-2} S/cm). In this regard, the aim of this work was to reveal the possibility to form similar compounds in silver, zinc, indium, and iron molybdate and tungstate systems and to determine the effect of the nature of tetrahedral anion and three-charged cations on their obtaining and properties.

Polycrystalline samples were synthesized using a ceramic technology and studied by differential thermal (DTA) and X-ray diffraction analysis (XRD).

The research resulted in obtaining a new ternary molybdates $AgZn_3R(MoO_4)_5$ (R = In, Fe) crystallising in the triclinic crystal system (space group P$\bar{1}$, Z = 2). The sequence of chemical transformations that occur during the formation of these compounds, their crystallographic and thermal characteristics were determined. Unit cell parameters for the indium compound are as follows: a = 6.9920(4), b = 7.0491(4), c = 17.9196(9) Å, α = 87.692(5), β = 87.381(5), γ = 79.173(5)°; and for the iron compound: a = 6.9229(3), b = 6.9828(4), c = 17.7574(8) Å, α = 87.943(4), β = 87.346(5), γ = 78.882(5)°. It was established that silver-containing ternary zinc tungstates with indium and iron with a similar structure are not formed.

Keywords: ternary molybdates, silver, tungsten, solid-state synthesis, X-ray diffraction analysis (XRD), thermal properties.

For citation: I. Yu. Kotova, T. S. Spiridonova, Yu. M. Kadyrova, A. A. Savina Synthesis and characterisation of ternary molybdates $AgZn_3R(MoO_4)_5$ (R = In, Fe). *Kondensirovannye sredy i mezhfaznye granitsy = Condensed Matter and Interphases.* 2020; 22(3): 336–343. DOI: https://doi.org/10.17308/kcmf.2020.22/2967

✉ Irina Yu. Kotova, e-mail: ikotova@binm.ru

1. Introduction

Currently, a lot of attention is paid to searching, synthesising, and extending the range of application of complex oxide compounds, and using them to develop new materials with functionally relevant properties.

An important role in the study and the obtaining of new phases with valuable physical and chemical properties is given to ternary compounds with a tetrahedral anion containing various combinations of mono- and multivalent cations, including ternary molybdates and tungstates. One of the largest families within this class of compounds are molybdates with one-, two-, and three- charged cations. Silver NASICON-like rhombohedral phases $Ag_{1-x}A_{1-x}R_{1+x}(MoO_4)_3$ (A = Mg, Co, R = Al, Sc; A = Mg, R = In) [1–4] and the triclinic $AgA_3R(MoO_4)_5$ (A = Mg, R = Cr, Fe, Ga; A = Zn, R = Ga; A = Fe^{II}, R = Fe^{III}; A = Mn, R = Al, Cr, Fe, Sc, In) [5–10] are of particular interest due to a high ionic conductivity (10^{-3}–10^{-2} S/cm) [4, 7, 10]. Both structural types occur in systems where two- and three-charged cations tend to have octahedral coordination and the radius of the three-charged cation does not exceed 1 Å.

The characteristic features of the phase formation in systems, where the considered phases are formed are shown in Fig. 1 (by the example of Ag_2MoO_4–$MgMoO_4$–$In_2(MoO_4)_3$ [3]). The subsolidus structure of this system is determined by the formation of the NASICON-type ternary molybdates $AgMgIn(MoO_4)_3$ (S_1) and $AgMg_3In(MoO_4)_5$ (S_2) without any visible homogeneity regions along the section $AgIn(MoO_4)_2$–$MgMoO_4$. The phase of variable composition $Ag_{1-x}Mg_{1-x}In_{1+x}(MoO_4)_3$ (S_1) is formed along the section $AgMgIn(MoO_4)_3$–$In_2(MoO_4)_3$ and is an omission solid solution based on the ternary molybdate $AgMgIn(MoO_4)_3$ where homogeneity region is up to x = 0.6.

According to X-ray diffraction analysis (XRD), triple molybdates $AgA_3R(MoO_4)_5$ are isotypical to $NaMg_3R(MoO_4)_5$, R = In, Al (triclinic crystal system, space group P$\bar{1}$, Z = 2 [11,12]).

Crystals were obtained and their structure was determined for $AgMg_3R(MoO_4)_5$ (R = Cr, Fe), $AgMn^{II}_3(Mn^{III}_{0.26}Al_{0.74})(MoO_4)_5$, $Ag_{0.90}Al_{1.06}Co_{2.94}(MoO_4)_5$, and $AgFe^{II}_3Fe^{III}(MoO_4)_5$ [5–8]. The data from the X-ray powder patterns obtained by a full-profile analysis (Rietveld method) [13] were used to refine the crystal structures of $AgM_3Ga(MoO_4)_5$ (M = Mg, Zn) [9, 10].

Research was conducted to reveal a possibility to form similar compounds in silver, zinc, indium, and iron molybdate and tungstate systems and to determine the effect of the nature of tetrahedral anion and three-charged cations on their obtaining and properties.

2. Experimental

The source components were molybdates and tungstates of silver, zinc, and indium iron molybdate obtained by annealing of the stoichiometric mixtures of AgNO$_3$ (analytical reagent grade), ZnO (chemically pure grade), In$_2$O$_3$ (extra-pure grade), Fe(NO$_3$)$_3$·9H$_2$O (analytical reagent grade), MoO$_3$ (chemically pure grade), and WO$_3$ (chemically pure grade) at 350–450 °C (Ag$_2$MoO$_4$), 500–700 °C (ZnMoO$_4$), 400–800°C (In$_2$(MoO$_4$)$_3$, 300–700 °C (Fe$_2$(MoO$_4$)$_3$), 480–520 °C (Ag$_2$WO$_4$), 650–850 °C (ZnWO$_4$), 700–900 °C (In$_2$(WO$_4$)$_3$). The single-phase of synthesised products was monitored by X-ray analysis and in some cases by thermographic analysis. The synthesised compounds were identified by comparing with the results of previous studies and the ICDD PDF-2 database [14–17].

$AgZn_3R(\ni O_4)_5$ (R = In, Fe; $\ni$ = Mo; R = In, $\ni$ = W) samples were prepared from molybdates and tungstates, taken in stoichiometric proportions. Ag$_2$WO$_4$, ZnWO$_4$, WO$_3$ and Fe(NO$_3$)$_3$·9H$_2$O were
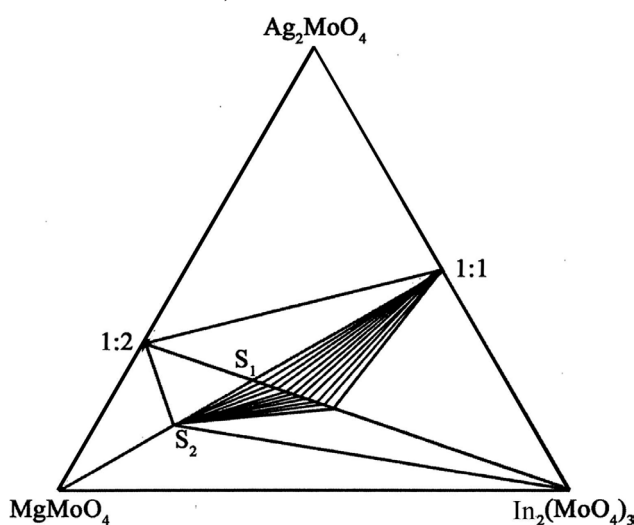
Fig. 1. Scheme of subsolidus phase relations in the Ag$_2$MoO$_4$–MgMoO$_4$–In$_2$(MoO$_4$)$_3$ system (S_1 – Ag$_{1-x}$Mg$_{1-x}$In$_{1+x}$(MoO$_4$)$_3$, S_2 – AgMg$_3$In(MoO$_4$)$_5$) [3]

used to synthesize AgZn$_3$Fe(WO$_4$)$_5$, in this case heat treatment started with 350°C.

The mixtures were gradually annealed in air with increments of 20–50 °C (in some cases 5–10°C) starting from 400–450 °C (for molybdates) and 550–600 °C (for tungstates), and finishing before they started to melt with intermediate homogenisation after 20–30 hours. The heat treatment time at each temperature was 30–70 hours. The phase composition of the sintered products was monitored by XRD before the annealing temperature was increased.

X-ray studies of polycrystalline products were carried out using a Bruker automated powder diffractometer D8 Advance (λCuK_α, scanning step 0.02076°) and Thermo ARL (λCuK_α, scanning step 0.02°).

Crystallographic characteristics of polycrystalline samples were determined based on isostructural compound data. Unit cell parameters were refined by the least-squares method using ICDD software package to prepare experimental standards. Smith-Snyder criterion F_{30} [18] was used as a validation criterion for XRD pattern indexing.

Thermoanalytical investigations were performed using a NETZSCH STA 449 F1 Jupiter device (Pt-crucible, heating rate 10 deg/min in a flow of argon).

3. Results and discussion

According to the XRD, the sequence of chemical transformations that occur during the formation of AgZn$_3R$(MoO$_4$)$_5$ (R = In, Fe) from a stoichiometric mixture of molybdates can be described in the following scheme:

$$\left.\begin{array}{l} Ag_2MoO_4 \\ ZnMoO_4 \\ R_2(MoO_4)_3 \end{array}\right\} \rightarrow \left.\begin{array}{l} Ag\,R(MoO_4)_2 \\ ZnMoO_4 \\ AgZn_3\,R(MoO_4)_5 \end{array}\right\} \rightarrow$$
$$\rightarrow AgZn_3\,R(MoO_4)_5$$
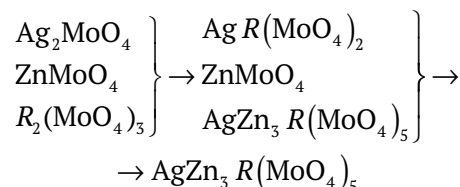
The primary product of the solid-phase interaction between Ag$_2$MoO$_4$, ZnMoO$_4$ and R_2(MoO$_4$)$_3$ (R = In, Fe) is double molybdate AgR(MoO$_4$)$_2$. An increase in temperature to 470–500 °C (R = In) and 420–450°C (R = Fe) leads to the formation of AgZn$_3R$(MoO$_4$)$_5$ in the reaction mixture. In the single-phase state, these compounds were obtained at 650–700 °C (R = In) and 600–650°C (R = Fe). The heat treatment time was 100–120 h. Further annealing only resulted in a better formation of the ternary molybdate structure.

As an example, Fig. 2 shows the AgZn$_3$Fe(MoO$_4$)$_5$ X-ray diffraction pattern.

X-ray diffraction analysis revealed that AgZn$_3R$(MoO$_4$)$_5$ synthesised compounds
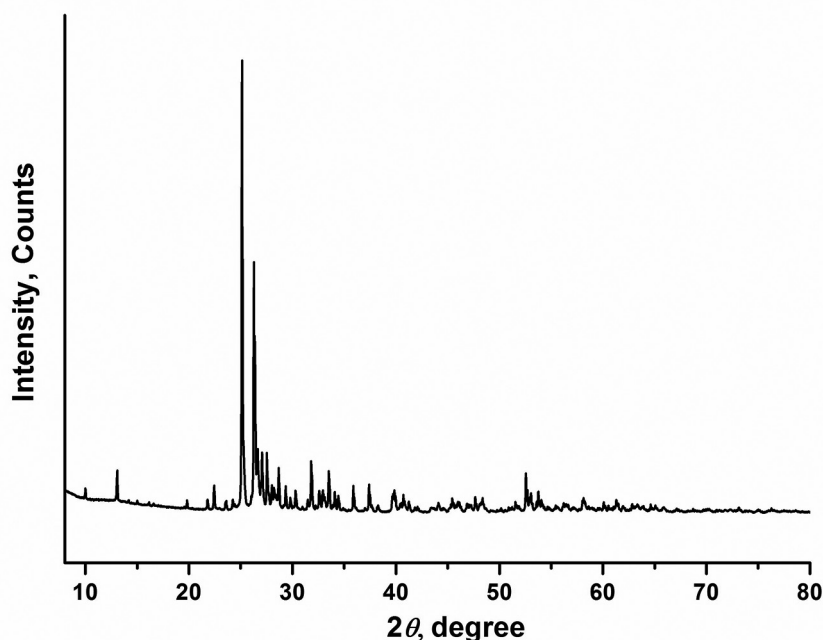
Fig. 2. X-ray diffraction pattern for ternary molybdate AgZn$_3$Fe(MoO$_4$)$_5$

are isostructural to each other and to the previously obtained $NaMg_3R(MoO_4)_5$ [11,12] and $AgA_3R(MoO_4)_5$ [5–10].

The structural features of the considered group of ternary molybdates are that MoO_4 tetrahedra and pairs and triplets of $(A, R)O_6$-octahedra connected along the edges share common vertices and form three-dimensional frameworks. Silver cations disordered over three closely-spaced positions are located in large frame voids.

Crystallochemical analysis of the inner space of the frame revealed the presence of channels located along the a axis, connected with channels along the c axis which contributes to increased ionic conductivity experimentally confirmed in

the case of $AgA_3R(MoO_4)_5$ (AR = MgAl, MnAl, MnGa) [7,10].

The indexing results of $AgZn_3R(MoO_4)_5$ (R = In, Fe) powder patterns are shown in Table 1, and their crystallographic characteristics are shown in Table 2 (it also contains previously published data for an isostructural gallium analogue). It is evident that the parameters a, b, and c and the volume of $AgZn_3R(MoO_4)_5$ unit cells decrease with a decreasing radius of the triply-charged cation.

Thermal characteristics of $AgZn_3R(MoO_4)_5$ were defined. All phases melt incongruently. The indium compound has the highest thermal stability, with a decrease in the size of the three-charged cation in $In^{3+} - Fe^{3+} - Ga^{3+}$ (r_R^{3+}= 0.80, 0.65,

Table 1. Indexing results for $AgZn_3R(MoO_4)_5$ (R = In, Fe) X-ray diffraction patterns

hkl	$AgZn_3In(MoO_4)_5$*				$AgZn_3Fe(MoO_4)_5$**			
	$2\theta_{exp}$,°	I/I_0	d_{exp}, Å	$\Delta = 2\theta_{exp} - 2\theta_{calc}$,°	$2\theta_{exp}$,°	I/I_0	d_{exp}, Å	$\Delta = 2\theta_{exp} - 2\theta_{calc}$,°
1	2	3	4	5	6	7	8	9
0 0 2	9.878	3	8.95	+0.001	9.966	2	8.87	+0.002
0 1 0					12.929	1L	6.842	−0.014
1 0 0	12.900	9	6.857	−0.010	13.024	6	6.792	+0.009
1 0 1	13.633	1	6.490	+0.005	13.769	1L	6.426	+0.001
−1 0 1	13.989	1	6.326	+0.000	14.148	1L	6.255	−0.002
0 0 3	14.841	2	5.964	+0.001	14.990	1L	5.905	−0.014
0 1 2	15.957	1	5.550	−0.034	16.105	1	5.499	+0.015
1 0 2				−0.001				+0.005
0 −1 2	16.448	1L	5.385	−0.015	16.550	1L	5.352	+0.008
1 1 1	16.874	1	5.250	−0.010	17.027	1L	5.203	−0.022
−1 −1 1	17.370	1L	5.101	+0.027				
1 0 3	19.300	1L	4.595	+0.019	19.508	1L	4.547	−0.009
−1 −1 2	19.643	1L	4.516	+0.007	19.779	2	4.485	+0.007
−1 1 0	19.824	1	4.475	+0.005	20.095	1L	4.415	−0.007
0 0 4				+0.009				
−1 0 3	20.080	1L	4.418	+0.005	20.291	1L	4.373	+0.007
−1 1 1	20.459	1L	4.337	+0.009				
1 1 3	21.549	2	4.120	+0.004	21.751	2	4.083	+0.009
1 −1 2	22.161	5	4.008	−0.002	22.390	6	3.968	+0.005
−1 −1 3	22.789	1	3.899	+0.012				
1 0 4	23.306	3	3.814	−0.013	23.507	2	3.781	−0.002
0 1 4				+0.003	23.575	1	3.771	+0.010
0 −1 4	24.017	2	3.702	−0.001	24.190	3	3.676	+0.004
−1 0 4	24.147	4	3.683	+0.002	24.397	1	3.645	+0.003
0 0 5	24.857	100	3.579	+0.005	25.088	100	3.547	+0.002
−1 1 3					25.243	11	3.525	+0.009
1 1 4	25.120	3	3.542	−0.011	25.361	4	3.509	−0.004
0 2 0	25.734	3	3.459	−0.007	25.997	1	3.425	+0.000

Continuation of Table. 1

1	2	3	4	5	6	7	8	9
2 0 0	25.949	51	3.431	−0.003	26.235	52	3.394	+0.003
0 2 1	26.055	35	3.417	−0.004	26.346	28	3.380	+0.002
2 0 1	26.233	10	3.394	+0.001	26.516	10	3.359	+0.004
0 −2 1	26.366	10	3.378	+0.006	26.622	11	3.346	+0.002
−1 −1 4	26.532	5	3.357	+0.019	26.735	3	3.332	+0.010
1 2 0	26.606	7	3.348	−0.023	26.790	1	3.325	+0.007
−2 0 1				+0.016	26.917	4	3.310	+0.007
1 2 1	26.806	16	3.323	−0.006	27.036	12	3.295	+0.002
2 1 1	26.948	2	3.306	−0.006	27.169	2	3.280	+0.011
−1 −2 1	27.303	21	3.264	−0.002	27.503	12	3.240	+0.002
0 2 2				+0.009	27.640	2	3.225	+0.001
−2 −1 1	27.473	2	3.244	+0.001	27.700	2	3.218	+0.008
1 0 5	27.634	2	3.225	+0.006				
0 1 5	27.675	4	3.221	−0.005	27.983	6	3.186	+0.006
0 −2 2	27.931	6	3.192	−0.007	28.164	3	3.166	+0.004
1 2 2				+0.007	28.202	2	3.162	+0.005
2 1 2	28.070	2	3.176	−0.011	28.303	1	3.151	+0.010
1 −1 4	28.135	2	3.169	−0.010	28.378	2	3.142	+0.004
−2 0 2	28.188	1	3.163	+0.004	28.504	1	3.129	+0.010
−1 1 4	28.263	1	3.155	−0.010	28.637	9	3.115	−0.011
0 −1 5	28.430	11	3.137	−0.006				+0.002
−1 −2 2	28.887	1	3.088	+0.009	29.101	1L	3.066	−0.002
−2 −1 2	29.088	7	3.067	−0.012	29.314	5	3.044	+0.007
1 1 5	29.168	1L	3.059	−0.037				
0 2 3	29.400	3	3.036	−0.002	29.767	3	2.999	−0.002
2 0 3	29.502	1	3.025	−0.001				+0.035
2 1 3	30.002	7	2.976	−0.005	30.270	5	2.950	+0.004
0 −2 3	30.267	1L	2.951	−0.013	30.502	1L	2.928	−0.001
−1 −1 5	30.708	2	2.909	−0.003	30.950	1L	2.887	−0.011
−1 2 0	31.020	1	2.881	−0.007	31.416	1L	2.845	−0.011
−1 −2 3	31.244	2	2.860	−0.001	31.454	2	2.842	+0.002
−1 2 1	31.372	16	2.849	−0.003	31.785	14	2.813	+0.002
−2 −1 3					31.679	1L	2.822	+0.012
2 −1 1	31.474	6	2.840	−0.010	31.859	2	2.807	−0.010
1 −1 5	31.944	2	2.799	−0.013	32.223	1	2.776	−0.011
0 2 4	32.167	3	2.780	−0.002	32.556	6	2.748	+0.015
2 0 4	32.231	5	2.775	+0.001				−0.005
0 1 6					32.642	1	2.741	+0.000
1 2 4	32.552	10	2.788	−0.005	32.883	5	2.722	+0.009
2 −1 2				+0.018	32.926	2	2.718	+0.027
1 −2 2	32.722	5	2.735	+0.006	33.085	4	2.705	+0.002
−2 1 2					33.384	1	2.682	+0.007
2 2 0	33.127	1	2.702	+0.013				+0.012
0 −2 4	33.224	17	2.694	−0.008	33.473	9	2.675	+0.002
2 2 1				+0.018	33.506	4	2.672	+0.006
1 1 6	33.488	1	2.674	−0.010	33.822	1L	2.648	−0.006
−2 0 4				+0.012	33.863	1	2.645	+0.013
−2 −2 1	33.823	8	2.268	−0.013	34.060	4	2.6301	+0.000

The end of the Table. 1

1	2	3	4	5	6	7	8	9
2 2 2	34.120	5	2.626	−0.012	34.398	2	2.6050	+0.002
−1 −2 4	34.203	2	2.619	+0.002	34.434	1	2.6024	+0.003
−2 −1 4				−0.012				
−1 2 3	34.398	1	2.605	−0.002	34.873	1L	2.5706	+0.004
2 −1 3				+0.005	34.788	1L	2.5767	−0.002
1 −2 3	34.709	1L	2.582	−0.017	35.041	1L	2.5587	+0.006
−2 1 3	34.926	1L	2.567	+0.011				+0.004
0 0 7	35.064	1L	2.557	+0.016	35.407	1L	2.5331	−0.001
−1 −1 6								+0.018
2 0 5	35.519	10	2.525	−0.011	35.854	7	2.5025	−0.002
2 2 3	35.643	1	2.517	+0.046	36.002	1	2.4925	+0.009
1 2 5	35.711	1	2.512	+0.039	36.139	1	2.4834	+0.000
2 1 5	35.790	1L	2.507	+0.018				+0.011
−1 1 6	36.257	1L	2.4756	−0.009				
0 −2 5	36.679	1	2.4481	−0.001	36.968	1	2.4296	−0.011
2 −1 4	36.899	2	2.4340	−0.030	37.233	1L	2.4129	+0.025
−1 2 4				+0.001	37.438	1	2.4002	−0.022
−2 0 5	36.963	11	2.4299	+0.001	37.367	8	2.4046	+0.007
1 −2 4	37.269	4	2.4107	+0.001	37.638	1	2.3879	−0.009
−2 −2 3				+0.005	37.514	1	2.3955	+0.024
−2 1 4	37.545	1L	2.3936	−0.007				
−1 −2 5	37.672	1L	2.3858	−0.015				
−2 −1 5	37.831	1	2.3761	+0.005	38.165	1	2.3561	−0.003
2 2 4	37.912	3	2.3712	−0.002	38.269	1	2.3499	−0.003
−1 0 7	38.013	1	2.3652	−0.003				
1 1 7					38.455	1L	2.3390	+0.000
1 3 1	38.884	1	2.3142	−0.018				
0 3 0					39.464	1L	2.2815	−0.028
3 1 1	39.113	1	2.3012	+0.034				
0 2 6	39.212	6	2.2956	−0.004	39.702	3	2.2684	−0.002
2 0 6				+0.005	39.605	4	2.2737	−0.013
3 0 0	39.361	4	2.2872	−0.004	39.816	5	2.2621	−0.007
1 2 6				+0.034				+0.015
3 0 1	39.479	2	2.2807	+0.009	39.937	2	2.2556	−0.003
1 3 2	39.619	1L	2.2729	+0.018				
−3 −1 1					40.053	1L	2.2493	−0.007
2 −1 5					40.251	1L	2.2387	+0.020
−3 0 1	39.896	5	2.2578	−0.003	40.360	2	2.2329	−0.003
−2 −2 4				+0.013	40.185	1	2.2422	+0.009
−1 2 5					40.499	2	2.2255	−0.013
0 3 2	40.015	4	2.2513	+0.002				−0.004
0 0 8	40.289	5	2.2367	+0.004	40.680	5	2.2161	−0.008
0 −2 6	40.529	3	2.2240	+0.008	40.851	1	2.2072	−0.007

$^{*}F_{30} = 83.2\ (0.0075, 48)$
$^{**}F_{30} = 96.4\ (0.0066, 47)$

Table 2. Crystallographic characteristics of $AgZn_3R(MoO_4)_5$ (R = In, Fe, Ga)

R	a, Å	b, Å	c, Å	$\alpha°$	$\beta°$	$\gamma°$	V, Å³
In	6.9920(4)	7.0491(4)	17.9196(9)	87.692(5)	87.381(5)	79.173(5)	866.13
Fe	6.9229(3)	6.9828(4)	17.7574(8)	87.943(4)	87.346(5)	78.882(5)	841.08
Ga [10]	6.9037(3)	6.9639(4)	17.7147(8)	88.107(4)	87.440(4)	78.982(4)	834.87
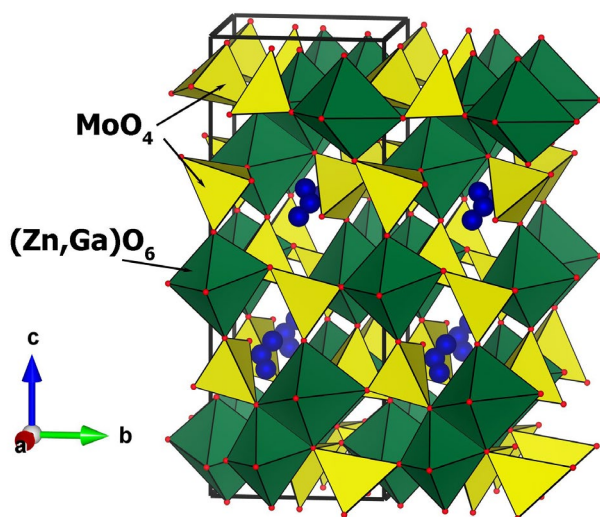
Fig. 3. A general view of $AgZn_3Ga(MoO_4)_5$ structure [10]

0.62 E for CN = 6 respectively [19]) the melting temperature decreases (832°C – 777°C – 644°C).

Despite similar values for Mo (VI) and W (VI) sizes (0.41 and 0.42 E for CN = 4, respectively [19]), ternary tungstates with a similar structure apparently do not exist. All our attempts to obtain $AgZn_3R(WO_4)_5$ triclinic phases (variation by thermal treatment and heat treatment modes) did not lead to any positive results, which is probably due to a significantly lower susceptibility of W (VI) (as compared to Mo (VI)) to tetrahedral coordination [20].

4. Conclusions

Thus, the possibility to form silver, zinc, and indium (iron) ternary molybdates and tungstates, of the $NaMg_3In(MoO_4)_5$ structural type (triclinic crystal system, space group P1̄, Z = 2) were studied for the first time. New ternary molybdates $AgZn_3R(MoO_4)_5$ (R = In, Fe) were obtained. The sequence of chemical transformations that occur during their synthesis from a stoichiometric mixture of molybdates was determined. The crystallographic and thermal characteristics of synthesized compounds were identified. The frame structure of this group of phases containing connected cavities, the defective

positions of silver cations, their low and open coordination can contribute to the increased Ag-ion conductivity of the received compounds. It was established that such phases do not form in tungsten systems.

Conflict of interests

The authors declare that they have no known competing financial interests or personal relationships that could have influenced the work reported in this paper.

References

1. Kotova I. Yu. Phase formation in the Ag_2MoO_4–$CoMoO_4$–$Al_2(MoO_4)_3$ system. *Russ. J. Inorg Chem.* 2014;59: 844–848. DOI: https://doi.org/10.7868/s0044457x14080133

2. Kotova I. Yu., Korsun V. P. Phase in the Ag_2MoO_4–$MgMoO_4$–$Al_2(MoO_4)_3$. *Russ. J. Inorg. Chem.* 2010;55(6): 955–958. DOI: https://doi.org/10.1134/S0036023610060203

3. Kotova I. Yu., Korsun V. P. Phase formation in the system involving silver, magnesium, and indium molybdates. *Russ. J. Inorg. Chem.* 2010;55(12): 1965–1969. DOI: https//doi.org/10.1134/S0036023610120247

4. Kotova I. Yu., Belov D. A., Stefanovich S. Yu. $Ag_{1-x}Mg_{1-x}R_{1+x}(MoO_4)_3$ Ag⁺-conducting NASICON-like phases, where R = Al or Sc and 0 ⩽ x ⩽ 0.5. *Russ. J. Inorg. Chem.* 2011;56(8): 1189–1 193. DOI: https//doi.org/10.1134/S0036023611080122

5. Bouzidi C., Frigui W., Zid M. F. Synthèse et structure crystalline d'un matériau noir $AgMn^{II}_3(Mn^{III}_{0.26}Al_{0.74})(MoO_4)_5$. *Acta Crystallographica Section E Crystallographic Communications.* 2015; 71(3): 299–304. DOI: https://doi.org/10.1107/S2056989015003345

6. Nasri R., Chérif S. F., Zid M. F. Structure cristalline de la triple molybdate $Ag_{0.90}Al_{1.06}Co_{2.94}(MoO_4)_5$. *Acta Crystallographica Section E Crystallographic Communications.* 2015; 71(4): 388–391. DOI: https//doi.org/10.1107/s2056989015005290

7. Kotova I. Yu., Solodovnikov S. F., Solodovnikova Z. A., Belov D. A., Stefanovich S. Yu., Savina A. A., Khaikina E. G. New series of triple molybdates $AgA_3R(MoO_4)_5$ (A = Mg, R = Cr, Fe; A = Mn, R = Al, Cr, Fe, Sc, In) with framework structures and mobile silver ion sublattices. *Journal of Solid State Chemistry.* 2016;238: 121–128. DOI: https//doi.org/10.1016/j.jssc.2016.03.003

8. Balsanova L. V. The synthesis of crystals of silver oxide phases based on molybdenum, investigation of their structure and properties. *ESSUTM Bulletin*. 2015;5: 63–69. (In Russ., abstract in Eng.)

9. Kotova I. Yu., Savina A. A., Khaikina E. G. Crystal structure of new triple molybdate AgMg$_5$Ga(MoO$_4$)$_5$ from Rietveld refinement. *Powder Diffraction*. 2017;32(4): 255–260. DOI: https//doi.org/10.1017/S0885715617000811

10. Kotova I. Yu., Savina A. A., Vandysheva A. I., Belov D. A., Stefanovich S. Yu. Synthesis, cristal structure and electrophysical properties of triple molybdates containing silver, gallium and divalent metals. *Chimica Techno Acta*. 2018;5(3): 132–143. DOI: https://doi.org/10.15826/chimtech.2018.5.3.02

11. Klevtsova R. F., Vasiliev A. D., Kozhevnikova N. M., Glinskaya L. A., Kruglik A. I., Kotova I. Yu. Synthesis and crystal structural study of ternary molybdate NaMg$_3$In(MoO$_4$)$_5$. *Journal of Structural Chemistry*. 1994;34(5): 784–788. DOI: https://doi.org/10.1007/BF00753580

12. Hermanowicz K., Maczka M., Wolcyrz M., Tomaszewski P. E., Paściak M., Hanuza J. Crystal structure, vibrational properties and luminescence of NaMg$_3$Al(MoO$_4$)$_5$ crystal doped with Cr^{3+} ions. *Journal of Solid State Chemistry*. 2006;179(3): 685–695. DOI: https://doi.org/10.1016/j.jssc.2005.11.032

13. Rietveld H. M. A profile refinement method for nuclear and magnetic structures. *Journal of Applied Crystallography*. 1969;2: 65–71. DOI: https://doi.org/10.1107/s0021889869006558

14. Kohlmuller R., Faurie J.-P. Etude des systemes MoO$_3$–Ag$_2$MoO$_4$ et MoO$_3$–MO (M – Cu, Zn, Cd). *Bull. Soc. Chim. France*. 1968;11: 4379–4382.

15. Trunov V. K., Kovba L. M. The reaction of In$_2$O$_3$ with WO$_3$ and MoO$_3$. *Vestnik Moskovskogo universiteta. Khimiya.* 1967;1: 114–115 (In Russ.).

16. Trunov V. K., Kovba L. M. On interaction of trioxides of molybdenum and tungsten with sesquioxides of iron and chromium. *Izvestiya Akademii Nauk SSSR. Neorganicheskie Materialy*. 1966;2: 151–154. (In Russ.).

17. ICDD PDF-2 Data Base, Cards ## 00-049-0337, 00-035-0765, 01-073-0554, 01-083-1701, 01-074-1791.

18. Smith G. S., Snyder R. L. FN: A criterion for rating powder diffraction patterns and evaluating the reliability of powder-pattern indexing. *Journal of Applied Crystallography*. 1979;12(1): 60–65. DOI: https//doi.org/10.1107/S002188987901178X

19. Shannon R. D. Revised effective ionic radii and systematic studies of interatomic distances in dalides and chalcogenides. *Acta Crystallographica Section A*. 1976;32(5): 751–767. DOI: https://doi.org 10.1107/S0567739476001551

20. Poraj-Koshic M.A., Atovmjan L.O. *Kristallohimija i stereohimija koordinacionnyh soedinenij molybdena* [Crystal chemistry and stereochemistry of coordination compounds of molybdenum]. Moscow: Nauka Publ.; 1974. 230 p. (In Russ.)

Information about the authors

Irina Yu. Kotova, PhD in Chemistry, Researcher, Laboratory of Oxide Systems, Baikal Institute of Nature Management, Siberian Branch of the Russian Academy of Sciences (BINM SB RAS), Ulan-Ude, Russian Federation; e-mail: ikotova@binm.ru. ORCID iD: https://orcid.org/0000-0003-3829-6516.

Tatiyana S. Spiridonova, Lead Engineer, Laboratory of Oxide Systems, Baikal Institute of Nature Management, Siberian Branch of the Russian Academy of Sciences (BINM SB RAS), Ulan-Ude, Russian Federation; e-mail: spiridonova-25@mail.ru. ORCID iD: https://orcid.org/0000-0001-7498-5103.

Yulia M. Kadyrova, PhD in Chemistry, Researcher, Laboratory of Oxide Systems, Baikal Institute of Nature Management, Siberian Branch of the Russian Academy of Sciences (BINM SB RAS), Ulan-Ude, Russian Federation; e-mail: yliychem@yandex.ru. ORCID iD: https://orcid.org/0000-0001-7569-6233.

Aleksandra A. Savina, PhD in Chemistry, Researcher, Laboratory of Oxide Systems, Baikal Institute of Nature Management, Siberian Branch of the Russian Academy of Sciences (BINM SB RAS), Ulan-Ude and Researcher, Skolkovo Institute of Science and Technology, Moscow, Russian Federation; e-mail: a.savina@skoltech.ru. ORCID iD: https://orcid.org/0000-0002-7108-8535.

All authors have read and approved the final manuscript.

Translated by Irina Charychanskaya
Edited and proofread by Simon Cox

Kinetics of Phase Transformations during Selective Dissolution of Cu$_5$Zn$_8$

© 2020 O. A. Kozaderov✉, D. M. Taranov, A. N. Krivoshlykov, S. V. Borodkina

Voronezh State University,
1 Universitetskaya pl., Voronezh 394018, Russian Federation

Abstract

The study determined the kinetics of the selective anodic dissolution of the copper-zinc intermetallic compound Cu$_5$Zn$_8$ (gamma-phase) in an acetate buffer solution. Microscopic and X-ray analysis methods demonstrated the selective nature of the corrosive dissolution of Cu$_5$Zn$_8$. The dissolution results in the dezincification of the intermetalic compound and morphological development of its surface accompanied by the formation of the copper phase. A theoretical model of the transition of the electrode surface to the critical state together with the experimental concentration dependencies of the critical potential and critical overvoltage demonstrated that the dissolution of zinc from Cu$_5$Zn$_8$ is most probably limited by the non-stationary diffusion mass-transfer in the solid phase of the intermetallic compound. The study also demonstrated that the phase transformation during the overcritical selective anodic dissolution of the gamma-phase of Cu$_5$Zn$_8$ in an acetate environment accelerates following the growth of the anodic potential and is controlled by the surface diffusion of adatoms towards the three-dimensional nucleus of the copper phase with instantaneous nucleation.

Keywords: copper-zinc alloy, gamma phase, selective dissolution, phase transformation, surface development, heterogeneous nucleation.

1. Introduction

Copper-zinc alloys and intermetallic compounds with comparatively high concentrations of electronegative components (>15 at% Zn) are susceptible to selective dissolution (SD) of zinc in aqueous solutions [1]. Dezincification belongs to a large group of processes caused by selective external influence (e.g. chemical, temperature, or laser) on multicomponent materials. In case of solid homogeneous copper-zinc alloys, the preferential dissolution of zinc may be accounted for by the difference in the volatility of Cu and Zn during vacuum evaporation [2–4] or in the rate of atomic diffusion during laser sublimation [5, 6]. The electrochemical dezincification of brasses, however, is based on the difference in the electrode potentials of the components in the medium [7–9].

Selective leaching of zinc results in the formation of a porous structure with a significantly reduced mechanical strength, as compared to the initial material, and often causes the complete destruction of the initial material [10–13]. In order to protect construction materials based on copper-zinc alloys from dezincification, it is necessary to determine the kinetics and mechanism of selective dissolution of zinc in aqueous electrolyte solutions. Furthermore, knowing the kinetics of the process, we can define the optimal conditions for the synthesis of a SD product, macro- and nanoporous copper [5, 6,

✉ Oleg A. Kozaderov, e-mail: ok@chem.vsu.ru

14–17], which is a promising material that can be used in electrochemical technologies and energy production.

The formation of the porous structure during the SD of a homogeneous Cu–Zn alloy or an intermetallic compound is possible given the following conditions. The initial system must be based on zinc. The ionisation of a certain (critical) amount of zinc results in such an increase in the thermodynamic activity of electrochemically stable copper, that phase transformation (PT) can take place accompanied by the formation of the metallic copper Cu^0 phase. Selective dissolution of Cu–Zn systems with phase transformation was experimentally demonstrated in [18–20]. The increased thermodynamic activity of the electropositive metal during the SD of the binary alloy was theoretically substantiated in [21–23] using the methods of nonequilibrium thermodynamics. Regarding copper-zinc alloys, it can be described as follows. Vacancies □ formed as a result of the dissolution of zinc serve as intermediates for the redistribution of the Gibbs free energy in the highly defective surface layer of the alloy. This results in the thermodynamic activation of copper undergoing phase transformation conjugated with zinc ionisation:

$$Zn \xrightarrow{-2e^-} \square + Zn^{2+}$$
$$|$$
$$Cu + \square \xrightarrow{activation} Cu^* \xrightarrow[transformation]{phase} Cu^0$$
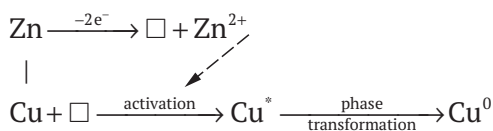
A characteristic feature of selective dissolution accompanied by phase transformation is a substantial morphological development of the surface layer of the alloy. For copper-zinc alloys this was demonstrated using impedancemetry [24] and physical methods of surface investigation [25].

In our research, we studied the dezincification of Cu–Zn systems accompanied by phase transformation of the alloy using industrially manufactured high-temperature copper-zinc solder PMTs-36. The chemical composition of this intermetallic system includes ~36 at% of copper. The intermetallic system is the gamma phase of Cu–Zn. PMTs-36 solder was chosen as the material for the study of the PT, because the probability of copper ionisation/deposition

(a process alternative to phase transformation) during the anodic dissolution of this solder is low

$$Cu^* \xrightarrow[-2e]{ionisation} Cu^{2+} \xrightarrow{deposition} Cu^0$$
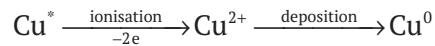
The fact is that anodic potentials during the electrochemical dealloying of zinc-rich alloys are negative, which means that copper does not get dissolved. Furthermore, to study the kinetics of the selective dissolution of PMTs-36 the sample was put into an acetate buffer solution. According to [9], in this medium the soluble corrosion products of the γ-phase of Cu–Zn are zinc ions Zn^{2+}, the insoluble product is metallic copper $Cu°$, and copper oxides are not formed. In other words, the anodic process involving the studied alloy is the selective dissolution proper. Therefore, the total anodic current equals the partial current of zinc ionisation.

We also took into account the fact, that the beginning of the phase transformation and morphological development of the surface of the Zn-based Zn–Cu alloy undergoing selective dissolution is characterised by certain critical values of the charge q_{cr} transferred through the electrode and the anodic potential E_{cr} [26]. The transition to the critical state is indicated on the polarization curves and chronoamperograms by a rapid increase in the anodic current i. According to the theoretical model of transition to the critical potential [27], the values E_{cr} for the copper-zinc alloy in the media with various activity levels of Zn^{2+} ions can be used to determine the kinetics of selective dissolution and the partial rates of SD and PT.

The aim of this paper was to determine the kinetics of the selective anodic dissolution of the copper-zinc intermetallic system (γ-phase) in an acetate buffer solution.

In order to achieve this we needed to complete the following tasks.

To determine the critical parameters for the development of the electrode surface during the selective anodic dissolution of the copper-zinc system (γ-phase) in an acetate buffer solution.

To determine the rate of partial electrode processes involving the components of the copper-zinc intermetallic system (γ-phase) (zinc ionisation and phase transformation of copper) and define the nature of the limiting stage of copper recrystallization.

2. Experimental

The study was carried out using polycrystalline metals (Cu, Zn) and an industrially manufactured copper-zinc solder, PMTs-36 (atomic fraction of copper – 0.36). According to the phase diagram and the results of X-ray diffractometry, the system was an intermetallic compound Cu_5Zn_8. To make the electrode, the metallic sample was cut, sanded, and mounted in polymerizable epoxy resin. The standard preparation of the surface of the electrode for the experiment included polishing with abrasive paper of decreasing grade, mirror-polishing with suede leather and an MgO alcohol-based suspension, washing, degreasing with isopropyl alcohol, and drying with filter paper.

The following solutions were used: 0.05 M CH_3COONa + 0.05 M CH_3COOH + x M $ZnSO_4$ ($x = 10^{-4} \div 10^{-2}$) and an acetate buffer solution 0.05 M CH_3COONa + 0.05 M CH_3COOH prepared using bidistilled aqueous solution and AR grade reagents. The solutions were also preliminary deaerated with chemically pure argon for 1.5 hours. The experiment was conducted on unstirred solutions.

The study was performed using a three-electrode glass cell with the working and the auxiliary (platinum) electrode being in the same compartment. A silver chloride reference electrode was placed in a separate container linked to the electrolytic cell by a salt bridge with a potassium nitrate saturated solution. The potential values E are given according to the standard hydrogen electrode (SHE) scale. The current i was calculated for the visible geometric area of the electrode S_{geom}.

The measurement and control of the electrode potential and the registration of the polarization curves was performed using an IPC-compact computer-aided potentiostat. A prepared electrode was put into the cell filled with a deaerated solution and held until the open-circuit potential reached quasi-stationary values. During the potentiodynamic measurements, the potential scan rate V was set and the i,E-dependency was recorded. During the chronoamperometric measurements, the potential E=const was set and the i,t-dependency of the current decay over time was recorded for 15–20 minutes.

The morphology of the surface of the alloy was studied using scanning electron microscopy (SEM) (JSM-6380LV microscope). The chemical composition of the surface layer was determined by means of energy dispersive X-ray spectroscopy (EDX) (INCA 250 system), and the phase composition was determined using X-ray diffractometry (ARL X'TRA diffractometer). The results of the SEM, EDX, and X-ray diffractometry studies were obtained using the equipment of the Centre for Collective Use of Scientific Equipment of Voronezh State University (http://ckp.vsu.ru).

3. Results and discussion

The results of the EDX proved that the dissolution of the copper-zinc alloy PMTs-36 in the acetate buffer solution is selective: after 400 days of incubation the concentration of copper increased from 36 to 76 at.% on average, which indicates deep dezincification of the system. The corrosion process is accompanied

Fig. 1. SEM photographs of the surface of the PMTs-36 alloy before (a) and after (b) 400 days of immersion in a 0.05 M CH_3COOH + 0.05 M CH_3COONa solution

by a substantial morphological development of the surface (Fig. 1). The results of the X-ray diffractometry indicate the formation of the copper phase during corrosive dissolution of the PMTs-36 alloy in the 0.05 M CH₃COOH + 0.05 M CH₃COONa solution (Fig. 2). Indeed, the initial sample was the intermetallic compound Cu₅Zn₈. However, after the PMTs-36 alloy was held in the acetate buffer solution for a long time, the X-ray diffraction pattern demonstrated peaks corresponding to metallic copper. Therefore, corrosion of PMTs-36 in the studied solution is selective. It is accompanied by the phase transformation of $Cu_5Zn_8 \rightarrow Cu$.

In order to determine the kinetics of selective dissolution of the intermetallic compound Cu_5Zn_8

we need to analyse the anodic behaviour of the studied copper-zinc alloy PMTs-36 in the acetate solution using the corresponding polarization curves (Fig. 3). We can see that the dissolution of the alloy proceeds at significantly more positive potentials than the dissolution of pure zinc. Judging by the position of the polarization curve of copper, we can suggest that within the studied range of potentials copper is electrochemically stable and does not dissolve.

Upon reaching a critical potential E_{cr} the polarization curve of the alloy demonstrates a region of rapid increase in the anodic current density. This increase might indicate the beginning of phase transformation and surface development, because other electrochemical processes, such as

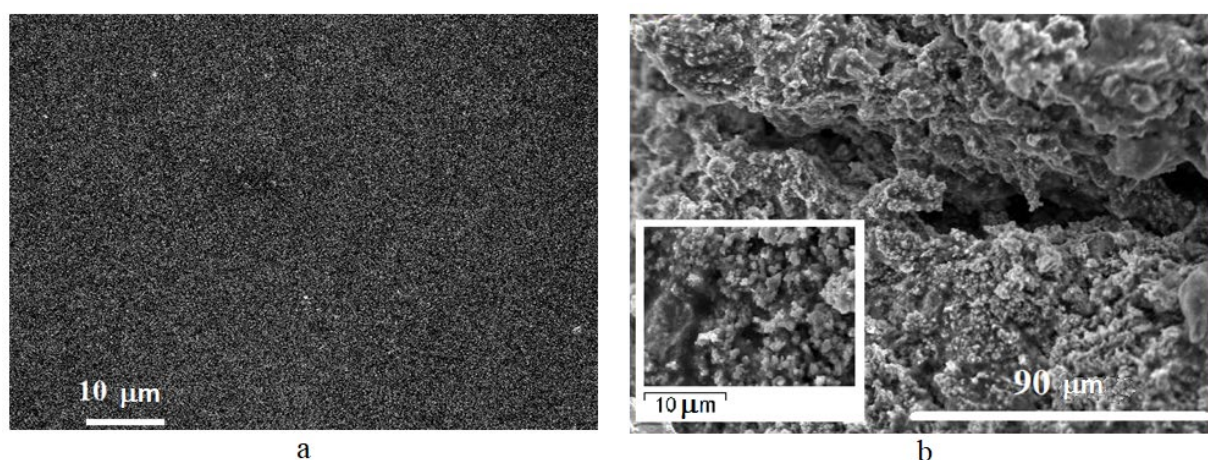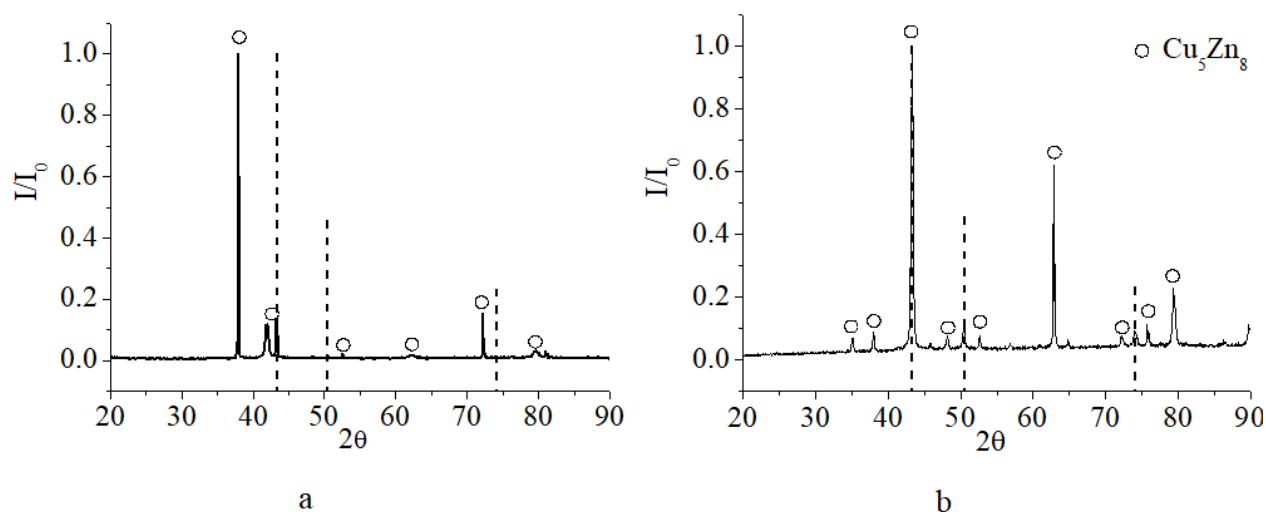**Fig. 2.** X-ray diffraction patterns of the surface of the PMTs-36 alloy before (a) and after (b) 400 days of immersion in a 0.05 M CH₃COOH + 0.05 M CH₃COONa solution. The peaks of the polycrystalline copper are marked with dotted lines [28]
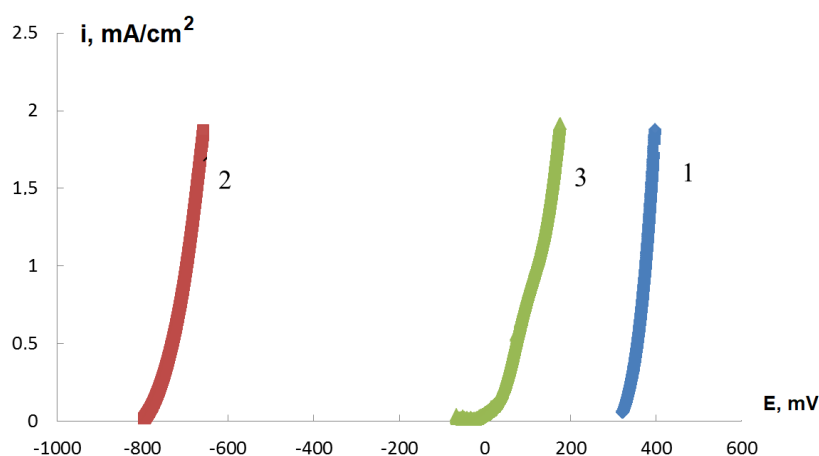
Fig. 3. Anodic polarization curves of Cu (1), Zn (2), and PMTs-36 (3) in a 0.05 M CH₃COOH + 0.05 M CH₃COONa solution with $V = 0.5$ mV/s

copper dissolution or oxygen evolution, take place at significantly more positive potentials. Values E_{cr} were determined by means of tangents to the high-current region of the i,E-curve [26]. The difference between E_{cr} and the open-circuit potential E(0) of the electrode in the solution was used to calculate the critical overpotential η_{cr} for the selective dissolution of PMTs-36. It appeared that the activity level of Zn^{2+} ions in the solution does not effect anodic polarization curves. However, an increase in ion activity is accompanied by a significant increase in E_{cr}. Within the studied concentration range, the dependency of E_{cr} on a_{Zn}^{2+} is linearized with the slope being ~42±2 mV (Fig. 4a). According to the theoretical model of E_{cr} [27], this indicates the fact that the diffusion process is hindered mainly in the solid phase. In turn, the critical overpotential η_{cr} alters unsystematically with various a_{Zn}^{2+} (Fig. 4b). This is another proof that in the vicinity of the critical potential the system PMTs-36 undergoes solid-phase-diffusion, because according to [27] $d\eta_{cr}/d\lg a_{Zn}^{2+} = 0$ under these conditions.

To determine the kinetics of phase transformation occurring at overcritical potentials parallel to the selective dissolution of zinc from Cu_5Zn_8 in the acetate buffer solution, we need to analyse the results of potentiostatic chronoamperometry presented as the current decay curves replotted in a bi-logarithmic scale (Fig. 5a).

These curves have linear regions which, following the Cottrell equation [29], indicate that the diffusion mass-transfer is the controlling stage of the SD. Combined with the above given data on the concentration dependence of the critical potential, the observed partial rectification of the chronoamperograms in a bi-logarithmic scale is another proof that the solid-phase diffusion SD takes place.

At some point, the current decay becomes less prominent, or the current begins to grow. The nonlinearity increases with higher anodic potential, which may be accounted for by the phase transformation taking place parallel to the SD. Indeed, the phase transformation allows the electrolyte to penetrate into the deeper layers of the alloy dissolving larger amount of zinc and thus increasing the rate of the SD [27].

Let's assume that the nonlinearity of the bi-logarithmic chronoamperogram is determined by two non-stationary processes: selective dissolution of Zn during the slow non-stationary diffusion mass-transfer at the rate $i_{diff}(t)$ and phase transformation involving Cu at the rate $i_{nucl}(t)$. Then the current transient of the PT $i_{nucl}(t)$ can be calculated [27] as the difference between the total (registered in the experiment) current density $i(t)$ and the diffusion current density calculated using the Cottrell equation:

$$i_{nucl}(t) = i(t) - i_{diff}(t),$$
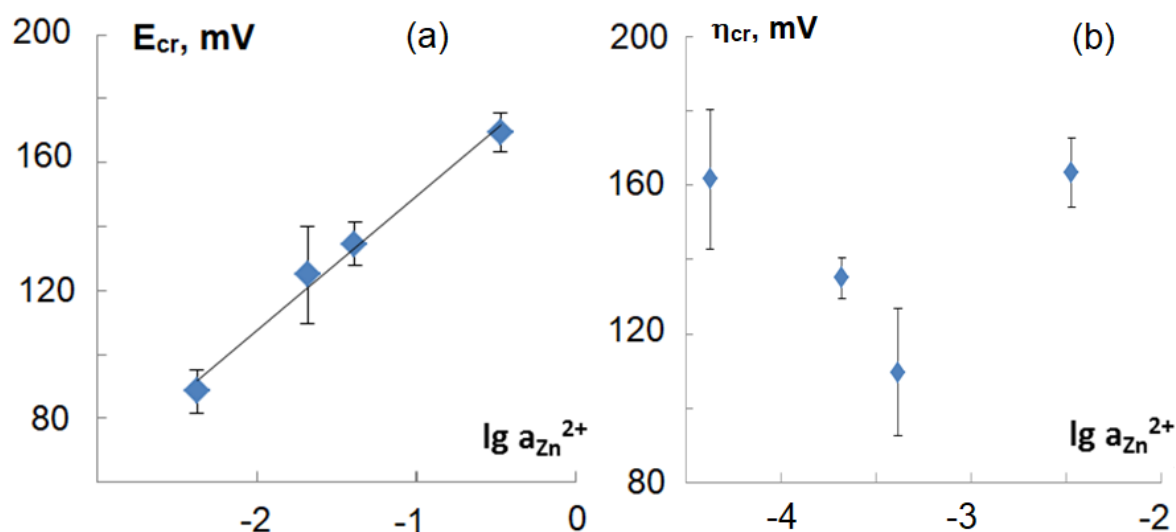
Fig. 4. Dependence of the critical potential (a) and critical overpotential (b) of the development of the PMTs-36 surface on the ion activity Zn^{2+} in the acetate buffer solution 0.05 M CH_3COOH + 0.05 M CH_3COONa with various concentrations of zinc ions
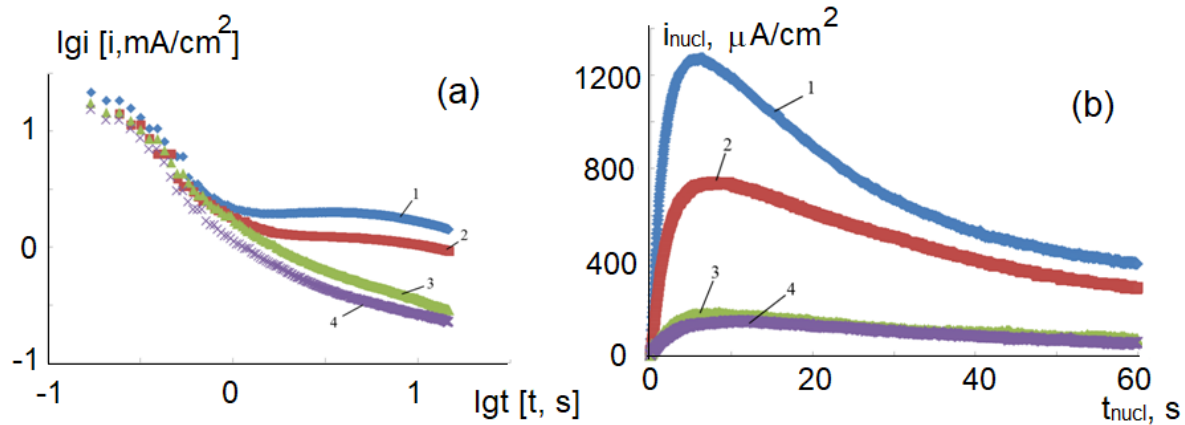
Fig. 5. Anodic chronoamperograms of zinc dissolution (a) and phase rearrangement of copper (b) during SD of Cu_5Zn_8 in a 0.05 M CH_3COOH + 0.05 M CH_3COONa solution with E = 50 mV (1), 0 mV (2), −50 mV (3), and −100 mV (4)

The resulting dependence of the phase formation current on time is given in Fig. 5b. We can see that the PT current grows over time. The rate of the growth increases with the growth of the anodic potential, and the chronoamperogram presents a curve with a peak, characteristic of the phase formation process.

To determine the kinetic-limitations to the formation of the Cu phase during selective dissolution of the intermetallic compound Cu_5Zn_8, the calculated current transients were replotted in the coordinate criterion for various models of heterogeneous nucleation. It appeared

that partial linearisation is only possible over a short period of time during the diffusive mode of three-dimensional nucleation only, provided that the activation of the potential nucleation centres is instantaneous (Fig. 6). The diffusion character of the formation of a new copper phase during the SD of Cu_5Zn_8 is also demonstrated by the comparison of experimental kinetic curves with the model dependencies calculated for various modes of heterogeneous nucleation (Fig. 7).

The quantitative estimation of the effect of anodic potential on the rate of copper PT was performed by analysing the values of the effective
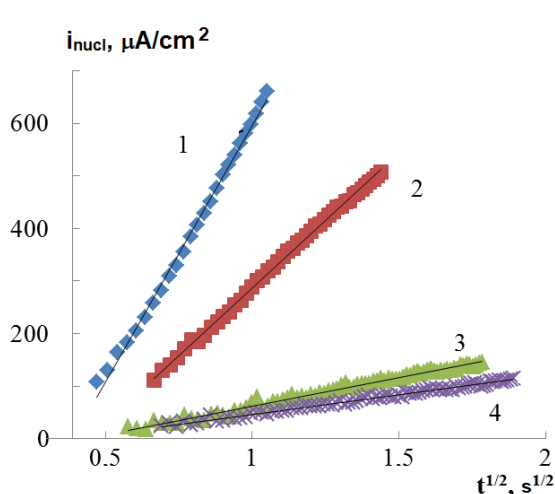
Fig. 6. Linearization of the current transients of PT and SD of the intermetallic compound Cu_5Zn_8 in the coordinates criterion for the instantaneous three-dimensional nucleation during the anodic dissolution in a 0.05 M CH_3COOH + 0.05 M CH_3COONa solution with E = 50 (1), 0 (2), −50 (3), and −100 mV (4)
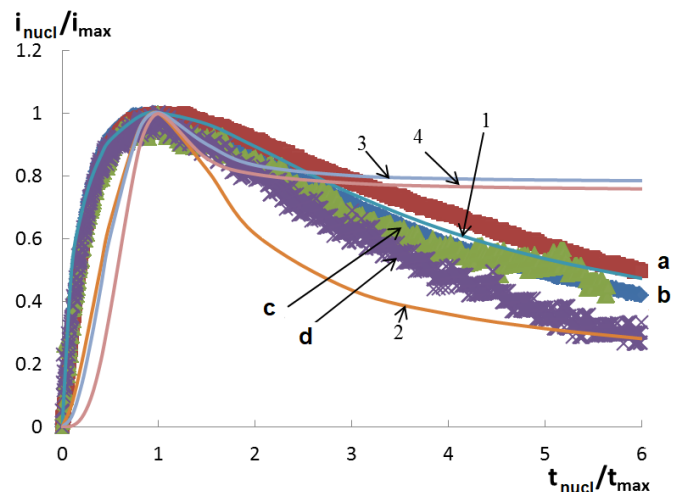
Fig. 7. Dependence of the phase transformation currents during selective dissolution of Cu_5Zn_8 in a 0.05 M CH_3COOH + 0.05 M CH_3COONa solution at various potentials: a, b, c, d – experimental curves; 1 – instantaneous activation, diffusion control; 2 – progressive activation, diffusion control; 3 – instantaneous activation, kinetic control; 4 – progressive activation, kinetic control

rate constant $k_{nucl} = \mathrm{d}i_{nucl}/\mathrm{d}t^{0.5}$, determined as the slope of the dependence of PT current density on time in the coordinates criterion for the instantaneous three-dimensional nucleation proceeding in the diffusion mode. Values k_{nucl} are given in Fig. 8. The effect of the anodic potential is obvious, since the shift towards the positive side results in a significant increase in k_{nucl}. This can be explained by the growth of the concentration and rate of the surface diffusion of copper adatoms appearing on the surface during the SD.

4. Conclusions

1. The study determined that corrosion of the copper-zinc alloy PMTs-36, (a single-phase intermetallic system Cu$_5$Zn$_8$) in the acetate buffer solution is a selective process. It results in the dezincification of the alloy and is accompanied by morphological development of its surface and phase transformations resulting in the formation of the copper phase.

2. The experiments allowed us to determine the critical potential E_{cr} and the critical overpotential η_{cr}, indicating the beginning of the phase transformation and morphological development in the surface layer of the intermetallic compound Cu$_5$Zn$_8$ during its selective anodic dissolution in the acetate buffer solution. Analysis of the dependence of E_{cr} and η_{cr} on the concentration of zinc ions in the solution by means of the theoretical model of transition of the electrode surface to the critical state demonstrated that the dissolution of zinc from Cu$_5$Zn$_8$ is most probably limited by the stage of non-stationary solid-phase diffusion.

3. The study determined that the rate and effective rate constant for the phase transformation during the overcritical anodic dissolution of the intermetallic compound Cu$_5$Zn$_8$ increase significantly with the growth of the anodic potential. The regression analysis of the nucleation dependencies using several deterministic models of heterogeneous three-dimensional nucleation demonstrated that copper phase formation is controlled by the surface diffusion towards the three-dimensional nucleus of the new phase with instantaneous nucleation.

Acknowledgements

The results of the SEM, EDX, and X-ray diffractometry studies were obtained using the
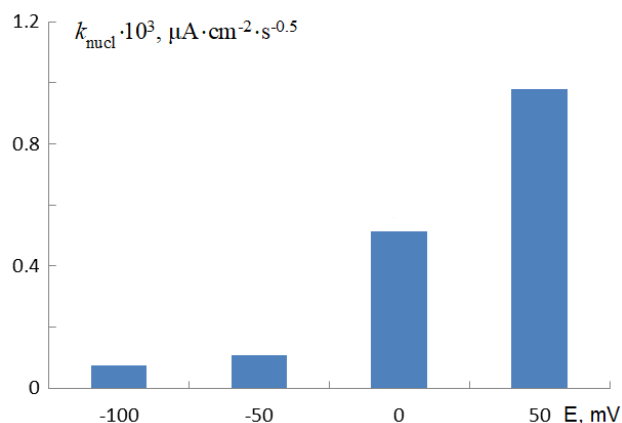
Fig. 8. Dependence of the effective rate constant of the phase transformation during selective dissolution of Cu$_5$Zn$_8$ in a 0.05 M CH$_3$COOH + 0.05 M CH$_3$COONa solution on the anodic potential

equipment of the Centre for Collective Use of Scientific Equipment of Voronezh State University (http://ckp.vsu.ru).

Conflict of interests

The authors declare that they have no known competing financial interests or personal relationships that could have influenced the work reported in this paper.

References

1. Francis R. *Corrosion of Copper and its Alloys – A Practical Guide for Engineers*. Houston (USA): NACE International, 2010. 388 p.

2. Troiani H. E., Baruj A. In situ optical microscopy study of a phase transformation induced by the dezincification of beta Cu–Zn. *Materials Science and Engineering A*. 2007;454–455: 441-445. DOI: https://doi.org/10.1016/j.msea.2006.11.092

3. Sun Y., Ren Y. New preparation method of porous copper powder through vacuum dealloying. *Vacuum*. 2015;122(A): 215–217. DOI: https://doi.org/10.1016/j.vacuum.2015.09.031

4. Sun Y., Ren Y., Yang K. New preparation method of micron porous copper through physical vacuum dealloying of Cu–Zn alloys. *Materials Letters*. 2016;165: 1–4. DOI: https://doi.org/10.1016/j.matlet.2015.11.102

5. Murzin S. P. Razrabotka sposobov intensifikatsii formirovaniya nanoporistykh struktur metallicheskikh materialov selektivnoi lazernoi sublimatsiei komponentov splavov [Development of methods for intensifying the formation of nanoporous structures of metallic materials by selective laser sublimation of alloy components]. *Komp'yuternaya optika [Computer Optics]*. 2011;35(2): 175–179. Available at: https://

www.elibrary.ru/download/elibrary_16372944_92770669.pdf(In Russ.)

6. Murzin S. P. Opredelenie uslovii obrazovaniya nanoporistykh struktur metallicheskikh materialov lazernym vozdeistviem [Determination of the conditions for the formation of nanoporous structures of metallic materials by laser exposure]. *Vestnik Samarskogo gosudarstvennogo aerokosmicheskogo universiteta im. akademika S. P. Koroleva (natsional'nogo issledovatel'skogo universiteta) [Vestnik of Samara University: Aerospace and Mechanical Engineering].* 2014;5-2(47): 67–74. Available at: https://www.elibrary.ru/download/elibrary_24041234_92964303.pdf(In Russ.)

7. Landolt D. *Corrosion and surface chemistry of metals*. Lausanne (Switzerland): EPFL Press, 2007. 632 p.

8. Marshakov I. K. *Termodinamika i korroziya splavov [Thermodynamics and corrosion of alloys]*. Voronezh: izd-vo Voronezh. un-ta, 1983. 168 p. (In Russ.).

9. Marshakov I. K., Vvedenskii A. V., Kondrashin V. Yu., Bokov G. A. *Anodnoe rastvorenie i selektivnaya korroziya splavov [Anodic dissolution and selective corrosion of alloys]*. Voronezh: izd-vo Voronezh. un-ta, 1988. 208 p. (In Russ.)

10. Selvaraj S., Ponmariappan S., Natesan M., Palaniswamy N. Dezincification of brass and its control: an overview. *Corrosion Reviews*. 2003;21(1): 41–74. DOI: https://doi.org/10.1515/CORRREV.2003.21.1.41

11. Revie R. W. *Uhlig's Corrosion Handbook*. Hoboken (USA): Wiley, 2011. 1296 p. DOI: https://doi.org/10.1002/9780470872864

12. Burzyńska L., Maraszewska A., Zembura Z. The corrosion of Cu-47.3 at% Zn brass in aerated 1.0 M HCl. *Corrosion Science*. 1996;38(2): 337–347. DOI: https://doi.org/10.1016/0010-938X(96)00132-1

13. Sohn S., Kang T. The effects of tin and nickel on the corrosion behavior of 60Cu-40Zn alloys. *J. Alloys Compounds*. 2002;335(1-2): 281–289. DOI: https://doi.org/10.1016/S0925-8388(01)01839-4

14. Assouli B., Srhiri A., Idrissi H. Characterization and control of selective corrosion of α, β'-brass by acoustic emission. *NDT & E International*. 2003;36(2): 117–126. DOI: https://doi.org/10.1016/S0963-8695(02)00102-0

15. Newman R. C. *Dealloying. In book: Shreir's Corrosion*. Oxford: Elsevier, 2010. P. 801–809. DOI: https://doi.org/10.1016/b978-044452787-5.00031-7

16. Erlebacher J. *Dealloying of binary alloys evolution of nanoporosity. In book: Dekker encyclopedia of nanoscience and nanotechnology (chapter 320)*. N.-Y. (USA): CRC Press, 2004. P. 893–902. DOI: https://doi.org/10.1201/9781439834398.ch320

17. Qiu H.-J., Peng L., Li X., Xu H. T., Wang Y. Using corrosion to fabricate various nanoporous metal structures. *Corrosion Science*. 2015;92: 16–31. DOI: https://doi.org/10.1016/j.corsci.2014.12.017

18. Marshakov I. K. Elektrokhimicheskoe povedenie i kharakter razrusheniya tverdykh rastvorov i intermetallicheskikh soedinenii [Electrochemical behaviour and the nature of the destruction of solid solutions and intermetallic compounds]. *Korroziya i zashchita ot korrozii (Itogi nauki i tekhniki. T. 1) [Corrosion and corrosion protection (Results of science and technology. V. 1)]*. Moscow: VINITI, 1971. p. 138–155. (In Russ.)

19. Marshakov I. K., Bogdanov V. P. Mekhanizm izbiratel'noi korrozii mednotsinkovykh splavov [Mechanism of selective corrosion of copper-zinc alloys]. *Zhurn. fiz. khim.[J. Phys. Chem.]*. 1963;37(12): 2767–2769. (In Russ.)

20. Marshakov I. K., Vyazovikina N. V. Izbiratel'noe rastvorenie β-latunei s fazovym prevrashcheniem v poverkhhnostnom sloe [Selective dissolution of b-brass with phase transformation in the surface layer]. *Zashchita metallov [Protection of metals]*. 1978;14(4): 410–415. (In Russ.)

21. Zartsyn I. D., Vvedenskii A. V., Marshakov I. K. Nonequilibrium behavior of the surface-layer in anodic dissolution ofhomogeneous alloys. *Russian Jornal of Electrochemistry*. 1994;30(4): 544–565. Available at: https://elibrary.ru/item.asp?id=23828139

22. Zartsyn I. D., Vvedenskii A. V., Marshakov I. K. Conversions of the noble component during selective dissolution of anhomogeneous alloy in an active state. *Protection of Metals*. 1991;27(1): 3–12. Available at: https://elibrary.ru/item.asp?id=23951443

23. Zartsyn I. D., Vvedenskii A. V., Marshakov I. K. Thermodynamics of nonequilibrium phase conversion under selective dissolution of homogeneous binary alloys. *Protection of Metals*. 1991;27(6): 883–891. Available at: https://elibrary.ru/item.asp?id=12712615

24. Pickering H. W., Byrne P. J. On preferential anodic dissolution of alloys in the low-current region and the nature of the critical potential. *J. Electrochem. Soc*. 1971;118(2): 209–215. DOI: https://doi.org/10.1149/1.2407969

25. Pickering H. W., Byrne P. J. Partial currents during anodic dissolution of Cu–Zn alloys at constant potential. *J. Electrochem. Soc*. 1969;116(11): 1492–1496. DOI: https://doi.org/10.1149/1.2411582

26. Pickering H. W. Characteristic features of alloy polarization curves. *Corrosion Sci*. 1983;23(10): 1107–1120. DOI: https://doi.org/10.1016/0010-938X(83)90092-6

27. Kozaderov O. A., Vvedenskii A. V. *Massoperenos i fazoobrazovanie pri anodnom selektivnom rastvorenii gomogennykh splavov [Mass transfer and phase formation during anodic selective dissolution of homogeneous alloys]*. Voronezh: Nauchnaya kniga, 2014. 287 p. (In Russ.)

28. Wyckoff R. W. G. *Crystal Structures. Vol. 1*. N.-Y. (USA): Interscience Publishers, 1963. p. 7–83.

29. Galyus Z. *Teoreticheskie osnovy elektro-khimicheskogo analiza [Theoretical Foundations of Electrochemical Analysis]*. Moscow: Mir, 1974. 256 p. (In Russ.)

Information about the authors

Oleg A. Kozaderov, DSc in Chemistry, Associate professor, Head of the Department of Physical Chemistry, Faculty of Chemistry, Voronezh State University, Voronezh, Russian Federation; e-mail: ok@chem.vsu.ru. ORCID iD: https://orcid.org/0000-0002-0249-9517.

Dmitrii M. Taranov, student, Department of Physical Chemistry, Faculty of Chemistry, Voronezh State University, Voronezh, Russian Federation; e-mail: taranovdm@list.ru. ORCID iD: https://orcid.org/0000-0003-0993-3707.

Aleksander N. Krivoslykov, postgraduate student, Department of Physical Chemistry, Faculty of Chemistry, Voronezh State University, Voronezh, Russian Federation; e-mail: alexdwatson@mail.ru. ORCID iD: https://orcid.org/0000-0001-7646-6841.

Sofia V. Borodkina, student, Department of Physical Chemistry, Faculty of Chemistry, Voronezh State University, Voronezh, Russian Federation; e-mail: boro-sonya@yandex.ru. ORCID iD: https://orcid.org/0000-0003-4676-261X.

All authors have read and approved the final manuscript.

Translated by Yulia Dymant
Edited and proofread by Simon Cox

Original articles

Obtaining Iron (III) – Containing Triple Molybdate $K_5FeZr(MoO_4)_6$ by Sol-Gel Technology

© 2020 A. V. Logvinova✉,[a], B.G. Bazarov[a,b], J. G. Bazarov[a]

[a]Baikal Institute of Nature Management, Siberian Branch of the Russian Academy of Sciences,
6 ul. Sakhyanova, Ulan-Ude 670047, Republic of Buryatia, Russian Federation

[b]Buryat State University,
24a ul. Smolina, Ulan-Ude 670000, Republic of Buryatia, Russian Federation

Abstract

Oxide compounds, as the basis of promising materials, are used in various fields of modern technologies due to their electrical and optical properties. Some of them, possessing a combination of ferroelectric, scintillation, electrical, and optical properties, are being studied as promising materials for electronics. In this case, their dispersion plays an important role.

Traditionally, the synthesis of oxide compounds is carried out by ceramic technology. More promising for the synthesis of fine powders are the methods of "soft" chemistry, among which we have identified and applied the sol-gel method. In this method, "mixing" occurs at the molecular level, which contributes to an increase in the reaction rates and a decrease in the synthesis temperature. The method involves the use of inorganic salts as precursors in combination with complexing agents (citric acid). The use of such precursors allows one to achieve high uniformity at relatively low temperatures. A feature of this approach is the use of fewer organic compounds: an aqueous solution of citric acid is used as a chelating agent. The aim of this work was to obtain triple molybdate by sol-gel technology (SGT) based on the example of iron-containing potassium zirconium molybdate.

The iron-containing triple potassium zirconium molybdate was obtained using the of citrate sol-gel technology and solid-phase synthesis (SPS) methods. The triple molybdate obtained by two methods was characterized by X-ray phase analysis, DSC, and impedance spectroscopy.

The developed sol-gel synthesis technique allowed lowering the synthesis temperature, to obtain triple molybdate with high values of homogeneity, dispersion, and electrical conductivity. This technique can be used to obtain double and triple zirconium (hafnium) molybdates containing a trivalent cation.

Keywords: iron-containing, triple molybdate, zirconium, potassium series, sol-gel synthesis.

✉ Alexandra V. Logvinova, e – mail: logvinova_alexsandra@bk.ru

1. Introduction

Molybdates of different valence elements are of interest due to their ion-conducting [1–7] and luminescent properties [8–15]. The methods developed to date for obtaining new promising molybdates are very diverse [16-18]. The most common method for the preparation of triple molybdates is solid-phase synthesis, which is characterized by the simplicity of the experiment. The main disadvantage of this method is the high temperature and duration of the synthesis. An alternative methods are the so-called "soft chemistry" or solution methods: sol-gel, precipitation from aqueous solutions, etc. Solution methods allow obtaining nanoscale objects and significantly reduce both the temperature and the duration of synthesis.

Now, special attention is paid to finely dispersed and nanodispersed materials. The reduction of the particle size of the compounds allows to obtain materials with unique properties (optical, ion-conducting, etc.).

The aim of this work was to obtain triple molybdate by solid-phase synthesis (SPS) and sol-gel technology (SGT) using the example of iron-containing potassium zirconium molybdate.

2. Experimental

For the synthesis of triple molybdate K$_5$FeZr(MoO$_4$)$_6$ we have developed a sol-gel method based on a citrate gel. Potassium nitrate KNO$_3$, iron nitrate Fe(NO$_3$)$_3$·9H$_2$O (CP) , zirconyl nitrate ZrO(NO$_3$)$_2$·2H$_2$O and ammonium paramolybdate (NH$_4$)$_6$Mo$_7$O$_{24}$·4H$_2$O were used as starting materials, citric acid was used as a complexing agent. The sol-gel synthesis scheme is shown in Fig. 1. Stoichiometric amounts of the source components were dissolved in distilled water.

Prepared solutions of potassium and iron nitrates, zirconium and ammonium paramolybdate were added to the citric acid solution with the formation of metal-citrate complex. The resulting solution was evaporated at a temperature of 70–80 °C until the solution passed into a sol and then into a gel. The resulting gel, which was a translucent mass, was first dried in the oven at a temperature of ~100–150 °C until the water was completely removed, and then it was dried in the furnace at a temperature of 200 °C for the conversion into a xerogel. Xerogel was an amorphous mass that was easily ground into powder in a mortar. Molybdate powders K$_5$FeZr(MoO$_4$)$_6$ (no.1) were obtained after annealing in the furnace at a temperature of 500–550 ° C.

Along with the synthesis of K$_5$FeZr(MoO$_4$)$_6$ using sol-gel technology, this molybdate was obtained using ceramic technology.

For solid-phase synthesis, commercial reagents K$_2$MoO$_4$ (CP), Fe(NO$_3$)$_3$·9H$_2$O (CP), MoO$_3$ (P.A.) and ZrO(NO$_3$)$_2$·2H$_2$O (P.A.) were used the starting materials. Molybdate Fe$_2$(MoO$_4$)$_3$ was obtained by solid-phase synthesis from molybdenum trioxide and iron nitrate by annealing at 400–800 °C for
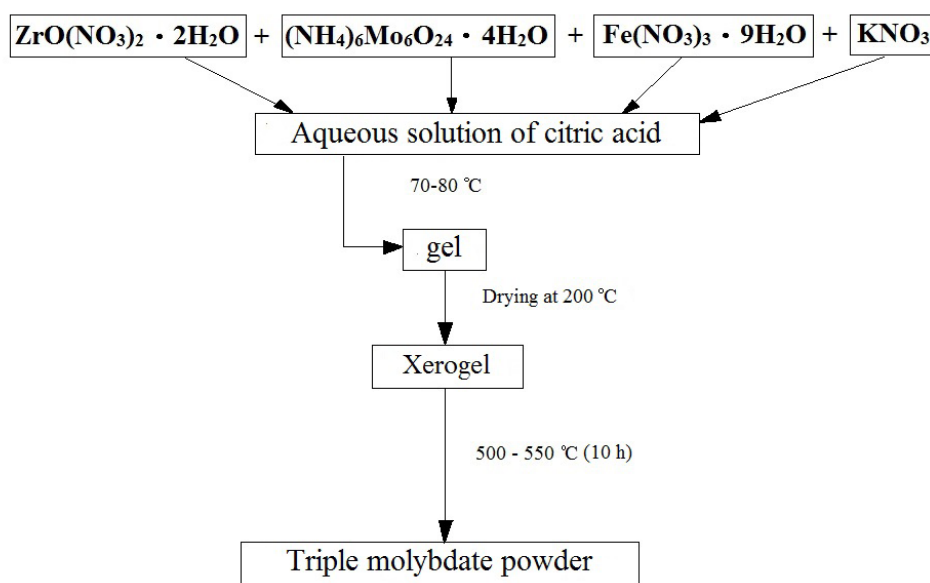
Fig. 1. Sol-gel synthesis scheme

150 h and intermediate homogenization of the samples. Synthesis of $Zr(MoO_4)_2$ was carried out according to the solid-phase method by stepwise annealing of a stoichiometric mixture of zirconyl nitrate and molybdenum trioxide in the temperature range of 450–750 °C for 100–150 h. Triple molybdate $K_5FeZr(MoO_4)_6$ (sample no. 2) was obtained using ceramic technology by annealing stoichiometric amounts of reaction mixtures K_2MoO_4, $Fe_2(MoO_4)_3$ and $Zr(MoO_4)_2$ in the temperature range 400–550 °C with a stepwise increase in temperature with a step of 50 °C and homogenization before each change in the heat treatment mode.

The powders of samples 1 and 2 obtained after annealing were studied by X-ray diffraction analysis (XRD) on a D8 Advance diffractometer (Bruker) using Cu$K\alpha$ radiation.

The diffractogram of the synthesized molybdate sample no. 2 (solid-phase synthesis) coincides with the diffractogram of the powder of sample no. 1 (sol-gel method).

Thermal analysis was performed on a NETZSCH STA 449 F1 Jupiter device. The recording was carried out in an argon atmosphere in platinum crucibles.

Electron microscopic studies of the samples were performed using a scanning electron microscope "Hitachi-3400N". The accelerating voltage was 20 keV, the operating distance was 10 mm.

3. Results and discussion

The diffractogram (no. 2) obtained during X-ray phase analysis $K_5FeZr(MoO_4)_6$ is shown in Fig. 2.

According to XRD data, synthesized molybdate $K_5FeZr(MoO_4)_6$ (sample no. 2) was isostructural to triple molybdate $Rb_5FeHf(MoO_4)_6$ [19] and crystallizes in the hexagonal system $P6_3$, Z = 2. The identification of parameters of the unit cells of the obtained phases was performed using single crystal data of the isostructural compound. The calculation was carried out according to the uniquely indexed lines of powder XRD patterns of triple molybdate using the TOPAS 4.2 software package. The parameters of unit cells are presented in the Table.

The thermal characteristics of the obtained compounds were studied by differential scanning calorimetry (DSC) in the temperature range 25–750 °C using NETZSCH STA 449 F1 Jupiter device. On the DSC curves of molybdate (sample no. 2) (Fig. 3), two endothermic effects were recorded. The first endothermic effect should be attributed to the presence of a polymorphic transition in the sample. The second endothermic effect on the DSC curves corresponded to the melting point. The compound melted incongruently. The same effects were recorded for molybdate (sample no. 1).

The morphology of the products was studied using scanning electron microscopy, which allowed estimating the particle size.

Fig. 2. The results of processing X-ray diffraction pattern of sample no. 2 of the composition $K_5FeZr(MoO_4)_6$ using the TOPAS 4.2 software package: blue line – experimental data; red line – calculated profile; strokes correspond to interplanar distances; the curve below is the difference between the experimental and calculated values

Table. Crystallographic and thermal characteristics of $K_5FeZr(MoO_4)_6$ (sample no. 2)

Compound	Unit Cell Parameters			T phase change	T melting
	a, Å	c, Å	V, Å³		
$K_5FeZr(MoO_4)_6$	10.088(1)	15.089(1)	1330.0(3)	554	668

Fig. 3. DSC curve for $K_5FeZr(MoO_4)_6$ sample (no. 2)

Electron microscopic examination of samples $K_5FeZr(MoO_4)_6$ obtained by solid-phase synthesis showed that the compounds are spherical particles with sizes from ~ 1 to ~ 6 μm. Samples of $K_5FeZr(MoO_4)_6$ obtained by sol-gel technology, consist of spherical particles with sizes from ~ 0.2. up to ~ 4 mm as can be seen on microphotographs (Fig. 4).

Temperature and frequency conductivity dependencies of $K_5FeZr(MoO_4)_6$ (sample no. 1) was investigated in the temperature range 473–863 K using a "Z-1500J" impedance meter in heating and cooling modes (2 K/min) at a frequency in the range of 1 Hz – 1 MHz.

Molybdate $K_5FeZr(MoO_4)_6$ was obtained by two methods in the form of a powder was compressed under pressure into tablets in the form of disks with the diameter of 10 mm and thickness of 1–2 mm. These tablets were annealed at 550–600 °C for 10 h. Electrodes were applied to the surface of the disks by firing with platinum paste before measurements. The temperature dependence of the conductivity $K_5FeZr(MoO_4)_6$ (sample no. 1) in Arrhenius coordinates is shown in Fig. 5. When the sample is heated, an abrupt increase in conductivity occurred in the phase transition region (880–900 K), reaching a value of $10^{-2.5}$ S/cm, which is an order of magnitude higher than the conductivity of $K_5FeZr(MoO_4)_6$ (sample no. 2), obtained by solid-phase synthesis (Fig. 6).
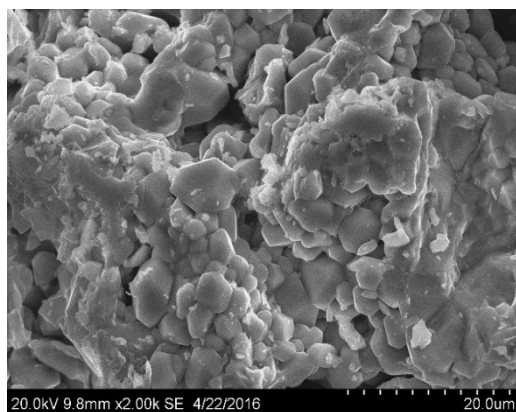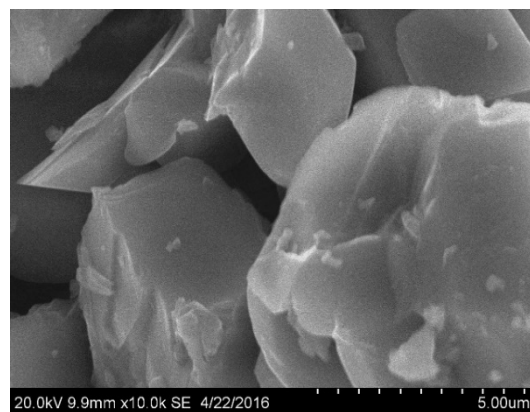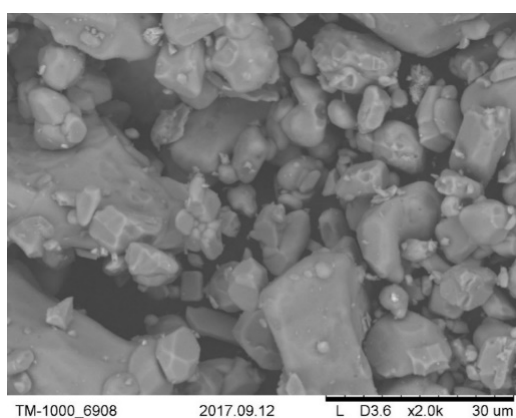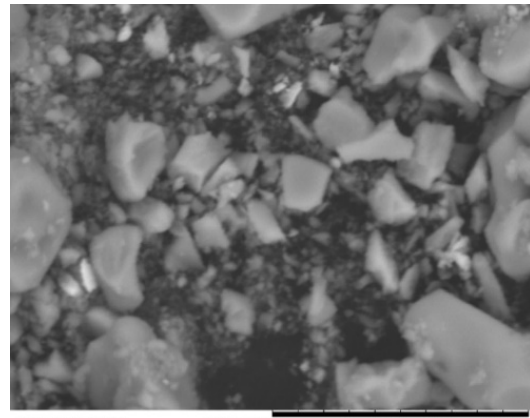
Fig. 4. Microphotographs of $K_5FeZr(MoO_4)_6$ samples obtained solid-phase synthesis (a, b) and sol-gel technology (c, d)
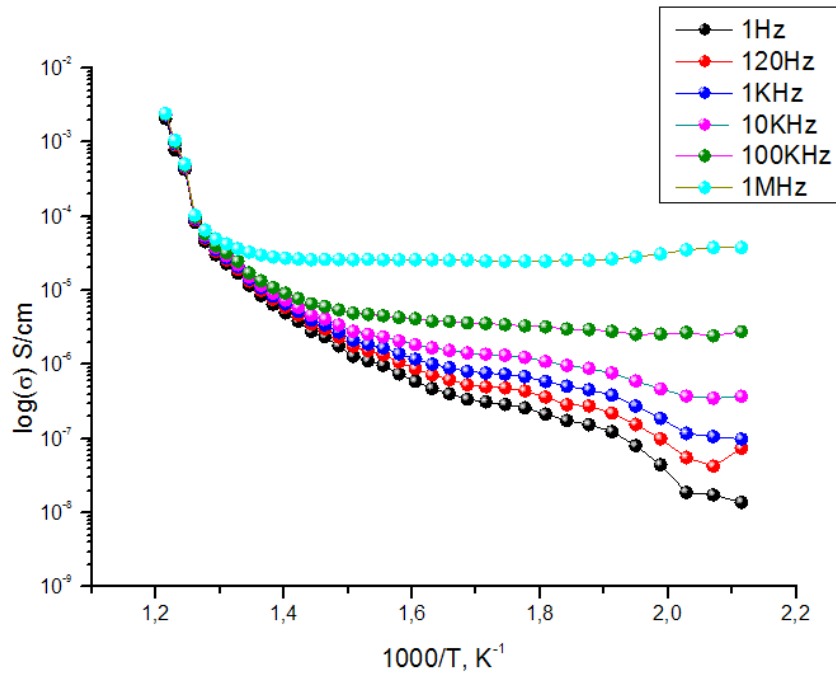
Fig. 5. Temperature dependence of conductivity $K_5FeZr(MoO_4)_6$ (sample no. 1) obtained by sol-gel technology
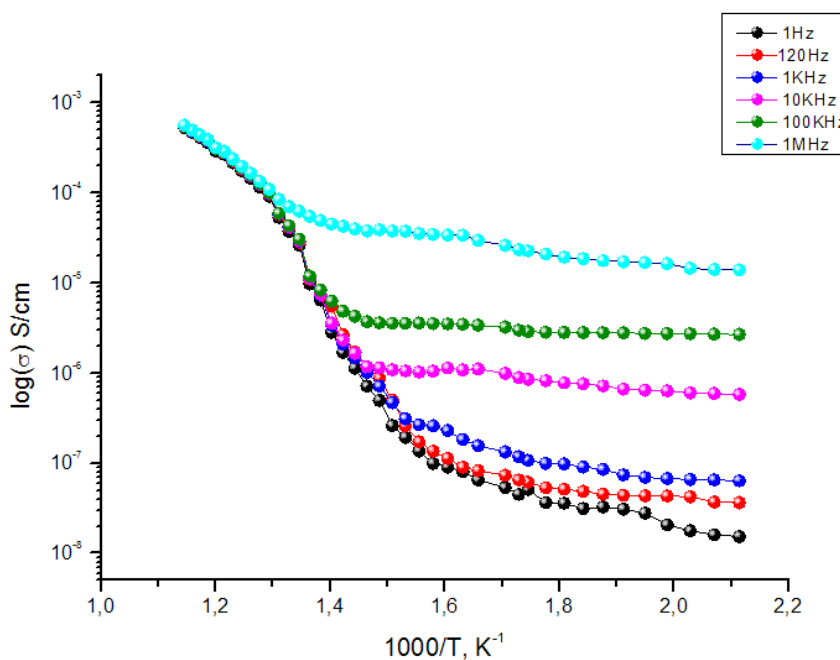
Fig. 6. A fragment of the temperature-frequency dependence of the conductivity $K_5FeZr(MoO_4)_6$ (sample no. 2) obtained by solid-phase synthesis

4. Conclusions

A sol-gel method for the synthesis of triple molybdates $M_5RZr(MoO_4)_6$ (R = trivalent metals) based on the for example of $K_5FeZr(MoO_4)_6$ was developed. Iron-containing triple molybdate was obtained by two methods: ceramic and sol-gel technology.

Studies of the obtained molybdates by X-ray diffraction analysis, DSC, electron microscopy, and impedance spectroscopy showed that the compounds crystallize in the hexagonal syngony, in the space group $P6_3$, $Z = 2$, undergoing a phase transition at 554 °C and melt incongruently at 668 °C. The molybdate obtained by the sol-gel

technology consists of particles with sizes from ~ 0.2 to ~ 4 μm. The developed technique for the synthesis of sol-gel technology, in comparison with ceramic technology, allows not only to reduce the synthesis temperature, but also to obtain compounds in a nanodispersed state with high electrical conductivity. The electrical conductivity of this molybdate is an order of magnitude higher than the conductivity of molybdate obtained by ceramic technology.

Acknowledgements

Conflict of interest

The authors declare that they have no known competing financial interests or personal relationships that could have influenced the work reported in this paper.

References

1. Sorokin N. I. Ionic conductivity of $KMgCr(MoO_4)_3$ molybdate. *Crystallography Reports*. 2017;62(3): 416–418. DOI: https://doi.org/10.1134/s106377451703021x

2. Pavlova Je. T., Cyrenova G. D., Lazorjak B. I., Solodovnikov S. F. Structure and properties of double silver-containing molybdates of the composition $Ag_2A_2(MoO_4)_3$ (A = Mg, Mn, Cu). *BSU bulletin. Chemistry. Physics*. 2015;3: 3–7. Available at: https://elibrary.ru/item.asp?id=23233672 (In Russ., abstract in Eng.)

3. Savina A. A., Solodovnikov S. F., Belov D. A., Basovich O. M., Solodovnikova Z. A., Pokholok K. V., Stefanovich S. Yu., Lazoryak B. I., Khaikina E. G. Synthesis, crystal structure and properties of alluaudite-like triple molybdate $Na_{25}Cs_8Fe_5(MoO_4)_{24}$. *Journal of Solid State Chemistry*. 2014;220: 217–220. DOI: https://doi.org/10.1016/j.jssc.2014.09.004

4. Jena P., Nallamuthua N., Patro P. K., Venkateswarlu M., Satyanarayana N. Structural characterization and electrical conductivity studies of $BaMoO_4$ nanorods prepared by modified acrylamide assisted sol–gel process. *Advances in Applied Ceramics*. 2014;113(6): 372–379. DOI: https://doi.org/10.1179/1743676114Y.0000000170

5. Balsanova L. V. The synthesis of crystals of silver oxide phases based on molybdenum, investigation of their structure and properties. *Vestnik VSGUTU*. 2015;5(56). 63–69. Available at: https://vestnik.esstu.ru/arhives/VestnikVsgutu5_2015.pdf (In Russ., abstract in Eng.)

6. Dorzhieva S. G., Bazarov B. G., Bazarova Zh. G. New molybdates in Rb_2MoO_4-MI_2MoO_4-$Zr(MoO_4)_2$ (MI = Na, K) systems as promising ion-conducting materials. *Letters on Materials*. 2019;9(1): 17–21. DOI: https://doi.org/10.22226/2410-3535-2019-1-17-21 (In Russ., abstract in Eng.)

7. Spiridonova T. S., Solodovnikov S. F., Savina A. A., Kadyrova Y. M., Solodovnikova Z. A., Yudin V. N., Stefanovich S. Y. and. Khaikina E. G. New triple molybdate $Rb_2AgIn(MoO_4)_3$: synthesis, framework crystal structure and ion-transport behavior. *Acta Crystallographica C Structural Chemistry*. 2018;74(12): 1603–1609. DOI: https://doi.org/10.1107/S2053229618014717

8. Lim C. S., Aleksandrovsky A. S., Molokeev M. S., Oreshonkov A. S., Ikonnikov D. A. and Atuchin V. V. Triple molybdate scheelite-type upconversion phosphor $NaCaLa(MoO_4)_3$: Er^{3+}/Yb^{3+}: structural and spectroscopic properties. *Dalton Transactions*. 2016;45(39): 15541–15551. DOI: https://doi.org/10.1039/C6DT02378A

9. Dorzhieva S. G., Tushinova Y. L., Bazarov B. G., Bazarova Z. G., Nepomniashchikh A. I., Shendrik R. Y. Luminescence of Ln-Zr molybdates. *Bulletin of the Russian Academy of Sciences: Physics*. 2015;79(2): 276–279. DOI: https://doi.org/10.3103/S1062873815020070

10. Liao J., Zhou D., Yang B., Liu R., Zhang Q. and Zhou Q. H. Sol-gel preparation and photoluminescence properties of $CaLa_2(MoO_4)_4$: Eu^{3+} phosphors. *Journal of Luminescence*. 2013;134: 533–538. DOI: https://doi.org/10.1016/j.jlumin.2012.07.033

11. Kozhevnikova N. M. Synthesis and luminescence properties of a $Li_3Ba_2La_3(MoO_4)_8$: Er^{3+} phosphor with a scheelite-like structure. *Inorganic Materials*. 2019;55(6): 607–611. DOI: https://doi.org/10.1134/s0020168519060098

12. Sofich D., Shendrik R. Y., Dorzhieva S. G., Chimitova O. D., Bazarov B. G., Tushinova Y. L., Bazarova Z. G. Luminescence of Pr^{3+} and Nd^{3+} ions in double molybdates. *Physics of the Solid State*. 2019;61(5): C. 844-846. DOI: https://doi.org/10.1134/s1063783419050342

13. Guo C., Yang H.K., Jeong J.-H. Preparation and luminescent properties of phosphor $MgD_2(MoO_4)_4$: Eu^{3+} (M=Ca, Sr, and Ba). *Journal of Luminescence*. 2010;130(8): 1390–1393 DOI: https://doi.org/10.1016/j.jlumin.2010.02.052

14. Liao C., Cao R., Wang W., Hu W., Zheng G., Luo Z. and Liu P. Photoluminescence properties and energy transfer of $NaY(MoO_4)_2$: R (R = Sm^{3+}/Bi^{3+}, Tb^{3+}/Bi^{3+}, Sm^{3+}/Tb^{3+}) phosphors. *Materials Research Bulletin*. 2018;97: 490–496. DOI: https://doi.org/10.1016/j.materresbull.2017.09.053

15. Song M., Liu Y., Liu Y., Wang L., Zhang N., Wang X., Huang Z., Ji C. Sol-gel synthesis and luminescent properties of a novel $KBaY(MoO_4)_3$: Dy^{3+} phosphor for white light emission. *Journal of Luminescence.* 2019; 211: 218–226. DOI: https://doi.org/10.1016/j.jlumin.2019.03.052

16. Grossman V. G., Bazarova J. G., Molokeev M. S. and Bazarov B. G. New triple molybdate $K_5ScHf(MoO_4)_6$: Synthesis, properties, structure and phase equilibria in the $M_2MoO_4–Sc_2(MoO_4)_3–Hf(MoO_4)_2$ (M = Li, K) systems. *Journal of Solid State Chemistry.* 2020;283: 121143. DOI: https://doi.org/10.1016/j.jssc.2019.121143

17. Bazarova Zh. G., Grossman V. G., Bazarov B. G., Tushinova Yu. L., Chimitova O. D., Bazarova Ts. T. Phase diagrams for the M_2MoO_4-$Ln_2(MoO_4)_3$-$Hf(MoO_4)_2$ systems, where M = Li-Cs, Tl and Ln = La-Lu. *Chimica Techno Acta.* 2017;4(4): 224–230. DOI: https://doi.org/10.15826/chimtech/2017.4.4.03

18. Braziulis G., Janulevicius G., Stankeviciute R., Zalga A. Aqueous sol–gel synthesis and thermoanalytical study of the alkaline earth molybdate precursors. *Journal of Thermal Analysis and Calorimetry.* 2014;118(2): 613–621. DOI: https://doi.org/10.1007/s10973-013-3579-0

19. Bazarov B. G., Klevcova R. F., Cyrendorzhieva A. D., Glinkaja L. A., Bazarova Zh. G. Crystal structure of triple molybdate $Rb_5FeHf(MoO_4)_6$ – a new phase in the Rb_2MoO_4 - $Fe_2(MoO_4)_3$ - $Hf(MoO_4)_2$ system. *Journal of Structural Chemistry.* 2004;45(6); 993–998. DOI: https://doi.org/10.1007/s10947-005-0091-9

Information about the authors

Aleksandra V. Logvinova, PhD student, Laboratory of Oxide Systems, Baikal Institute of Nature Management, Siberian Branch of the Russian Academy of Sciences (BINM SB RAS), Ulan-Ude, Russian Federation; e-mail: Logvinova_Alexsandra@bk.ru. ORCID iD: https://orcid.org/0000-0001-9850-2719.

Bair G. Bazarov, DSc in Physics and Mathematics, Leading Researcher, Laboratory of Oxide Systems, Baikal Institute of Nature Management, Siberian Branch of the Russian Academy of Sciences (BINM SB RAS), Associate Professor at the Department of Inorganic and Organic chemistry, Banzarov Buryat State University, Ulan-Ude, Russian Federation; e-mail: bazbg@rambler.ru. ORCID iD: https://orcid.org/0000-0003-1712-6964.

Jibzema G. Bazarova, DSc in Chemistry, Chief Scientist, Laboratory of Oxide Systems, Baikal Institute of Nature Management, Siberian Branch of the Russian Academy of Sciences (BINM SB RAS), Ulan-Ude, Russian Federation; e-mail: jbaz@binm.ru. ORCID iD: https://orcid.org/0000-0002-1231-0116....

All authors have read and approved the final manuscript.

Translated by Valentina Mittova
Edited and proofread by Simon Cox

Quantum Chemical Modelling of the Scandium Sub-Group Metal Endofullerenes

© 2020 D. A. Machnev✉, I. V. Nechaev, A. V. Vvedenskii, O. A. Kozaderov

Voronezh State University,
1 Universitetskaya pl., Voronezh 394018, Russian Federation

Abstract

Endofullerenes with one or several metal atoms inside the carbon cage (metallofullerenes) are of considerable practical interest as promising basic materials for creating highly effective contrasting agents for magnetic resonance imaging (MRI) as well as antioxidant and anticancer drugs. These compounds can also be used in spintronics to build nanoscale electronic devices. In the framework of the density functional theory, this work presents a calculation of the structural, electronic, and thermodynamic characteristics of scandium sub-group metal endofullerenes with the number of encapsulated atoms from one to seven in the gaseous phase. The stable structures with symmetries C_s, C_2, C_3, and C_i, were described. They correspond to the positions of the metal atoms inside the fullerene cage. The theoretical limit for the number of metal atoms at which the endofullerene structure remains stable is six atoms for scandium, four for yttrium, and three for lanthanum. The calculations showed that the most stable structures are the ones with two and three encapsulated atoms. The relationship between the number of encapsulated atoms and the nature of electron density distribution were described. The total charge on the encapsulated metal cluster is positive for $Me@C_{60} - Me_3@C_{60}$ compounds, weakly positive for $Me_4@C_{60}$ (some of the atoms have negative charge), and negative for $Me_5C_{60} - Me_6@C_{60}$ compounds. The spin leakage effect was described for the structures with a doublet spin state. As for the endofullerenes with three and more encapsulated atoms, this effect is insignificant, which makes the creation of contrasting agents for MRI based on them impractical.

Keywords: endofullerenes, metallofullerenes, quantum chemical calculations, density functional theory, molecular symmetry, spin leakage.

1. Introduction

Discovered in 1985, during experiments dedicated to the study of circumstellar space [1], fullerenes have greatly influenced the development of materials science, nanotechnologies, and instrument engineering, as well as biology and medicine. The interest in these compounds has brought together such different areas of natural science as pharmaceutical and medicinal chemistry, solid-state physics, organic chemistry, and geology. By the beginning of the 1990s, only 5 years after the discovery of these nanomaterials, a large amount of data was collected on structural, chemical, and physicochemical properties of fullerenes, and the methods of their synthesis, fractionation, and purification were developed [2].

Unique chemical properties of fullerenes offer great opportunities for obtaining new compounds and materials based on them through chemical modification of the carbon cage. There are methods of obtaining heterofullerenes,

---

✉ Dmitriy A. Machnev, e-mail: machnev.dmitry@gmail.com

products of substitution of one or several carbon atoms for heteroatoms, and exofullerenes, formed by chemical functionalisation of the carbon cage. A separate group in the large family of derivatives of fullerenes is comprised by endofullerenes containing separate atoms or atom clusters inside the carbon cage. Molecules of paramagnetic endofullerenes (as a rule, the structures containing encapsulated metal atoms) are characterised by preferential localisation of unpaired electrons on the atoms of carbon as part of the fullerene cage. This phenomenon, first theoretically predicted by A. L. Buchachenko [3] and later experimentally discovered for La@C_{82} [4], is called spin leakage. It allows such compounds to be considered as promising candidates for the creation of contrasting agents for NMR tomography as well as the creation of nanoscale electronic devices.

To date, a large amount of experimental data has been accumulated on the chemistry and physics of endohedral derivatives of fullerene C_{82}, while derivatives with a C_{60} cage have not been thoroughly studied due to the lack of sufficiently reliable methods of macroscale synthesis of such structures [5]. For this reason, the theoretical study of these compounds using the methods of quantum chemistry is especially valuable. *Ab initio* calculations can not only supplement and interpret the results of experimental research, but also provide fundamentally new information on the structural, spectral, and spin characteristics of endohedral cage structures.

2. Experimental

Modelling of scandium sub-group metal endofullerenes was performed within the framework of the density functional theory (DFT) using the programmes *Gaussian* 09 [6], *Orca* 3.0.3 [7], and *Priroda* 10 [8].

To choose a calculation scheme that can properly describe structural and energetic properties of the structures studied in this work, a preliminary calculation was performed for the values of standard enthalpy of atomisation of particles of carbides of the MeC_n (Me = Sc, Y, La; n = 2-6) scandium sub-group metals in the framework of the following calculation schemes (see Table 1). The results of the corresponding calculations are presented in the Table (Table 2).

The data presented in the Table 2 shows that scheme 3 allows obtaining the values of standard enthalpy of atomisation of the MeC_n particles that are the closest to the experimental data. Absolute error for the determination of this value does not exceed 94 kJ/mol.

Also, in the framework of each of the specified schemes, a calculation was performed for the following structural, spectral, and thermodynamic properties of fullerene C_{60}:

• r_{5-6} is the length of the C–C bond representing a common edge between five and six-membered cycles in the carbon cage of fullerene.

• r_{6-6} is the length of the C–C bond representing a common edge between two six-membered cycles.

• $\nu_1 - \nu_4$ are the oscillation frequencies recorded in the IR spectrum of fullerene.

• $\Delta_f H^0$ is the standard enthalpy of formation of fullerene in the state of the ideal gas by graphite.

The data obtained while testing the calculation schemes is presented in the Table (Table 3).

The following scheme was used to calculate the value of $\Delta_f H^0$:

$C_{(s)} \rightarrow C_{(v)}; \Delta H_{at}^{\ 0}$,
$60C_{(v)} \rightarrow C_{60(v)}; \Delta H_{calc}^{\ 0}$,
$60C_{(s)} \rightarrow C_{60(v)}; \Delta_f H^0$,
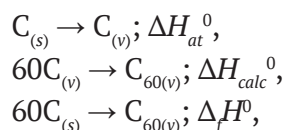
where $\Delta H_{at}^{\ 0}$ is the standard enthalpy of graphite atomisation (716.682 kJ/mol [14]), $\Delta H_{calc}^{\ 0}$ is the

Table 1. Tested Calculation Schemes

№	Functional	Basis Set for Carbon Atoms	Basis Set or Pseudopotential for Metal Atoms	Software Used for Calculation
1	B3LYP	D95(d, p)	SDD	Gaussian 09
2	mPW3PBE	D95(d, p)	SDD	Gaussian 09
3	mPW3PBE	DZP	DZP	Gaussian 09
4	PBE1PBE	D95(d, p)	SDD	Gaussian 09
5	PBE0	Def2-SVP	SDD	Orca 3.0.3
6	PBE	L1	L1	Priroda 10

Table 2. Standard Enthalpies of Atomisation of the MeCn Particles in the Gaseous Phase (Me = Sc, Y, La; n = 2–6)

Scheme	ΔH_{at}^0, kJ/mol						
	1	2	3	4	5	6	Experiment
ScC$_2$	1121	1170	1183	1160	1178	1284	1182 [9]
ScC$_3$	1645	1728	1748	1718	1773	1880	1777 [9]
ScC$_4$	2338	2432	2456	2425	2542	2621	2453 [9]
ScC$_5$	2896	3030	3057	3025	3173	3256	3131 [9]
ScC$_6$	3486	3642	3672	3638	3822	3907	3766 [9]
YC$_2$	1165	1210	1239	1206	1197	1310	1229 [10]
YC$_3$	1658	1740	1773	1736	1849	1881	1800 [9]
YC$_4$	2382	2475	2529	2472	2574	2658	2523 [9]
YC$_5$	2913	3044	3112	3044	3213	3270	3073 [9]
YC$_6$	3500	3644	3726	3644	3845	3919	3772 [9]
LaC$_2$	1217	1263	1286	1259	1287	1334	1259 [9]
LaC$_3$	1765	1851	1907	1850	1931	1946	1819 [11]
LaC$_4$	2453	2539	2597	2539	2655	2695	2515 [9]
LaC$_5$	3016	3151	3203	3153	3301	3315	3121 [11]
LaC$_6$	3601	3756	3802	3756	3940	3958	3757 [9]

Table 3. Calculated and Experimental Parameters of Fullerene C$_{60}$

Scheme	1	2	3	4	5	6	Experiment
r_{5-6}, pm	145.6	145.0	145.1	144.9	144.8	145.2	145.2 [12]
r_{6-6}, pm	140.0	139.6	139.7	139.4	139.4	139.7	139.7 [12]
v_1, sm^{-1}	521	522	523	527	536	522	527 [13]
v_2, sm^{-1}	586	593	595	598	600	577	576 [13]
v_3, sm^{-1}	1212	1230	1233	1241	1253	1183	1182 [13]
v_4, sm^{-1}	1466	1497	1497	1512	1515	1436	1429 [13]
$\Delta_f H^0$, kJ/mol	4082	2296	2405	2056	167	636	2530 [15]

enthalpy of formation of fullerene C$_{60}$ in the state of the ideal gas from gaseous (monoatomic ideal gas) carbon that was obtained during a computational experiment. Through a combination of corresponding thermochemical equations, the following expression was obtained for the calculation of $\Delta_f H^0$:

$$\Delta_f H^0 = 60\Delta H_{at}^0 + \Delta H_{calc}^0.$$

The presented data shows good reproducibility of geometric and spectral characteristics in the framework of the calculation scheme No.6 (values of the lengths of the C–C bonds correspond to the published data, deviations of oscillation frequencies do not exceed 7 cm^{-1}). However, none of the schemes allow obtaining the data corresponding to the experiment on the value of enthalpy of formation of fullerene (in the case of scheme No.3, the deviation $\Delta_f H^0$ is 125 kJ/mol, which is about 5%). Since all thermodynamic characteristics are highly important for the assessment of the stability of compounds, it was decided to use scheme No.3 for further calculations as the one that describes the modelled structures most adequately, although the value of oscillation frequencies is reproduced worse in this scheme (deviation v_4 from the experimental value is 68 cm^{-1}).

To determine the possible isomers of endohedral derivatives of fullerene C$_{60}$, many

structures were generated that are different in the position of the metal atoms inside the carbon cage of fullerene and then optimised. The absence of imaginary frequencies in the IR spectra of these compounds showed that the obtained structures corresponded to the minimum on the surface of PE foam. To evaluate the thermodynamic stability, the values of enthalpy $\Delta_f H^0$ and the Gibbs energy of the formation $\Delta_f G^0$ of the endofullerene $Me_n@C_{60}$ from graphite and the crystal of the corresponding metal were determined as follows:

$$60C_{(s)} + nMe_{(s)} \to Me_n@C_{60(v)}.$$
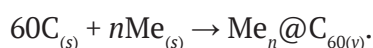
This characteristic was calculated using the reported data and the results of the computational experiment in the following way:

$$60C_{(s)} \to C_{60(v)}; \Delta_f H^0(C_{60(v)}), \Delta_f G^0(C_{60(v)}),$$
$$Me_{(s)} \to Me_{(v)}; \Delta H_{at}{}^0(Me), \Delta G_{at}{}^0(Me),$$
$$C_{60(v)} + nMe_{(v)} \to Me_n@C_{60(v)}; \Delta H_{calc}{}^0, \Delta G_{calc}{}^0,$$
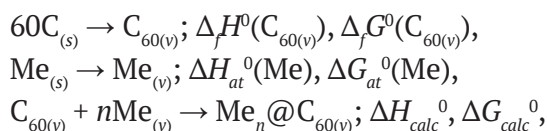
where $\Delta_f H^0(C_{60(v)})$ and $\Delta_f G^0(C_{60(v)})$ are standard enthalpy and Gibbs energy of formation of the gaseous fullerene C_{60} from graphite (2.530.0 and 2.474.5 kJ/mol [15]), $\Delta H_{at}{}^0(Me)$ and $\Delta G_{at}{}^0(Me)$ are atomisations of the corresponding metals (377.8 and 336.03 kJ/mol for scandium, 421.3 and 381.1 kJ/mol for yttrium, 431.0 and 393.56 for lanthanum [14]), $\Delta H_{calc}{}^0$ and $\Delta G_{calc}{}^0$ are corresponding calculation characteristics based on the results of quantum chemical modelling. Through a combination of these thermochemical equations, the following equations were obtained for the calculation of $\Delta_f H^0$ and $\Delta_f G^0$:

$$\Delta_f H^0 = \Delta_f H^0(C_{60(v)}) + n\Delta H_{at}{}^0(Me) + \Delta H_{calc}{}^0,$$
$$\Delta_f G^0 = \Delta_f G^0(C_{60(v)}) + n\Delta G_{at}{}^0(Me) + \Delta G_{calc}{}^0.$$

Enthalpy $\Delta H_b{}^0$ and Gibbs energy of encapsulation $\Delta G_b{}^0$ were used as another criterion of stability of endofullerenes. They quantitatively characterise energy costs for the process of the embedding of the originally formed cluster Me_n inside the carbon cage of fullerene, which occurs as follows:

$$Me_{n(v)} + C_{60(v)} \to Me_n@C_{60(v)}.$$
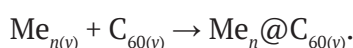
3. Results and discussion

3.1. Endofullerenes with one encapsulated atom

The results of the optimisation of the $Me@C_{60}$ structures indicate the absence of isomers for these compounds; the only possible structure

with the C_s symmetry is characterised by the location of the metal atom near one of the six-membered cycles in the fullerene structure (Fig. 1). The distance from the encapsulated metal atom to the nearest carbon atoms in the fullerene structure increases in the Sc < Y < La series (Table 4), which correlates with the ratio of covalent radii of these metals (144, 163, and 169 pm, respectively [14]). It should be noted that the sums of covalent radii of these metals and carbon are 221, 239, and 245 pm for scandium, yttrium, and lanthanum [14], which is 9–12 pm more than the greatest of the distances $r_i(Me-C_i)$, which is indicative of smaller covalent radii of these metals inside the carbon cage than in the corresponding crystal lattices. The basic doublet state is typical for these structures.
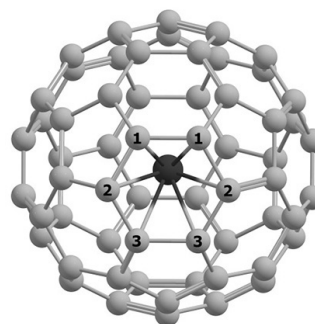
Fig. 1. Structure of the $Me@C_{60}$ (C_s) Endofullerenes

In the Sc > Y > La series (Table 4) a decrease of the values $\Delta_f H^0$ and $\Delta_f G^0$ was observed, which indicates the reduction of energy costs on the formation of corresponding endofullerenes in the series. It was also confirmed by negative values of enthalpy and encapsulation energies.

The process of formation of endofullerene is accompanied by redistribution of electron density between the penetrating metal atom and the carbon cage of fullerene. As the calculations show, the metal atom can obtain only a positive charge inside the fullerene cell in the $Me@C_{60}$ structures (Table 4), and there is no correlation between the value of this charge and the atomic number of the element: in the endofullerene $Y@C_{60}$ the metal atom has the highest charge (1.064 a.u.), $Sc@C_{60}$ has the lowest (0.577 a.u.), and an average value (0.865 a.u.) is typical for $La@C_{60}$.

The transfer of spin density from the encapsulated metal atom to the fullerene cage is also typical for the structures analysed in this section. In this case, a direct correlation is found

Table 4. Calculated Parameters for Endofullerenes of the Scandium Sub-Group with One Encapsulated Atom

	$Sc@C_{60}$	$Y@C_{60}$	$La@C_{60}$
Symmetry	C_s	C_s	C_s
$r(Me{-}C_1)$, pm	217	236	251
$r(Me{-}C_2)$, pm	224	240	254
$r(Me{-}C_3)$, pm	233	248	259
$\Delta_f H^0$, kJ/mol	2592	2540	2387
$\Delta_f G^0$, kJ/mol	2528	2478	2325
ΔH_b^0, kJ/mol	−315	−411	−575
ΔG_b^0, kJ/mol	−282	−378	−543
$Q(Me)$, a.u.	0.577	1.064	0.865
$S(C_{60})$	0.881	0.975	0.990

between the total spin density on the carbon cage and the atomic number of the element: the value $S(C_{60})$ is 0.881, 0.975, and 0.990 for $Sc@C_{60}$, $Y@C_{60}$, and $La@C_{60}$ respectively.

3.2. Endofullerenes with two encapsulated atoms

As opposed to endofullerenes with one encapsulated atom, there are isomers of $Me_2@C_{60}$ compounds and, particularly, of $Sc_2@C_{60}$. The calculation registered the presence of two types of structures in these compounds (Fig. 2):

A structure with the C_i symmetry, where the Me_2 cluster is located along the line connecting the centres of the opposite six-membered cycles in the structure of fullerene (Fig. 2.1), typical for $Y_2@C_{60}$ and the first isomer of $Sc_2@C_{60}$.

A structure with C_s symmetry, where the metal cluster is turned regarding the position described for the structure with C_i symmetry towards the edge that is common for two six-membered cycles (Fig. 2.2); this type of structure is typical for the second isomer of $Sc_2@C_{60}$ and $La_2@C_{60}$.
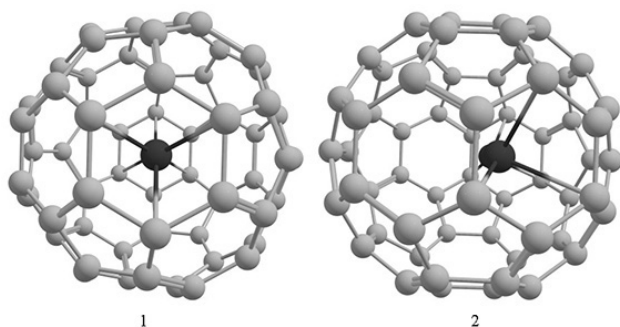
Fig. 2. Structure of the $Me_2@C_{60}$ Endofullerenes. C_i (1) and C_s (2) Symmetry

The basic singlet state is typical for the structures studied in this section.

As the calculation shows, during the encapsulation the length of the Me−Me bond increased by 20–65 pm depending on the nature of the metal (Table 5), and there was only a slight deformation of the carbon cage (the change in the lengths of the C−C bonds did not exceed 10 pm near the embedded atoms).

The values of $\Delta_f H^0$ and $\Delta_f G^0$ indicate a non-monotonic nature of the dependence of the enthalpy of formation of endofullerenes $Me_2@C_{60}$ on the nature of the metal: the formation of $Y_2@C_{60}$ is characterised by the greatest energy costs as compared to any isomers of $Sc_2@C_{60}$, while the formation of $La_2@C_{60}$ is more advantageous. On the contrary, the process of embedding a diatomic metal cluster inside a fullerene cell in the case of $Sc_2@C_{60}$ and $La_2@C_{60}$ is less preferable than for $Y_2@C_{60}$ (Table 5, ΔH_b^0, ΔG_b^0).

Just like for the structures described in the previous section, the transfer of electron density on the carbon cage from the encapsulated metal atoms is typical for $Me_2@C_{60}$. These atoms acquire a positive charge, which, in the case of $Y_2@C_{60}$, reaches 0.552 a.u. per atom. Since the basic singlet state is typical for the structures containing diatomic metal clusters inside a fullerene cell, the transfer of electron density on the carbon cage does not occur. Therefore, the values of total spin density on carbon atoms contained in fullerene for all the structures studied in this section are zero and are not presented in Table 5.

Table 5. Calculated Parameters for Endofullerenes of the Scandium Sub-Group with Two Encapsulated Atoms

	$Sc_2@C_{60}$ (1)	$Sc_2@C_{60}$ (2)	$Y_2@C_{60}$	$La_2@C_{60}$
Symmetry	C_i	C_s	C_i	C_s
r_0(Me–Me), pm	259	259	290	263
r(Me–Me), pm	324	310	310	290
$|r-r_0|$, pm	65	51	20	27
$\Delta_f H^0$, kJ/mol	2582	2594	2605	2393
$\Delta_f G^0$, kJ/mol	2517	2529	2547	2338
ΔH_b^0, kJ/mol	−640	−629	−689	−640
ΔG_b^0, kJ/mol	−593	−580	−635	−591
Q(Me), a.u.	0.254	0.234	0.552	0.512

3.3. Endofullerenes with three encapsulated atoms

The results of optimisation of geometry of the $Me_3@C_{60}$ compounds indicate the presence of isomers of $Sc_3@C_{60}$ и $La_3@C_{60}$, and the calculation shows the presence of two types of structures:

A structure with C_s symmetry, where a triatomic metal cluster is located along the line connecting the centres of two diametrical six-membered cycles (Fig. 3.1), typical for the first isomer of $Sc_3@C_{60}$ and the second isomer of $La_3@C_{60}$.

A structure with C_2 symmetry, where the Me_3 cluster is located along the line connecting the centres of two diametrical bicyclic fragments of C_{10} (Fig. 3.2); this structure was found in the second isomer of $Sc_3@C_{60}$, $Y_3@C_{60}$, and the first isomer of $La_3@C_{60}$.

The basic doublet state is typical for these structures.

As the calculation shows, triatomic clusters of the metals of the scandium sub-group are

shaped as an equiangular triangle both outside and inside the fullerene cell, so for the definitive description of their structures only one geometric parameter, the length of one of the Me–Me bonds, is sufficient. The presented data (Table 6) shows that the increase of the lengths of the Me–Me bonds (up to 17 pm) is typical for $Sc_3@C_{60}$ and $Y_3@C_{60}$, and a slight decrease (2 pm) is typical for $La_3@C_{60}$ during the encapsulation. In other words, the shape and the size of the cluster remain virtually unchanged when it is embedded in the fullerene cell. Particularly, the lengths of the C–C bonds near the encapsulated atoms increase more than in the case of the $Me_2@C_{60}$ structures (up to 20 pm), and a significant deformation of the carbon cage is observed as its shape becomes considerably different from the original spherical one.

During the transition from yttrium to lanthanum, the values of Δf_H^0 and Δf_G^0 decrease, which indicates the reduction of energy costs on the formation of endofullerenes corresponding to the metals from individual substances, while the increase of ΔH_b^0 in this series shows that La_3 is less inclined to be embedded in the fullerene structure when the process occurs in the gaseous phase (Table 6).

Different values of natural charges on metal atoms (particularly, for the first isomer of $Sc_3@C_{60}$) prove a thesis about the inequivalence of these atoms naturally arising from the analysis of the geometric structure of endofullerenes. For instance, the presence of two atoms with almost identical charges in the second isomer of

Fig. 3. Structure of the $Me_3@C_{60}$ Endofullerenes. C_s (1) and C_2 (2) Symmetry

Table 6. Calculated Parameters for Endofullerenes of the Scandium Sub-Group with Three Encapsulated Atoms

	$Sc_3@C_{60}$ (1)	$Sc_3@C_{60}$ (2)	$Y_3@C_{60}$	$La_3@C_{60}$ (1)	$La_3@C_{60}$ (2)
Symmetry	C_s	C_2	C_2	C_2	C_s
r_0(Me−Me), pm	281	281	281	284	284
r(Me−Me), pm	297	298	296	282	282
$|r-r_0|$, pm	16	17	15	2	2
$\Delta_f H^0$, kJ/mol	2635	2637	2913	2834	2847
$\Delta_f G^0$, kJ/mol	2565	2581	2852	2790	2801
ΔH_b^0, kJ/mol	−782	−780	−573	−343	−329
ΔG_b^0, kJ/mol	−727	−710	−507	−270	−258
Q(Me), a.u.	0.044 0.067 0.068	0.024 0.025 0.025	0.349 0.349 0.349	0.319 0.320 0.320	0.327 0.328 0.330
$S(C_{60})$	0.942	0.721	0.204	0.223	0.356

$Sc_3@C_{60}$ correlates with the presence of the C_2 point group in this structure. However, the inverse proposition does not hold true: similar values of natural charges on the three atoms contained in the encapsulated cluster are typical for $Y_3@C_{60}$, although the analysis of the geometric structure does not reveal the presence of the lines of threefold symmetry in these compounds. The values of Q(Me) decrease during the transition from yttrium to lanthanum and, on the whole, have smaller values than the $Me@C_{60}$ and $Me_2@C_{60}$ compounds, although they remain positive, which also indicates that triatomic metal clusters of the scandium sub-group are less inclined to be embedded into a cell of fullerene C_{60}. This is also confirmed by smaller values of total spin density on the carbon cage of $Y_3@C_{60}$ и $La_3@C_{60}$, which makes the prospect of using the compounds of this type as contrasting agents for tomography highly questionable.

3.4. Endofullerenes with four encapsulated atoms

The calculation establishes the presence of two types of structures in the $Me_4@C_{60}$ endofullerenes:

A structure with C_s symmetry is characterised by the presence of a square Me_4 cluster inside a fullerene cell, and this cluster is located perpendicular to the line connecting the centres of two diametrically opposite five-membered cycles (Fig. 4.1); this type of structure is typical for the first isomer of $Sc_4@C_{60}$ and the first isomer of $Y_4@C_{60}$;

A structure with C_s symmetry, where the Me_4 cluster has a shape of a tetrahedron with the apexes located opposite four six-membered cycles in the structure of the carbon cage (Fig. 4.2); this type of structure is found in the second isomer of $Sc_4@C_{60}$, the second isomer of $Y_4@C_{60}$, and $La_4@C_{60}$.

Isolated tetratomic clusters of metals of the scandium sub-group have the shape of dihedral angles formed by two congruent isosceles triangles, and their geometry, in the general case, can be described by three parameters: the length of the bond r corresponding to the lateral side of one of the triangles, the length of the bond b forming the base of one of the triangles, and the angle α formed by the planes of the
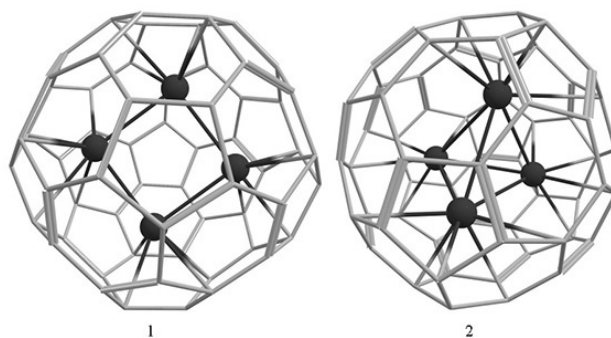
Fig. 4. Structure of the $Me_4@C_{60}$ Endofullerenes. Cs (First Isomer, 1) and C_2 (Second Isomer, 2) Symmetry

Table 7. Calculated Parameters for Endofullerenes of the Scandium Sub-Group with Four Encapsulated Atoms

	$Sc_4@C_{60}$ (1)	$Sc_4@C_{60}$ (2)	$Y_4@C_{60}$ (1)	$Y_4@C_{60}$ (2)	$La_4@C_{60}$
Symmetry	C_s	C_s	C_s	C_s	C_s
r_0, pm	288	288	288	288	275
r, pm	261	291	259	297	286
$|r-r_0|$, pm	27	3	29	9	11
b_0, pm	291	291	291	291	346
b, пм	366	294	370	293	285
$|b-b_0|$, pm	75	3	78	2	61
α_0, °	74.095	74.095	74.095	74.095	107.277
α, °	179.011	74.548	172.497	70.348	70.585
$|\alpha-\alpha_0|$, °	104.916	0.453	98.402	3.747	36.692
V_0, Å³	2.882	2.882	2.882	2.882	2.530
V, Å³	–	2.970	–	3.029	2.766
$\Delta_f H^0$, kJ/mol	2992	2778	3688	3398	3471
$\Delta_f G^0$, kJ/mol	2933	2718	3637	3353	3440
ΔH_b^0, kJ/mol	−574	−788	56	−234	297
ΔG_b^0, kJ/mol	−496	−710	138	−146	379
$Q(Me)$, a.u.	−0.020 −0.017 −0.085 −0.089	−0.042 −0.077 −0.088 −0.088	0.148 0.182 0.219 0.220	0.200 0.244 0.244 0.244	0.236 0.237 0.244 0.250

triangles (Fig. 5). The corresponding values of these parameters for isolated and encapsulated clusters are presented in Table 7. It is clear that a significant reduction in the lengths of the bonds r (by 27–29 pm) is typical for endofullerenes with square clusters; as for the compounds with tetrahedral clusters, only the dihedral angle noticeably changes assuming such values for $La_4@C_{60}$ and for the second isomer of $Y_4@C_{60}$
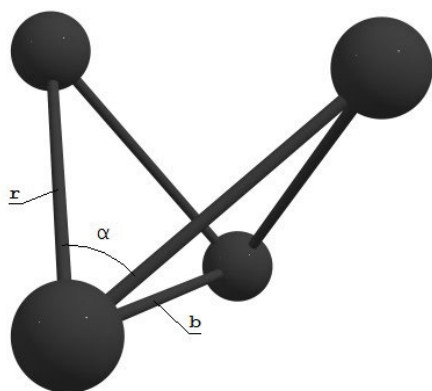
Fig. 5. Structural Parameters of the Me_4 Particles

that are almost identical to the value of the dihedral angle of the tetrahedron (~70.529°), and the lengths of the bonds slightly change (by 3–11 pm). At the same time, however, in all the cases an increase was observed in the volume V (Table 7) of the Me_4 particle in the encapsulated state by 3 – 5% as compared to the volume of the isolated particle.

The values of enthalpy and energy of formation of the $Me_4@C_{60}$ compounds are much higher than the values of the derivatives with triatomic encapsulated clusters; the values of enthalpy and energy of encapsulation become less negative. Positive values of ΔH_b^0 (for the isomer of $Y_4@C_{60}$ with a square cluster and $La_4@C_{60}$), which appear for the first time in the endofullerenes with this number of encapsulated atoms, are indicative of the thermodynamic impossibility of the formation of these compounds. Therefore, the maximum number of atoms that are capable of being embedded inside the carbon cage is three for lanthanum.

As for both isomers of $Sc_4@C_{60}$, the transfer of electron density from the carbon cage to the encapsulated cluster is typical for them, which leads to the appearance of a small negative charge (0.020–0.089 a.u. in the absolute value) on the atoms of the latter; as for $Y_4@C_{60}$ with a tetrahedral cluster, the transfer occurs in the opposite direction, and the metal atoms acquire the charge of 0.200–0.244 a.u.

3.5. Endofullerenes with five encapsulated atoms

As it was previously mentioned, the formation of endofullerenes with four or more encapsulated atoms is not typical for lanthanum, therefore only the results of modelling for the compounds $Sc_5@C_{60}$ and $Y_5@C_{60}$ are presented in this section. The calculation shows the presence of two types of structures in these compounds:

A structure with the C_s symmetry where the Me_5 cluster has a shape of a trigonal bipyramid and is placed inside the fullerene cell so that its line of threefold symmetry coincides with the line connecting the centres of two diametrically opposite bicyclic fragments of C_{10} (Fig. 6.1); this structure was found both in $Sc_5@C_{60}$ and $Y_5@C_{60}$.

A structure with the C_3 symmetry where the line of threefold symmetry of the Me_5 cluster (also having a shape of a trigonal bipyramid) coincides with the line of threefold symmetry of fullerene going through the centres of two diametrically opposite six-membered cycles (Fig. 6.2); this type of structure is also formed both in the case of $Sc_5@C_{60}$ and $Y_5@C_{60}$.

The basic doublet state is typical for these structures.

Both outside and inside the fullerene cell, the Me_5 clusters of metals of the scandium sub-group have the shape of a distorted trigonal bipyramid,
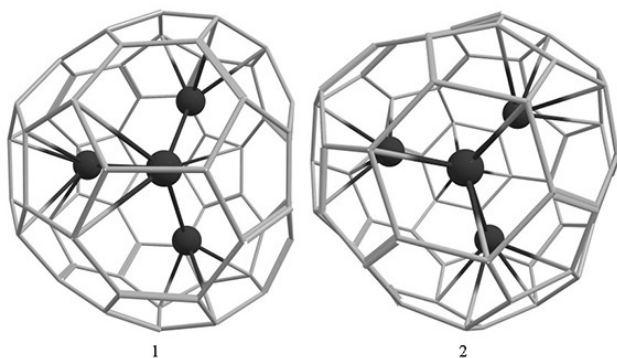
therefore only two parameters are sufficient for the description of their geometry: the lengths of the bonds r and d corresponding to the lateral edges and edges at the base of the pyramids forming a bipyramid (Fig. 7). The corresponding values are presented in Table 8. It is clear that the length of the bonds r decreases by 26–68 pm, while d can either decrease (by 15–48 pm in the case of $Sc_5@C_{60}$) or slightly increase (by 1–10 pm in the case of $Y_5@C_{60}$). It should be noted that the volume of the encapsulated cluster decreases as compared to the volume of the isolated one (V and V_0 respectively, see Table 8) regardless of the direction of the change of separate parameters. Moreover, while the volumes of isolated particles significantly differ (5.876 Å³ and 7.924 Å³ for Sc_5 and Y_5 respectively), they are rather similar for the encapsulated ones (5.521–5.693 Å³).

Negative values of enthalpy and the energy of encapsulation for endofullerenes of scandium indicate that they can be potentially formed by embedding the Sc_5 particle in the fullerene cell in the gaseous phase; in the case of $Y_5@C_{60}$, ΔH_b^0 is comparable with the energies of bond breaking in the fullerene (417 and 507 kJ/mol for $r6$–6 and $r5$–6 respectively [16]). Therefore, the formation of $Y_n@C_{60}$ compounds with $n > 4$ is not typical for endofullerenes of yttrium.

Atoms of scandium inside the carbon cage acquire a small negative charge (Table 8), and while for the first of isomers of $Sc_5@C_{60}$ the most negative charges (−0.218 a.u.) are found in the atoms located along the line of threefold symmetry of the encapsulated cluster, for the second isomer the most negative charges are located on the atoms of the equatorial section

Fig. 6. Structure of the $Me_5@C_{60}$ Endofullerenes C_s (1) and C_3 (2) Symmetry
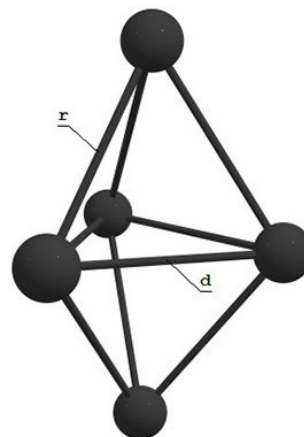
Fig. 7. Structural Parameters of the Me_5 Particles

Table 8. Calculated Parameters for Endofullerenes of the Scandium Sub-Group with Five Encapsulated Atoms

	$Sc_5@C_{60}$ (1)	$Sc_5@C_{60}$ (2)	$Y_5@C_{60}$ (1)	$Y_5@C_{60}$ (2)
Symmetry	C_s	C_3	C_s	C_3
r_0, pm	290–296	290–296	321–327	321–327
r, pm	262–270	265–271	254–273	253–274
$|r-r_0|$, pm	26–28	25	54–67	53–68
d_0, pm	287–298	287–298	317–330	317–330
d, pm	302–346	314–326	307–336	310–331
$|d-d_0|$, pm	15–48	27–28	6–10	1–7
V_0, Å³	5.876	5.876	7.924	7.924
V, Å³	5.531	5.693	5.521	5.572
$\Delta_f H^0$, kJ/mol	3164	3175	4292	4298
$\Delta_f G^0$, kJ/mol	3109	3119	4251	4256
ΔH_b^0, kJ/mol	−560	−549	504	510
ΔG_b^0, kJ/mol	−471	−461	599	604
$Q(Me)$, a.u.	−0.033 −0.033 −0.100 −0.218 −0.218	−0.079 −0.090 −0.107 −0.141 −0.147	−0.012 0.059 0.084 0.212 0.212	0.025 0.051 0.074 0.224 0.235
$S(C_{60})$	0.127	0.363	0.412	0.391

of the Me_5 particle. Despite the direction of the transfer of electron density from the carbon cage towards the metal cluster, the value of total spin density on the carbon cage for these compounds is within the range of 0.127–0.363.

3.6. Endofullerenes with six and seven encapsulated atoms

As it was previously shown, the maximum number of encapsulated atoms is 4 and 5 for the endohedral derivatives of yttrium and lanthanum respectively, and the formation of such endohedral derivatives $Me_6@C_{60}$ and $Me_7@C_{60}$ is typical only for scandium. The calculation states the presence of three types of structures in $Sc_6@C_{60}$:

A structure with C_s symmetry (isomer 1), where the Me_6 cluster has the shape of a tetragonal bipyramid with the apexes located opposite the centres of bicyclic fragments of C_{10} in the fullerene structure (Fig. 8.1);

A structure with C_s symmetry (isomer 2), where the metal cluster has the shape of a tetragonal bipyramid with one metal atom in
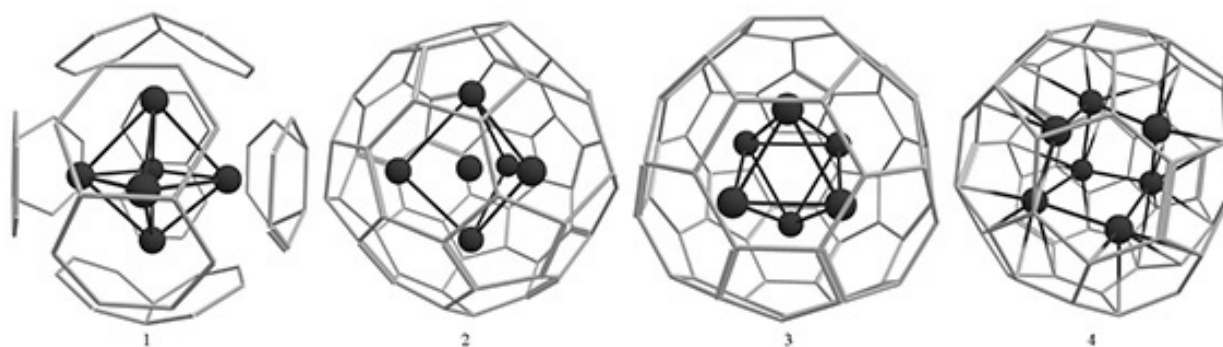
Fig. 8. Structure of the $Me_6@C_{60}$ and $Me_7@C_{60}$ Endofullerenes. C_s (1), C_s (2), and C_{3v} (3) Symmetry for the $Me_6@C_{60}$ Isomers. Index (4) Indicates the Structure of $Me_7@C_{60}$ Endofullerene with Undefined Symmetry

the centre and a line of threefold symmetry directed along the line connecting the centres of two diametrically opposite fragments of C_{12}, formed by two six-membered cycles and one five-membered cycle (Fig. 8.2);

A structure with C_{3v} symmetry (isomer 3), where the metal cluster has the shape of an octahedron with one of the lines of threefold symmetry coinciding with the line of threefold symmetry of fullerene going through the centres of diametrically opposite six-membered cycles (Fig. 8.3).

The Sc_6 cluster in the gaseous phase has the shape of a pentagonal bipyramid devoid of one of the atoms located in the equatorial plane. Due to the great differences in the geometry of isolated and encapsulated clusters, the comparison of their geometric parameters is meaningless, therefore in this section we will compare only the volumes of the corresponding particles. The data presented in Table 9 shows that the deformation of the metal cluster during the encapsulation is typical for all the $Sc_6@C_{60}$ compounds and is accompanied by a decrease in its volume. As for the first and the third isomers of $Sc_6@C_{60}$, the volume of the Sc_6 particle inside the fullerene cell is 5 – 6% smaller than the original. As for the second isomer, this effect is more pronounced and the volume of the encapsulated cluster is 31% smaller than the volume of the isolated one. However, it should be noted that in the structure that is typical for this isomer, the central atom of scandium becomes close to the atoms forming a trigonal bipyramid at a distance of 195–202 pm, which is 86–93 less than a double covalent radius of scandium (288 pm), and the distance between the atoms themselves reaches 371 pm, thus exceeding the double covalent radius of scandium by 83 pm. Due to considerable strains in the structure, the formation of such a compound is thermodynamically disadvantageous, as was evidenced by strongly positive values of enthalpy and energy of encapsulation (693 kJ/mol, see Table 9). For the first and the third isomers of $Sc_6@C_{60}$ this value becomes negative, which shows that corresponding structures can be potentially formed as a result of embedding of the Sc_6 particles in the fullerene cell in the gaseous phase. Metal atoms inside the carbon cage acquire small negative charges within the range of $-0.261 - -0.053$ a.u.

The addition of one atom of scandium to the Sc_6 particle in the gaseous phase results in the formation of the Sc_7 cluster with a shape of a regular pentagonal bipyramid. However, in the encapsulated state the symmetry of this cluster is broken, and it acquires the shape of a deformed cube devoid of one of the apexes (Fig. 8.4). In

Table 9. Calculated Parameters for Endofullerenes of the Scandium Sub-Group with Six and Seven Encapsulated Atoms

	$Sc_6@C_{60}$ (1)	$Sc_6@C_{60}$ (2)	$Sc_6@C_{60}$ (3)	$Sc_7@C_{60}$
Symmetry	C_s	C_s	C_{3v}	-
V_0, Å³	9.311	9.311	9.311	15.254
V, Å³	8.818	6.410	8.725	9.184
$\Delta_f H^0$, kJ/mol	3723	4591	3752	4578
$\Delta_f G^0$, kJ/mol	3673	4541	3702	4530
ΔH_b^0, kJ/mol	−176	693	−146	599
ΔG_b^0, kJ/mol	−76	792	−47	705
Q(Me), a.u.	−0.261 −0.156 −0.130 −0.114 −0.114 −0.084	−0.738 −0.579 −0.563 −0.491 −0.474 3.328	−0.203 −0.190 −0.124 −0.100 −0.054 −0.053	−0.328 −0.206 −0.152 −0.056 −0.019 0.002 0.014
S(C_{60})	–	–	–	0.197

this case, the distortions of the carbon cage are so significant that it is impossible to assign any group of symmetry to the $Sc_7@C_{60}$ structure; analysis of the elements of symmetry points to the C_2 group, where the line of two-fold symmetry is in one plane with the diagonal of the "cube" and goes through its edge, as the one that describes the structure of endofullerene most adequately, although the error in this case is 16.7%.

The Sc_7 cluster appears to be highly compressed inside the carbon cage, and its volume in the encapsulated state is 40% smaller than in the isolated state (see Table 9); the bonds between the metal atoms have the length of 230–267 pm, which is 21–58 pm less than in the case of the double covalent radius of scandium. As for this structure, the values of enthalpy and energies of encapsulation are positive (599 kJ/mol), which indicates that it is impossible to form the $Sc_7@C_{60}$ endofullerene by embedding a metal cluster inside the carbon cage in the gaseous phase. Therefore, the formation of the endohedral derivatives of $Me_n@C_{60}$ with $n > 6$ is not typical for scandium.

4. Conclusions

Analysis of structural and thermodynamic characteristics of endofullerenes of the scandium sub-group metals allows revealing a number of patterns that become apparent with the growing number of encapsulated atoms. For instance, the theoretical limit at which the formation of the endohedral structure of $Me_n@C_{60}$ through embedding of the Me_n particle in the fullerene cell remains possible from the thermodynamic point of view is $n = 6$ for scandium, 4 for yttrium, and 3 for lanthanum. In addition, the most stable derivatives are those with a diatomic (or triatomic, in the case of scandium) metal cluster inside the carbon cage, as considerable deformations of both the fullerene cage and the Me_n particle were observed in the models of endofullerenes with larger encapsulated clusters.

A redistribution of electron density between two parts of the structure being formed is typical for endofullerenes of the scandium sub-group metals, however, the direction of the transition and the degree of manifestation of this effect depend on the number of encapsulated atoms. As the number of metal atoms grows, the total charge on the encapsulated cluster decreases in the structure of endofullerene: in the $Me@C_{60} - Me_3@C_{60}$ endofullerenes the metal atoms have a positive charge, in $Me_4@C_{60}$ separate atoms acquire small in the absolute value negative charges, while the presence of only negative charge on the metal atoms is typical for the $Me_5@C_{60} - Me_6@C_{60}$ structures.

A considerable decrease in the value of the total spin density in the carbon cage for structures in a basic doublet state is also observed with the growing number of encapsulated atoms in the structure of the endofullerene, which limits the possibility of the use of endofullerenes with more than one encapsulated atom as contrasting agents for NMR tomography.

Conflict of interests

The authors declare that they have no known competing financial interests or personal relationships that could have influenced the work reported in this paper.

References

1. Kroto H. W., Heath J. R., O'Brien S. C., Curl R. F., Smalley R. E. C60: Buckminsterfullerene. *Nature*. 1985;318(6042): 162–163. DOI: https://doi.org/10.1038/318162a0

2. Kratschmer W., Lamb L. D., Fostiropoulos K., Huffman D. R. Solid C60: a new form of carbon. *Nature*. 1990;347(6291): 354–358. DOI: https://doi.org/10.1038/347354a0

3. Buchachenko A. L. Compressed atoms. *J. Phys. Chem. B*. 2001;105(25): 5839–5846. DOI: https://doi.org/10.1021/jp003852u

4. Koltover V. K., Bubnov V. P., Estrin Y. I., Lodygina V. P., Davydov R. M., Subramoni M., Manoharan P. T. Spin-transfer complexes of endohedral metallofullerenes: ENDOR and NMR evidences. *Phys. Chem. Chem. Phys*. 2003;5(13): 2774–2777. DOI: https://doi.org/10.1039/b302917d

5. Raebiger J. W., Bolskar R. D. Improved production and separation processes for gadolinium metallofullerenes. *J. Phys. Chem. C*. 2008;112(17): 6605–6612. DOI: https://doi.org/10.1021/jp076437b

6. *Gaussian 09, Revision D.01*. M. J. Frisch, G. W. Trucks, H. B. Schlegel, G. E. Scuseria, M. A. Robb, J. R. Cheeseman, G. Scalmani, V. Barone, G. A. Petersson, H. Nakatsuji, X. Li, M. Caricato, A. Marenich, J. Bloino,

B. G. Janesko, R. Gomperts, B. Mennucci, H. P. Hratchian, J. V. Ortiz, A. F. Izmaylov, J. L. Sonnenberg, D. Williams-Young, F. Ding, F. Lipparini, F. Egidi, J. Goings, B. Peng, A. Petrone, T. Henderson, D. Ranasinghe, V. G. Zakrzewski, J. Gao, N. Rega, G. Zheng, W. Liang, M. Hada, M. Ehara, K. Toyota, R. Fukuda, J. Hasegawa, M. Ishida, T. Nakajima, Y. Honda, O. Kitao, H. Nakai, T. Vreven, K. Throssell, J. A. Montgomery, Jr., J. E. Peralta, F. Ogliaro, M. Bearpark, J. J. Heyd, E. Brothers, K. N. Kudin, V. N. Staroverov, T. Keith, R. Kobayashi, J. Normand, K. Raghavachari, A. Rendell, J. C. Burant, S. S. Iyengar, J. Tomasi, M. Cossi, J. M. Millam, M. Klene, C. Adamo, R. Cammi, J. W. Ochterski, R. L. Martin, K. Morokuma, O. Farkas, J. B. Foresman, and D. J. Fox, Gaussian, Inc., Wallingford CT, 2016. Available at: http://gaussian.com/g09citation

7. Neese F. The ORCA program system. *WIREs Computational Molecular Science*. 2012;2(1): 73–78. DOI: https://doi.org/10.1002/wcms.81

8. Laikov D. N., Ustynyuk Y. A. PRIRODA-04: a quantum-chemical program suite. New possibilities in the study of molecular systems with the application of parallel computing. *Russian Chemical Bulletin.* 2005;54(3): 820–826. DOI: https://doi.org/10.1007/s11172-005-0329-x

9. Chandrasekharaiah M. S., Gingerich K. A. Chapter 86 Thermodynamic properties of gaseous species. In: *Handbook on the Physics and Chemistry of Rare Earths*. 1989;12: 409–431. DOI: https://doi.org/10.1016/s0168-1273(89)12010-8

10. Kohl F. J., Stearns C. A. Vaporization thermodynamics of yttrium dicarbide–carbon system and dissociation energy of yttrium dicarbide and tetracarbide. *J. Chem. Phys.*, 1970;52(12): 6310–6315. DOI: https://doi.org/10.1063/1.1672942

11. Gingerich K. A., Nappi B. N., Pelino M., Haque R. Stability of complex dilanthanum carbide molecules. *Inorganica Chimica Acta.* 1981;54: L141–L142. DOI: https://doi.org/10.1016/s0020-1693(00)95414-8

12. Hedberg K., Hedberg L., Bethune D. S., Brown C. A., Dorn H. C., Johnson R. D., de Vries M. S. Bond lengths in free molecules of buckminsterfullerene, C60, from gas-phase electron diffraction. *Science.* 1991;254(5030): 410–412. DOI: https://doi.org/10.1126/science.254.5030.410

13. Bethune D. S., Meijer G., Tang W. C., Rosen H. J., Golden W. G., Seki H., Brown C. F., de Vries M. S. Vibrational Raman and infrared spectra of chromatographically separated C60 and C70 fullerene clusters *Chem. Phys. Lett.*, 1991; 179(1–2): 181–186. DOI: https://doi.org/10.1016/0009-2614(91)90312-w

14. Emsley J. *Elements.* Moscow: Mir Publ.; 1993. 256 p. (in Russ.)

15. Rakov E. G. *Nanotrubki i fullereny* [Nanotubes and Fullerenes]. Moscow: Logos Publ.; 2006. 376 p. (in Russ.)

16. Eletskii A. V., Smirnov V. M. *Fullerenes. Phys. Usp.* 1993;36(3): 202–224. Available at: https://ufn.ru/ru/articles/1993/2/b/

Information about the authors

Dmitrii A. Machnev, postgraduate student at the Department of Physical Chemistry, Voronezh State University, Voronezh, Russian Federation; e-mail: machnev.dmitry@gmail.com. ORCID iD: https://orcid.org/0000-0002-5773-3403.

Igor V. Nechaev, PhD in Chemistry, Assistant of the Department of Physical Chemistry, Voronezh State University, Voronezh, Russian Federation; e-mail: nechaev_iv@chem.vsu.ru. ORCID iD: https://orcid.org/0000-0002-1232-8869.

Alexander V. Vvedenskii, DSc in Chemistry, Professor, Professor of the Department of Physical Chemistry, Voronezh State University, Voronezh, Russian Federation; e-mail: alvved@chem.vsu.ru. ORCID iD: https://orcid.org/ 0000-0003-2210-5543.

Oleg A. Kozaderov, DSc in Chemistry, Associate Professor, Head of the Department of Physical Chemistry, Voronezh State University, Voronezh, Russian Federation; e-mail: kozaderov@vsu.ru. ORCID iD: https://orcid.org/0000-0002-0249-9517.

All authors have read and approved the final manuscript.

Translated by Marina Strepetova
Edited and proofread by Simon Cox

Condensed Matter and Interphases
(Kondensirovannye sredy i mezhfaznye granitsy)

Hydration and Intermolecular Interactions in Carboxylic Acids

© 2020 V. F. Selemenev[a], O. B. Rudakov[b], N. V. Mironenko[a], S. I. Karpov[a], V. N. Semenov[a], N. A. Belanova✉[a], L. A. Sinyaeva[a], A. N. Lukin[a]

[a]*Voronezh State University,*
1 Universitetskaya pl., Voronezh 394018, Russian Federation

[b]*Voronezh State Technical University,*
84 ul. 20-Letiya Oktyabrya, Voronezh 394006, Russian Federation

Abstract

At the moment, the most accurate and reliable information about intermolecular interactions in low-molecular compounds and their polymer analogues can be obtained by means of combined UV, visible, and IR spectroscopy. However, this combination is not always used when interpreting the results of intermolecular interactions in carboxylic acids. Therefore, the aim of our study was to investigate the intermolecular interactions in carboxylic acids and their hydration properties using the UV, visible, and IR spectroscopy.

The article presents the results of the investigation of intermolecular interactions and hydration in carboxylic acids by means of UV, visible, and IR spectroscopy, and the microscopic study of the swelling/contraction curves of the beads of the sorbents with slightly acidic –COOH groups in exchange reactions of $R–COOH + NaOH \leftrightarrow R–COO^-Na^+ + H_2O$. The study revealed that in water dimers, the total energy of hydrogen bonds is determined by the Coulomb, exchange, charge transfer, polarization, and dispersion components. In our study we also tested the formulas for the calculation of the energy of the H-bond, enthalpy, the force constants of the H-bond, and the elongation of the covalent bond. The article suggests a formula for estimation of the distance $RCH_2...O$. The calculations of the length of H-bonds between the donor and the acceptor of the proton based on the information about stretching vibrations in the IR spectra of carboxylic acids. The article demonstrates the possibility of the formation of five- and six-membered cycles, resulting from the formation of H-bonds between CH_2 groups of the chain and –COOH end groups of carboxylic acids.

The characteristic electron and vibrational frequencies in the UV and IR spectra were used to determine the intermolecular interactions in ion exchangers CB-2 and CB-4. The microscopic and microphotographic study of the swelling of certain beads of carboxylic cationites help us to register the presence of the external shell $R–COO^-...Me^+$ and the internal shell $R-COOH$ during the exchange reactions: $R–COOH + Me^+ + OH^- \leftrightarrow R–COO^-...Me^+ + H_2O$.

Keywords: UV-vis spectroscopy, IR spectroscopy, visible spectroscopy, carboxylic acids, intermolecular interactions.

For citation: Selemenev V. F., Rudakov O. B., Mironenko N. V., Karpov S. I., Semenov V. N., Belanova N. A., Sinyaeva L. A., Lukin A. N. Hydration and intermolecular interactions in carboxylic acids. *Kondensirovannye sredy i mezhfaznye granitsy = Condensed Matter and Interphases*. 2020; 22(3): 373–387. DOI: https://doi.org/10.17308/kcmf.2020.22/2998

✉ Natalya A. Belanova, e-mail: belanovana@mail.ru

1. Introduction

When assessing an analytical method, we should take into account the three most important parameters: its accuracy, sensitivity, and cost. Unfortunately, in the modern industrial world there are few people who realise that without analytical chemistry it is difficult to combine these criteria when assessing industrial technological solutions. Indeed, analytics, being just a supplementary discipline at first, is now becoming a popular interdisciplinary branch. This indicates the restoration of analytical chemistry as an independent scientific field.

Most of the information about the structure of the initial components and the physicochemical properties of target products can be obtained by means of spectroscopy. Therefore, spectroscopy is the study of the interaction between matter and light. The electromagnetic spectrum covers electromagnetic waves ranging from high-energy cosmic radiation to X-rays, ultraviolet, visible light, infrared, and low-energy radio waves [1–4]. γ-rays, with the wavelength of just 10^{-11} cm, are emitted during nuclear reactions. X-rays (with the wavelengths of 10^{-8} cm) are formed as a result of electronic transitions between the inner shells of the so-called core electrons (Table 1).

The electronic excitation of molecules, atom vibrations, and excitation of molecular rotation are possible within a single spectrum region (a relatively small one) with the wavelengths ranging from 10^{-1} to 10^{-6} cm. This region of the UV, visible light, and IR radiation is referred to as the "optical spectrum". When wavelengths are

shorter than 800 nm (i.e. the UV and visible light), the radiation energy is high enough to interact with the electrons in molecules [1-3]. In this case, only the valence electrons of compounds are excited. The strongly bonded σ electrons (Table 1) of simple (single) bonds absorb radiation of shorter wavelengths than weakly bonded π electrons of multiple bonds and n (nonbonding) electrons of heteroatoms.

The vibrations of molecules are excited by lower energy as compared to the ultraviolet and visible light regions of the spectrum, i.e. at longer waves. The molecular rotations are also excited, and therefore we can call these spectra rotational-vibrational [1–4]. To rotate a molecule along the three inertial axes x, y, z, minimal radiant energy is required. Therefore, at wavelengths of more than 800 nm, the rotational, vibrational, and electronic spectra are observed.

At the moment, the most accurate and reliable information about intermolecular interactions in low-molecular compounds and their polymer analogues can be obtained by means of combined UV, visible, and IR spectroscopy. However, this combination is not always used when interpreting the results of intermolecular interactions in carboxylic acids. The effect of the solvent (solvation or hydration) as one of the factors determining the character of intermolecular interactions in solutions and polymers is also rarely taken into account. Therefore, the aim of our study was to investigate the intermolecular interactions in carboxylic acids and their hydration properties using UV, visible, and IR spectroscopy.

Table 1. Classification of the spectral regions

Spectrum	Interaction	Spectral region	Wavelength
X-ray spectrum	Inner electrons	X-rays	0.01–1.0 nm
Electron spectrum	Electrons of the σ-bonds (sp³-orbitals)	UV in vacuum	10–190 nm
	Electrons of the π-bonds (sp²-orbitals)	UV	190–380 nm
	n electrons (sp-orbitals)	Visible region	380–800 nm
Vibration spectrum	Higher harmonic vibrations	Near IR	0.8–2.5 μm
	Molecular vibrations	Mid-IR	2.5–50 μm
Rotation spectrum	Rotation of the molecules	Far IR	50–500 μm
		Microwaves	0.5–3.0 mm

σ, σ^* bonding and antibonding orbitals;
π, π^* bonding and antibonding orbitals

2. Experimental

The objectives of the study determined the use of the spectroscopy methods commonly applied for detecting various structures in solutions of target substances. The UV spectra were registered using the Shimadzu 2401 spectrophotometer. Each spectrum was interpreted based on a single wavelength. The absorbance was measured at the maximum peak of the spectrum, followed by the calculation of the concentration [3–7].

The character of the swelling kinetic curves $f = V_\tau/V_n$ (V_τ, V_n is the volume of the bead at the moment τ and the initial volume in the H shape) of the sorbents with slightly acidic –COOH groups was used as a criterion for the transitions taking place in the ion exchanger phase. Therefore, we used the microscopic methodology [8, 9] to study the interaction between the sorbent and the –COOH groups. The character of the swelling kinetic curves (concentrations of separate beads of the sorbent) was studied in special plexiglass cuvettes using the MIR-12 and MBI-6 microscopes. The size of the beads was registered with a precision of up to ±0.002 mm.

The IR spectra of liquids were recorded during the analysis of either a pure substance or its mixtures with solvents. Solid samples were prepared in the form of oil suspensions, thin films on the surface of NaCl, KBr, and CaF$_2$ wafers, and pressed tablets with alkali metals halides. The samples were ground in an agate mortar so that the size of the particles was no more than 0.5 μm. The samples were prepared for the analysis using the methodology described in [5]. The spectra were registered by means of the Bruker Vertex 70v vacuum FTIR spectrometer using a "Platina" single-pass ATR adapter. The preparation of samples for the IR spectroscopy most commonly involves pressing them together with KBr [6–9]. To produce the tablets, the press die described in [6] was used until the KBr crystals formed a translucent matrix with the powder of the studied substance regularly distributed within it.

The dependence of the energy of the H-bond (E_{int}) and its components on the distance R(O...O) is demonstrated in Fig. 1. The curves were calculated for the water dimer [10] and they demonstrate that, when the distance is large, the Coulomb energy (E_{coul}) of two neighbouring molecules with intact electron shells is predominant [2, 4].

Near the equilibrium, the energy of the H-bond is determined by the Coulomb (E_{coul}) and exchange (E_{ex}) contributions [2, 4, 10], where E_{ex} is bonded taking into account the equality of the electrons of the interacting molecules, when their wave functions overlap.

Besides the Coulomb E_{coul} and exchange E_{ex} contributions, the energy of the H-bond (E_{int}) is also contributed to by the following components: the polarisation interaction energy (E_{ind}); the charge transfer energy (E_{cht}) reducing the H-bond energy as a result of the redistribution of the electron density within the subsystem (polarisation) and between the subsystems (charge transfer) [2,4,10]; and the dispersion energy (E_{disp}), which takes into account the correlation in the transmission of electrons of different molecules. Therefore,

$$E_{int} = E_{coul} + E_{ex} + E_{ind} + E_{cht} + E_{disp} + E^{(n \geqslant 3)}. \qquad (1)$$

Depending on the value, the energies of the H-bond are classified as weak, medium, and strong [7]. The formation of the hydrogen bond significantly alters the properties of the molecules
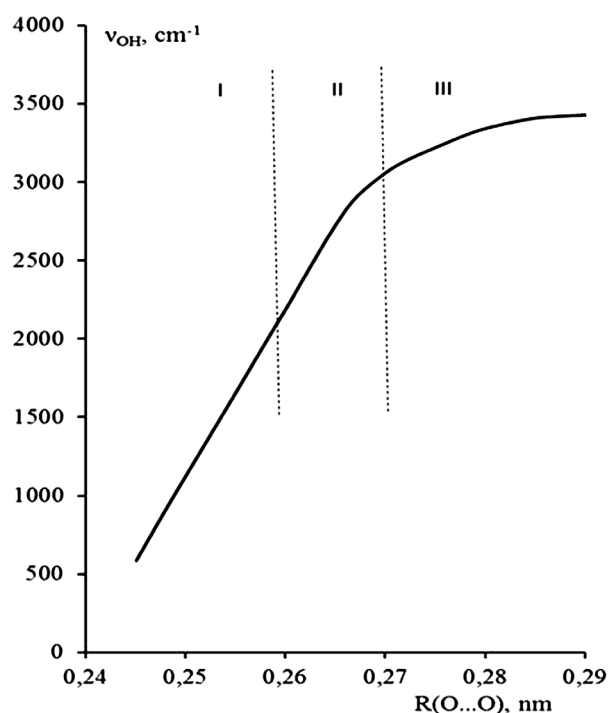

Fig. 1. The dependence of the total H-bond energy E_{int} and its individual components in the H$_2$O dimer on R(O...O) [7, 8]

of the associates R_1A-H...BR_2 (particularly of the A...H group). Our experiment demonstrated (Fig. 2, Table 2) the reduction in the frequency of stretching vibrations of the A-H (R_1O...OR_2) bond in the 10-2600 cm^{-1} range depending on the strength of the H-bond.
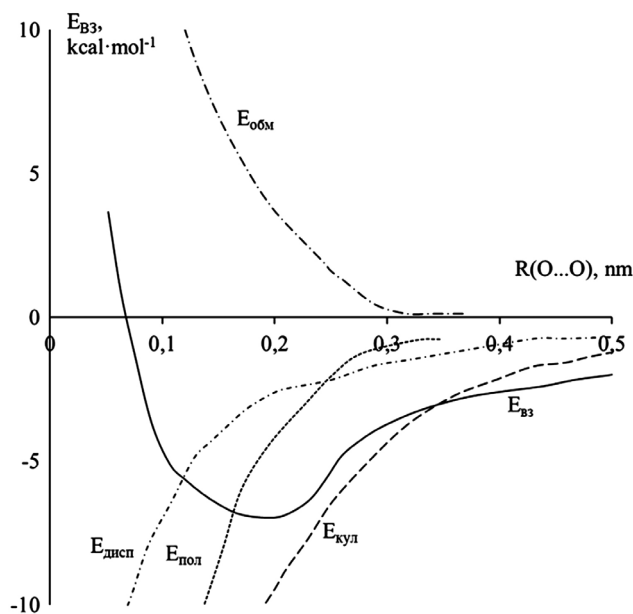
Fig. 2. The correlation between O-H-bond vibration frequency and the equilibrium distance R_0(O...O) in crystals [8]

It should be noted that the characteristic frequencies of absorption of the groups of atoms in carboxylic acids obtained in [11] (Table 3) are similar to those presented in this article (Table 4, Figs. 3 and 4).

However, the results shown in Table 4 and Figs. 3 and 4 allowed us to determine the stretching vibrations and deformation vibrations to be certain functional groups and suggest a new description of the formation mechanisms of cyclic structures with H-bonds in carboxylic acids.

It is somewhat difficult to interpret the IR spectra of carboxylic acids, when the absorption bands of –COOH and –CH_2 groups overlap (Table 5). Therefore, we performed a preliminary comparison of the UV spectra (Fig. 3a and 4c) demonstrating the electronic transitions (scheme 1) with the characteristic vibrations of the groups in the IR spectra (Fig. 3a, 3b, 3c).

Scheme (1) demonstrates that the peaks at 2962 and 2834 cm^{-1} are characteristic for –OH-bonds in associates with carboxylic groups and for –CH_2– in "hydrophobic" chains of carboxylic acids [2–6]. For –CH_2, C–O, and -OH in COOH groups the peaks at 1525, 1379, 1300, 1245, 960-944, and 737 cm^{-1} appeared to be joint absorption bands. This, although making

Table 2. Formulas used to calculate the parameters of the hydrogen bridge using the values of the shift in the IR spectra

No.	Parameter	Symbol	Unit of measurement	Formula	Source
1	Energy of the H-bond	E_H	kJ/mol	$-\Delta v / v^o_{OH} = E_H \cdot 1.6 \cdot 10^{-2}$	[1]*
2	Enthalpy	ΔH	kJ/mol	$-\Delta H = 2.9 \cdot \Delta A^{1/2}$; $\Delta v = [\Delta A^{1/2}]^2 \cdot 80$	[2]
3	Force constant of the H-bond	K_H	cm^{-2}	$K_H = (5.5 \pm 1.2) \cdot 10^4 \cdot E_H$	
4	Force constant of the OH-bond	K_{OH}	cm^{-2}	$-K_{OH} = 8.63(5.5 \pm 1.2) \cdot 10^4 \cdot E_H - 12.879 \cdot 10^6$	
5	Length of the hydrogen bridge	$R_{OH...O}$	Å	$\Delta v = 4.4 \cdot 10^3 (2.84 - R_{O...O})$	[3, 4]
		$R_{OH...N}$	Å	$\Delta v = 6.92 \cdot 10^2 (3.04 - R_{O...N})$	
		$R_{NH...O}$	Å	$\Delta v = 5.48 \cdot 10^2 (3.21 - R_{N...O})$	
		$R_{NH...H}$	Å	$\Delta v = 1.05 \cdot 10^3 (3.38 - R_{N...N})$	
		$R_{CH2...O}$	Å	$\Delta v = 0.89 \cdot 10^2 (3.42 - R_{CH_2...O})$	
6	Elongation of the covalent bond	Δr_{OH}	Å	$\Delta r_{OH} = 5.3 \cdot 10^2 \cdot \Delta v$	

* v^o for $R_{OH...O}$=3700 cm^{-1}; v^o for $R_{OH...N}$ = 3400 cm^{-1} [2, 6]; v^o for $R_{NH...O}$ = 3550 cm^{-1}; v^o for $R_{NH...H}$ = 3300 cm^{-1} [1, 2, 5, 6]; v^o for $R_{CH_7...O}$ = 3200 cm^{-1} [1, 2, 5, 6].

Table 3. Characteristic frequencies of absorption of the groups of atoms of fatty acids [2–8]

| Vibrational frequency ν, cm^{-1}			$\Delta\nu^*$, cm^{-1}	Assignment of vibrations
[7, 9, 13]	Stearic acid	Oleic acid		
3010	–	3008	–2;	ν =CH – in RCH=CHR'(trans);
2962	2956	–	–6	CH$_3$(ν_{as})
2925	–	2918	–7;	ν_{as}*CH$_2$
	2911	–	–14	
2853	–	2844	–9;	ν_s**CH$_3$; ν_sCH$_2$
	2843	-	–10	
2726	2686	2883	–40;	–OH in COOH (bonded)
			–43	
1720	1698	1705	–22;	ν C=O in COOH
			–12	
1467	1471	1472	4; 5;	δ^*_{as} CH$_3$; sciss. CH$_2$ in the chain δ_{as} CH$_2$ (scissoring);
1421	1431	1433	10;12;	δ_{as}, if CH$_2$ is with C=O; CH in –C=CH
1400	1413	1413	13	
1375	1379	1382	4;	δ_s CH$_3$; δ –O–H
			7	
1300	1312	1316	12;	CH$_2$ wagging; –COOH in dimers
			16	
1245–1180	1252–1182	1266–1192	Group of bands	CH$_3$; CH$_2$ rocking stretching with an unbranched chain; with COOH end groups
1125–1120	1104	1104	–21; –21	νOH in C–O groups with five or six-membered cycles
935	944; 886	953; 895	9; 18	Wide bands nonplanar δ vibrations of OH in COOH
750; 720	817; 737	817; 744	67; 67	(CH$_2$)$_n$ rocking stretching
–	608	612		δ CH in cycles

* ν, δ are stretching and deformation vibrations respectively;
** as, s are asymmetrical and symmetrical stretching vibrations respectively.

the interpretation of the spectra difficult, has a positive effect. For example, it allows determining the form (open or lactone) of levulinicc acid, if the spectrum includes the bands 3260, 2970, 2930, 2870, 2850, 1720, 1705, and 900 cm^{-1} [7].
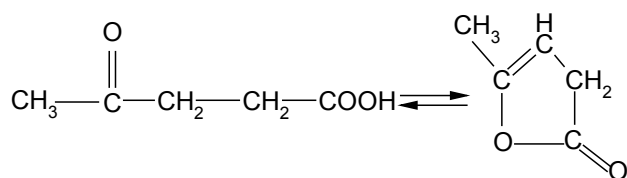
C=O peaks are characteristic for the open structure in ketonic (1720 cm^{-1}) and carboxylic (1705 cm^{-1}) acid; 3260 cm^{-1} (ν OH), and 900 cm^{-1} (δ OH). Frequencies 2970, 2930 cm^{-1} and 2870, 2850 cm^{-1} are determined to be stretching vibrations of methyl CH$_3$ and methylene CH$_2$ groups. The cyclic structure should be demonstrated by

the bands C=C and lactone C=O (1800–1785 cm^{-1} and 1735 cm^{-1} respectively) [2–5].

It is interesting that there are clear groups of absorption bands at 1433–1104 cm^{-1} (Table 4, scheme 1). This characterises the transition from planar conformation (scissoring – and rocking γ_r stretching) in hydrophobic tails to the nonplanar conformation (wagging γ_w and twisting γ_t stretching) caused by the mixture of the stretching vibrations ν_s and ν_{as} of OH polar groups with γ_r and γ_t deformation vibrations of CH$_2$ groups of the methylene chain [3, 5, 8]. Each of these transitions is accompanied by the absorption of a photon of a certain value. The $\sigma\rightarrow\sigma^*$ transition requires the most energy (scheme 1). The corresponding absorption bands are observed in the vacuum UV region (λ < 200 nm).

Table 4. Characteristic frequencies of absorption of the groups of atoms of carboxylic acids [2–8]

\[2–8\]	Acetic acid	$\Delta\nu$, cm^{-1}	Stearic acid	$\Delta\nu$, cm^{-1}	Oleic acid	$\Delta\nu$, cm^{-1}	Assignment of vibrations
3550			3583	−33			Free OH group
3005	3028	−23	3125	−120	3052	−47	bonded by 2 H-bonds (ν CH$_2$);
2925	2925	0	2927	−2	2918	+7	bonded by 3 H-bonds (ν CH$_3$);
2853	2857	+4	2843	−10	2844	−9	bonded by OH in dimers (ν CH$_2$);
2726	2686	−40	2726	0	2683	−43	OH-bonded in dimers
1720	1700	−20	1680	−40	1692	−28	ν C=O in COOH;
–	–	–	1600	–	1606	–	ν_{as} COO$^-$;
1525	–	–	1525	0	1551	+26	ν_{as} COO$^-$
1430	1466	+33	1480	+50	1472	+42	ν_s COO$^-$, ΔCH$_2$ scissoring scissoring in chains, if CH$_2$ is next to C=O or C-CH=CH$_2$
	1438	+8	1400	−30	1435	+5	
1375*	1350	+25	1379	−4	1380	−5	δ CH$_3$ in the dimeric ring; γ_w wagging; -COOH in dimers; $Q = \nu$ C–O; δ CH$_2$ twisting in the dimeric ring
1300	1300	0	1320	−20	1305	−5	
1245	1266	−21	1263	−18	1238	+7	
1192	1192	0	1195	−3	1192	0	γ_r CH2 with an unbranched chain with end COOH
1125	1104	−21	1104	−21	1104	−21	νOH in C-OH groups with five or six-membered cycles
940	940	0	926	+14	953	−13	Any OH group; γ_t twisting in the dimeric ring; planar stretching vibrations Q(C–C) = ν_s rocking; γ_r CH$_2$ of the methylene chain
750	744	+6	728	+22	756	−6	γ OCO; γ CCC; γ OCC in dimeric rings of carboxylic acids
646	642	+4	636	+10	638	+8	

Designations for the vibrations:
$Q = \nu_s$; ν_{as} – symmetric and asymmetric deformation vibrations;
δ_s; δ_{as} – deformation scissoring, symmetric and asymmetric stretching;
γ_w; γ_t; γ_r – wagging, twisting, and rocking deformation vibrations;
Δ – deformation vibrations of the skeleton of the chain;
ν C=O=q=Q=γOCO; γOCC; γCCC –vibrations in the dimeric ring;
γOCC; γCCC – nonplanar vibrations in the stretched chain
*transition from the planar to the nonplanar conformation due to the shift of ν OH polar vibration with γ_t and γ_r in the methylene chain of the −CH$_2$− groups
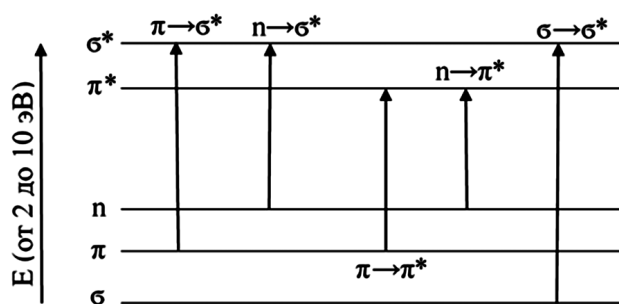
Scheme 1

region indicate the π and n electronic states. The following functional groups

are called chromophoric and cause the absorption in the UV region [2–6].
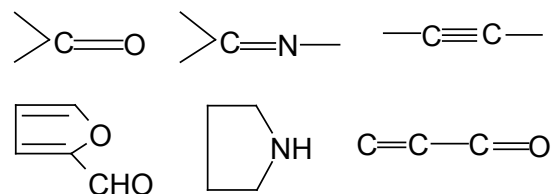
The absorption of light in the visible region and absorption of the UV light in the near UV
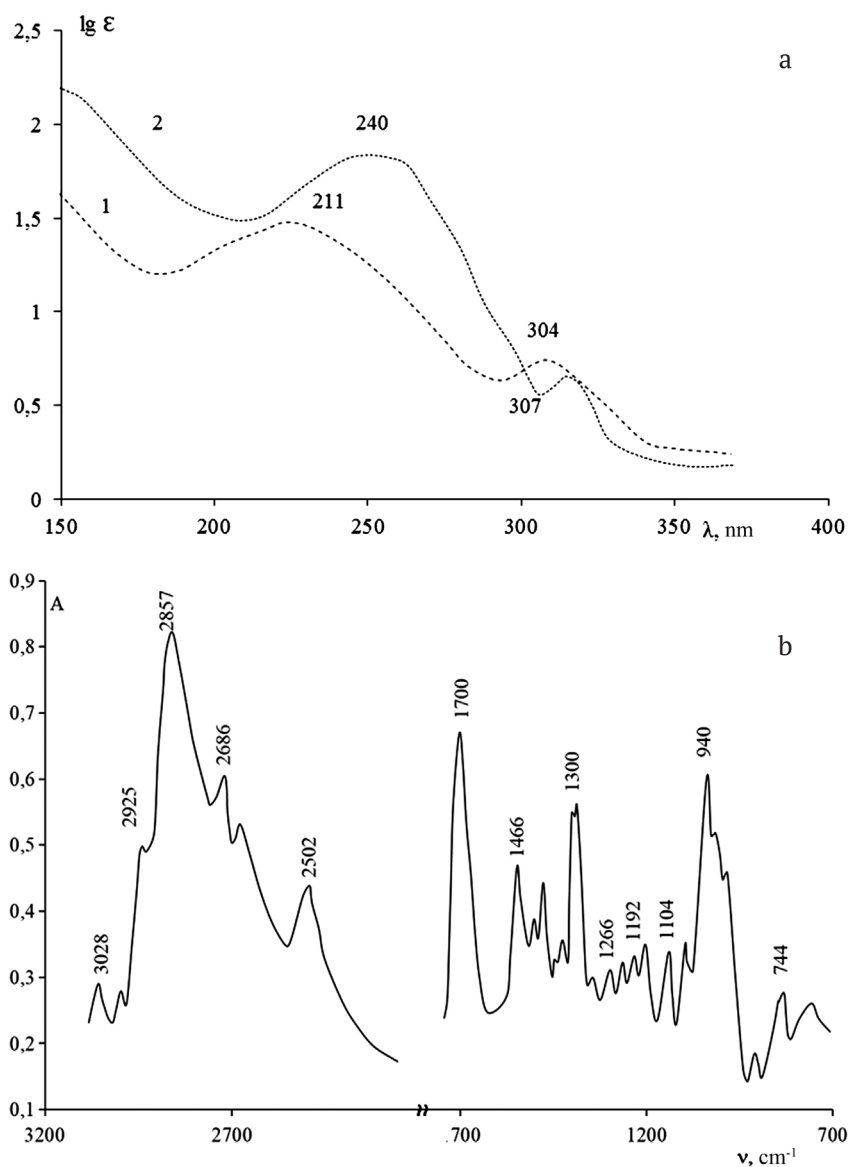
Fig. 3. UV (a) and IR spectra (b) of acetic (*1*) and oleic acid (*2*)

It should be noted that such transitions are one of the causes of the formation of dimers by −COOH end groups:

Scheme 2
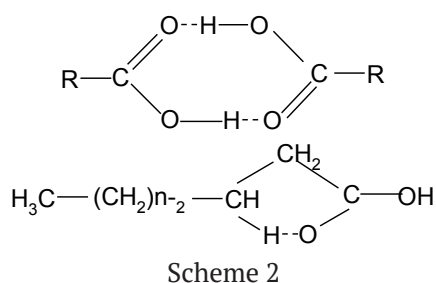
as well as the formation of five-membered cycles due to the appearance of hydrogen bonds between CH_2 methyl groups of hydrophobic chains and oxygen in carboxylic groups [2, 3, 11]:

Scheme 3
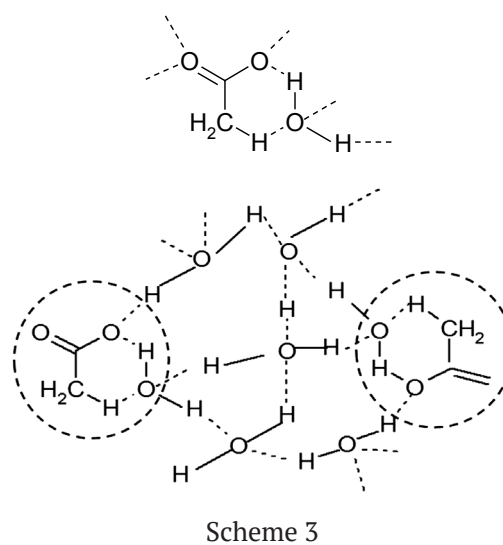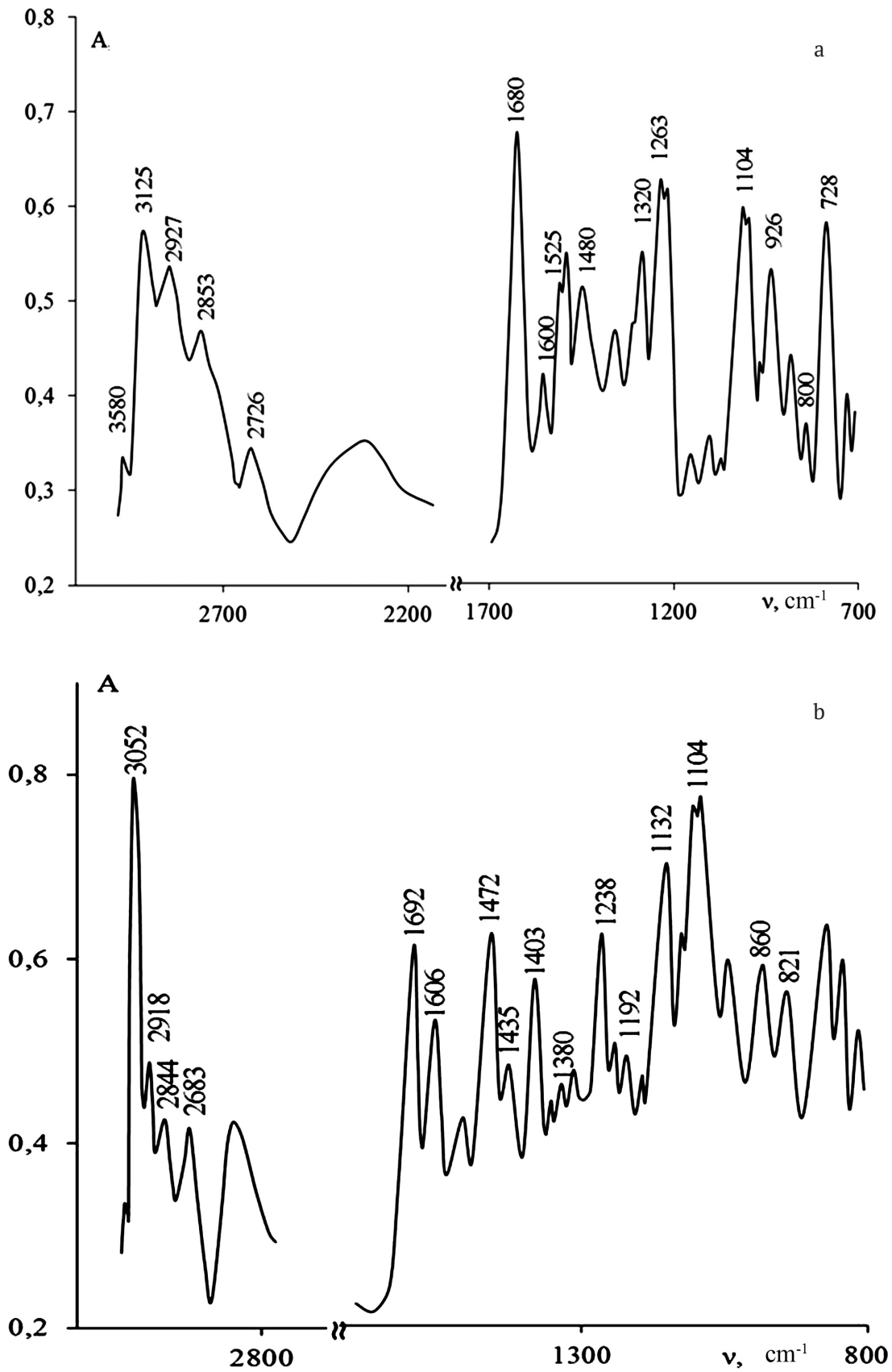
Fig. 4. UV and IR spectra of stearic (a) and oleic (b) acids. UV spectra of stearic (*1*) and oleic (*2*) acids (c)

c
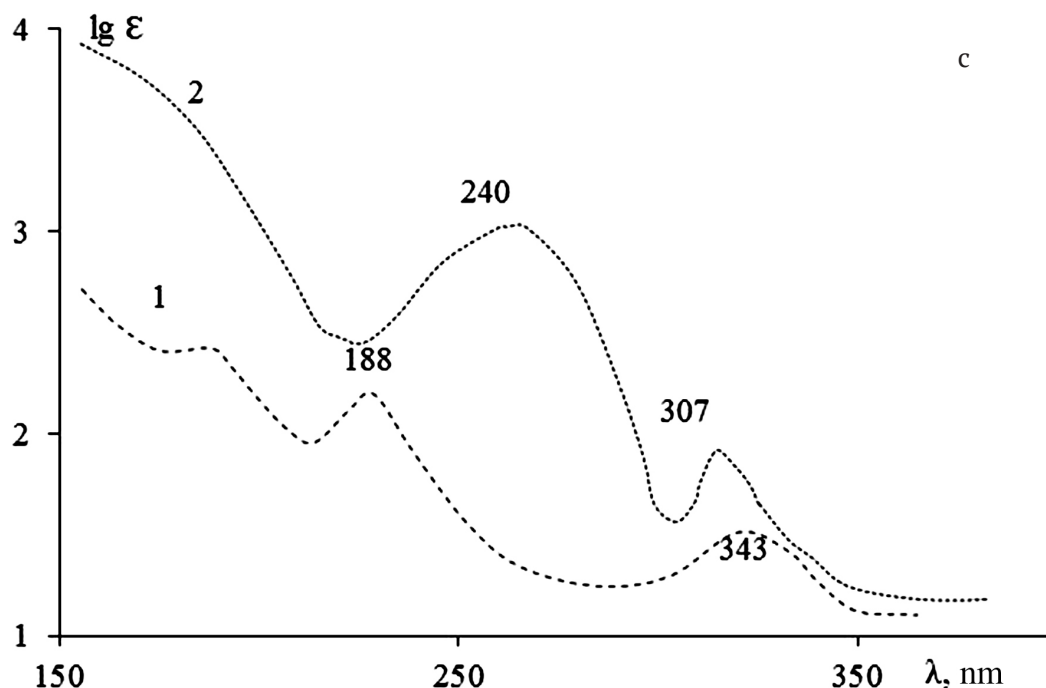
End of Fig. 4

This is demonstrated by the peaks 1192, 1104, 940, 744, and 638 cm^{-1}. Intense bands at 182 nm ($n{\to}\sigma^*$ transitions), 240 nm ($\pi{\to}\pi^*$ transitions), and 305–343 ($n{\to}\pi$ transitions) in the UV spectra of carboxylic acids (Fig. 3a, 4b) indicate the possibility of the formation of cyclic structures in the solutions and the mentioned bands prove the accuracy of the description of their structure (scheme 2 and 3) based on the results of the IR spectroscopy.

Besides experiments with monomers, UV and IR spectroscopy can be used in experiments with polymers containing carboxylic groups [3–6]. The most interesting examples of this group of polymers are poly(methyl methacrylate) and poly(methacrylic acid):
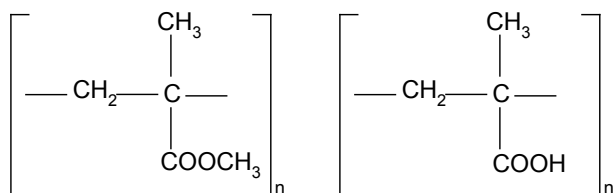
In the IR spectra of poly(methacrylic acid), the bands at 1750 and 1700 cm^{-1} are assigned to the vibrations of carbonyl in monomer and dimer groups, and the bands at 3540 and 2650 cm^{-1} are assigned to the vibrations of free and bonded hydroxyl groups [3, 5, 6]. Peaks 1490 and 1460 cm^{-1} indicate the presence of σ_s and σ_{as} (deformation vibrations) of the methyl group $=CH_2$. In the spectra of copolymers of metacrylic acid with acrylonitrile, a shift in the location of the bands is observed at 1263 and 1167 cm^{-1}, caused by the vibrations of the C–O-bond [4, 5, 11].

The IR spectra of syndiotactic poly(methyl methacrylate) reveal a group of bands in the 3460–2835 cm^{-1} region, caused by the vibrations of free and bonded hydroxyl groups [3, 5, 6, 9]. It should be noted that the peaks 2948–2835 cm^{-1} also characterise the vibrations of methyl and methylene groups [3, 6, 7] (Table 6). The variability of the bands at 1270, 1240, 1190, 1172, and 1163 cm^{-1} is accounted for by intramolecular interactions, since the multiplet is also observed in the spectrum of diluted solutions, i.e. without intermolecular interaction.

Similar to the monomers of carboxylic acids, poly(methyl methacrylate) demonstrates clear peaks at 1430–910 cm^{-1}, indicating the transition from planar conformation (scissoring ρ_s and rocking γ_r) in hydrophobic tails to the nonplanar conformation (wagging γ_w and twisting γ_t) caused by the mixture of the stretching vibrations

Table 5. Assignment of close absorption bands of -COOH- and -CH$_2$ groups in the IR spectra of carboxylic acids

Vibrations of COOH groups ν, cm^{-1}	Vibrations of CH$_2$ groups ν, cm^{-1}
3580 – free OH	
3028 – OH with two H-bonds	3008 =CH in RCH=CHR' (trans)*
2962 – OH with three H-bonds	2962 ν_{as} CH$_2$
2843 – OH in dimers	2843 ν_s CH$_2$
1700 – C=O in COOH⁻ groups	
1525 – C=O in COO⁻ groups	1480 ΔCH$_2$ next to C=O
1379 – C-O in dimers	1375 σ C$^+$H$_3$ in the dimeric ring
1300 – COOH in dimers	1300 γ_w CH$_2$ wagging stretching in the ring
1245 – C-OH in the dimeric ring	1245 γ_t twisting in the ring
1104 – C-OH in five-membered cycles	1122 γ_r rocking next to COOH
944 – OH groups in COOH	960 γ_w; γ_t; γ_r in the dimeric ring
737 – OCC in the dimeric ring	638 γOCO; γCCO in dimers with COOH

Assignment of vibrations:
$Q = \nu_s$; ν_{as} – symmetric and asymmetric stretching;
φ = ρ = σ_s; σ_{as} – deformation scissoring, symmetric and asymmetric stretching;
γ_w; γ_t; γ_r – wagging, twisting, and rocking stretching;
Δ – deformation vibrations of the skeleton of the chain;
ν C=O=q=QC=O; γOCO; γOCC; γCCC –vibrations in the dimeric ring; nonplanar vibrations in the completely stretched chain.

ν_s and ν_{as} of the polar groups with γ_r- and γ_t deformation vibrations of CH$_2$groups of the methylene chain (Fig 5, Table 6) [3, 5, 8, 9]. Thus, dimeric rings are formed in polyacrylates and poly(methyl methacrylates) due to intramolecular interactions. The transition form the planar to the nonplanar conformation is also observed in the polymer chain.

Microscopic and microphotographic methods of studying polymers with carboxyl functional groups are supplementary methods used to visualise the process of swelling and contraction of carboxyl sorbents during their contact with aqueous solutions [13, 14]. The objects of our study were carboxylic cationites CB-2×2 and CB-4 (scheme 7):

CB-4

CB-2
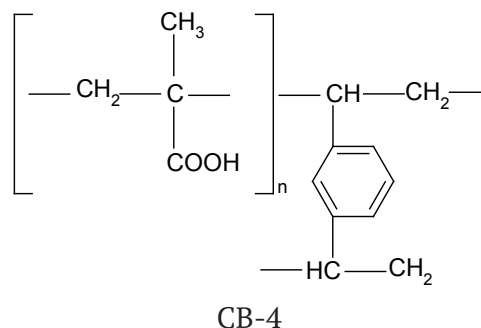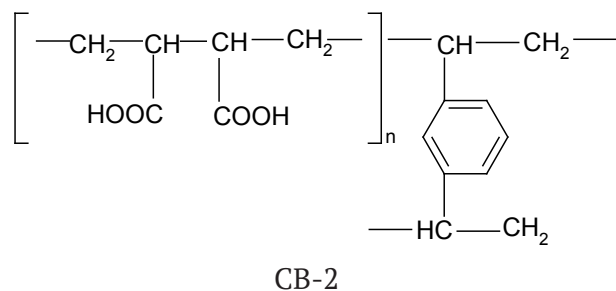
Fig. 5b demonstrates that the IR spectra of the sorbents are close to the IR spectra of poly(methyl methacrylates) (Fig. 5a), namely in the vibration areas of the carboxylic groups, formation of dimers, and intramolecular H-bonds. There is a difference in the vibration areas characterising the presence of divinyl benzene: 1310, 1053, 922, 896, and 700 cm^{-1}.

The microscopic study of the swelling of certain beads of carboxylic cationites, the kinetic curves of volume change, and the swelling diagrams demonstrated that slightly acidic ion exchangers have the minimal volume in the H form as compared to the salt forms (Fig. 6). This effect is accounted for by the formation of associates presented as dimer cycles with methyl –CH$_2$ groups
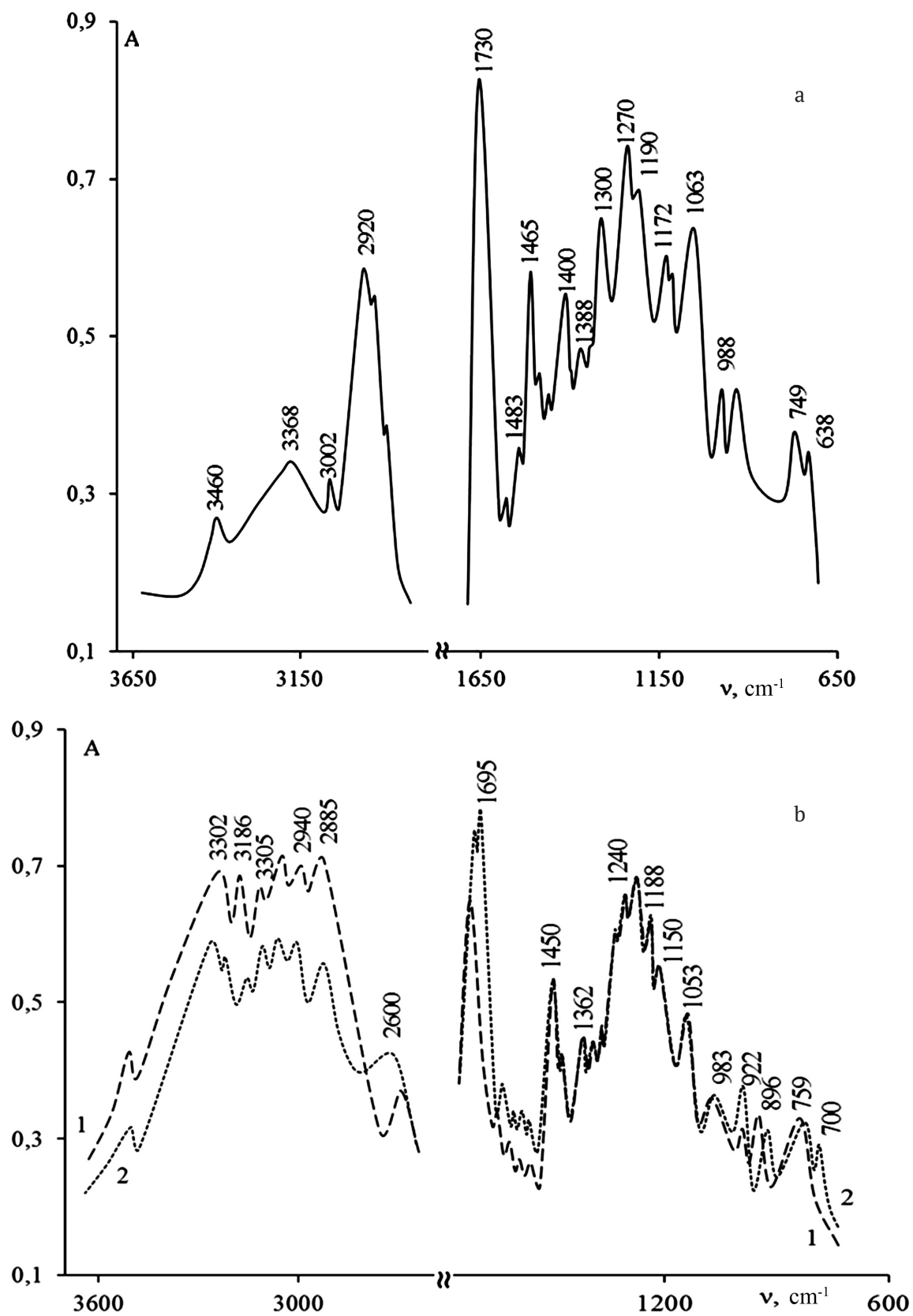
Fig. 5. IR spectra of poly(methyl methacrylate) (5a) CB-2 and CB-4 (5b): *1* – CB-2; *2* – CB-4
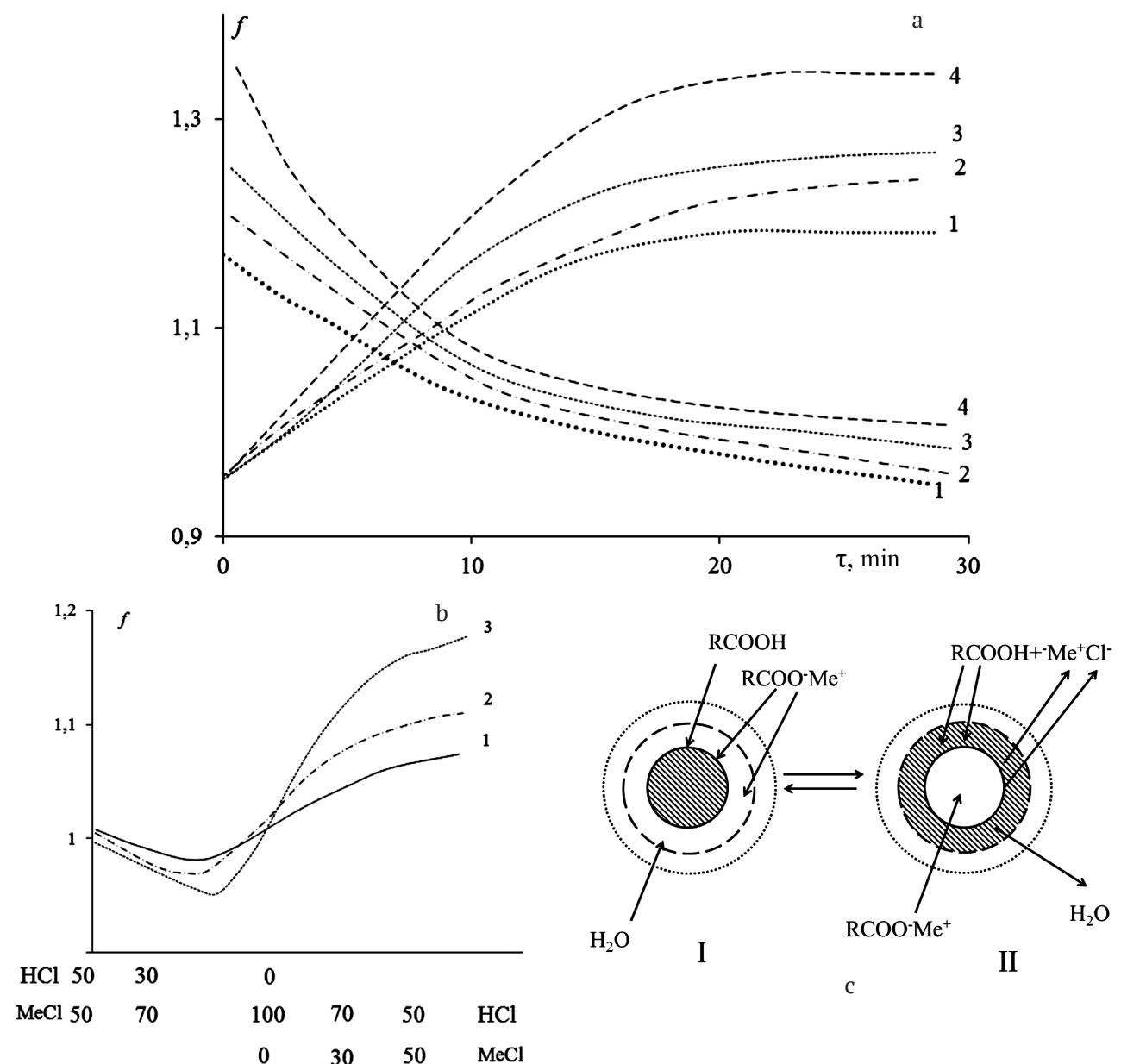
Fig. 6. The swelling curves of the CB-2 cationite (a) and the bead volume change of the cation exchanger CB-4 (b): *1* – R–COOH; *2* – R–COOLi; *3* – R–COONa; *4* – R–COOK $f = V_\tau/V_n$, where V_τ, V_n are the bead volume at the moment τ and initial bead volume in the H form respectively. A scheme of the exchange processes RCOOH+MeOH (I) and RCOOMe+HCl (II) (c)

and as intramolecular H-bonds formed due to the $\pi \to \pi^*$ transitions in benzol cycles [1–6,15–21].

When the reaction takes place in the surface layers of the cationite bead, the carboxylic groups are ionised through the reaction:

$$R–COOH + Me^+ + OH^- \to R–COO^-...Me^+ + H_2O.$$
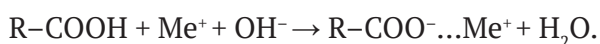
During this reaction, the metal ions neutralise the negative charge R–COO⁻. As a result, two shells are formed in the bead of the carboxylic cationite: the external shell R–COO⁻...Me⁺ and

the internal shell R–COOH (Fig. 6c). The exchange reaction is accompanied by the swelling of the bead. The amount of water transported by the ions during the reaction is not sufficient for the hydration of the cationite in salt form, which results in further introduction of water from the solution into the sorbent (Fig. 6c) [15–19].

During the R–COO⁻ + Me⁺ + H⁺ + Cl⁻ → R–COOH...Me⁺ + Cl⁻ transition, in the first stages of the exchange process the –COO⁻ groups located on the bead's surface absorb H⁺ ions from the solution

Table 6. Poly(methyl methacrylate) IR spectrum

Wave number, cm^{-1}	Vibrations
3460	Free OH groups; 2 (ν C=O)
3368	Bonded OH groups; ν_{as} CH$_2$+ ν_s(CH$_3$-O)
3002	ν_s(CH$_3$-O)+ ν_{as}(L-CH$_3$)+ ν_s(L-CH$_3$) + ν_{as}(CH$_2$)
2920	Combination tone bonded with CH$_3$ in an ester group
2835	Id.
1730	ν C=O in COO$^-$ groups
1483	δ_{as} (CH$_3$-O); Δ CH$_2$ next to C=O
1465*	σ_{as} (CH$_3$-O); Δ CH$_2$ scissoring stretching next to C–CH=CH$_2$
1452 1438	δ (CH$_2$); σ_s (CH$_3$-O);
1388	σ_s (CH$_3$-O); σ^+(CH$_3$) in the dimeric ring
1300	γ_w wagging; –COOH in dimers
1270 1260	ν_{as}(C-C-O); Q = ν(C-O); σCH$_2$= γ_t(CH$_2$) in the dimeric ring
1190	γ_r(CH$_2$) rocking; νC-C)+ σ(CH) groups
1172	σ_s in esters (intramolecular)
1150	ν(C-C) mixed with deformation vibrations σCH
1063	То же
988 967	ν_s(C-O-C)= γ_r(CH$_3$-O)+ γ_r(L-CH$_3$)+γ_t in the ring; γ_r(L-CH$_3$) mixed with γ_t in the dimeric ring;
749 638	γ_r(CH$_2$) mixed with ν(C-C)+ σ (OCO)+ ν(OCC) in the dimeric rings with COOH groups

* ρ, γ_w; γ_t; γ_r – scissoring, wagging, rocking, and twisting vibrations;
Δ – deformation vibrations of the skeleton of the chain.

and become non-dissociated RCOOH groups. Thus, the bead is once more divided into two zones (Fig. 6c). Then the H$^+$ ions diffuse through the outer shell towards the boundary and replace the metal ions which are, in turn, eliminated from the cationite bead. The process can be described as interdiffusion between the hydroxonium ions and metal ions through the layer of the cationite in the H form. Processes (II) and (I) are accompanied by contraction and swelling respectively (Fig. 6c) as well as by the migration of the solvent either from or to the sorbent phase. Both processes have a clear boundary visible through a microscope. Processes I and II are indirectly proved by the calculation of the elongation of covalent bonds r (A–H) as the function of R(A...B) for bonds R(O...O) R(O...N); R(N...O); R(N...N), and R(CH$_2$...O), according to the results of the IR spectroscopy (Fig. 7). Each curve was obtained by shifting curve 1 (Fig. 7) horizontally according to the van der Waals radii

$$[R_{eq}(O...O) = R_{exp}(A...B) + 2r_\upsilon(0) - r_\upsilon(A) - r_\upsilon(B)];$$
$$[r_{substr}(A-H) = r_{eq}(O-H) + r_c(A) - r_c(0)], \quad (2)$$

where r_υ is the van der Waals radius, r_c is the covalent radius.

The vertical shift is performed taking into account the covalent radii. Taking into account the processes in (2), we obtained an equation for calculating R(CH$_2$...O), based on the value of the band shift $\Delta\nu$:

$\Delta\nu°$ for R(CH$_2$...O) = 3200 cm^{-1};
$\Delta\nu = 0.89 \cdot 10^5(3.42 - R_{CH_2...O})$.

Similar interactions accompanied by the formation of H-bonds between hydrophobic CH groups and hydrophilic C=O, N–H, C≡H (in acetylene), and S–H groups were described earlier in [2, 4], which makes it necessary to explain the term "hydrophobic interactions". The term "hydrophobic interactions" was introduced to describe the joint effect of the London dispersion
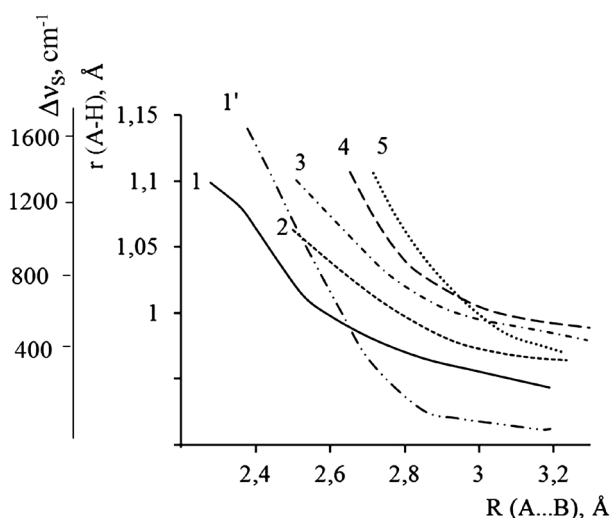
Fig. 7. The values of the covalent bonds r(A–H) calculated as a function of R (A...B) for the associates *1* – R(O...O); *2* – R(O...N); *3* – R(N...O); *4* – R(N...N); *5* – R(CH$_2$...O). Curves *1'* represent the dependence between R(O...O) and Δv_s

forces (forces resulting from the formation of the instantaneous dipoles), the van der Waals forces (orientation, induction, and steric repulsion), and hydrogen bonds on the processes taking place in aqueous solutions [1, 2, 8]. The nature of these interactions is similar to that of other intermolecular (noncovalent) interactions, although in some cases they are characterised by small enthalpy changes [1, 2, 4], calculated based on the values of Δv (curve *1'* in Fig. 7). It is noteworthy that the shape of the curves showing the dependencies for [R(O...O) – r(A–H)] and [R(O...O) – Δv_s], are symbatic. This proves the correctness of the methods used and accuracy of the calculations presented in this article.

4. Conclusions

The article described the method and analysed the results of the combined use of UV-vis and IR spectroscopy, as well as the microscopic and microphotographic studies of intermolecular interactions and hydration properties of acetic, stearic, and oleic acids, and carboxylated cationites CB-2 and CB-4 in the exchange reactions R-COOH + NaOH ↔ R–COO$^-$⋮Na$^+$ + H$_2$O. The energy of the hydrogen bond (E_H), the enthalpy (ΔH), the force constant of the H-bond (K_H) and OH-bond (K_{OH}), and the elongation of the covalent bond (Δr_{OH}) were calculated based on the results of the IR spectroscopy for intermolecular interactions of

carboxylic acids in solutions. The article suggested a method for calculating the length of the H-bond and R$_{CH2...O}$ between the donor (CH$_2$ group) of the non-polar chains of fatty acids and the acceptor (O- in COOH groups) resulting from the formation of cyclic structures in carboxylic acids.

The microscopic method was used to obtain the swelling/contraction curves for the beads of the cationites CB-2 and CB-4. The first description of the formation of two boundaries (shells) in the beads of carboxylic cationites during the ion exchange reaction R–COOH + NaOH ↔ R–COO$^-$⋮Na$^+$ + H$_2$O was provided.

The study demonstrated that the combined use of the UV, IR, and visible spectroscopy is the most effective for studying the intermolecular bonds and hydration properties in solutions and polymers.

Conflict of interests

The authors declare that they have no known competing financial interests or personal relationships that could have influenced the work reported in this paper.

References

1. Tinoco I., Sauer K., Wang J.C., Puglisi J. D., Harbison G., Rovnyak D. *Physical Chemistry: Principles and Applications in Biological Sciences*. (4th Ed.). Prentice Hall; 2002. 704 p.

2. Pimentel G. C., McClellan A. L. *The hydrogen bond*. San Francisco: W.H. Freeman; 1960. 475 p.

3. Dehant I., Danz R., Kimmer W., Shmolke R. *Infrakrasnaja spektroskopija polimerov*. [Infrared spectroscopy of polymers]. Moscow: Himiya Publ.; 1976. 472 p. (in Russ.)

4. Bökker Ju. *Spektroskopie*. Wurzburg: Vogel Buchverlag; 1997. 526 p.

5. *Zundel* G. *Hydration and intermolecular interaction*. Germany by Verlag Chemie; 1969. 324 p.

6. Ugljanskaja V. A., Chikin G. A., Selemenev V. F., Zav'jalova T. A. *Infrakrasnaja spektroskopija ionoobmennyh materialov*. [Infrared spectroscopy of ion exchange materials]. Voronezh: VGU Publ.; 1989. 208 p. (in Russ.)

7. Kazicyna L. A., Kupletskaja N. B. *Primenenie IK-, UF-, JaMR-spektroskopii v organicheskoj himii* [Applications of IR, UV, and NMR spectroscopy in organic chemistry]. Ucheb. posobie dlja vuzov. Moscow: Vyssh. Shkola Publ.; 1971. 248 p. (in Russ.)

8. Selemenev V. F., Kotova D. L., Oros G. Ju., Hohlov V. Ju. Supersaturation processes and methods for obtaining amino acids on ion-exchangers. *Sorbcionnye i hromatograficheskie processy = Sorption*

and Chromatographic Processes. 2013;13(5): 623–633. Available at: https://journals.vsu.ru/sorpchrom/article/view/1684/1740 (In Russ., abstract in Eng.)

9. Selemenev V. F., Hohlov V. Ju., Bobreshova O. V., Aristov I. V., Kotova D. L. *Fiziko-himicheskie osnovy sorbcionnyh i membrannyh metodov vydelenija i razdelenija aminokislot* [Physicochemical fundamentals of sorption and membrane methods for the isolation and separation of amino acids]. Voronezh. VGU Publ.; 2002. 300 p. (in Russ.)

10. Babkov L. M., Puchkovskaja G. A., Makarenko S. P., Gavrilko T. A. *IK-spektroskopija molekuljarnyh kristallov s vodorodnymi svjazjami* [IR spectroscopy of molecular crystals with hydrogen bonds]. Kiev: Naukova Dumka Publ.; 1989. 160 p. (in Russ.)

11. Selemenev V. F., Nazarova A. A., Sinjaeva L. A., Zjablov A. N., Popov V. N. Interaction processes with the participation of higher carboxylic acids. *Sorbcionnye i hromatograficheskie process = Sorption and Chromatographic Processes*. 2013;13(3): 307–312. Available at: https://journals.vsu.ru/sorpchrom/article/view/1647/1702 (In Russ., abstract in Eng.)

12. Mur R., Flik Dzh. Vlijanie koncentracii vody na mehanicheskie i reostaticheskie svojstva polimetil-metakrilata. V kn.: *Voda v polimerah* [The effect of water concentration on the mechanical and rheostatic properties of polymethyl methacrylate. In: *Water in polymers*. Moscow: Mir Publ.; 1984: 513–527. (in Russ.)

13. Shamritskaja I. P., Matveeva M. V. A microphotographic method for studying the kinetics of the swelling of ion-exchange resins. *Teorija i praktika sorbcionnyh processov = Theory and practice of sorption processes*. Voronezh: Izd. VGU Publ.; 1971. vol. 5. p. 61-64. (in Russ.)

14. Broejr M., Bjura E., Fukson A. Izmenenie ob'ema pri svyazyvanii vody fibrillami volos. V kn.: *Voda v polimerah* [A change in volume occurring when water binds to hair fibrils. In: *Water in polymers*]. Moscow: Mir Publ.; 1984. p. 304–314. (in Russ.)

15. Shtykov S. N. Ljuminescentnyj analiz v organizovannyh sredah. V kn. *Problemy analiticheskoj himii* [Luminescent analysis in organised media. In: *Problems of analytical chemistry*]. Moscow: Nauka Publ., 2015. vol. 19. p. 121–155. (in Russ.).

16. Erdey-Grűz T. *Grundlagen der Strukrur der Materie*. Leipzig: Teubner; 1967. 498 p. DOI: https://doi.org/10.1007/978-3-663-02531-3

17. Dawson R., Elliot D. C., Elliot W., Jones K. M. *Data for biochemical research*. London: Oxford Science Pub.; 1986. 543 p.

18. Maurice P. *Environmental surfaces and interfaces from the nanoscale to the global scale*. Wiley; 2013. 540 p.

19. Bökker J. *Chromatographie. Instrumentale analytik: mit chromatographie und kapillarelectrophorese*. Wurzburg: Vogel Buchverlag; 1997. 472 p.

20. Dzhatdoeva A. A., Polimova A. M., Proskurnina E. V., Vladimirov Y. A., Proskurnin M. A.

Determination of lipids and their oxidation products by IR spectrometry. *Journal of Analytical Chemistry*. 2016;71(6): 542–548. DOI: https://doi.org/10.7868/S0044450216060050

21. Max J.-J., Chapados C. Infrared spectroscopy of aqueous carboxylic acids: Comparison between different acids and their salts. *J. Phys. Chem. A*. 2004;108: 3324–3337. DOI: https://doi.org/10.1021/jp036401t

Information about the authors

Vladimir F. Selemenev, DSc in Chemistry, Professor, Department of Analytical Chemistry, Voronezh State University, Voronezh, Russian Federation; e-mail: common@chem.vsu.ru. ORCID iD: https://orcid.org/0000-0002-5061-2588.

Oleg B. Rudakov, DSc in Chemistry, Professor, Head of the Department of Chemistry and Chemical Technology of Materials, Voronezh State Technica University, Voronezh, Russian Federation; e-mail: rudakov@vgasu.vrn.ru. ORCID iD: https://orcid.org/0000-0003-2527-2857.

Natalya V. Mironenko, PhD in Chemistry, lecturer, Department of Analytical Chemistry, Voronezh State University, Voronezh, Russian Federation; e-mail: natashamir@yandex.ru. ORCID iD: https://orcid.org/0000-0002-3049-6647.

Sergey I. Karpov, PhD in Chemistry, Associate Professor, Department of Analytical Chemistry, Voronezh State University, Voronezh, Russian Federation; e-mail: karsiv@mail.ru. ORCID iD: https://orcid.org/ 0000-0001-8469-7236.

Victor N. Semenov, DSc in Chemistry, Professor, Head of the Department of General and Inorganic Chemistry, Voronezh State University, Voronezh, Russian Federation; e-mail: semenov@chem.vsu.ru. ORCID iD: https://orcid.org/ 0000-0002-4247-5667.

Natalya. A. Belanova, PhD in Chemistry, lecturer, Department of Analytical Chemistry, Voronezh State University, Voronezh, Russian Federation; e-mail: belanovana@mail.ru. ORCID iD: https://orcid.org/0000-0002-3869-7160.

Liliia A. Sinyaeva, PhD in Chemistry, lead engineer at the Department of Analytical Chemistry, Voronezh State University, Russian Federation; e-mail: liliya.sinyaevavsu@mail.ru. ORCID iD: https://orcid.org/0000-0002-7378-346X.

Anatoly N. Lukin, PhD in Physics and Mathematics, Associate Professor, Department of Solid State and Nanostructure Physics, Voronezh State University, Voronezh, Russian Federation; e-mail: ckp_49@mail.ru. ORCID iD: https://orcid.org/0000-0001-6521-8009.

All authors have read and approved the final manuscript.

Condensed Matter and Interphases
(Kondensirovannye sredy i mezhfaznye granitsy)

Solid Dosage Forms of Nootropic Action Based on Pantogam and Succinic Acid

© 2020 D. A. Slivkin[a], Yu. A. Polkovnikova[✉,b], A. I. Slivkin[b], A. S. Belenova[b], S. N. Suslina[a], A. A. Kashchavtseva[b]

[a]Peoples Friendship University of Russia,
6 Miklukho-Maklaya ul., Moscow 117198, Russian Federation

[b]Voronezh State University,
1 Universitetskaya pl., Voronezh 394018, Russian Federation

Abstract

In recent years, research related to the search and study of the mode of action of new and used in medicine nootropic agents has been carried out at a high rate. The research related to the search for new combined drugs of nootropic action based on the substances of d-gamma-Pantothenate of calcium and succinic acid, which have neurometabolic, atigipoxic, and adaptogenic properties, is of interest. The purpose of this study was to develop and justify the optimal composition and manufacturing technologies of tablets with nootropic effect and standardise the proposed dosage forms containing Pantogam and succinic acid.

The method for preparing the tablet mixture is as follows: all components were weighed in the required amount, Pantogam was placed in the mortar, then succinic acid was added and ground to a consistent white powder. The tablets were pressed on a manual press at a pressure of 120 mn/m². The coating was applied on a laboratory fluidised bed unit with a single nozzle in a perforated drum with a volume of 1000 ml. The obtained tablets were evaluated according to the requirements for State Pharmacopoeia XIII and State Pharmacopoeia XIV. The comparison of the Pantogam tablets with succinic acid obtained by direct pressing and by wet granulation showed that the method of direct pressing allows obtaining tablets with good physical and mechanical properties and bioavailability. The methods based on acid-base titration and spectrophotometric determination were developed for the quantitative determination of Pantogam in tablets. The method of quantitative determination of succinic acid in dosage forms was validated.

Based on the study of physicochemical and technological properties of substances and excipients, the compositions and technology for obtaining tablets containing Pantogam and succinic acid were justified and developed. It was found that solid-phase interactions occur with the combined presence of Pantogam and succinic acid in the tablets. The methods of qualitative and quantitative analysis of dosage forms containing Pantogam and succinic acid based on complexometric titration and high-performance liquid chromatography were developed. The procedure of validation of the method for determining succinic acid by HPLC in the developed dosage forms confirmed the validity of the proposed method.

Keywords: Pantogam, succinic acid, tablets, complexometry, high-performance liquid chromatography, validation.

✉ Yulia A. Polkovnikova, e-mail: juli-polk@mail.ru

1. Introduction

Cerebrovascular diseases remain an acute medical and social issue of modern society [1-3]. The pharmacological correction of cerebral circulation is a pressing problem of modern medicine as a significant number of cerebral diseases are based on the factors of vascular origin while the diseases themselves are accompanied by loss of capability to work, disablement, and death [4–7]. Today, pharmaceutical science and pharmaceutical technology, in particular, pay great attention to the search and creation of drugs that increase the resistance of the brain and the nervous system to disturbing factors, improve mental activity, activate memory and learning processes, protect the brain neurons from premature neurodegradation, and postpone senile dementia [8-11]. Nootropic drugs that are successfully used for the treatment of psychoneurological disorders in adults and children hold a valuable place among neuropsychotropics [12–15].

Pantogam, the calcium salt of D-homopantothenic acid, is one of the drugs used in psychoneurology. It is successfully used as a nootropic drug in paediatrics for the treatment of arrested development, complicated oligophrenia, hyperkinetic disorders, epilepsy, neurotic-like conditions, post traumatic stress disorder, etc. [16]. The neurometabolic action of Pantogam consists of the normalisation of energetic processes of metabolism of gamma-aminobutyric acid in the central nervous system and the improvement of cerebral circulation [17]. The neurotrophic activity is associated with the improved utilisation of glucose and the stimulation of synthesis of RNA, protein, and ATP in neurons. The neuroprotection is conditioned by the increase in the resistance of nerve cells to hypoxia and ischemia as well as the decrease in the blood cholesterol level [18].

Succinic acid (SA) can be categorised as a nootropic drug. Antihypoxic action of SA is associated with its ability to intensify the utilisation of oxygen by tissues and the restoration of NAD-dependent cell respiration. SA's antistress and nootropic effect is conditioned by its influence on the transport of transmitter amino acids and the increased content of gamma-aminobutyric acid in the brain through the activation of Roberts shunt. The quick oxidation of SA by succinate dehydrogenase accelerates the resynthesis of ATP by cells, increases the concentration of restorable glutathione, and improves the resistance of mitochondria to peroxide degradation. SA can significantly intensify the diffusion of oxygen into different tissues and organs by stimulating cell respiration under stress and hypoxia [18]. This compound also shows cardiotropic, antioxidant, detoxicative, and adaptogenic actions [19].

Due to the unique pharmacological properties of Pantogam and succinic acid, the development of new effective dosage forms, which are more convenient for paediatrics, based on these substances is considered reasonable and prospective. Potentiation by the principal lines of Pantogam and SA's action on the organism should intensify the pharmacotherapeutic nootropic effect.

The purpose of this study was the experimental development and justification of the optimal compositions and manufacturing technologies of the tablets with nootropic effect as well as the standardisation of the proposed dosage forms containing Pantogam and succinic acid.

2. Experimental

To create tablets for the experiment, Pantogam substances (manufacturer FGUP "SKTB "Tekhnolog" of the Ministry of Education of the Russian Federation FSP 42-0348395903) and succinic acid substances (manufacturer OOO "Polisintez", Russia-FSP 42-0009-00) were used as well as the excipients that are registered in the Russian Federation and comply with the requirements of regulatory documents of Russian and foreign manufacturers in relation to the qualitative and quantitative content.

The method of preparation of the tablet mixture is as follows: all components were weighed in the required amount, Pantogam was placed in the mortar, then succinic acid was added and ground to a consistent white powder.

The coating was applied on a laboratory fluidised bed unit with a single nozzle in a perforated drum with a volume of 1000 ml. A commercial sonometer of ethyl acrylate with metacrylic acid, Kollicoat MAE 100, was used as a filming agent. After the conducted experiments, the following composition of the film coating was found optimal: copolymer Kollicoat MAE 100 –

5%, propylene glycol (plasticiser) – 0.9%, titanium dioxide (photoprotector) – 2.30%, and ethanol up to 100 %, viscosity η_{rel} = 1.98. Over the course of the experiment, the following parameters of the process and installation were determined: drum capacity – 30 %, drum rotation speed – 77 rpm, suspension feed rate – 20 ml/min, frequency of suspension solution spray – 2.0 ml after each 2.5 min, solution feed pressure – 2 kgf/cm², temperature of blast air – 75–80 °C.

IR spectroscopy was used to identify medicinal drugs [21, 22]. The spectra were collected on a Bruker Vertex 70. The quantitative determination of SA in tablets was conducted using high-performance liquid chromatography on an Agilent 1100 liquid chromatograph equipped with a multiwave detector with a diode matrix. A column with a reversed phase was used (Zerbax Extend-c18), size of the column – 2×150 mm, and a sorbent a particle size of 5 μm was used [23]. Detection was conducted with a wavelength range of 190–950 nm. The temperature of column thermostating was 35±0.3 °C, the volume of the induced sample was 20 mcl. The content of SA was calculated based on the peak areas on chromatograms of the working standard sample and the studied dosage forms.

Technological and biopharmaceutical studies of the substances and mixtures with the excipients were conducted at the Shared Research and Educational Centre of the People's Friendship University of Russia using testers to determine the density of the powders (Erweka "SVM 102"), a tester to determine the characteristics of the granulate (Erweka "GT"), an analytical sifting machine (Retsch "AS 200"), disintegration systems (Sotax "DT-2"), and a device for control of dissolution of solid dosage forms (Distek "Evolution 6100"). The microbiological research was conducted at the microbiological laboratory of the state unitary enterprise "Voronezhfarmatsia".

3. Results and discussion

3.1. Developing the composition of the tablets containing Pantogam and succinic acid

The tablet mixture of Pantogam with SA has a white colour and sourish taste. Experimentally determined technological properties of the mixture are presented in Table 1.

Six model mixtures using various combinations of the excipients were created in order to develop the production technology of the tablet cores of Pantogam with succinic acid (Table 2).

The granulate was assessed using the optimal technological characteristics (Table 3). The table shows that the compositions using 5 % of starch paste provide granules that are not solid enough (screening 27–30 %, compressibility 42.1–50.0). The granulate of composition No. 6 provides the least amount of screening, has the best flowability (11.2 g/s), and rather high compressibility (84 %).

The tablets were pressed on a manual press at a pressure of 120 mn/m². The technological characteristics of the obtained granulates and tablets confirm that composition No. 6 will provide the most solid tablets with the optimal disintegration (10.5 min). The average weight of the tablets is 0.20 g.

The dynamics of the release of Pantogam and SA from the obtained tablets of the composition No. 6 was assessed using an Erweka "SVM 102". The data of the dissolution test are presented in Table 4.

The obtained tablets meet the requirements for State Pharmacopoeia XIII and State Pharmacopoeia XIV.

The studies of the development of tablets using direct mixture pressing were conducted in order to compare the qualitative characteristics of solid dosage forms of the new composition

Table 1. Technological characteristics of substances and their mixtures

Name of the measured indicator	Characteristics of the components		
	Succinic acid	Pantogam	Mixture of Pantogam and succinic acid
Flowability, g/cm	12.2	7.8	11.58
Bulk weight, g/cm³	0.65	0.91	0.6
Compressibility, N	52	Does not compress	46
Angle of natural slope, °	32	50	39
Residual moisture, %	3.1	2.2	3.7

Table 2. Composition of model mixtures of Pantogam tablets with succinic acid

Name of the component	Number of components in the composition per tablet, g					
	1	2	3	4	5	6
Substances						
Pantogam	0.05	0.05	0.05	0.05	0.05	0.05
Succinic acid	0.05	0.07	0.04	0.05	0.05	0.05
Fillers						
Potato starch	0.088					0.044
Lactose		0.068				
Mannitol			0.099		0.086	0.04
Magnesium carbonate basic				0.088		
Binders						
*Starch (5 % paste)	0.002	0.002	0.001			
*Polyvinylpyrrolidone (10 % aqueous)				0.002	0.004	0.006
Lubricants						
Stearic acid	0.004	0.004	0.004	0,004	0,004	0.004
Aerosil	0.006	0.006	0.006	0.006	0.006	0.006
Tablet weight	0.2	0.2	0.2	0.2	0.2	0.2

Table 3. Technology characteristics of granulates and obtained tablets (x_1 n = 6)

Sub-item No.	Name of the indicator	No. of the mixture composition					
		1	2	3	4	5	6
Granulate							
1	Flowability, g/cm	8.7	8.0	9.1	10.2	10.8	11.2
2	Bulk weight, g/cm³	0.67	0.62	0.70	0.60	0.58	0.60
3	Compressibility, N	58	62	53	63	78	84
4	Porosity	47.4	42.1	50.0	51.0	47.4	49.2
5	Angle of natural slope, °	34	31	35	36	33	32
Tablets							
6	Ejection pressure, MN/m²	3.2	4.0	3.1	3.8	4.1	3.5
7	True density, g/cm²	1.67	1.52	1.48	1.40	1.42	1.40
8	Disintegration, min	5.5	5.0	6.5	7.0	8.5	10.5
9	Abrasion resistance, %	93.2	94.3	97.0	96.8	96.8	98.9
10	Compression ratio	3.82	2.85	4.04	3.20	4.60	4.10

containing Pantogam and SA and to optimise the compositions and conditions of production of the tablet dosage form.

The study of the technological properties of the pharmaceutical mixtures shows that composition No. 5 has the best characteristics.

Good compressibility and flowability allow obtaining the tablets using the method of direct pressing. The quality of the obtained tablets was evaluated by their appearance, disintegration, and durability in accordance with the requirements of State Pharmacopoeia XIII and State Pharmacopoeia XIV (Table 5). The obtained tablets are of white colour and planocylindric shape with a bevel and a score line. Their weight is 0.50±0.05 g and their appearance complies with the requirements of State Pharmacopoeia XIV. As for disintegration and abrasion resistance (Table 6), composition No. 5 allows obtaining tablets with good parameters. The dynamics of the release of Pantogam and SA from the tablets with composition No. 5 was assessed using a

Table 4. Dynamics of release of Pantogam and SA from coated tablets

Time, min	Content of Pantogam, %	Content of succinic acid, %
15	30.8	28.9
22	42.8	46.2
30	60.5	65.3
37	79.0	75.4
45	99.0	98.7

Table 5. Technological characteristics of tablets based on Pantogam and succinic acid

Sub-item No.	Name of the indicator	Number of the composition					
		1	2	3	4	5	6
1	Abrasion resistance, %	97.8	98.0	98.3	97.9	98.5	97.7
2	Disintegration, min	6.5	7.5	9.0	10.0	11.0	8.0

PC-1 "rotating basket" device. The comparison of the obtained results (Table 7) with the data on the release of active ingredients from the coated tablets allows drawing the following conclusion: it is unreasonable to use a complicated and expensive production technology for Pantogam tablets with SA using the granulation method and further application of the protective polymer coating. The method of direct pressing allows obtaining the tablets with good physicochemical parameters and bioavailability, although not protected from the aggressive action of gastric juice.

The tablets with Pantogam and SA with a polymer coating were subject to testing in artificial gastric juice and artificial intestinal juice (Table 8). The results allow drawing a conclusion that these tablets correspond to the requirements of State Pharmacopoeia XIII and State Pharmacopoeia XIV.

Table 6. Dynamics of release of Pantogam and succinic acid from tablets

Time, min	Content of Pantogam, %	Content of succinic acid, %
15	31.4	27.6
22	45.2	48.3
30	59.6	63.3
37	78.0	82.7
45	98.7	98.9

Table 7. Test results of the tablets coated with an intestinal-soluble polymer shell

Name of the indicator		ND requirements	Test results
Resistance to artificial gastric juice		At least 1 hour	Corresponds to: 1.8 hours
Dissolution in artificial intestinal juice, %		At least 70	Corresponds to: 89±2
Quantitative content	Pantogam, g	0.047–0.053	0.049±0.002
	Succinic acid, g	0.047–0.053	0.0048±0.002
Disintegration in artificial intestinal juice, min		No more than 60	28±0.5

Table 8. Results of quantitative determination of succinic acid in tablets

Sample	Area S of the peak (S)	Content of SA	
		г	%
Sample No. 1	2996	0.197	98.6
Sample No. 2	1625	0.049	98.3

3.2. Development of standardisation methods for tablets

Analysis of IR spectra shows that in the region of 1700–400 cm^{-1} the characteristic maxima of the dosage form mainly coincide in the intensity and the position of wave numbers on the axis with those of Pantogam and SA, which can be indicative of possible solid phase interactions and allows using IR spectroscopy to identify medicinal drugs in the developed tablets. Quantitative determination of Pantogam of the new dosage forms required the development of several variations of the methods based on: 1) acid-base titration of the solution obtained after the release of the fatty base on ice. The titrant was a 0.05 M solution of Trilon B (EDTA). The obtained results comply with the requirements of regulatory documentation. 2) spectrophotometric determination based on the interaction of the solution obtained after the release of the fatty base on ice with hydroxylamine and further interaction of the obtained hydroxamate with FeCl$_3$.

The solution of the working standard sample of Pantogam and the buffer solution of hydroxylamine were prepared in accordance with FS 42-2480-00 (Pantogam tablets 0.25 and 0.5 g).

The identification of Pantogam in the tablets was conducted by a typical reaction to calcium ion (from the water extract of the powder of the ground tablet) during its interaction with ammonium oxalate.

The content of SA was calculated based on the peak areas on the working standard samples and the tested dosage forms (Fig. 1–3).

Quantitative determination of Pantogam in tablets was conducted using complexometric
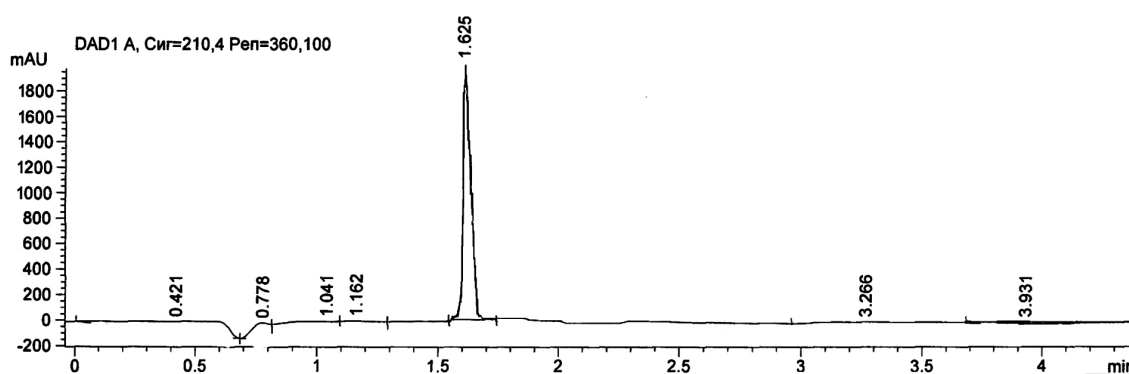

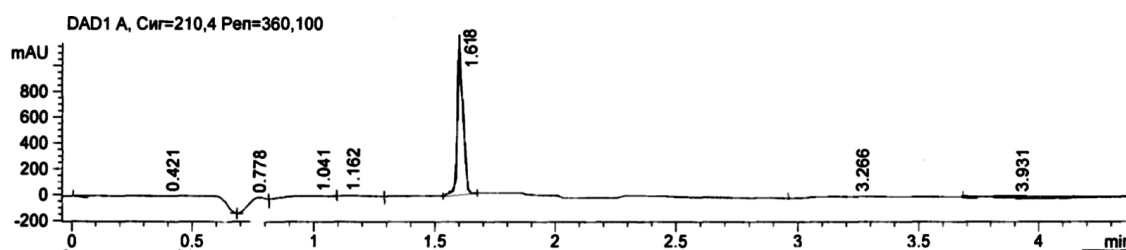**Fig. 1.** Chromatogram of the working standard sample of succinic acid

Fig. 2. Chromatogram of succinic acid in tablets of sample No. 1
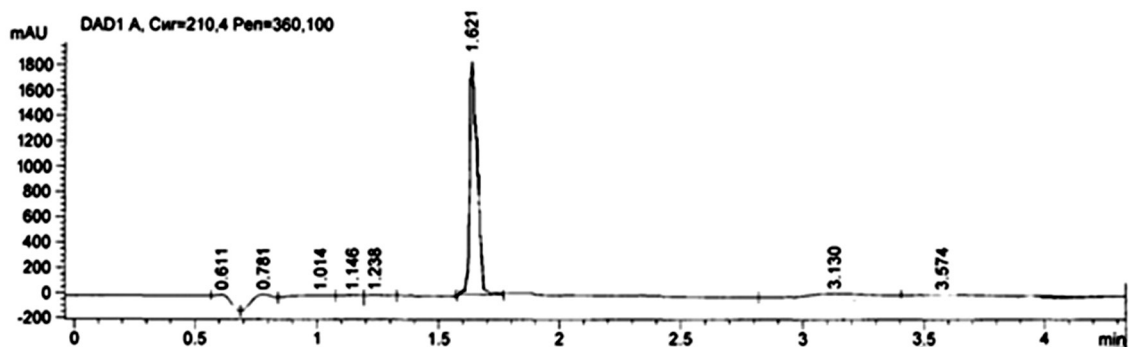

Fig. 3. Chromatogram of succinic acid in tablets of sample No. 2

titration of the solution of the powder made from the ground samples by Trilon B with the indicator mixture of Eriochrome Black T up to the bright blue colour. As a result of using this method, the content of Pantogam found in the tablets was 0.198 and 0.050 g, which complies with the requirements of State Pharmacopoeia XIV. This methodology provides clear reproducible results with the relative error of 1.14–1.20 %.

The obtained results of the quantitative determination of SA in tablets using HPLC (Table 8) showed that samples No. 1 and No. 2 of the studied tablets comply with the requirements of State Pharmacopoeia XIII and State Pharmacopoeia XIV.

To acknowledge HPLC, a method of determination of SA in dosage forms, and prove its viability, it was subject to validation assessment according to the requirements of GOST R ISO 5725 and recommendations of the International conference on harmonisation ICH Q2(RI) for such characteristics as linearity, analytical region, correctness, and precision.

The results of the validation assessment of the method are presented in Table 9.

The data presented in Table 9 allows drawing a conclusion that the method is reproducible and free from systematic errors.

Based on the results of the validation assessment of the SA determination method in dosage forms, it was established that the suggested method is characterised by correct accuracy and reproducibility, linear dependency (correlation coefficient for SA R = 0.999) in the analytical region in relation to the claimed content of SA in the medicinal product, which allows using it for the reliable assessment of the quality of medicinal products.

The stability of the developed dosage forms while in storage was determined for the studied samples on 5 series of each of them using standard measures in accordance with State Pharmacopoeia XIII and State Pharmacopoeia XIV.

The determination of shelf life of the developed tablet dosage forms based on Pantogam and SA conducted under standard conditions complying with the requirements of State Pharmacopoeia XIV (table 10) allows recommending the storage time of up to two years for these dosage forms at room temperature. The qualitative and quantitative

Table 9. Metrological characteristics of the method for determining succinic acid p = 99, t =2.4

x, %	S^2	S	Δx	E, %	$t_{calc.}$	F_{calc}
99.97	0.713	0.850	3.016	2.80	−0.85	1.6

Table 10. Quality indicators of the tablets with Pantogam and succinic acid during natural storage at 18-22 °C

Storage time, months	Requirements of ND to tablets (indicators of quality)						Category No. 3
	content, %		appea-rance	average weight of the tablet	abrasion resistance	disintegra-tion, min	Microbiological purity
	Pantogam	succinic acid					
tablets weighing 0.20 g							State Pharmacopoeia XIV
0	99.1	99.9	corresp.	204	98.6	10.8	corresp.
6	99.8	101.2	corresp.	201	98.0	10.2	corresp.
12	97.8	100.3	corresp.	198	97.2	10.5	corresp.
18	101.0	98.8	corresp.	199	97.8	9.8	corresp.
24	99.0	99.8	corresp.	202	97.9	10.0	corresp.
таблетки массой 0.50 г							State Pharmacopoeia XIV
0	99.2	99.7	corresp.	501	98.4	9.0	corresp.
6	98.7	99,8	corresp.	498	97.4	8.6	corresp.
12	99.0	100.0	corresp.	499	97.6	8.8	corresp.
18	98.0	100.9	corresp.	507	98	8.2	corresp.
24	100.5	99.4	corresp.	501	98.1	8.4	corresp.

content of the developed tablets remained unchanged over the course of 24 months.

4. Conclusions

1. Based on the study of physicochemical and technological properties of substances and excipients, the compositions and technology for obtaining tablets containing Pantogam and succinic acid were justified and developed. The composition of the tablets is as follows: Pantogam – 0.050 g; succinic acid – 0.050 g; mannitol – 0.086 g; aqueous polyvinylpyrrolidone 10 % – 0.004 g; stearic acid – 0.004 g; Aerosil – 0.006 g; total weight of the tablet – 0.200 g.

2. Methods of qualitative and quantitative analysis of medicinal forms containing Pantogam and succinic acid based on complexometric titration and high-performance liquid chromatography were developed. It was found that solid-phase interactions occur in case of the combined presence of Pantogam and succinic acid in tablets.

3. The method for the quantitative determination of succinic acid in the developed dosage forms was validated using HPLC for the following parameters: correctness, linearity, precision, and reproducibility.

4. The stability of the tablets in storage was studied in accordance with State Pharmacopoeia XIII and State Pharmacopoeia XIV. The study results allow recommending a storage time of two years for the developed tablets.

Conflict of interests

The authors declare that they have no known competing financial interests or personal relationships that could have influenced the work reported in this paper.

References

1. Voronkov A. V., Pozdnyakov D. I., Nigaryan S. A. Cerebroprotective effect of some phenolic acids under conditions of experimental brain ischemia. *Pharmacy & Pharmacology*. 2019;7(6): 332–339. DOI: https://doi.org/10.19163/2307-9266-2019-7-6-332-338

2. Cornelis E., Gorus E., Beyer I., Bautmans I., De Vriendt P. Early diagnosis of mild cognitive impairment and mild dementia through basic and instrumental activities of daily living: development of a new evaluation tool. *PLoS Med*. 2017;14(3): e1002250. DOI: https://doi.org/10.1371/journal.pmed.1002250

3. Wang P., Wang W., Hu Y., Li Y. Prolonged soluble epoxide hydrolase reactivity in brain endothelial cells is associated with long cognitive deficits in sepsis.

Molecular Neurobiology. 2020;57(6): 2846–2855. DOI: https://doi.org/10.1007/s12035-020-01925-2

4. Sun M. K. Potential therapeutics for vascular cognitive impairment and dementia. *Current Neuropharmacology*. 2018,16(7): 1036–1044. DOI: https://doi.org/10.2174/157015 9X15666171016164734

5. Lowry E., Puthusseryppady V., Coughlan G., Jeffs S., Hornberger M. Path integration changes as a cognitive marker for vascular cognitive impairment? – A pilot study. *Frontiers in Human Neuroscience*. 2020;21(14): 131. DOI: https://doi.org/10.3389/fnhum.2020.00131

6. Beggiato S., Borelli A. C., Ferraro L., Tanganelli S., Antonelli T., Tomasini M. C. Palmitoylethanolamide blunts amyloid-β42-induced astrocyte activation and improves neuronal survival in primary mouse cortical astrocyte-neuron co-cultures. *J. Alzheimer's Disease*. 2018;61(1): 389–399. DOI: https://doi.org/10.3233/jad-170699

7. Moretti R., Caruso P., Storti B., Saro R., Kassabian B., Sala A., Giannini A., Gazzin S. Behavior in subcortical vascular dementia with sight pathologies: visual hallucinations as a consequence of precocious gait imbalance and institutionalization. *Neurological Sciences*. 2020;14: 131. DOI: https://doi.org/10.1007/s10072-020-04445-y

8. Chen N., Yang M., Guo J., Zhou M., Zhu C., He L. Cerebrolysin for vascular dementia. *Cochrane Database of Systematic Reviews*. 2019;11. DOI: https://doi.org/10.1002/14651858.CD008900

9. Solleiro-Villavicencio H., Rivas-Arancibia S. Effect of chronic oxidative stress on neuroinflammatory response mediated by CD4+T cells in neurodegenerative diseases. *Frontiers in Cellular Neuroscience*. 2018;12: 114. DOI: https://doi.org/10.3389/fncel.2018.00114

10. Voronkov A. V., Shabanova N. B., Voronkova M. P., Lysenko T. A. Study of cerebrotropic dose-dependent effect of pyrimidine derivative under pir-9 code against the background of experimental cerebral ischemia in rats. *Pharmacy & Pharmacology*. 2018;6(6): 548–567. DOI: https://doi.org/10.19163/2307-9266-2018-6-6-548-567 (In Russ.)

11. Muzyko E. A., Tkacheva G. A., Perfilova V. N., Matvienko L. S., Naumenko L. V., Vasil'eva O. S., Tyurenkov I. N. Bulletin of experiment effects of gaba derivatives on anxious and compulsive behavior in offspring of rats with experimental preeclampsia. *Bulletin of Experimental Biology and Medicine*. 2020;168(4): 457–464. DOI: https://doi.org/10.1007/s10517-020-04731-x

12. Wilms W., Woźniak-Karczewska M., Corvini P. F., Chrzanowski Ł. Nootropic drugs: Methylphenidate, modafinil and piracetam – Population use trends, occurrence in the environment, ecotoxicity and removal methods. *Chemosphere*. 2019;233: 771–785. DOI: https://doi.org/10.1016/j.chemosphere.2019.06.016

13. Fekete S., Hiemke C., Gerlach M. Dose-related concentrations of neuro-/psychoactive drugs expected in blood of children and adolescents. *Therapeutic Drug Monitoring.* 2019;42(2): 315–324. DOI: https://doi.org/10.1097/FTD.0000000000000685

14. Saad C. Y., Fogel J., Rubinstein S. Awareness and knowledge among internal medicine resident trainees for dose adjustment of analgesics and neuropsychotropic medications in CKD. *South Med J.* 2018;111(3): 155–162. DOI: https://doi.org/10.14423/smj.0000000000000781

15. Woźniak-Karczewska M., Čvančarová M., Chrzanowski Ł., Kolvenbach B., Corvini P.F., Cichocka D. N. Isolation of two ochrobactrum sp. strains capable of degrading the nootropic drug - Piracetam. *New Biotechnology.* 2018;43: 37–43. DOI: https://doi.org/110.1016/j.nbt.2017.07.006

16. Zavadenko N. N., Suvorinova N. Yu., Zavadenko A. N. Attention deficit hyperactivity disorder in children: effectiveness of hopantenic acid pharmacotherapy. *Voprosy prakticheskoj pediatrii.* [Clinical Practice in Pediatrics] 2018;13(2): 11–18. DOI: https://doi.org/10.20953/1817-7646-2018-2-11-18

17. Voronina T. A., Litvinova S. A. Pharmacological effects and clinical application of Pantogam and Pantogam active. *Zhurnal nevrologii i psikhiatrii im. S. S. Korsakova.* 2017;117(8): 132–139. DOI: https://doi.org/10.17116/jnevro201711781132-139

18. Zavadenko N. N., Guzeva V. I., Gaynetdinova D. D., Davydova L. A., Zavadenko A. N., Romanova T. A. Pharmacotherapy of psychomotor developmental delay in 6–12 months preterm infants with hypoxic-ischemic encephalopathy (the double-blind comparative multicenter placebo-controlled study). *Zhurnal nevrologii i psikhiatrii im. S. S. Korsakova.* 2019;119(10): 30–39. DOI: https://doi.org/10.17116/jnevro201911910130

19. Stylianou E., Pateraki C., Ladakis D., Cruz-Fernández M., Latorre-Sánchez M., Coll C., Koutinas A. Evaluation of organic fractions of municipal solid waste as renewable feedstock for succinic acid production. *Biotechnology for Biofuels.* 2020;13(1): 13:72. DOI: https://doi.org/10.1186/s13068-020-01708-w

20. Jiang M., Ma J., Wu M., Liu R., Liang L., Xin F., Zhang W., Jia H., Dong W. Progress of succinic acid production from renewable resources: Metabolic and fermentative strategies. *Bioresource Technology.* 2017;245: 1710–1717. DOI: https://doi.org/10.1016/j.biortech.2017.05.209

21. Chetverikova A. G., Kanygina O. N., Alpysbaeva G. Z., Yudin A. A., Sokabayeva S. S. Infrared spectroscopy as the method for determining structural responses of natural clays to microwave exposure. *Kondensirovannye Sredy i Mezhfaznye Granitsy = Condensed Matter and Interphases.* 2019;21(3): 446–454. DOI: https://doi.org/10.17308/kcmf.2019.21/1155

22. Seredin P. V., Goloshchapov D. L., Nikitkov K. A., Kashkarov V. M., Ippolitov Y. A., Jitraporn (Pimm) V. Application of synchrotronic IR-microspectroscopy for analysis of integration of biomimetic composites with native dental tissues. *Kondensirovannye sredy i mezhfaznye granitsy = Condensed Matter and Interphases.* 2019;21(2): 262–277. DOI: https://doi.org/10.17308/kcmf.2019.21/764 (In Russ., abstract in Eng.)

23. Eltsova N. O., Budko E. V. Application of HPLC with optical and thermal methods in complex analysis of inter-component interactions of pharmaceutical compositions. *Sorbtsionnye i Khromatograficheskie Protsessy.* 2019;19(4): 474–480. DOI: https://doi.org/10.17308/sorpchrom.2019.19/786 (In Russ., abstract in Eng.)

Information about the authors

Denis A. Slivkin, Candidate of the Department of General Pharmaceutical and Biomedical Technology of the Medical Institute, Peoples Friendship University of Russia, Moscow, Russian Federation; e-mail: slivkin@pharm.vsu.ru. ORCID iD: https://orcid.org/0000-0002-1933-2123.

Yulia A. Polkovnikova, PhD in Pharmacy, Associate Professor of the Department of Pharmaceutical Technology and Pharmaceutical Chemistry, Faculty of Pharmacy, Voronezh State University, Voronezh, Russian Federation; e-mail: juli-polk@mail.ru. ORCID iD: https://orcid.org/0000-0003-0123-9526.

Alena S. Belenova, PhD in Biology, Assistant of the Department of Pharmaceutical Chemistry and Pharmaceutical Technology, Voronezh State University, Voronezh, Russian Federation; e-mail: alenca198322@mail.ru. ORCID iD: https://orcid.org/0000-0002-9036-7302.

Aleksey I. Slivkin, DSc in Pharmacy, Professor, Head of the Department of Pharmaceutical Chemistry and Pharmaceutical Technology, Voronezh State University, Voronezh, Russian Federation; e-mail: slivkin@pharm.vsu.ru. ORCID iD: 0000-0001-6934-0837.

Svetlana N. Suslina, PhD in Pharmacy, Head of the Department of General Pharmaceutical and Biomedical Technology of the Medical Institute, Peoples Friendship University of Russia, Moscow, Russian Federation; ORCID iD: https://orcid.org/0000-0002-7333-2263.

Anastasia A. Kashchavtseva, Engineer, Department of Pharmaceutical Technology and Pharmaceutical Chemistry, Faculty of Pharmacy, Voronezh State University, Voronezh, Russian Federation; e-mail: farmnastya92@gmail.ru ORCID iD: https://orcid.org/0000-0003-3592-2497.

All authors have read and approved the final manuscript.

Translated by Marina Strepetova
Edited and proofread by Simon Cox

Possibilities and peculiarities of spray technologies in organic synthesis

© 2020 E. N. Fedoseeva✉,a, V. B. Fedoseevb

aN. I. Lobachevsky State University of Nizhny Novgorod – National Research University,
23 Gagarina pr., 603950 Nizhny Novgorod, Russian Federation

bG. A. Razuvaev Institute of Organometallic Chemistry of the Russian Academy of Sciences, 49 ul. Tropinina, Nizhny Novgorod 603950, Russian Federation

Abstract

Size effects considerably change the state and physicochemical properties of dispersal systems. The peculiarities of chemical processes occurring in small (nano, pico, and femtolitre) volumes are of a great importance for the production technologies of unique materials. The aim of this work was the experimental confirmation of size effects during chemical processes in small volumes and their interpretation based on the concepts of chemical thermodynamics.

The object of the study consisted in reactions of organic synthesis conducted in ensembles of sessile drops formed by aqueous solutions of organic compounds with the participation of a gaseous medium. The methods of optical microscopy with digital image processing were used for observation. The experiments definitely demonstrate the influence of geometric parameters (radius, contact angle) on the kinetics of phase and chemical transformations in polydisperse ensembles of sessile drops of organic and aqueous-organic mixtures interacting with volatile reagents in a gaseous medium. These features are manifested in the kinetics of changes in the size of drops as well as in the morphology of products obtained by their evaporation.

The interpretation of size effects in the framework of equilibrium chemical thermodynamics explains the shifts in chemical equilibrium and changes in the reaction rate. The equilibrium conditions arising in drops of different volumes during mass transfer with the gas phase were described. It is stated that the most important factor in the processes of organic synthesis using spray technologies is the high surface activity of organic substances. Comprehension and practical application of these peculiarities allows adjusting the reaction rate, improving the mutual solubility of partially miscible reagents, and affecting the composition and properties of the final product.

Keywords: organic synthesis in spray, size effects, chemical equilibrium constants, liquid-vapour equilibrium, nanoreactor.

✉ Victor N. Fedoseev, e-mail: vbfedoseev@yandex.ru

1. Introduction

Chemical processes involving nanoreactors are a rapidly developing area of nanotechnologies [1]. Any system with the size of the reaction zone comparable with colloid sizes can be called a nanoreactor. Most commonly the following are studied: nanoreactors in micelles formed by surfactants, in liposomes, nanocapsules, pores of nanostructured materials, and in microemulsions [2–5]. Drops in spray technologies are sometimes also considered to be nanoreactors. In fact, spray pyrolysis has already been used as an energy-efficient way of obtaining nanoparticles of metals, oxides, and other compounds [8, 9] used for the creation of functional and construction materials with special properties [10, 11]. The voids of porous materials in the volumes of which the synthesis is conducted, for example, for the modification of the properties of the surface of pores [14] should also be considered as nanoreactors.

The total amount of inorganic materials manufactured using spray technology is so far significantly greater than the amount of organic ones. At the same time, in organic synthesis these technologies have been successfully implemented in the production of pharmaceutical drugs [15] and polymers [16, 17], in particular through photopolymerisation [18,19], during the synthesis of particles with special morphology [20]. The effectiveness of spray processes allows creating green technologies for organic synthesis based on them [21].

Any volatile reagents or monomers can be quickly introduced to the synthesis during the spray stage. However, the prospects of using micro and nanoreactors are mainly associated with the peculiarities of chemical and phase composition of dispersed phases which are formed differently from macroscopic systems in the process of evolution of dispersed particles. The comprehension and practical application of these peculiarities allows increasing the reaction rate, improving the mutual solubility of partially miscible reagents, and affecting the composition and the properties of the final product [20, 22], etc. The processes in spray drops with organic components are more complicated as compared to inorganic substances [23]. In this case, the knowledge of patterns and correlation between physicochemical properties of the components

with size effects allows engaging a greater number of control parameters, which means that there are more opportunities for obtaining a wider range of materials.

In works [24–27] it is shown that a decrease in the size of drops contributes to an increase of the solubility of partially soluble components to the point of thermodynamic instability of heterogeneous state of nonmiscible components, while high supersaturation is more thermodynamically stable in small drops than in large ones. An expected consequence for reversible chemical reactions is additional influence of the volume of such heterogeneous "reactor" on chemical equilibrium. In a trivial version, an increase of the solubility or concentration of a solution of one of the reagents shifts the equilibrium towards the formation of the products when the solvent evaporates.

If the components of the reaction show surface activity, even more complicated patterns are formed. For such reagents, the Gibbs energy of the formation is different in the subsurface layer and in the volume. Correspondingly, constants of the reaction's chemical equilibrium should also be different in the subsurface layer and in the volume, while the effective equilibrium constant becomes dependent on the volume fraction of the subsurface layer. Then, according to the Van 't Hoff equation associating Gibbs energy of the reaction with equilibrium constants, surface activity of the products contributes to the shift of equilibrium towards the products, while the surface activity of the reagents decreases the equilibrium concentration [23]. In the general case, volume, specific area, and radii of curvature of the surface of drops become the factors regulating the conditions of the course and kinetics of chemical processes in a drop or an ensemble of drops exchanging components through the disperse medium.

As a rule, it is almost impossible to control the course of chemical processes in a quickly flying drop of spray, separate drops of concentrated emulsion, or pores of the material. However, the description of chemical processes occurring in small volumes is definitely of interest for many areas of modern technologies. Therefore, one of the goals of this research was the experimental simulation of size effects for

chemical transformations in a small volume based on visual observation and interpretation of these effects based on concepts of chemical thermodynamics. Ensembles of sessile drops partly allow simulating such processes [23–27].

2. Experimental

Reactions were conducted both in open and in partially or completely closed systems. During the reaction, the conditions corresponding to an open system were implemented in the simplest way. A transparent slide with an ensemble of drops of the solution of one of the reagents obtained while spraying was placed on the object plate of the microscope. In close proximity to the ensemble of drops there was a reservoir with volatile reagents (or their solution) or blotting paper soaked in a corresponding solution. Closed and partially closed conditions were implemented in a more complicated way. The unit used in these experiments is presented on a scheme (Fig. 1). The ensemble of drops was placed on the lower surface of the object plate *2*, lying on supports *3*. The volatile reagent solution *4* was placed under the object plate *2* on a movable object plate *5*. The choice of the shape of support *3* allows partially or completely limiting the mass transfer with the environment. Such structure allowed adjusting the presence of volatile reagents and the solvent in the system as well as controlling the rate of their evaporation into the external environment or recondensation between the drops and the reservoir.

The solution of a substrate was applied to the slide using a push-button sprayer. Glass treated with a chromic mixture and washed with distilled water or Lavsan were used as slides. Some object plates were treated with chlorosilane to increase the hydrophobicity.

The described microscopic observations can be performed using any microscope with a digital interface. The following microscopes were used in this work: MBS-10 with a DEM-200 eyepiece camera, Dino-Lite AM451, and Levenhuk D670T. To eliminate the thermal effect of the lighting, LED lights and mirrors were used. The evolution of the ensemble of drops in the course of the reaction was recorded as video files or a series of images. Two methods of observation were used: 1) two directly interacting solutions were continuously
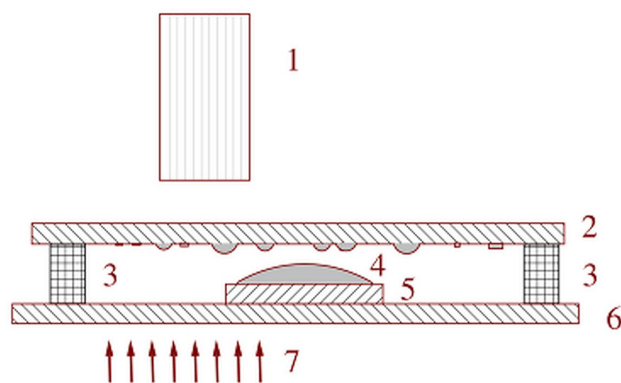

Fig. 1. Installation diagram. *1* – microscope objective, *2* – object plate with sprayed droplets, *3* – support, *4* – solvent, *5* – glass reservoir for volatile reagents, *6* – transparent base, moved by the microscope's target, *7* – lower illumination

recorded on video under the microscope; 2) the reaction was conducted in a chamber for a certain period of time, and after that the slide with drops was placed on the object plate of the microscope and the process of their evaporation from the open slide was recorded. In this case, the slide with the reagent was kept above distilled water for the same period of time as a blank experiment.

The experiments were conducted under room conditions (humidity: 25–45 %; temperature: 20–24 °C). To improve observability, medium and low-concentrated solutions were used, which allowed increasing the time of maturation of the ensemble of drops before the start of crystallisation.

All the reagents used were chemically pure.

3. Results and discussion

The description of phase transformations in a small volume [24] has demonstrated that microscopy is a convenient tool for experimental verification of the results of thermodynamic simulation. The developed methodology allowed discovering and observing for the first time two unusual effects in the solutions drops being evaporated: oscillating crystal–solution phase transformations as well as non-Ostwald behaviour of the ensemble of the drops of the solution where the lifetime of large drops in homogeneous state is shorter than the lifetime of small drops [24, 25].

Using ensembles of drops of different sizes, it is also possible to prove the influence of size effects on the dynamics of the course of reaction predicted in the framework of formal kinetics

and chemical thermodynamics. The search for these patterns was one of the main tasks of experimental observations.

Simple well-known reactions with volatile components were chosen for the observations. This allowed spatially separating the interacting components so that one or both reagents could be absorbed by a drop of the solution from the vapour phase. In this case, the dissolution rate of the reagent and its concentration in drops of different sizes as well as the reaction rate must depend on the curvature of the surface of the drop. In most cases, such criteria of the process as the morphology of the phase being formed and the evaporation rate of the drops were mostly sensitive to size effects.

Let us consider some of the options.

An example of the interaction between two volatile reagents is the reaction of formation of hexamethylenetetramine (urotropin) when formaldehyde is interacting with ammonia $6CH_2O + 4NH_3 \rightarrow C_6H_{12}N_4 + 6H_2O$. When a solution of any of the reagents is sprayed, drops evaporate from the open surface completely and rather quickly. If a slide with a solution of formaldehyde is sprayed on it remains for a short time (for 1 minute or longer) above the reservoir with the ammonia solution, a crystallization (Fig. 2) is observed during the evaporation of drops, which is definitely indicative of the formation of urotropin. It should be noted that the experiment reproduced the size effect described in [23] where formation of a multitude of secondary drops was observed on the surface free from evaporating drops. Fig. 2c shows that the reaction occurs both in the original and the newly formed drops. Fig. 2b shows that crystallisation takes place in large drops first. This is the manifestation of another size effect, non-Ostwald behaviour, that we previously described in [24, 28]. It is associated with the fact that significantly greater supersaturation of the solution can be achieved in small drops.

A similar example is the formation of crystals during the interaction between the ensemble of drops of the hydrogen peroxide solution and acetone vapour.

The interaction between the aqueous solution of urotropin and iodine is an example of reaction of low-volatile substrate with the vapour of a volatile reagent. Complex compounds (clathrates) are formed in the reaction of urotropin with iodine. An ensemble of drops of the aqueous solution of urotropin on a glass slide was kept above the alcohol solution of iodine, after which the structures formed during the evaporation of the drops were recorded. In this case, significant differences were observed in the morphology and the colour of urotropin crystals growing from the solution before and after the interaction with iodine vapour. It should be noted that there are also significant differences in morphology of crystals growing from the drops of aqueous and alcohol solution, which was taken into account during the observation.

An example of interaction between a non-volatile reagent with a volatile one is also presented by the reaction of glycine with formaldehyde. In this case, the interaction between the solution of glycine and the formaldehyde vapour shows only in the significant decrease in the evaporation rate. After being sprayed, the drops of the aqueous solution of glycine on an open glass slide evaporate and crystallise (at $t = 22\pm1$ °C, humidity 40–53 %) for several minutes (Fig. 3a) in a sequence reproducing non-Ostwald behaviour. Under the same conditions, crystallisation does
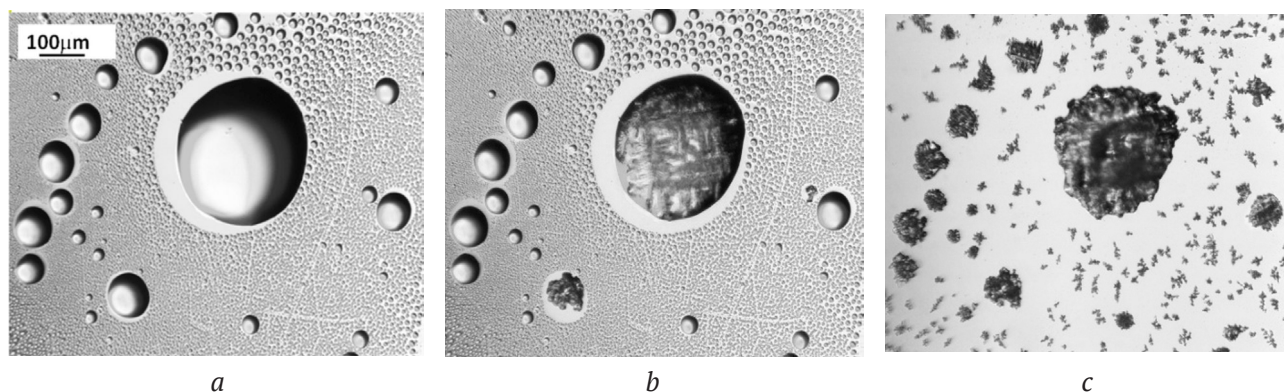

a   *b*   *c*

Fig. 2. The sequence of states of drops of formaldehyde solution kept in ammonia vapour during its evaporation (hydrophobised slide)
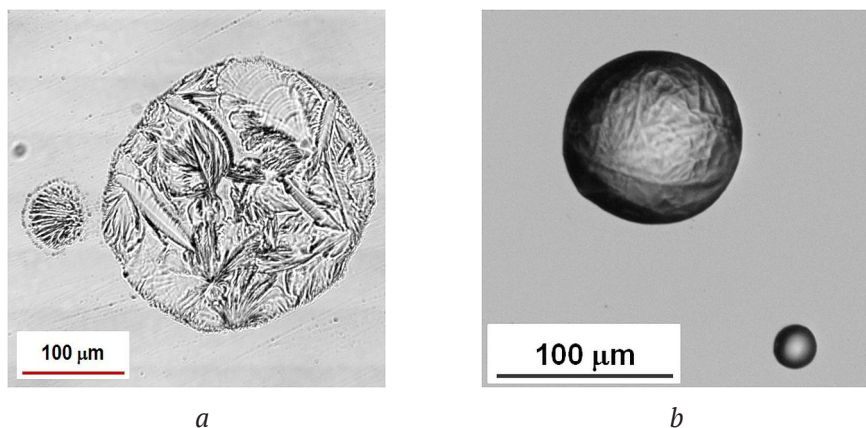
a   *b*

Fig. 3. Glycine crystals (a), droplet surface after reaction with formaldehyde (b)

not occur after the contact with formaldehyde vapour, and a film is formed on the surface of the largest drops (Fig. 3b). It can be assumed that the result of the interaction was the trimerisation or polymerisation of N-methylene glycine [29, p. 334].

The experiments with aqueous solutions of resorcinol interacting with formaldehyde turned out to be the most demonstrative, and the interpretation of the obtained images was definitive (Fig. 4). The criteria of the process were the morphology of the structures formed on the slide after the evaporation of the drops and the evaporation rate. Crystallisation with the formation of clusters of needle crystals subject to weathering occurs in the drops of the original resorcinol solution on the slide only in case of forced drying with a warm airflow (Fig. 4a). The product of the reaction is an amorphous polymer, resorcinol formaldehyde resin.

In a series of experiments, the aqueous solution of resorcinol sprayed on the object plate was in contact with formaldehyde vapour over the time from 15 seconds to 30 minutes. In case of a short duration of interaction, the smallest drops produced an amorphous film when evaporating (Fig. 4b), while typical needle crystals were formed in the drops of medium and large size. With the increased time of reaction, thin structures remained even when larger drops were evaporating. After a ten-minute exposure, needle crystals were not found. It should be noted that resorcinol crystals were completely sublimated from the glass after several days, while the structures formed as a result of the reaction remained unchanged during long-term observation.

A relevant example of a reversible reaction is polycondensation of lactic acid. Elimination of one of the products of the reaction from the reaction mixture shifts the equilibrium towards the
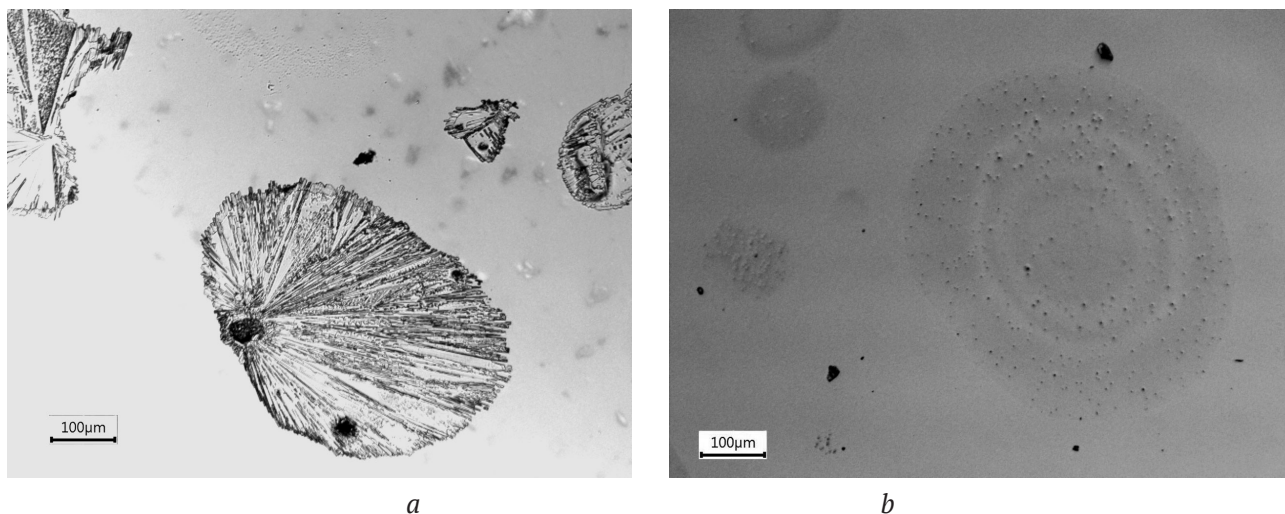

a   *b*

Fig. 4. Crystals formed from drops of an aqueous solution of resorcinol upon forced drying (a); film obtained from this solution after treatment with formaldehyde vapour (10% CH_2O) (b)

formation of a polymer. Therefore, the elimination of water is the key process in the production of polylactide from lactic acid. The task is complicated by the increased viscosity of the reaction mixture hindering heat and mass transfer, which causes local overheating that leads to reactions of gumming and other undesirable transformations. Conditions of heat and mass transfer in the spray allow effectively maintaining the concentration and temperature of the reaction mixture during the whole process. Observations showed that a solid product, which is insoluble when water is applied to the object plate, was formed in the sprayed drops of the aqueous solution of lactic acid at room temperature. Thus, it can be stated that lactide or oligolactide are formed in the spray without any additional influence (heating, vacuuming) and accessory reagents (solvents, catalysts) that are used in existing technologies.

The described experiments allow observing the differences in the reaction occurring in "microreactors" of different volumes. The interpretation presented below explains the thermodynamic nature of these size effects.

3.1. Thermodynamic interpretation

The thermodynamic approach to the study of peculiarities of the course of chemical processes in nanoscale systems is sufficiently widespread and effective [30].

In the case of a spray, the existence of drops of a multi-component solution in the vapour of volatile components is determined by the equilibrium of chemical potentials of the components in the gaseous and condensed phases. As for perfect solutions, this condition is converted using the Kelvin equation, the Ostwald–Freundlich equation, and Raoult's law. Generally, they can be presented in the following way:

$$P_k(r, x_k) = P_{0,k} x_k \exp\left(\frac{2\sigma V_k}{rRT}\right) = P_{ex,k}, \qquad (1)$$

$$P_k(r, L_k) = $$
$$= P_{0,k} x_{k,sat} \exp\left(\frac{4\sigma_{SL}}{L} \frac{V_1}{RT}\right) \exp\left(\frac{2\sigma V_k}{rRT}\right) = P_{ex,k}, \qquad (2)$$

where σ is surface tension, V_k is the molar volume of a component, k, R is the universal gas constant, T is temperature, $P_{0,k}$ is the saturated vapour pressure above the flat surface of a pure component k, $x_{k,sat}$ is the concentration of a saturated

solution of the component forming the crystal, L is the size of the crystal, σ_{SL} is the surface energy of the solution–crystal interphase. Imperfection of the solution can be accounted for by supplementing ratios (1) and (2) with the activity coefficients $\gamma_k(x_i)$ using the corresponding models of an actual solution and the dependence of surface tension on the composition $\sigma(x_i)$ [25].

The equation (1) describes the equilibrium partial pressure of the components that are not present in the crystal. The equation (2) describes the equilibrium partial pressure of the component forming the crystal. If all the components of a drop are volatile, the following identity is established

$$\sum x_k = \sum \frac{P_{ex,k}}{P_{0,k}} \exp\left(-\frac{2\sigma}{r} \frac{V_k}{RT}\right) = 1 \qquad (3)$$

which definitively [27] determines the radius of a drop. The presence of non-volatile components (marked with index c) changes the identity:

$$\sum \frac{P_{ex,k}}{P_{0,k}} \exp\left(-\frac{2\sigma}{r} \frac{V_k}{RT}\right) + \sum x_c(r) = 1. \qquad (4)$$

In case of reversible chemical transformations, the ratios (1)–(4) are supplemented by constants of chemical equilibrium and describe the connection between equilibrium composition, partial pressures of the components in the external environment, radius of a drop, and the size of the crystal. In case of irreversible reactions, the radius of a drop changes over time becoming a function of the transformation degree.

Let us consider the size effect through the reaction

$$A + B \rightleftarrows C, \qquad (5)$$

occurring in a volatile solvent.

Let us describe some variants of the equilibrium state for this reaction:

1. All components are volatile, but their pressure in the external environment $P_{ex,k}$ is determined by external sources. The equilibrium constant K_x of the reaction (5) for a drop is presented as the expression

$$K_x = \frac{x_C}{x_A x_B} = $$
$$= \frac{P_{0,A} P_{0,B}}{P_{0,C}} \frac{P_{ex,C}}{P_{ex,A} P_{ex,B}} \exp\left(-\frac{2\sigma(V_C - V_B - V_A)}{rRT}\right). \qquad (6)$$

This assessment neglects the dependence of surface tension on the composition of $\sigma(x_i)$. The condition $\frac{4}{3}\pi r^3 = n_0 V_0 + n_A V_A + n_B V_B + n_C V_C$ associates the radius of a drop with the amount of the solvent n_0, reagents n_A, n_B and the product n_C in the drop. The radius of a drop and the equilibrium constant are definitely determined by the identity (3), while partial pressure of the solvent influences the equilibrium composition. According to (6), in case of small volume the equilibrium shifts toward the formation of a product if the reaction occurs with the decrease of the volume ($V_C - V_B - V_A < 0$).

2. All components, except for the solvent, are non-volatile, and the pressure of the solvent $P_{ex,0}$ in the system is constant. The equilibrium constant is presented as follows

$$K_x = \frac{x_C}{x_A x_B} = \frac{n_C \left(n_{0A} + n_{0B} - 2n_C + n_0\right)}{\left(n_{0A} - n_C\right)\left(n_{0B} - n_C\right)}, \qquad (7)$$

here n_k is the amount of moles of the components. For non-volatile components in the reaction (5), the conditions of preserving the substance are $n_A + n_C = n_{0A}$, $n_B + n_C = n_{0B}$, here n_{0A} and n_{0B} are the original amount of moles of reagents A and B in the drop.

Substitution (1) gives the following result:

$$K(r) = \frac{n_C n_0}{\left(n_{0A} - n_C\right)\left(n_{0B} - n_C\right)} \frac{P_{ex,0}}{P_0} \exp\left(\frac{2\sigma V_0}{rRT}\right). \qquad (8)$$

The condition associates the radius of a drop and the amount of the solvent. Taking into account the identity (4), the equilibrium constant and the radius are a function of the solvent pressure and the original composition of the drop. In this case, the radius of the drop in the process of achieving chemical equilibrium will decrease (the decrease in the number of moles of non-volatile components is accompanied by the evaporation of the solvent and volatile components). Another kinetic effect is associated with the fact that when highly diluted reaction mixtures are sprayed, the solvent quickly evaporates, which increases the concentration of reagents and accelerates the reaction. As for reversible reactions, the increased concentration of reagents shifts the equilibrium towards the product yield.

Through a variation in the volatility and non-volatility of products, reagents, or solvent, different types of reaction (5) can be analysed. Notably, in the general case, the equilibrium composition and the radius of drops are determined by partial pressures of volatile components.

A thermodynamic model (1)–(8) explains the size effects associated with chemical transformations in disperse systems with a gaseous disperse medium. It involves a number of significant approximations, the rejection of which allows considering more complicated patterns of behaviour of reaction mixtures in a small volume. The introduction of activity coefficients into (1)–(4) allows using different equations for the state of actual solutions. A comparison of the results obtained using the concepts of ideal and real solutions, is described in the work [23]. Dependence of surface tension on the composition of the solution ($\sigma = \sigma(x_i)$ has an additional effect on the state of the dispersal phase. The interaction with the interphase surface changes chemical potentials of the components and, correspondingly, the Gibbs energy of the reaction in the subsurface layer. At the same time, the effective equilibrium constant becomes a function of the volume fraction of the subsurface layer and the specific surface, complicating the correlation (8) between the composition of vapour, radius of spray drops, and the product content. High surface activity typical for most organic compounds allows significantly affecting the transformation degree in the disperse phase [23], which allows expecting a high level of effectiveness of spray technologies during organic synthesis.

Size effects during phase transformations are equally important for chemical processes [26]. Such influence was simulated in the work [31]. In this case, the course of chemical processes is determined by redistribution of components between co-existing condensed phases. The growth of solubility and the increase of homogeneity region create such conditions for the synthesis of substances that are almost impossible to implement in macroscopic systems with low-soluble reagents and can influence the kinetics of chemical processes, thus significantly increasing the rate of processes.

4. Conclusions

The experiments demonstrating chemical interactions in disperse systems with gaseous disperse medium confirm the existence of size effects that are mostly pronounced when observing the kinetics of evaporation of polydispersed ensembles of drops and morphology or solid products formed as a result of this. Thermodynamic interpretation of these effects for reversible chemical processes describes the correlation between equilibrium chemical composition of the disperse phase and the composition of gaseous medium. Size dependence of the chemical equilibrium constants (6)–(8) shows that the transition to micro and nanosized reactors allows significantly changing the product yield and the kinetics of its formation. Large specific surface with a small reaction volume ensures quick interphase mass and heat transfer stabilising the concentrations of reagents and the temperature of processes. Taking into account the effect of the form [32,33] with the same thermodynamic basis can considerably supplement size patterns during chemical processes. The described patterns allow using additional factors expanding the opportunities of spray and sol-gel technologies in the chemical synthesis of new materials.

Conflict of interests

The authors declare that they have no known competing financial interests or personal relationships that could have influenced the work reported in this paper.

References

1. Tretyakov Y. D., Lukashin A. V., Eliseev A. A. Synthesis of functional nanocomposites based on solid-phase nanoreactors. *Russ. Chem. Rev.* 2004;73(9): 899–921. DOI: http://dx.doi.org/10.1070/RC2004v073n09ABEH000918

2. *Nanoreactor Engineering for Life Sciences and Medicine*. Ostafin A., Landfester K. (eds.). AR Tech house; 2009. 283 p.

3. Chen C., Chen Z., Zeng X., Fang X., Zhang Z. Fabrication and characterization of nanocapsules containing n-dodecanol by miniemulsion polymerization using interfacial redox initiation. *Colloid Polym Sci.* 2012;290(4): 307–314. DOI: http://dx.doi.org /10.1007/s00396-011-2545-2

4. Vriezema D. M., Garcia P. M. L., Sancho Oltra N., Hatzakis N. S., Kuiper S. M., Nolte R. J. M., et al. Positional assembly of enzymes in polymersome nanoreactors for cascade reactions. *Angew Chemie Int Ed*. 2007;46(39): 7378–7382. DOI: https://doi.org/10.1002/anie.200701125

5. Wheeler A. Reaction rates and selectivity in catalyst pores. *Advances in Catalysis*. 1951;3: 249–327. DOI: https://doi.org/10.1016/S0360-0564(08)60109-1

6. Zhukalin, D. A. Droplet reactor in nanotechnology. *Kondensirovannye Sredy I Mezhfaznye Granitsy = Condensed Matter and Interphases*, 2018;20(1): 66–74. DOI: https://doi.org/10.17308/kcmf.2018.20/478 (In Russ., abstract in Eng.)

7. Jambovane S. R., Nune S. K., Kelly R. T., McGrail B. P., Wang Z., Nandasiri M. I., et al. Continuous, one-pot synthesis and post-synthetic modification of nanoMOFs using droplet nanoreactors. *Sci. Rep.* 2016;6: 36657-9. DOI: https://doi.org/10.1038/srep36657

8. Penyazkov O. G., Saverchenko V. I., Fisenko S. P. Low-temperature synthesis of nanoparticles in the process of evaporation of femtoliter droplets of a solution at a low pressure. *J. Eng. Phys. Thermophys*. 2014;87(4): 796–801. DOI: https://doi.org/10.1007/s10891-014-1074-5

9. Jaworski R., Pawlowski L., Pierlot C., Roudet F., Kozerski S., Petit F. Recent developments in suspension plasma sprayed titanium oxide and hydroxyapatite coatings. *J. Therm. Spray. Technol*. 2010;19(1–2): 240–247. DOI: https://doi.org/10.1007/s11666-009-9425-z

10. Al-Hamdani K. S., Murray J. W., Hussain T., Clare A. T. Heat-treatment and mechanical properties of cold-sprayed high strength Al alloys from satellited feedstocks. *Surf. Coatings. Technol*. 2019;374: 21–31. DOI: https://doi.org/10.1016/j.surfcoat.2019.05.043

11. Mesquita R. A., Barbosa C. A. High-speed steels produced by conventional casting, spray forming and powder metallurgy. *Mater. Sci. Forum*. 2005;498–499: 244–50. DOI: https://doi.org/10.4028/www.scientific.net/MSF.498-499.244

12. Bronstein L. M., Sidorov S. N., Valetsky P. M. Nanostructured polymeric systems as nanoreactors for nanoparticle formation. *Russ. Chem. Rev.* 2004;73(5): 501–515. DOI: https://doi.org/10.1070/RC2004v073n05ABEH000782

13. Zheng X., Lv Y., Kuang Q., Zhu Z., Long X., Yang S. Close-packed colloidal SiO_2 as a nanoreactor: Generalized synthesis of metal oxide mesoporous single crystals and mesocrystals. *Chem. Mater*. 2014;26(19): 5700–5709. DOI: https://pubs.acs.org/doi/10.1021/cm5025475

14. Len'shina N. A., Arsenyev M. V., Shurygina M. P., Chesnokov S. A., Abakumov G. A. Photoreduction of o-benzoquinone moiety in mono- and poly(quinone methacrylate) and on the surface of polymer matrix pores. *High Energy Chem*. 2017;51(3): 209–214. DOI: https://doi.org/10.1134/s0018143917030080

15. Wanning S., Süverkrüp R., Lamprecht A. Pharmaceutical spray freeze drying. *Int. J. Pharm*. 2015;488(1–2): 136–153. DOI: https://doi.org/10.1016/j.ijpharm.2015.04.053

16. Hergeth W., Jaeckle C., Krell M. Industrial process monitoring of polymerization and spray drying processes. *Polym. React. Eng.* 2003;11(4): 663–714. DOI: https://doi.org/10.1081/PRE-120026369

17. Sinha-Ray S. Spray in Polymer Processing. In: Basu S., Agarwal A., Mukhopadhyay A., Patel C. (eds) *Droplet and Spray Transport: Paradigms and Applications. Energy, Environment, and Sustainability.* Springer, Singapore; 2017. p. 31–54. DOI: https://doi.org/10.1007/978-981-10-7233-8_3

18. Akgün E., Hubbuch J., Wörner M. Perspectives of aerosol-photopolymerization: Nanoscale polymer particles. *Chem. Eng. Sci.* 2013;101: 248–252. DOI: https://doi.org/10.1016/j.ces.2013.06.010

19. Akgün E., Muntean A., Hubbuch J., Wörner M., Sangermano M. Cationic aerosol photopolymerization. *Macromol. Mater. Eng.* 2015;300(2): 136–139. DOI: https://doi.org/10.1002/mame.201400211

20. Zhang Y., Suslick K. S. Synthesis of poly(3,4-ethylenedioxythiophene) microspheres by ultrasonic spray polymerization (USPo). *Chem. Mater.* 2015;27(22): 7559–7563. DOI: https://doi.org/10.1021/acs.chemmater.5b03423

21. Zhang W., Cue B. W. (eds) *Green techniques for organic synthesis and medicinal chemistry.* Chichester, UK: John Wiley & Sons, Ltd; 2012. 842 p. DOI: https://doi.org/10.1002/9780470711828

22. Carné-Sánchez A., Imaz I., Cano-Sarabia M., Maspoch D. A spray-drying strategy for synthesis of nanoscale metal–organic frameworks and their assembly into hollow superstructures. *Nat. Chem.* 2013;5(3): 203–211. DOI: https://doi.org/10.1038/nchem.1569

23. Fedoseev V. B., Fedoseeva E. N. Samoformirovanie ansamblei kapel vodno-organicheskikh i vodno-polimernykh rastvorov v parakh letuchikh komponentov. In: *Oligomery-2019: Sbornik trudov XVIII Mezhdunarodnoi konferentsii po khimii i fizikokhimii oligomerov, 16-21 September 2019.* [Self-formation of drops ensembles of aqueous-organic and aqueous-polymer solutions in vapour of volatile components. In: *Oligomers: Proc. 18th Int. Conf. on the Chemistry and Physical Chemistry of Oligomers*] Chernogolovka: IPKHF RAN Publ.; 2019. T1. p. 218–235. (In Russ.)

24. Titaeva E. K., Fedoseev V. B. Specific features of crystallization of supersaturated solution in femtoliter-volume systems. *Crystallogr. Reports.* 2014;59(3): 437–441. DOI: https://doi.org/10.1134/s1063774514030195

25. Fedoseev V. B., Fedoseeva E. N. States of a supersaturated solution in limited-size systems. *JETP Lett.* 2013;97(7): 408–412. DOI: https://doi.org/10.1134/s0021364013070059

26. Fedoseev V. B., Fedoseeva E. N. Size effects during phase transformations in stratifying systems. *Russ. J. Phys. Chem. A.* 2014;88(3): 436–441. DOI: https://doi.org/10.1134/s0036024414020083

27. Fedoseev V. B., Fedoseeva E. N. Formation of Bi- and polymodal distributions and the non-ostwald behavior of disperse systems. *J. Eng. Phys. Thermophys.* 2019;92(5): 1191–1200. DOI: https://doi.org/10.1007/s10891-019-02033-2

28. Fedoseeva E. N., Fedoseev V. B. Non-Ostwald behavior of disperse systems in evaporation and crystallization of droplets of water–organic solutions. *Technical Physics,* 2020;65(6): 839–845. DOI: https://doi.org/10.1134/S1063784220060110

29. Vorozhtcov N. N. *Osnovy sinteza promezhutochnykh produktov i krasitelei* [Basics of the synthesis of industrial products and dyes]. Moscow-Leningrad: Gosudarstvennoe himiko-tekhnicheskoe izdatel`stvo ONTI Publ; 1934. 540 p. (In Russ.)

30. Vigdorovich V. I. Some property features of nanostructured materials as participants of chemical processes. *Kondensirovannye Sredy I Mezhfaznye Granitsy = Condensed Matter and Interphases,* 2018;20(2): 211–217. DOI: https://doi.org/10.17308/kcmf.2018.20/512 (In Russ., abstract in Eng.)

31. Shishulin A. V., Fedoseev V. B. On some peculiarities of stratification of liquid solutions within pores of fractal shape. *J. Mol. Liq.* 2019;278: 363–367. DOI: https://doi.org/10.1016/j.molliq.2019.01.050

32. Shishulin A. V., Fedoseev V. B. On Mutual Solubility in Submicron-Sized Particles of the Pt–Au Catalytic System. *Kinetics and Catalysis.* 2019;60(3): 315–319. DOI: https://doi.org/10.1134/s0023158419030121

33. Shishulin A. V., Shishulina A. V. Equilibrium phase composition and mutual solubilities in fractal nanoparticles of the W-Cr heavy pseudo-alloy. *Physical and Chemical Aspects of the Study of Clusters, Nanostructures and Nanomaterials.* 2019;(11): 380–388. DOI: https://doi.org/10.26456/pcascnn/2019.11.380

Information about the authors

Elena N. Fedoseeva, PhD in Chemistry, Research Fellow at the Laboratory of Applied Chemistry and Ecology*, Lobachevsky State University of Nizhny Novgorod, Nizhny Novgorod,* Russian Federation; e-mail: el.nik.fedoseeva@gmail.com. ORCID iD: https://orcid.org/0000-0002-5066-2331.

Victor B. Fedoseev, DSc in Chemistry, Leading Researcher, G. A. Razuvaev Institute of Organometallic Chemistry of the Russian Academy of Sciences, Nizhny Novgorod, Russian Federation; e-mail: vbfedoseev@yandex.ru. ORCID iD: https://orcid.org/0000-0001-9281-3137.

All authors have read and approved the final manuscript.

Translated by Marina Strepetova
Edited and proofread by Simon Cox